



TEAM TAO



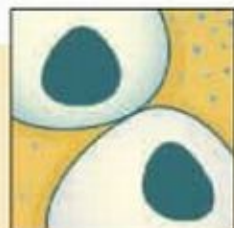
26 November 2004

Science

Vol. 306 No. 5701
Pages 1421-1632 \$10

**Cell
Signaling**

 AAAS



SPECIAL ISSUE

CELL SIGNALING

A set of Viewpoints in this issue provides a close-up view of signaling mechanisms by which cells detect and respond to cues in their environment. These overviews accompany pathways presented in the STKE Connections Map database at Science's STKE. See page 1505. [Image: Julie White/Science]

Volume 306
26 November 2004
Number 5701

INTRODUCTION

1505 Common Signaling Themes

VIEWPOINTS

1506 Common and Distinct Elements in Cellular Signaling via EGF and FGF Receptors
J. Schlessinger

1508 Pheromone Signaling Mechanisms in Yeast: A Prototypical Sex Machine
Y. Wang and H. G. Dohlman

1509 Jekyll and Hyde in the Microbial World
D. M. Truckses, L. S. Garrenton, J. Thorer

1511 When the Stress of Your Environment Makes You Go HOG Wild
P. J. Westfall, D. R. Ballou, J. Thorer

1513 The Ethylene Signaling Pathway
J. M. Alonso and A. N. Stepanova

1515 Keeping the Leaves Green Above Us
A. Gfeller and E. E. Farmer

1517 Natural Killer Cell Signaling Pathways
E. Vivier, J. A. Nunes, F. Vély

related Editorial page 1437

For related online content, see page 1431, or go to www.sciencemag.org/sciext/cellsignaling

DEPARTMENTS

- 1431 SCIENCE ONLINE
- 1433 THIS WEEK IN SCIENCE
- 1437 EDITORIAL by Lee E. Eiden
A Two-Way Bioinformatic Street
related Cell Signaling section page 1505
- 1439 EDITORS' CHOICE
- 1444 CONTACT SCIENCE
- 1449 NETWATCH
- 1496 AAAS NEWS AND NOTES
- 1579 NEW PRODUCTS
- 1592 SCIENCE CAREERS

NEWS OF THE WEEK

- 1450 U.S. NATIONAL ACADEMIES
Advice on Science Advising Leaves Plenty of Questions
- 1450 PALEOANTHROPOLOGY
Skeptic to Take Possession of Flores Hominid Bones
- 1451 SCHOLARLY PUBLISHING
NIH Flooded With Comments on Public Access Proposal
- 1453 OBESITY RESEARCH
New Data on Appetite-Suppressing Peptide Challenge Critics
- 1453 SCIENCE SCOPE
- 1454 EVOLUTION
Ice Ages May Explain Ancient Bison's Boom-Bust History
related Report page 1561
- 1455 MEDICINE
Bone Marrow Cells: The Source of Gastric Cancer?
related Report page 1568
- 1457 BIOCHEMISTRY
Immune Cells Speed the Evolution of Novel Proteins



1460



1488
& 1565

- 1458 AGRICULTURE
China Could Be First Nation to Approve Sale of GM Rice
- 1458 PARTICLE PHYSICS
Neutrinos Are All Flip-Floppers, Japanese Study Shows
- 1459 EUROPEAN SCIENCE
New Commissioner Calls for Evolution, Not Revolution
- 1460 THEORETICAL PHYSICS
String Theory Gets Real—Sort Of
The Children of the Revolution
- 1463 U.S. SCIENCE POLICY
What Can NIH Do for Physicists?
- 1465 MIDDLE EAST
X-ray Source Produces a Glimmer of Hope
- 1466 MEETING
Society of Vertebrate Paleontology
Head Games Show Whether Dinosaurs Went on Two Legs or Four
Antiextinction Tip: Eat to Live
Timing Complicates History of Horses
Snapshots From the Meeting
- 1469 RANDOM SAMPLES

LETTERS

- 1473 Using Stimulants in Children with ADHD
D. A. Waschbusch and W. E. Pelham Jr.
Outbreak of West Nile Virus in North America
A. Spielman et al. Response D. M. Fonseca et al.
Mouse Biology at Monterotondo
F. C. Kafatos
Beauty, Art, and Foreplay? *M. Grayson*
- 1477 Corrections and Clarifications

BOOKS ET AL.

- 1478 PRACTICE OF SCIENCE
The Nature of Scientific Evidence: Statistical, Philosophical, and Empirical Considerations
M. L. Taper and S. R. Lefe, Eds., reviewed by M. Mangel

Contents continued

BOOKS ET AL. CONTINUED

- 1479 **ENVIRONMENT**
Forests in Time The Environmental Consequences of 1,000 Years of Change in New England
D. R. Foster and J. D. Aber, Eds., reviewed by M. Williams

1480 **Nota Bene on Eyes, Lies, and Illusions**

POLICY FORUM

- 1482 **SOCIAL PSYCHOLOGY**
Why Ordinary People Torture Enemy Prisoners *S. T. Fiske, L. T. Harris, A. J. C. Cuddy*

PERSPECTIVES

- 1484 **MOLECULAR BIOLOGY**
A Higher Order of Silence *A. Mohd-Sarip and C. P. Verrijzer* *related Reports pages 1571 and 1574*
- 1485 **PHYSICS**
What is Dark Matter Made Of? *K. Zioutas, D. H. H. Hoffmann, K. Dennerl, T. Papaevangelou*
- 1488 **ECOLOGY**
Oh the Locusts Sang, Then They Dropped Dead *R. S. Ostfeld and F. Keesing* *related Report page 1565*
- 1489 **PLANETARY SCIENCE**
Nothing Simple About Asteroids *E. Asphaug* *related Report page 1526*
- 1492 **EVOLUTION**
Epistasis in RNA Viruses *Y. Michalakis and D. Roze* *related Report page 1547*

SCIENCE EXPRESS www.scienceexpress.org

PHYSICS: Electron Coherence in a Melting Lead Monolayer

F. Baumberger, W. Auwärter, T. Greber, J. Osterwalder

Fixing a thin lead layer to a solid copper substrate allows the electronic properties of molten lead to be successfully probed, revealing how conducting electrons become localized as the metal melts.

CHEMISTRY: A Late-Transition Metal Oxo Complex: $K_7Na_9[O=Pt^{IV}(H_2O)L_2]$, $L = [PW_9O_{34}]^{9-}$

T. M. Anderson et al.

A stable molecule contains a single oxygen atom bound only to platinum, contrary to the paradigm that noble metals do not form such compounds.

DEVELOPMENTAL BIOLOGY: Epithelial-to-Mesenchymal Transition Generates Proliferative Human Islet Precursor Cells

M. C. Gershengorn, A. A. Hardikar, C. Wei, E. Geras-Raaka, B. Marcus-Samuels, B. M. Raaka

Cultured human insulin-secreting cells can be coaxed to become less differentiated and then to divide into insulin-producing cells that are potentially useful for treating diabetes.

TECHNICAL COMMENT ABSTRACTS

- 1477 **OCEAN SCIENCE**
Comment on "Enhanced Open Ocean Storage of CO₂ from Shelf Sea Pumping"
W.-J. Cai and M. Dai

full text at www.sciencemag.org/cgi/content/full/306/5701/1477c

- Response to Comment on "Enhanced Open Ocean Storage of CO₂ from Shelf Sea Pumping"**
H. Thomas, Y. Bozec, K. Elkalay, H. J. W. de Baar

full text at www.sciencemag.org/cgi/content/full/306/5701/1477d

BREVIA

- 1525 **APPLIED PHYSICS: Stokes Drag on a Sphere in a Nematic Liquid Crystal**
J. C. Loudet, P. Hanusse, P. Poulin

Measurement of the Brownian motion of droplets in an anisotropic liquid confirms the theoretical predictions of how drag varies in different directions.

REPORTS

- 1526 **PLANETARY SCIENCE: Impact-Induced Seismic Activity on Asteroid 433 Eros: A Surface Modification Process**

J. E. Richardson, H. J. Melosh, R. Greenberg

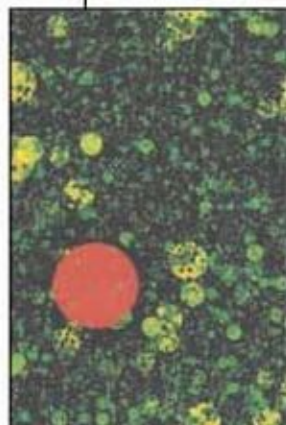
Impact-induced seismic reverberations on the asteroid Eros, despite its low gravity, cause its loose soil to accumulate in craters covering some small craters completely. *related Perspective page 1489*

- 1529 **CHEMISTRY: Periodic Mesoporous Dendrisilicas**
K. Landskron and G. A. Ozin

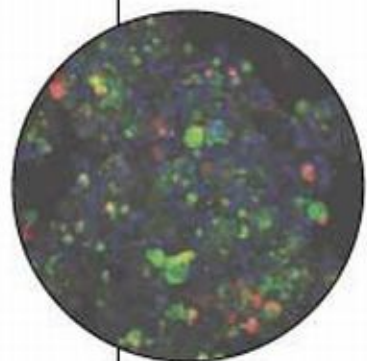
Branched organic molecules and siloxy groups can self-assemble to yield a material with large linear pores surrounded by porous walls that can transmit fluids or act as a sieve.

- 1532 **CHEMISTRY: A Reversible Synthetic Rotary Molecular Motor**
J. V. Hernández, E. R. Kay, D. A. Leigh

Chemical reactions can drive a small molecular ring sequentially around a larger ring in either direction.



1489 &
1526

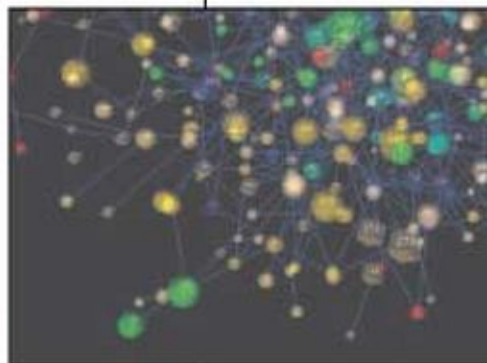


1537

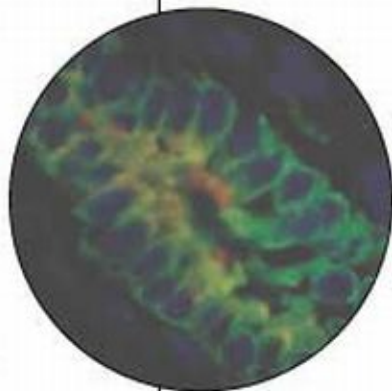
Contents continued

REPORTS CONTINUED

- 1537 **MATERIALS SCIENCE:** Three-Dimensional Hydrogen Microscopy in Diamond
P. Reichart, G. Datzmann, A. Hauptner, R. Hertzenberger, C. Wild, G. Dollinger
 Proton-proton scattering reveals hydrogen impurities in artificial diamonds, providing critical information for improving their synthesis and material properties.
- 1540 **APPLIED PHYSICS:** Probing Electronic Transitions in Individual Carbon Nanotubes by Rayleigh Scattering
M. Y. Sfeir, F. Wang, L. Huang, C.-C. Chuang, J. Hone, S. P. O'Brien, T. F. Heinz, L. E. Brus
 Semiconducting and metallic nanotubes can be distinguished by how they scatter a bright white light.
- 1543 **GEOPHYSICS:** Seismic Anisotropy Beneath Ruapehu Volcano: A Possible Eruption Forecasting Tool
A. Gerst and M. K. Savage
 Magma ascent likely altered the distribution of cracks beneath a New Zealand volcano over several years, affecting the speed of seismic waves traveling in different directions.
- 1547 **EVOLUTION:** Evidence for Positive Epistasis in HIV-1
S. Bonhoeffer, C. Chappey, N. T. Parkin, J. M. Whitcomb, C. J. Petropoulos
 The effect of multiple mutations on the growth of HIV is less than expected from the sum of their individual effects, contradicting current genetic theories of sexual reproduction. *related Perspective page 1492*
- 1550 **BIOCHEMISTRY:** Femtomolar Sensitivity of a NO Sensor from *Clostridium botulinum*
P. Nioche, V. Berka, J. Vipond, N. Minton, A.-L. Tsai, C. S. Raman
 Prokaryotes contain an ancient protein with an unusual heme-nitrosyl complex that strongly binds and sequesters the otherwise deadly signaling molecule nitric oxide.
- 1553 **GENETICS:** Compensated Deleterious Mutations in Insect Genomes
R. J. Kulathinal, B. R. Bettencourt, D. L. Hartl
 During the evolution of *Drosophila*, genetic mutations commonly canceled out the effects of other, harmful mutations.
- 1555 **GENETICS:** A Probabilistic Functional Network of Yeast Genes
I. Lee, S. V. Date, A. T. Adai, E. M. Marcotte
 Bayesian combination of connections from protein interaction and microarray studies in yeast yields a gene interaction map that is more robust than that produced by only one approach.
- 1558 **CELL SIGNALING:** Requirement of JNK2 for Scavenger Receptor A-Mediated Foam Cell Formation in Atherogenesis
R. Ricci et al.
 Inhibition of a stress-related kinase can help to prevent atherosclerosis in a mouse model of the disease.
- 1561 **EVOLUTION:** Rise and Fall of the Beringian Steppe Bison
B. Shapiro et al.
 A sharp decline in the genetic diversity of fossil bison in Eastern Siberia and North America began about 35,000 years ago, when glaciers were advancing, not later when human hunting peaked. *related News story page 1454*
- 1565 **ECOLOGY:** Periodical Cicadas as Resource Pulses in North American Forests
L. H. Yang
 Experimental treatments imply that the numerous cicada carcasses that litter forest floors every 17 years fertilize the forest ecosystem, first below ground, then above. *related Perspective page 1488*
- 1568 **MEDICINE:** Gastric Cancer Originating from Bone Marrow-Derived Cells
J. Houghton et al.
 The stem cells that give rise to gastric cancer in mice are derived from bone marrow, not from the local epithelia as previously assumed. *related News story page 1455*
- 1571 **MOLECULAR BIOLOGY:** Nucleosome Arrays Reveal the Two-Start Organization of the Chromatin Fiber
B. Dorigo, T. Schalch, A. Kulangara, S. Duda, R. R. Schroeder, T. J. Richmond
 The 30-nanometer-wide fiber of chromatin is formed by two side-by-side helices of nucleosomes, not a single helix as suggested by the classical solenoid model. *related Perspective page 1484*
- 1574 **MOLECULAR BIOLOGY:** Chromatin Compaction by a Polycomb Group Protein Complex
N. J. Francis, R. E. Kingston, C. L. Woodcock
 A development protein silences chromatin by inducing the nucleosomes to cluster. *related Perspective page 1484*



1555



1455
& 1568



ADVANCING SCIENCE. SERVING SOCIETY

SCIENCE (ISSN 0036-8073) is published weekly on Friday, except the last week in December, by the American Association for the Advancement of Science, 1200 New York Avenue, NW, Washington, DC 20005. Periodicals Mail postage (publication No. 406400) paid at Washington, DC, and additional mailing offices. Copyright © 2004 by the American Association for the Advancement of Science. The title SCIENCE is a registered trademark of the AAAS. Domestic individual membership and subscription (\$1 issue) \$130 (\$74 allocated to subscription). Domestic institutional subscription (\$1 issue) \$500. Foreign postage extra: Mexico, Caribbean (surface mail) \$15; other countries (air assist delivery) \$45. First class, airmail, student, and emerita rates on request. Canadian rates with GST available upon request. GST #R123488122. Publications Mail Agreement Number 1069624. Printed in the U.S.A.

Change of address: allow 4 weeks, giving old and new addresses and 8-digit account number. Postmaster: Send change of address to Science, P.O. Box 10811, Danbury, CT 06815-1011. Single copy sales: \$10.00 per issue prepaid includes surface postage; bulk rates on request. Authorization to photocopy material for internal or personal use, or the internal or personal use of specific clients, is granted by AAAS to libraries and other users registered with the Copyright Clearance Center (CCC) Transactional Reporting Service, provided that \$13.00 per article is paid directly to CCC, 222 Rosewood Drive, Danvers, MA 01923. The identification code for Science is 0036-8073/04 \$13.00. Science is indexed in the Reader's Guide to Periodical Literature and in several specialized indexes.

Contents continued ▶

Virus's Plan of Attack Identified

Findings may help AIDS patients with rare brain disease.

Psychologists Probe Perfect Pitch

Ability may have more to do with native language than musical training.

Wave on a Wire

Simple technology may help harness terahertz ray.



Confronting lab rage.

science's next wave www.nextwave.org CAREER RESOURCES FOR YOUNG SCIENTISTS

MiSciNET: Scientific Entrepreneurship Is an Option *S. Clemmons*

A Ph.D. student is interested in transforming his thesis work into a successful biotech company.

US: Educated Woman—Chapter 33, The Heart of Grad School Darkness *M. P. DeWhyse*

Lab rage and desperation overtake advanced graduate students when motivation wanes.

GLOBAL/US: Smart Dust *J. Link*

A graduate student talks about the bright future for women researchers in materials science.

GLOBAL/US: Materials Science—Let's Do the Numbers *J. Austin*

Materials science research is full of opportunities and talented scientists chasing a limited number of jobs.

GLOBAL/EU: Materials to Make Music *A. Forde*

The COLLAPSE project is investigating the corrosion of lead-tin alloys of Baroque Organ pipes in Europe.

EUROPE: European Science Bytes *Next Wave Staff*

Read about the latest funding, training, and job market news from Europe.

science's sage ke www.sageke.org SCIENCE OF AGING KNOWLEDGE ENVIRONMENT

REVIEW: Nuclear Hormone Receptors, Metabolism, and Aging—

What Goes Around Comes Around *K. Pardee, J. Reinking, H. Krause*

Transcription factors link lipid metabolism and aging-related processes.

News Focus: Young at Heart *R. J. Davenport*

Life-extending mutation preserves fly hearts.

News Focus: Pay by the Pound *M. Leslie*

Added weight might take a toll on the brain.



Numerous roles of nuclear receptors.



A common signaling module.

science's stke www.stke.org SIGNAL TRANSDUCTION KNOWLEDGE ENVIRONMENT

Related Cell Signaling section page 150S

EDITORIAL GUIDE: Focus Issue on Cell Signaling—Making New Connections

N. R. Gough, E. M. Adler, L. B. Ray

Learn about the new signaling pathways and data export options now available.

CONNECTIONS MAPS

Browse this database of cell signaling pathways and components.

Separate individual or institutional subscriptions to these products may be required for full-text access.

Romancing the Shaken Stone

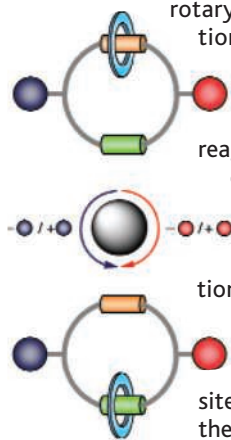
The surface of asteroid 433 Eros is heavily cratered, covered with loose regolith and ubiquitous boulders. The regolith shows evidence for sliding down slopes and ponding in small valleys, and has evidently obscured small craters (diameters less than 100 meters), even though the asteroid has minimal gravity. **Richardson et al.** (p. 1526; see the Perspective by **Asphaug**) show that the regolith movements are caused by seismic reverberations after impact events. Their model of this process finds that the number of observed and buried craters on Eros is consistent with the modeled impactor population in the main asteroid belt where Eros resides.

Imaging Hydrogen in Diamond

The thermal, mechanical, and electronic properties of diamond make it a desirable material to use in high-power electronics. However, the preparation techniques for synthetic and thin-film diamond that produce material of sufficient quality unavoidably introduce hydrogen into the structure. **Reichart et al.** (p. 1537) introduce a technique based on proton-proton scattering that allows the hydrogen in the diamond to be imaged. A knowledge of where the hydrogen resides and in what amounts should help in optimizing deposition and synthetic processes.

Synthetic Motors That Reverse

Biological motors can display reversible motion, such as the F_1F_0 -adenosine triphosphatase motor. A chemically synthesized rotary motor that displays reversible unidirectional motion is reported by **Hernández et al.** (p. 1532), in which a smaller ring moves between positions defined along a larger ring. The stepwise addition of reagents destabilizes noncovalent bonding at one site on the larger ring, which allows the small ring to move but only after deprotection and reprotection steps allow it to reach a more favorable recognition site. The small ring can be returned back to its starting position with a similar sequence of reagents. The authors note that unlike random motion between the sites, chemical energy must be expended for the motion to be deterministic.



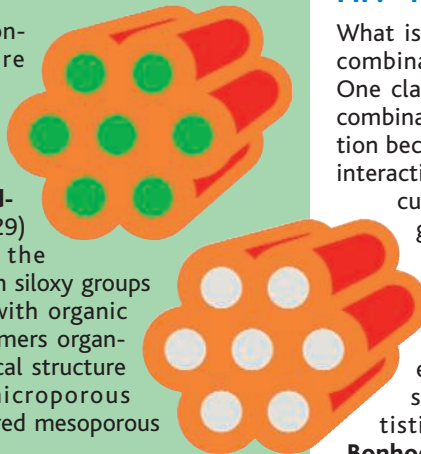
Eruption Precursors: This Wave or That

Seismic anisotropy, in which a shear wave can be split into fast and slow moving modes by oriented minerals or structures

such as aligned cracks, may be useful for determining the state of stress beneath a volcano. **Gerst and Savage** (p. 1543) found that the anisotropy beneath Ruapehu volcano, New Zealand, changed because of the pressurization and depressurization of the magma system when magma was erupted and new magma filled the evacuated conduits.

Dendrimer Templates

Organic dendrimers consist of a central core structure, surrounded by successive branches or arms, that sprout outward much like the branches on a tree. **Landskron and Ozin** (p. 1529) have functionalized the ends of dendrimers with siloxy groups and templated them with organic surfactants. The dendrimers organize to form a hierarchical structure with well-defined microporous channel walls and ordered mesoporous channels.



Positive Epistasis in HIV-1 Evolution

What is the evolutionary benefit of recombination and sexual reproduction? One class of theories suggests that recombination has been favored by selection because of its influence on epistatic interactions, whereby a gene at one locus influences the expression of a gene at another. Retroviruses such as human immunodeficiency virus-type 1 (HIV-1) offer the opportunity to test such theories because they exhibit rates of recombination sufficiently large to provide, statistically significant sample sizes. **Bonhoeffer et al.** (p. 1547; see the Perspective by **Michalakis and Roze**) analyzed a data set of nearly 10,000 HIV-1

sequences with precise fitness estimates, based on an assay that measures the total production of progeny virus after a single full round of replication. They find evidence for positive epistasis, which calls into question theories that are based on negative epistasis. In addition, it appears that recombination slows down, rather than accelerates, the evolution of drug resistance in HIV-1.

A Bacterial Nose for NO

Nitric oxide is an important signaling molecule in mammals, where it acts in part when sensed by a heme protein, soluble guanylate cyclase. **Nioche et al.** (p. 1550, published online 7 October 2004) searched for ancestral proteins with related NO-binding heme domains in the bacterium *Clostridium botulinum*. NO is toxic to *C. botulinum*, and the bacterium actively moves away from nitrite-preserved meat. The authors identified a bacterial protein with an extreme (femtomolar) binding affinity for NO, and elucidated the crystal structure of a related molecule from *Thermoanaerobacter tengcongensis*. NO-binding domains thus provide prokaryotes with a highly sensitive sensor for NO.

Evolution Through Compensation

Comparisons between the previously sequenced genomes of the fruit fly, *Drosophila melanogaster*, and its relative, *D. pseudoobscura*, have allowed **Kulathinal et al.** (p. 1553, published online 21 October 2004) to explore the landscape of protein evolution. Amino acid replacements that are harmful in *D. melanogaster* were often observed as the wild type in *D.*

CONTINUED ON PAGE 1435

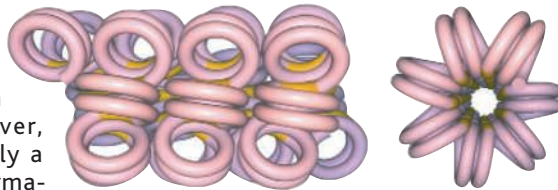
pseudoobscura. Similar results were seen with the more distantly related mosquito, *Anopheles gambiae*. Thus, compensating mutations must occur and become fixed very frequently in populations.

Integrating Gene Interaction Data

Genes can interact in many more ways than through direct protein-protein associations. **Lee et al.** (p. 1555) have developed a unified scoring scheme that enables integration of different kinds of data weighted according to the data quality. An integrated network of *Saccharomyces cerevisiae* genes was built from co-expression, phylogenetic, gene-fusion, as well as physical and genetic interaction data sets. The addition of different kinds of data resulted in greater certainty that the linkages made were correct and made it easier to predict gene function.

Jnking Atherosclerosis

Atherosclerosis is the most common cardiovascular disease in Europe and North America. The c-jun-NH₂-terminal kinase (Jnk) family is implicated in atherogenesis. **Ricci et al.** (p. 1558) addressed the function of JNK in atherogenesis, using atherosclerosis-prone apolipoprotein E (ApoE)-deficient mice simultaneously lacking either Jnk1 or Jnk2. Jnk2 deletion strikingly reduced plaque formation in ApoE deficient mice. However, deletion of Jnk1 revealed only a slight effect on atheroma formation. Pharmacological inhibition of overall Jnk activity substantially suppressed atherosclerosis in ApoE-deficient mice. Specific inhibition of JNK2 activity may thus represent a therapeutic approach to ameliorate atherosclerosis.



Bone Marrow Contribution to Gastric Cancers?

Although the cellular origin of epithelial cancers, such as gastric cancer induced by *Helicobacter pylori* infection, remains to be established, a prevailing assumption is that they derive from resident epithelial stem cells. In contrast to this theory, **Houghton et al.** (p. 1568; see the news story by **Marx**) find that gastric cancers caused by experimental *Helicobacter* infection in mice were of bone marrow, rather than epithelial cell, origin. Bone marrow-derived cells from donor mice were tracked in chronically infected recipients and predominated in the gastric mucosa where they displayed features of neoplastic progression, eventually forming epithelial cancers. If an equivalent contribution of bone marrow-derived cells to epithelial cancers could be established in humans, this finding would significantly revise our understanding of the origin and progression of malignancy.

Compact DNA and Gene Regulation

The DNA of all eukaryotes is compacted into chromatin, the primary unit of which is the nucleosome. Although the structure of the nucleosome core bound to DNA is known to atomic resolution, the higher order, compacted structures of chromatin, and the role of this compaction in regulating gene expression, are less clear (see the Perspective by **Mohd-Sarip** and **Verrijzer**). **Dorigo et al.** (p. 1571) analyzed the first level of higher order chromatin organization, the 30-nanometer fiber, using in vitro reconstituted nucleosome arrays cross-linked for stability. Unlike the classical solenoid model for the 30-nanometer fiber, which forms a "one-start helix," the fibers assume a "two-start helix" of nucleosomes. The Polycomb Group (PcG) genes are critical for metazoan development and maintenance of developmental patterning. It has been suggested that PcG proteins repress genes by nucleating a condensed chromatin structure. **Francis et al.** (p. 1574) now confirm the compaction of a nucleosomal array by the addition of PcG proteins to chromatin.

A Two-Way Bioinformatic Street

The rapid emergence of Web-based bioinformatics systems reflects the research community's attempts to embrace the biological complexity uncovered by high-throughput genome, transcriptome, and proteome data acquisition and the sheer size of the modern scientific endeavor. If information systems can match this complexity, biology will be enriched as a result. If not, scientific excitement may paradoxically be dampened by data flow. The question is, how should biological information systems and the relationship between those who use them and contribute to them further evolve?

Before the advent of high-throughput research genres such as genomics and proteomics, fields already replete with information such as cell signaling (focused on uncovering the flow of information through a cell) advanced through scientists cross-communicating and assembling and synthesizing their own information. Because deciphering cell signal transduction is crucial to understanding normal and diseased biological processes, curating reliable data in the field has become at once a necessity and an enormous challenge, given the massive increase in available data. Cross-communication between the users and curators (also enlisted as experts, authorities, and gurus) of databases is now at the heart of enhancing data reliability. Efforts including the Connections Maps at *Science's* Signal Transduction Knowledge Environment (STKE) and pathway-building at Biocarta, Inc., exemplify Web-based databases that include an avenue for making the curator/user interface a two-way street. Enhancing curator/user exchanges might make visiting these environments a more lively and entertaining experience and increase their usage, large-scale participation being the sine qua non of usefulness to the scientific community.

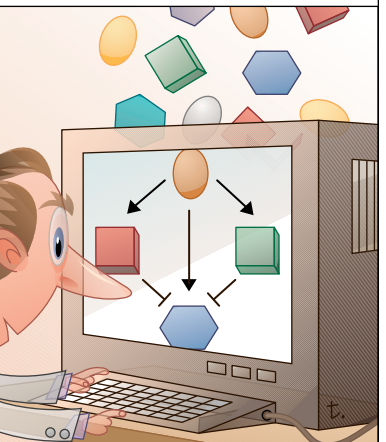
A primary ingredient for massive exchange of information among multiple bioinformatics tools and databases is curator tagging of input information to enable proofreading and data correction. Minor changes in a protein or DNA sequence entered into a gene or protein database can be corrected and generally will not propagate error throughout the entire informational system. Bad information in a protein interaction or pathways database is trickier. If information gatherers skip a step (for example, entering interaction information based on one experimental approach before it is confirmed by another), the line between potential and actual information is blurred, and the data must be filtered for reliability to constrain legitimate signaling possibilities. Users should assert the primacy of stubborn experimental facts at all stages of signaling bioinformatics analysis, and curators must respond quickly to this input. At STKE, for example, information is encoded as either established or speculative, the latter to be deemed reliable or jettisoned in response to user input. Coupling a robust curator/user interface with the obligate entry of signaling data into a centralized repository upon publication, analogous to obligate submission of new DNA sequence information, is one way to combine greater intensity of curator/user interaction with increased database population, fostering greater data reliability. This might help both to accelerate the growth of cell signaling bioinformatics and to increase genuine open access to the knowledge derived from taxpayer-supported research.

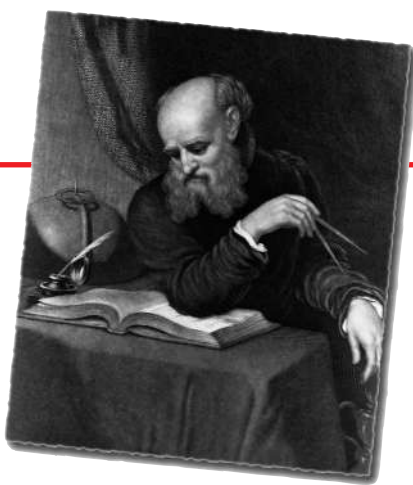
Another critical element in developing cell signaling databases is providing access to the raw data for swapping among various software platforms for visualization and analysis of biological information, including cell signaling pathways. Molecular interaction data from the Biomolecular Interaction Network Database (BIND), for instance, can be exported to an assembly-based information software system such as Cytoscape, greatly enhancing the value of the underlying data set. The availability of curator-tagged input data wrapped for portability should promote efficient distribution of data entered at any port, into the entire network of signaling tools. It will also improve curation, avoid duplication of effort, and eliminate tools that lack content for application. The gurus should argue strongly for it.

Used intensively, a well-connected array of bioinformatic tools can form a computational "working memory" for assembling biological information from specialized organism, cell system, and molecular data that the scientist can access for designing new experiments that are maximally informative. Movement toward centralized electronic pathway submission and improved data portability will make it possible to integrate new sources of data, including cellular locations of signaling complexes and components, quantitative aspects of signaling, and pharmacological data, into current pathway analysis databases and tools. This should be a strong motivation for the scientific community to increase its collective investment in the next phase of signal transduction bioinformatics development.

Lee E. Eiden

Lee E. Eiden is chief of the Section on Molecular Neuroscience and chairs the Bioinformatics Users Group in the National Institute of Mental Health Intramural Research Program, Bethesda, MD.





EXHIBITS

The Galileo Files

The Galileo Project from science historians at Rice University in Houston, Texas, lets you follow the life and work of Galileo Galilei (1564–1642), who made the telescope into a serious observing instrument and became a scientific martyr. From a brief biography, visitors can explore pages on Galileo's scientific accomplishments and inventions. For example, after boosting the magnifying power of existing telescopes, he discovered four moons orbiting Jupiter and observed the phases of Venus. But his work contradicted the Catholic Church's view that the solar system revolved around Earth. A chronology details Galileo's conflict with the Inquisition, which kept him under house arrest for the last decade of his life.

Adding context to these events are backgrounders on contemporaries, such as Johannes Kepler, who showed that the planets' orbits are elliptical, and the virtuoso Danish observer Tycho Brahe. Another site highlight is translations of 124 letters from Galileo's eldest daughter Maria Celeste, who became a nun.

galileo.rice.edu

DATABASE

Where the Bones Are

Images of *Tyrannosaurus rex* might be everywhere, from TV shows to lunch boxes, but its bones have turned up at only a few locales around western North America. At the Paleobiology Database, visitors can find out where researchers have collected particular species or tackle broader questions about patterns in the fossil record.

The 5-year-old site, headed by paleontologist John Alroy of the University of California, Santa Barbara, lets you scan Alroy's and other experts' records of more than 43,000 fossil collections, dating back to more than 540 million years ago. Searching for a species returns a roster of collecting locales. Click on a particular one for a detailed profile that includes lists of other remains discovered there, descriptions of the strata, evaluations of how well the fossils had held up, and other information. You can also map the finds—above, collection sites for saber-toothed tigers (*Smilodon*). Researchers can use the data to ask “big-picture questions” about the history of life—for example, tallying the diversity of ferns since the demise of the dinosaurs.



to ask “big-picture questions” about the history of life—for example, tallying the diversity of ferns since the demise of the dinosaurs.

paleodb.org

RESOURCES

Jewels of the Americas

Cichlids—the fish group that includes oscars, angelfish, and Jack Dempseys—are the aquatic equivalents of Darwin's finches. The handsome creatures have hooked the interest of evolutionists and ecologists because of their dazzling diversity of shapes, behaviors, and feeding habits, which include nibbling the fins and scales of other fish. This guide from ichthyologist Sven Kullander of the Swedish Museum of Natural History in Stockholm summarizes the South American cichlids, which constitute about one-quarter of the world's 1600 or so species. The site profiles more than 30 genera, offering physical descriptions, keys for sorting species, geographical distributions, and notes on nomenclature. Some species warrant their own pages. Unlike most fishes, cichlids are conscientious parents. This *Cichlasoma dimerus* (above), which lives in areas from Bolivia to Argentina, stands guard over a swarm of hatchlings.

www2.nrm.se/ve/pisces/acara/welcome.shtml



NET NEWS

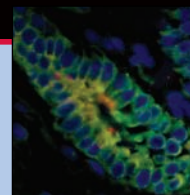
Computing for Humanity

If you haven't already donated your desktop computer's downtime to searching for new drug candidates or signs of alien life, here's your chance. A new site launched by IBM and partners is recruiting volunteers to help crunch research problems. The goal is to aid society, for example, by studying diseases or predicting natural disasters.

Participants will download software that lets their PC analyze chunks of a problem when the machine is idling, as was first done in 1999 by SETI@Home, which combs through radio signals from space for possible messages. Yoked together, the computers will add up to a giant supercomputer. The World Community Grid will begin with the Human Proteome Folding Project run by the Institute for Systems Biology in Seattle, Washington, which aims to determine the shapes of human proteins. IBM is also soliciting proposals for five or six other projects a year.

www.worldcommunitygrid.org

Send site suggestions to netwatch@aaas.org. Archive: www.sciencemag.org/netwatch



U.S. NATIONAL ACADEMIES

Advice on Science Advising Leaves Plenty of Questions

A panel of the U.S. National Academies has taken a political hot potato, slathered rhetoric over it, and produced a report that satisfies those on all sides. Unfortunately, the report's Rorschach-like quality may also lessen its impact.

The hot potato is the Bush Administration's practice of asking some appointees to scientific advisory panels about their political affiliations, voting records, and stance on issues within the panel's purview, leading to criticism in the media and from several watchdog groups. The response from White House and various agency officials has ranged from attacks on the critics' credibility to a vigorous defense of the need for balance.

Last week the academy's Committee on Science, Engineering, and Public Policy (COSEPUP) appeared to condemn political vetting in a report covering

both president-appointed science jobs and appointments to federal advisory panels (nationalacademies.org). Its key recommendation, with respect to advisory boards, declares that "persons nominated to provide [scientific or technical] expertise should be selected on the basis of their scientific knowledge and credentials. ... It is inappropriate to ask them to provide nonrelevant information,



Tough job. Richard Meserve, John Porter, and Frank Press discuss National Academies' new report on government service.

such as [their] voting record, party affiliation, or position on particular policies." Such information, says panel chair John Porter, a former Republican congressman turned Washington lobbyist, is no more appropriate than asking scientists about "their height or hair color."

Porter emphasized that the committee did not investigate specific allegations, nor was its advice focused on the current Administration. But that didn't prevent Kurt Gottfried, chair of the Union of Concerned Scientists (UCS), the most visible of the Administration's critics on the subject, from claiming victory. "The report echoes the concerns of 60,000 scientists," he said in a UCS press statement shortly after its release.

On closer inspection, however, the report's seemingly clear language starts to blur. The report only deals with scientists on advisory panels, notes committee member Richard Meserve, president of the Carnegie Institution of Washington. He said it might be appropriate to ask questions eliciting political views of other members of an advisory panel, such as those selected to represent patients, companies, or other special interests. It would also be reasonable, he notes, for an agency dealing with sensitive topics such as testing drugs on children, or disposing of low-level nuclear waste, to make sure that all views were represented.

Exactly right, says UCS's bête noire, presidential science adviser John Marburger, ▶

PALEOANTHROPOLOGY

Skeptic to Take Possession of Flores Hominid Bones

A leading Indonesian paleoanthropologist who questions whether a tiny 18,000-year-old hominid found on the island of Flores is really a new species plans to take at least temporary possession of the skeleton and similar hominid remains by the end of November. Earlier this month, Teuku Jacob of Gadjah Mada University in Yogyakarta had the skull of the hominid—dubbed *Homo floresiensis* by the Indonesian-Australian team that discovered it—transferred to his own laboratory from its official depository at the Center for Archaeology in Jakarta (*Science*, 12 November, p. 1116). Center officials have agreed to Jacob's request to have the skeleton's remaining bones, as well as the fragmentary remains of several other tiny hominids unearthed during this year's season, transported to Gadjah Mada as well, according to Radien Soejono, the center's

senior archaeologist and co-leader of the discovery team.

Jacob, who was not a member of the team, says he has already concluded that the tiny Flores hominids belong to a population of microcephalic, pygmylike modern humans rather than to a new species.

Some researchers are worried that Jacob will prevent others from studying the bones; he is well known for jealously guarding access to fossils (*Science*, 6 March 1998, p. 1482). "This development seems to threaten all future studies of *Homo floresiensis*," says Chris Stringer, a paleoanthropologist at the Natural History Museum in London. "One wonders how Professor Jacob is able to take over discoveries made, studied, and published by other workers." Stringer's concerns are echoed by a number of other researchers, including one Indonesian archaeologist who

asked not to be identified. "We are very unhappy," the archaeologist said. "The hominid is important to the whole world." Peter Brown of the University of New England in Armidale, Australia, who originally analyzed the hominid bone, says, "I doubt that the material will ever be studied again."

Soejono expects Jacob to return all of the bones to Jakarta eventually, although he's not sure when. "I am not going to push" for their return, Soejono says, adding that Jacob is a "very experienced" scientist.

Jacob told *Science* he will probably need until the end of this year to complete his study. He says that it is up to the center to decide the bones' ultimate fate but adds that the remains would be "much safer" in his own vaults in Yogyakarta, where many of Indonesia's famous hominid fossils are also stored.

—MICHAEL BALTER

CREDIT: MARTY KATZ

1458

China debates growing GM rice



1460

Can string theory connect with the real world?



1463

Can physical scientists connect with NIH?



who asserts that the quest for balance is paramount. “The law requires that these committees be balanced, and you can’t tell if they are balanced without asking questions.” Marburger praises the report and says that COSEPUP “has done a great service” in analyzing the topic. Although he agrees that asking scientists how they voted “is not appropriate,” he doesn’t see a need to change the Administration’s methods.

That’s also how things look to Representative Vernon Ehlers (R-MI), who last summer staunchly defended the practice of questioning prospective panelists in testimo-

ny before COSEPUP (*Science*, 30 July, p. 593). “Aside from policy differences, there are also scientific differences—like the question of setting appropriate levels of arsenic in drinking water—where you want to make sure you’ve got all sides represented.”

The report’s other recommendations, which Porter acknowledges echo a 2000 COSEPUP report, are meant to lower or remove hurdles standing between a prominent scientist and an appointment to the executive branch. Redundant and intrusive background checks, months of waiting, and low salaries are enough to knock good people

out of the running, say Porter and Meserve. Marburger and Ehlers agree that reform would help, although Marburger thinks that the system “works pretty well” whereas Ehlers believes it’s “broken.”

Despite its solid reviews, the report faces tough sledding. “It will take an irate president who’s fed up with the system” to even put it on the country’s political radar screen, laments Ehlers. Meserve says that the parties involved—both Congress and the executive branch—“have to want to do the right thing. If not, nothing’s going to change.”

—JEFFREY MERVIS

SCHOLARLY PUBLISHING

NIH Flooded With Comments on Public Access Proposal

Prodded by Congress, the National Institutes of Health this fall solicited the public’s views on a plan that would require NIH-funded investigators’ papers to be posted on the Internet 6 months after a journal publishes them (*Science*, 10 September, p. 1548). And the public took notice.

NIH received about 6000 comments by the 16 November deadline. A brief review of the first batch of 800 or so—the only ones NIH made available by press time—indicates support from librarians, patient advocates, teachers, and individual scientists. But although some major research organizations back NIH’s proposal, many scientific societies and commercial publishers have called for NIH to delay or scrap it.

NIH has tallied a preliminary count based on 95% of the responses submitted on a Web form. NIH officials caution against drawing conclusions because large organizations only got a single vote, and some people didn’t answer all the questions. Of those who did, however, four of five clicked “agree” to the concept that research results should be freely available (see table). Two-thirds of commenters said they liked NIH’s implementation plan, which would require that NIH-funded investigators submit their final, peer-reviewed manuscripts to PubMedCentral, NIH’s free on-

line full-text archive, for posting 6 months after publication. The Scholarly Publishing and Academic Resources Coalition, which represents libraries, urged NIH to resist pressure to extend the 6-month delay, arguing that taxpayers actually need “immediate access.”

Some major scientific groups also offered a qualified endorsement. These include the Council of the National Academy of Sciences, the Association of American Medical Colleges, and the Association of American Universities. All three advised, however, that NIH make sure it replaces the accepted manuscript with the published version to avoid confusion.

Other scientific societies, worried about the potential loss of income to sustain their activities, asked NIH to reconsider. AAAS, which publishes *Science*, urged NIH to “delay implementing any policy,” while the Federation of American Societies for Experimental Biology (FASEB) said the plans were “unac-

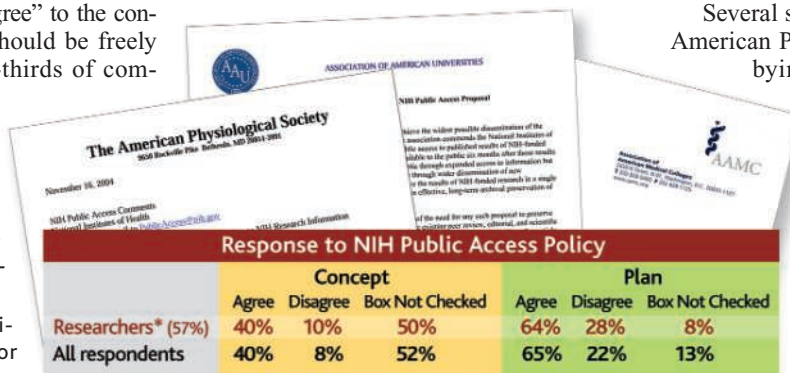
ceptable” and should be withdrawn. Three large patient organizations that also publish journals, the American Cancer Society, American Diabetes Association, and American Heart Association, said they support the “goal” but that NIH needs to “conduct an analysis” before moving forward.

These groups and others question the need for the archive when many journals already make full text articles free after a delay. They also note that NIH has not explained its estimate that it would cost only \$2 million to \$4 million a year to post 60,000 to 65,000 papers. FASEB fears that the project “will reduce funding available for research.”

AAAS and some other societies, such as the American Academy of Pediatrics, are also worried about how PubMedCentral will deal with corrections, which are sometimes published months after the paper. And AAAS wonders how NIH would ensure that government officials or Congress don’t interfere with the posting of controversial papers.

Several societies and the Association of American Publishers, which has been lobbying Congress to stop the NIH plan, argue that tools for searching publishers’ own archives—such as Google—could accomplish the same goals. The proposal also raises legal issues such as copyright, argues the American Physiological Society.

Congress asked NIH to settle on a policy by 1 December. But NIH officials say they may need more time. —JOCELYN KAISER



Notes: Based on preliminary count of 6047 comments submitted by Web form. Includes an estimated 200 duplicates. *Clicked “scientific researcher.”

SOURCE: NIH OFFICE OF EXTRAMURAL RESEARCH

Asked, answered. A preliminary tally shows support for NIH’s open-access plan among all groups, including scientists.

New Data on Appetite-Suppressing Peptide Challenge Critics

It's extremely unusual in science for dozens of investigators to band together and announce publicly, in a major journal no less, that they can't repeat a colleague's results. But it happened this summer, and now the band of skeptics is mounting a partial retreat. So goes the latest twist in the saga of peptide PYY_{3-36} (PYY₃₋₃₆), a molecule originally hailed for its ability to curb appetite and its potential as an antiobesity drug.

In 2002, endocrinologist Stephen Bloom's group at Imperial College, London, reported in *Nature* that PYY₃₋₃₆, when



Closer to agreement. Stephen Bloom (left) and Matthias Tschoep (right) now concur that PYY₃₋₃₆ curbs appetite.

injected into the abdominal cavity of rodents and intravenously in people, could dampen hunger for at least 12 hours. In July, however, more than 40 scientists from 12 labs challenged those findings by publishing negative data in a joint letter to *Nature*; the investigators reported that they could not reproduce the original appetite-squelching results in some 1000 rodents, of eight different strains (*Science*, 9 July, p. 158).

This month, however, physiologist Roger Reidelberger's group at the Creighton University School of Medicine in Omaha, Nebraska, published data demonstrating that rats given intravenous infusions of PYY₃₋₃₆ ate less than controls, in a dose-dependent fashion. Meanwhile, a team led by behavioral neurologist Timothy Moran of the Johns Hopkins School of Medicine in Baltimore, Maryland, who signed the critical *Nature* letter, has documented a similar PYY₃₋₃₆-induced curb in consumption in rhesus monkeys.

With PYY₃₋₃₆, "you can produce a potent effect on appetite," says Reidelberger. "And that confirms what Dr. Bloom showed in humans."

Reidelberger had no intention of resolving a scientific fracas when he designed his exper-

iments—in fact, he submitted them for publication in *Endocrinology* before the dispute broke out. He simply wanted to better simulate what researchers had assumed happens with PYY₃₋₃₆ in the body after a meal.

Evidence shows that, beginning at the start of a meal, cells of the lower intestine spew out PYY₃₋₃₆ into the bloodstream. There it accumulates, slowing the stomach from emptying and—according to Bloom and his supporters—signaling fullness to the brain. So, instead of injecting animals' bellies with a whopping dose or two of the peptide, as other researchers, including Bloom, had done, Reidelberger delivered it directly into the animals' jugular veins in a way that allowed the rats to get a steady flow of lower doses of PYY₃₋₃₆—for 3 hours before and during feeding. Rats receiving PYY₃₋₃₆ in this manner ate less chow than controls—anywhere from 41% to 69% less at maximum, depending on dose. And the effects lasted up to 11 hours after infusion began.

The same cumulative amount of PYY₃₋₃₆ given in 15-minute infusions had a much less potent effect, highlighting the importance of timing. Single, high-dose injections of PYY₃₋₃₆ "are unreliable," says Reidelberger. "The lack of response that a lot of people saw was due to subtle differences based upon dosing."

Bloom says he "never had any doubts." He only wishes that dissent hadn't been so public. "We have also failed to get other people's stuff to work and produced a paper saying we couldn't get it to work. But we didn't involve the media," he says.

Although the dissenters haven't completely let Bloom off the hook—some point out that his results haven't been exactly replicated—many seem willing to acknowledge that the mechanism of delivery may be key to the peptide's immediate appetite-suppressing potency. "We certainly have the most positive effects when we give PYY₃₋₃₆ in rodents with pumps, chronically," says Matthias Tschoep of the University of Cincinnati in Ohio, who led the group reporting the negative data.

Moran's work adds another wrinkle to the debate: species differences. Moran was and still is unable to reproduce Bloom's results in rodents. Hoping for better results in primates, he injected PYY₃₋₃₆ into the leg muscles of monkeys. The treated animals waited ▶

A Bare-Bones Budget for Science

Congress left town this week after belatedly finishing its work on the 2005 federal budget. The \$388 billion bill, which covers most of the government's domestic discretionary spending, is a turkey for most U.S. scientists. Details were still being worked out as *Science* went to press, however. Unless noted otherwise, the numbers below don't include an across-the-board cut of nearly 1% imposed to make the package more palatable to fiscal conservatives.

National Institutes of Health: In the second year of a sharp slowdown after a 5-year budget doubling, NIH received a 2% increase to \$28.1 billion, according to figures in flux at press time. The roughly \$586 million raise—which would reflect the across-the-board cut—falls short of the president's request of \$729 million more. Funds available for programs will be even lower because of a 2.3% to 2.5% "tap" to fund other Public Health Service programs and an up to \$150 million set-aside for the Global Aids Fund. Biomedical research watchers anticipate severe trims to grant success rates in 2005. The good news: The final bill drops House language barring funds for two psychology research grants opposed by conservatives.

National Science Foundation: For the first time in nearly 20 years, NSF's research account will fail to grow. Freezing the \$4.25 billion account is part of a deal that shrinks the agency's total budget by nearly 2%, to \$5.5 billion. That drop of more than \$100 million compares with the president's request for a \$167 million increase.

NSF's plans for building major research facilities will be reined in. The bill also accepts the president's request to slash the math-science partnerships program linking university scientists with local school districts. Overall, the budget "is not good news," says one senior NSF official.

NASA: The space agency appears to have scored a victory with a \$15.9 billion budget that's \$344 million shy of the president's request but far more than either the House or a Senate panel had recommended. But agency officials say NASA could still find itself more than \$800 million in the hole. One reason is nearly \$400 million in earmarks. Another is the loss of at least \$120 million from the across-the-board cut. Then there is the rising price of returning the space shuttle to flight and the urgent need to begin funding a repair mission to the Hubble Space Telescope. "Most grim" is how one agency official put the news.

—JOCELYN KAISER, JEFFREY MERVIS,
& ANDREW LAWLER

longer to eat their first meal than controls did and then, for the next 6 hours, ate less at each meal. As the team reported in September in the *American Journal of Physiology*, monkeys receiving the peptide also held food in their stomachs longer than controls did, which may explain, in part, why subsequent appetite diminished.

Still, Tschoöp and Moran point out, and

Bloom concedes, no study, except the original 2002 paper, demonstrates loss of body fat or body weight, the ultimate goal for an anti-obesity drug. For example, in Moran's study, PYY₃₋₃₆ completely lost its efficacy after the first day of injection. And Reidelberger never measured animals' weights because of experimental design: Each animal ultimately received each of all six doses of PYY₃₋₃₆ in

random order and would have weighed the same at the end of the experiment.

Thus, for now, PYY₃₋₃₆ would seem far too fickle to make a decent antiobesity drug. "Our data suggest that PYY₃₋₃₆ does do something to feeding," Moran concedes. "But we still have a lot to learn." —TRISHA GURA

Trisha Gura is in Boston writing a book about eating disorders in women older than 25.

EVOLUTION

Ice Ages May Explain Ancient Bison's Boom-Bust History

The pounding hooves of buffalo stampeding across the plains is an enduring symbol of the American West. Once numbering in the tens of millions, these 1-ton shaggy-headed beasts dwindled to less than 1000, hunted down for sport, hides, and meat during the 1800s. Thousands of years earlier, buffalo in the northern reaches of North America suffered a similar decline. But despite what some paleontologists have long thought, people were not to blame, at least not initially, says Alan Cooper, a molecular evolutionist at Oxford University, U.K.



Iced out. DNA from buffalo fossils lighten blame on humans for ancient bison's decline.

bridge. Eventually, people crossed the bridge to America and, some researchers believe, hunted the mammals to extinction or near-extinction.

To check out this hypothesis, Cooper, Oxford's Beth Shapiro, and colleagues obtained ancient DNA from 442 bison fossils found in North America, Siberia, and China. For each specimen, they sequenced 685 bases from the fastest mutating part of the animal's mitochondrial genome and used differences in the sequence to assess the genetic diversity of ancient herds. The researchers also obtained radiocarbon dates on 220 samples. The approach "brought together information that we have had a hard time getting to with fossils," Graham says.

The data reveal that all the bison specimens belong to a single subspecies whose common ancestor lived about 140,000 years ago. Changes in the genetic diversity of specimens from particular areas indicated when herds thrived and when they did not. Until now, "we've not had a good way of teasing out the bumps and wiggles in [their]

population history," says David Meltzer, an archaeologist at Southern Methodist University in Dallas, Texas.

Bison in North America spread southward, some as far as Mexico, 100,000 or more years ago. Beginning approximately 37,000 years ago, the bison began to decline, perhaps because of climate and habitat changes associated with the deepening ice age. To make matters worse, about 22,000 years ago, the expanding glaciers cut the northern group off from their southern kin. By the time the last glaciers receded some 8000 years later, genetic diversity in the northern bison had plummeted, the researchers report. It never recovered completely—probably, they conclude, because changes in habitat, particularly forest growth, kept populations small and isolated from the southern herds, which had less severe declines in diversity.

Such conclusions have elicited at least one strong reaction. "I think the interpretation is overblown and not supported by the data," says John Alroy, a paleobiologist at the University of California, Santa Barbara. He points out that other data suggest that bison in many places have weathered dramatic shifts in climate just fine. Therefore, Alroy asserts, it must have been human intervention that caused local extinctions and an overall decline in bison.

Shapiro notes that Alroy's traditional views could still be partly correct. "We are not arguing that these early human populations had no impact on bison populations but suggest that whatever events instigated the decline of bison populations occurred well before large numbers of humans had settled in the region," she says. John Pastor, an ecosystem ecologist at the University of Minnesota, Duluth, agrees that the new work adds an important perspective to this debate: "What [Shapiro] is getting people to think about is that it's not one factor" that pushed these mammals toward extinction.

—ELIZABETH PENNISI

CREDITS: B. SHAPIRO ET AL./SCIENCE; (INSET) LAYNE KENNEDY/CORBIS

Bone Marrow Cells: The Source of Gastric Cancer?

Stomach cancer is a major cause of cancer deaths, especially in developing countries; it claims roughly 600,000 lives worldwide every year. About 15 years ago, researchers linked stomach cancer to infection with the ulcer-causing bacterium *Helicobacter pylori*. Now, a surprising twist in the *Helicobacter* story raises questions about the origin of the cells that give rise to gastric tumors.

H. pylori infections apparently foster stomach cancer because of the persistent inflammation they produce. Recent work has shown that inflammatory cells can promote tumors in several ways, including the production of growth-stimulating proteins and DNA-damaging chemicals that can trigger cancer-causing mutations (*Science*, 5 November, p. 966).

On page 1568 of this issue of *Science*, a team led by JeanMarie Houghton and Timothy Wang of the University of Massachusetts (UMass) Medical School in Worcester offers a more radical possibility. Working with mice infected by an *H. pylori* relative, they found that the damage the microbe-induced inflammation causes to the epithelial cells of the stomach lining leads to an influx of bone marrow stem cells that apparently try to repair the lining. What's more, the evidence suggests that these visiting cells—and not the cells of the epithelium—ultimately give rise to stomach cancer. "It's really quite a novel concept," says Emad El-Omar, a *Helicobacter* researcher at the University of Aberdeen, U.K. "It will set people to thinking quite hard" about the origins of stomach cancer, he says.

To study the role of bone marrow-derived cells in stomach cancer, Houghton, Wang, who is now at Columbia College of Physicians and Surgeons in New York City, and their colleagues used the C57BL/6 strain of mice. When infected with *H. felis*, these animals develop gastric changes—beginning with chronic inflammation and ultimately progressing to cancer—similar to those seen in humans infected with *H. pylori*. Before infecting the mice, however, the researchers irradiated them to destroy their bone marrow; the team then gave the rodents transplants of marrow cells bearing a genetically engineered marker that allows the cells to be distinguished from the animals' own cells.

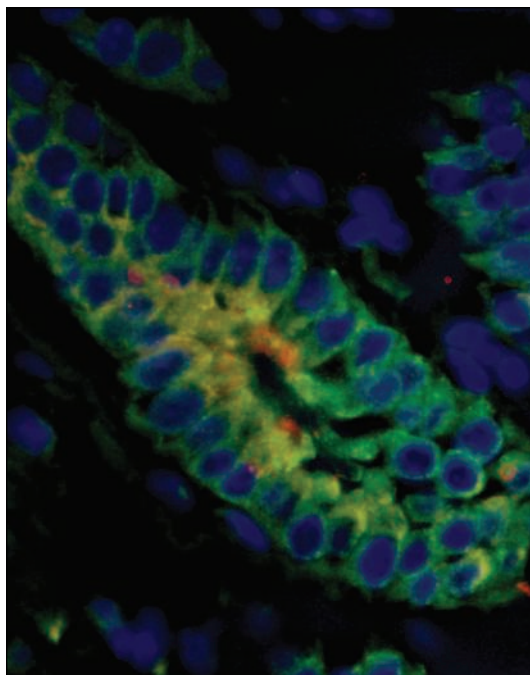
After about 20 weeks of infection, the labeled bone marrow cells

began engrafting in the stomach lining. There they started to differentiate, taking on some of the characteristics of stomach epithelial cells while still retaining bone marrow cell markers. But the resulting cells weren't completely normal. Their shapes were distorted and they showed enhanced growth—abnormalities similar to those of cells undergoing early cancerous transformation. Eventually, they produced cancerous tumors. "These bone marrow-derived cells were coming in to attempt to heal the tissue, but under chronic inflammation [they] couldn't develop normally and progressed down the road to cancer," Wang says.

The results further support the idea that persistent inflammation fosters cancer development. "It's absolutely clear that [chronic inflammation] is a necessary condition" for the bone marrow cell migration, says Jeffrey Pollard of Albert Einstein College of Medicine in New York City.

Perhaps more intriguing, Houghton and Wang's results lend credence to the controversial new notion that cancer may arise from stem cells (*Science*, 5 September 2003, p. 1308)—but with a key difference. In this study, the stem cells seem to come from a different tissue than the one in which the tumor arises.

Some stem cell experts, however, ▶



Two in one. The yellow color denotes gastric tumor cells that have stained positive for both a bone marrow-derived cell marker and a gastric epithelial cell marker.

Wisconsin Proposes Stem Cell Boost

Wisconsin is making a bid to keep up with California as a stem cell research mecca. Governor James Doyle last week proposed that the state invest up to \$750 million in stem cell and related studies over the next several years, including more than \$500 million in new facilities and research at the University of Wisconsin, Madison.

The plan's biggest plum is a \$375 million public-private interdisciplinary research institute to be known as the Wisconsin Institute for Discovery. Based at the university, it will combine stem cell research with research on other areas, such as bioinformatics and computer science.

Carl Gulbrandsen, director of the Wisconsin Alumni Research Foundation, says the funding plan—portions of which must still be approved by the legislature—has been in the works for the past 6 months. But the recent passage of California's \$3 billion stem cell research initiative "really helped to jell it." Anti-abortion groups say they will ask the legislature to make sure the funds aren't used for "unethical" research.

Gulbrandsen says WiCell, created to permit University of Wisconsin researchers to do stem cell work that doesn't involve federal funds, will continue as a private entity. But prominent WiCell researcher James Thomson will have a "central role" in the larger plans.

—CONSTANCE HOLDEN

Hungary Again Eyes Cuts to Science Budget

In what is shaping up to be a yearly ritual, the Hungarian government is taking an ax to its science budget. It has proposed a 15% spending cut for its \$33 million basic research agency, OTKA, on top of a 10% government-wide spending reduction. The government dealt a similar financial blow to the agency's 2004 budget (*Science*, 19 March, p. 1745), but a letter-writing campaign to the prime minister helped win back \$1.5 million for post-doctoral stipends and Internet resources for universities.

This time, researchers are rallying Parliament to their side: An amendment to a spending bill passed late last month by the Education and Science Committee would restore most of OTKA's funds. But the rescue amendment faces several hurdles, says OTKA president Gábor Makara, who warns that this year's cut would be disastrous for research and training.

—RICHARD STONE

CREDITS: J.M. HOUGHTON ET AL./SCIENCE

aren't convinced that the bone marrow cells are behaving as proposed by the UMass team. Bone marrow cells have a tendency to fuse with other cells, a trait that has lent controversy to highly publicized reports that bone marrow stem cells can form heart, brain, and other nonblood cells. The new work is subject to similar uncertainty, as stem cell experts caution that Houghton, Wang, and their colleagues have not proven that the transplanted cells differentiated into epithelial cells rather than fused with them. "Fusion was not adequately addressed" in the gastric cancer experiments, says Irving Weissman of Stanford University School of Medicine in

California.

The UMass workers did show that the labeled gastric cells had only one nucleus, not two, and a normal complement of DNA. In one experiment they even transplanted female mice with male bone marrow. The resulting gastric cells had one Y and one X chromosome. But Weissman remains skeptical, suggesting that one of the two X chromosomes originally present in a gastric-bone marrow fusion cell might have been lost. If fusion is taking place, however, that would still be a novel mechanism for cancer development—but a different one from that suggested by Houghton-Wang team.

Wang agrees that more evidence is need-

ed to sort out the fusion issue. Other questions remain as well. One concerns whether a similar phenomenon occurs in different types of inflammation-linked cancers. And currently, there's no way to tell whether bone marrow-derived stem cells are involved in human gastric cancer, as there are no markers that would allow unequivocal identification of the cells.

Still, the Houghton-Wang paper will likely spark a great deal of research interest. "What this has done is open up a new field in gastric carcinogenesis," says *Helicobacter* expert Richard Peek of Vanderbilt University School of Medicine in Nashville, Tennessee.

—JEAN MARX

BIOCHEMISTRY

Immune Cells Speed the Evolution of Novel Proteins

Evolution isn't known for its quick work. In recent years, researchers have come up with numerous ways to give it a kick in order to evolve proteins with new functions. But most of these techniques are painfully slow, taking as long as a month to go through a single round of evolution. The immune cells of vertebrates long ago perfected a faster approach, which they use to generate the myriad antibody proteins that fight off infections. Now a team of California

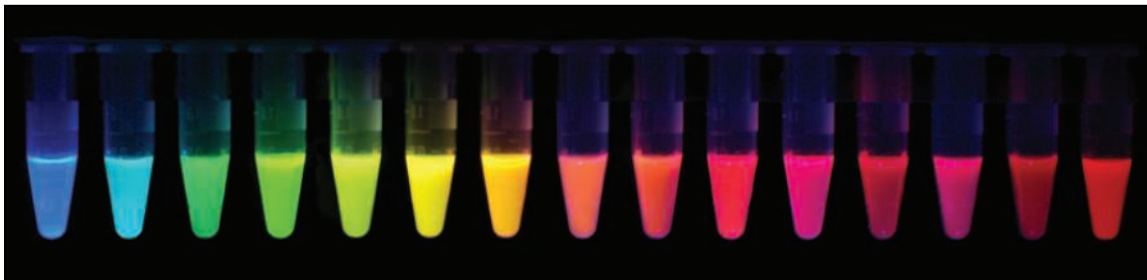
body tissue absorbs, they are useless for following molecules in whole animals.

Tsien's group has sought to improve matters by evolving proteins to shine infrared light, which penetrates tissue. Researchers typically start by isolating the gene for a fluorescent protein. Then they use an error-prone gene-copying method to introduce random mutations, splice the new gene variants into bacteria, and select out the microbes that shine the most interesting

an altered protein to its natural function. But little had been done to use the approach to evolve proteins with novel functions.

Tsien's group started with the gene for red fluorescent protein (RFP), which they linked to a promoter DNA sequence that turns on production of RFP in response to an antibiotic called doxycycline. They then transfected this genetic tandem into millions of human B cells. When exposed to doxycycline, the cells started mutating the RFP

gene and making variants of the original protein. The researchers then stimulated the cells with laser light and selected out those that showed a shift in fluorescence toward the infrared. After giving the cells time to multiply, the researchers treated them with



Bright idea. This palette of fluorescent proteins includes ones recently evolved in immune cells (third from right, far right).

researchers has coaxed immune cells to apply their skill to other proteins, an ability that could speed the development of novel proteins for studies from catalysis to cell biology. "It's very elegant work," says David Liu, a protein evolution expert at Harvard University.

The team hoped to improve the fluorescent properties of proteins that shine red when stimulated by green light. Molecular biologists link these and similar beacons to proteins of interest to reveal their location inside cells. In recent years, Roger Tsien, a biochemist at the University of California, San Diego (UCSD), has evolved fluorescent proteins to shine different colors of light, a trick that makes it possible to track more than one protein at a time. But because the new proteins still emit visible light, which

colors. Researchers must then clone the desired genes to identify how their sequences differ from the original. "Someone who is good at it can do about one round in 1 month," Tsien says.

To speed up the process, Tsien and his colleagues—postdoc Lei Wang and technicians W. Coyt Jackson and Paul Steinbach—turned to antibody-generating factories called B cells that mutate some genes 1 million times faster than other cells. Specifically, B cells generate antibody diversity with a built-in system that frequently mutates cytosine into one of the other three bases that make up DNA. Over the past 3 years, researchers in the United States and Switzerland have induced B cells to apply this process, called somatic hypermutation, to non-antibody proteins, in one case to restore

doxycycline again and repeated a new round of evolution. Each round took only a few days. In the current issue of the *Proceedings of the National Academy of Sciences*, the UCSD team reports that after 23 such rounds of evolution, the wavelength at which the evolved proteins' emitted light shifted from 610 nanometers to 650 nanometers, about halfway from the red to the infrared.

The effectiveness of this new technique shouldn't be limited to fluorescent proteins. As long as there is a good way to screen the resulting cells for the desired activity, "we think this can work on practically any protein," Tsien says. That should give a green light to the evolution of new catalysts and help molecular biologists who evolve proteins in order to study their function.

—ROBERT F. SERVICE

AGRICULTURE

China Could Be First Nation to Approve Sale of GM Rice

BEIJING—China is pondering the future of its most important crop. Next week the biosafety committee of China's Ministry of Agriculture (MOA) will meet to decide whether to approve the commercial use of the first varieties of genetically modified (GM) rice. If the committee says yes, the world's biggest producer and consumer of that staple grain will also become the first country to give its farmers a chance to grow GM rice.

Proponents say the varieties will deliver higher yields and greater resistance to pests without posing any risk to the environment.

But some scientists believe that Chinese farmers can achieve comparable gains in productivity by conventional technologies without risking transfer of the engineered traits to the country's cultivated and wild rice. "It will be a tough decision to make, as policy-makers must weigh the consequences," says Zhu Zhen, a biotechnologist at the Institute of Genetics and Developmental Biology of the Chinese Academy of Sciences (CAS) in Beijing.



Green light? China's Zhu Zhen hopes his line of GM rice, designed to withstand insect infestation, will win government approval.

Chinese scientists have developed dozens of transgenic rice strains since the 1980s. Zhu and his colleagues have developed an insect-resistant rice line that is one of four candidates for approval at the 30 November to 2 December meeting. According to Huang Jikun, who directs the CAS Center for Chinese Agricultural Policy in Beijing, all the candidate strains have gone through the small-scale, greenhouse trials and larger field trials required by the

country's 1996 biosafety laws. The other candidates include one line that is resistant to stem borers and two that withstand bacterial blight and other plant diseases.

Ministry officials declined comment on the upcoming meeting. "It's a very sensitive issue," says Shi Yansheng of MOA's science department. Xue Dayuan, a researcher at the Nanjing Institute of Environmental Science involved in biosafety and biodiversity issues for the State Environmental Protection Administration, predicts that the committee, whose members meet twice a year, is "very likely" to approve at least some of the GM rice candidates. Even so, he believes that there are risks. "China is home to wild and cultivated rice," he says. "In case of gene floating, which is quite possible, the damage will be irreversible."

Zhu's strain, which received its preproduction trial permit in 2002, carries a *Bt* gene and a modified proteinase inhibitor gene. This approach increased the expression level of the transgene, he says. A recent study by Huang of test plots in Hubei and Fujian provinces ▶



PARTICLE PHYSICS

Neutrinos Are All Flip-Floppers, Japanese Study Shows

It's the dog that didn't bark: For decades neutrinos have been failing to appear in detectors where they should be. Physicists think it's because the nearly massless particles "oscillate" into harder-to-detect varieties, or flavors, and have long sought ironclad evidence of the oscillations. Within the past few years, they have found such evidence for neutrinos from two of their three main sources: the sun and the atmosphere. Now, physicists in Japan and the United States have added the third by showing that electron antineutrinos produced by nuclear reactors in Japan and South Korea change type as they travel through Earth.

"It's strong evidence that it's [the] oscillations" that are responsible for the missing neutrinos, says Kevin Lesko, a collaborator at Lawrence Berkeley National Laboratory (LBNL) in Berkeley, California. Janet Conrad, a physicist at Fermi National Accelerator Laboratory in Batavia, Illinois, agrees. "It's a very nice result," she says, adding that the results

"significantly" narrow the possible relative masses of two flavors of neutrino—crucial information for characterizing the particle.

Scientists have known since the 1950s that they were seeing too few neutrinos coming from the sun. But they first nailed down the case for the oscillation in 2001, when Canada's Sudbury Neutrino Observatory spotted a deficit of solar electron neutrinos together with a matching surplus of muon and tau neutrinos. It was clear that electron neutrinos were turning into the harder-to-detect muon and tau types. With atmospheric neutrinos, the story was similar: There were too few muon neutrinos compared with electron neutrinos (*Science*, 22 June 2001, p. 2227). In 1998, the Super-Kamiokande detector in Japan showed that the proportion of muon to electron neutrinos varied smoothly depending on how far the neutrinos traveled, a clear indication that the muon neutrinos were changing flavors as they move.

This same story arc has now repeated itself with reactor antineutrinos. In 2002, the KamLAND collaboration, a group of scientists in Japan and the United States, used a large sphere filled with scintillating fluid buried underneath mountains near Toyama, Japan, to spot a shortfall of the particles (*Science*, 13 December 2002, p. 2107). Now, in a paper just accepted by *Physical Review Letters*, the KamLAND group reports that sorting 258 neutrino collisions by energy yielded the distribution that oscillation would produce. If some other mechanism (such as neutrino decay) were causing the neutrinos to disappear, "the dependence would be completely different," says Patrick Decowski, a KamLAND collaborator and physicist visiting LBNL. Together with the sharper constraints on mass, the results make it clear that scientists are hot on the trail of neutrino properties. The game is afoot.

—CHARLES SEIFE

CREDITS: CAS INSTITUTE OF GENETICS AND DEVELOPMENTAL BIOLOGY; (INSET) XIONG LEI/CNHA FEATURES

found that insect-resistant rice can reduce the use of pesticide by 80% and lower average yield losses from pests by 6% to 7%. The reduced dependence on pesticides was also a timesaver for farmers and put more money in their pockets.

“Traditional rice farming is particularly labor intensive,” says Zhu. “As more and more able-bodied farmers leave villages to seek better paid jobs in cities, women and old people are doing more of the work. GM rice can help alleviate their workload, and reduced pesticide use will improve their health and the environment.”

But some scientists say there are alternative biological approaches to control pests and increase outputs that do not require GM rice. Zhu Youyong, president of Yunnan Agricultural University, says that he has increased yields by 10% and reduced pesticide use by 60% since 1997 by planting many different varieties of rice developed with traditional techniques: “GM technology could be a good way to resist pests and disease, but in the long run, the best method is biodiversity.” Zeng Yawen, a researcher at the Yunnan Academy of Agricultural Sciences, puts it more bluntly: “Why should we take the risks if we have a safer approach to raise our rice production?”

There is also the problem of an informed consumer, says Nanjing’s Xue. In the far western Xinjiang region, Bt cotton has become widespread, despite rules against its use there, after seed companies told farmers that they were being given high-yield, pest-resistant varieties but failed to highlight its transgenic nature.

Zhu Zhen says that rigid rules have been followed in the breeding, shipment, and planting of GM rice to prevent contamination. “Even if the commercial release is issued, the GM rice is unlikely to be promoted on a large scale immediately,” he says. “We’ll take steps to tailor the different lines to varying environment and local conditions.”

The most vocal opponent of growing GM rice in China is the nonprofit environmental group Greenpeace. Sze Pang Cheung, a campaign manager of Greenpeace China, compares the commercial release to “a gamble with life” and scolds MOA for what he terms its secretive biosafety procedures. “Rice is the staple food of millions of Chinese, so the public must have a say in its fate,” he says. He also notes that a majority of the biosafety panel members are biotechnologists, and few members are knowledgeable about environmental and biodiversity issues.

What will the biosafety committee decide? Huang is optimistic, but Zhu is hedging his bets. “I’m confident our product will be released,” he says, “if not this time, then in 2 years.”

—XIONG LEI

Xiong Lei writes for *China Features* in Beijing.

EUROPEAN SCIENCE

New Commissioner Calls for Evolution, Not Revolution

BRUSSELS—A few weeks later than expected, Europe has a new leader at the helm of science policy. Slovenian economist Janez Potočnik will oversee a \$22 billion research fund, Framework 6, as well as development of its successor, Framework 7. If the new commissioner gets his way, that program will double in size during his 5-year term.

Potočnik and the other 24 members of the European Union’s leadership group were due to be sworn in on 1 November, but controversy over Italy’s nominee for justice commissioner caused a delay (*Science*, 5 November, p. 959). After new candidates were named from Italy and Latvia, and the Hungarian nominee shifted portfolios, the Parliament approved the slate on 18 November. The new commission took office on 22 November.

An economist, Potočnik seems keenly interested in linking science to social and industrial growth. In a conversation with *Science* before taking office, Potočnik stressed that research is an indispensable part of the Lisbon



New face. Janez Potočnik took office this week as the European Union’s commissioner for science and research.

Strategy, a 10-year plan endorsed by European leaders in 2000 that calls for sustainable economic growth in balance with environmental protection and Europe’s traditionally generous social policies. Part of the strategy requires Europe to boost its R&D spending from 1.9% of gross domestic product in 2000 to 3% by 2010. To work toward that goal, Potočnik will make his case for doubling the budget for the Framework 7 program—which would boost E.U. research spending to \$13 billion per year between 2007 and 2013. If Europe wants to come close to meeting the Lisbon goals, he says, it must devise a formula in which “knowledge, science, and research are definitely playing a major role.”

Potočnik, who has little background in the natural sciences, admits that he has a lot to

learn. “Since high school, this has been the peak of my learning curve,” he says of his first months preparing to take over the research portfolio. At least at first, he has said he will hew close to the priorities of his predecessor, Belgian former commissioner Philippe Busquin, now a member of the European Parliament (*Science*, 10 September, p. 1551). During a 1 October confirmation hearing in the European Parliament, Potočnik said, “There is no need for revolution. There is a strong need for evolution of what has been achieved.” He has expressed strong support for the idea of a European Research Council (ERC), a basic science–funding body that has strong grass-roots support among scientists across Europe and which Busquin embraced toward the end of his term.

The new chief will inherit some problems as well. Researchers have made impassioned calls for less red tape in the grantmaking process, for example. Potočnik says he is empathetic, and he is already advocating a two-tier application system that would allow scientists to submit an outline or abstract of a project for initial evaluation. Only those that make this first cut would be asked to put together a full application. “Since the acceptance rate is very low, quite a lot of that time is thrown away” in the current system, he says.

Potočnik speaks enthusiastically about the role of small- and medium-sized enterprises—SMEs in E.U. lingo—as drivers for scientific research. Although some basic researchers have complained about the E.U.’s emphasis on applied research—about 15% of the current Framework budget is dedicated to funding SMEs—Potočnik sees them as key in using science to boost Europe’s economy. That enthusiasm doesn’t bother Jose Mariano Gago, former Portuguese science minister and head of a group lobbying for the ERC, who says, “I think he understands quite well that scientific development in Europe needs a coalition of everyone.”

Potočnik is diplomatic when asked if any particular area of science has caught his interest since taking on the research job. “In practically all the areas you touch, you see interesting things going on,” he says. “It’s a wonderful world of science.” It is a world Potočnik will now have plenty of chance to explore—and shape—in the coming years.

—GRETCHEN VOGEL

It's time the grand theory accounted for the details in familiar data, some physicists argue. But is string theory ready for the test?

String Theory Gets Real—Sort Of

ASPEN, COLORADO—Twenty years ago, this chic playground for skiers and celebrities gave birth to a scientific revolution. An abstruse mathematical discovery made here sparked the explosion of “string theory,” humanity’s best attempt at the ultimate explanation of matter and energy, space and time. Now, 2 decades later, physicists have returned to a cloistered compound at the north end of town to mull over a nagging question: Can string theory account for what we already know about the universe? At a month-long workshop,* more than 50 researchers have gathered to discuss whether the theory can accommodate the data they already have and make predictions about future experiments—fundamental scientific tests that this vaunted “theory of everything” has yet to pass.

The revolution began “right over there in Bethe,” says John Schwarz, a physicist at the California Institute of Technology (Caltech) in Pasadena and one of the revolutionaries. Lounging on a bench, he motions toward one of three tiny single-story buildings that house the Aspen Center for Physics. In 1984, Schwarz and Michael Green, a physicist at the University of Cambridge in the U.K., found a way around key mathematical pitfalls in string theory, which assumes that every elementary particle is a tiny vibrating string and that space has more dimensions than we see. The esoteric advance suggested that the theory might be a viable explanation of all the forces of nature. “Almost overnight, hundreds of people started working on this stuff,” Schwarz says. “People were almost too enthusiastic—naïve about the problems we had to overcome.”

String theory promises to reconcile Einstein’s theory of gravity with the bizarre rules

of quantum mechanics, answer the deepest conceptual questions in particle physics, and even explain how the universe sprang into existence. Hundreds of physicists and mathematicians work on one aspect of string theory or another. Now a small but growing number of them are trying to forge connections between string theory and detailed data—a practice physicists call “phenomenology.” Some say the effort is long overdue.



Idyllic. Theorists Massimo Porrati of New York University (left) and Gary Shiu of the University of Wisconsin swap ideas at the Aspen Center.

Theorists in other sciences focus on explaining experimental data, but most string theorists study formal aspects of the theory itself, says Gordon Kane, a particle theorist at the University of Michigan, Ann Arbor. “Only in string theory is there a complete disconnect in which string theorists don’t make any effort to make contact with experiment,” Kane says. Stuart Raby, a particle theorist at Ohio State University in Columbus, says string theorists must find a way to account for experimental observations, especially in particle physics, in order to maintain the theory’s credibility. “You’re not going to believe string theory until you see the real world coming out of it,” he says.

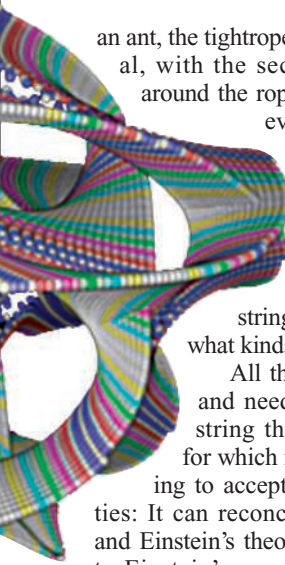
Recent astronomical observations, the construction of a huge new particle collider in Europe, and advances in the theory itself have whetted researchers’ appetites for analyzing hard data. But the task remains daunting, and some string theorists say the theory isn’t ready for this kind of test. “There’s a lot of stuff that we know, but I still feel that there’s some missing idea or some very difficult mathematics that needs to be done before we can tie that [information] to string theory,” says string theorist Jeffrey Harvey, in a phone interview from his office at the University of Chicago, Illinois. Moreover, most researchers believe that a huge number of distinct versions of the theory may jibe with what we know and can measure. If so, physicists may have to rethink what it means for a theory to explain experimental data.

Not quite a gimme

In summer, Aspen lends itself to contemplation. At the physics center, sunlight shimmers silver on fluttering aspen leaves as researchers chat in the shade or work at picnic tables. A brook babbles across the courtyard, branching once, then once again, like diverging lines of inquiry. Yet newcomers to the center often struggle to sleep. They rise in the morning with dry eyes and headaches. It’s the effect of the thin mountain air. Or perhaps it’s the strain of thinking that particles are tiny strings and that the universe has 10 dimensions.

But that’s precisely what string theory says. We observe only four dimensions—three spanning space and one ticking away time—because the other six curl up tight. In effect, spacetime is a bit like a tightrope, which appears essentially one dimensional to a large creature such as a human. But to

* Strings and the Real World, 15 August–12 September.



an ant, the tightrope appears two dimensional, with the second dimension curled around the rope. In string theory, however, the six “compactified” dimensions of the universe curl together to form a kind of six-dimensional multiholed doughnut. The intricate shape determines how strings can vibrate and, hence, what kinds of particles exist.

All this may seem far-fetched and needlessly complicated, but string theory possesses a virtue for which many physicists are willing to accept these seeming absurdities: It can reconcile quantum mechanics and Einstein’s theory of gravity. According to Einstein’s general theory of relativity, mass and energy warp spacetime, producing the effects we call gravity. However, the uncertainty principle of quantum mechanics implies that at very short length and time scales, spacetime cannot remain smooth but must burst into a chaotic froth in which notions such as before and after and ahead and behind can lose their meanings. This “quantum foam” overwhelms any conventional theory of pointlike particles, causing it to go mathematically haywire.

String theory avoids this problem because the strings are long enough to stretch over ripples and bubbles in the quantum foam. They ignore the effects of the foam much as a large ocean liner plows through the buffeting of small, choppy waves. As a quantum theory of gravity, string theory remains mathematically reasonable, as physicists have known since the 1970s.

But it wasn’t until Green and Schwarz ignited the “first string revolution” that physicists realized string theory might realistically account for particle physics, too. Within months, others found that if the six extra dimensions wound into a shape called a Calabi-Yau manifold, the theory came very close to producing the particles we see in nature, says string theorist Andrew Strominger from his office at Harvard University. “It was like hitting a golf ball from 200 yards away and coming within a centimeter of the hole,” he says. “There was a feeling that it was going to take only one more shot to get it in.”

Twenty years later physicists have yet to pick up that gimme. For a while researchers hoped there would be only one way to curl up the extra dimensions—and, perforce, only one logically consistent explanation of all the forces of nature. But fairly quickly researchers realized that there were a great number of Calabi-Yau manifolds, Strominger says. And directly observing the

putative strings would require collisions more than a million billion times more energetic than any that have been produced in a particle collider.

Over the years string theory has continued to attract bright young physicists (see sidebar). But most researchers have focused on more formal matters, such as drawing connections between the various subspecies of string theory, exploring the subtle symmetries built into the theory, or even studying the entropy of highly idealized black holes. For years it seemed that the real world could wait.

Surveying the landscape

Now, in the monasterial quiet and austerity of the Aspen Center, some researchers argue that it’s time to return to the data. Many are striving to reconcile string theory with our current understanding of elementary particles, which is embodied in a point-particle theory called the Standard Model. The Standard Model neatly accounts for the electromagnetic force, the strong force that binds the atomic nucleus, and the weak force that causes certain types of radioactive decay. It

assumes that matter and energy consist of a few dozen fundamental particles such as the photons that make up light and the up and down quarks that make up the protons and neutrons in atomic nuclei. Fitting those particles into string theory isn’t that difficult, says Gary Shiu, a string theorist at the University of Wisconsin, Madison.

Instead, the hard part is explaining away the extra particles and phenomena that string theory predicts but that experimenters have not observed. Thanks to recent advances in string theory, however, researchers are closing in on their goal. In particular, string theorists have found a way to stabilize the wound-up dimensions, which tend to spring open or collapse entirely. Known as “moduli stabilization,” the advance makes more-realistic calculations possible—maybe. “It’s as close as you can get,” Shiu says. “It’s like running in a race, and the finish line is always moving an inch away from you. But we *do* see the finish line.”

Theorists also savor the prospect of fresh data. Experimenters are constructing a gargantuan particle smasher called the Large Hadron Collider (LHC) at the European

The Children of the Revolution

String theorists have struggled with their immensely complicated theory for decades, and most agree it will take decades more to complete their work. Yet string theory continues to attract the brightest and most ambitious young theorists. *Science* asked several what drew them to a field that promises little personal glory and long-delayed gratification.

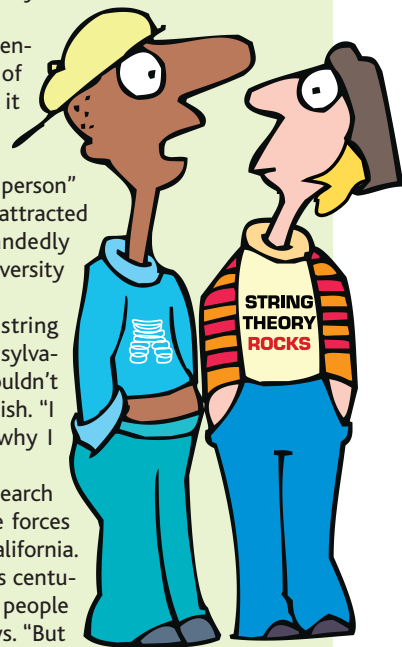
All agreed that string theory’s main appeal is its potential to answer the deepest questions about the nature of the universe. “Maybe I won’t be the one to understand it all,” says Liliana Velasco-Sevilla, a postdoc at the University of Michigan, Ann Arbor. “But if it happens while I’m alive, I’ll be happy to understand the formulation of the person” who figures it out. The brightest physicists may also be attracted by the chance—no matter how remote—to single-handedly discover the next great idea, says Keith Dienes of the University of Arizona in Tucson: “We all have the Einstein complex.”

Some cite distinctly personal reasons for pursuing string theory. Brent Nelson, a postdoc at the University of Pennsylvania, says he read about string theory as a teenager and couldn’t believe so many people accepted something so outlandish. “I haven’t learned enough,” he says. “I still don’t know why I should believe.”

String theory has opened so many new avenues of research that it’s worth pursuing even if it doesn’t explain all the forces in nature, says Eva Silverstein of Stanford University in California. “If string theory as a theory of gravity were ruled out this century, then certainly it would be a disappointment to the people who dedicated all their efforts to developing it,” she says. “But it still should be done.”

Whatever its appeal, string theory’s ability to draw top-notch young talent is “the litmus test of whether the field is exciting,” says veteran string theorist Herman Verlinde from his office at Princeton University. “If string theory stops doing that,” he says, “then I might stop doing string theory.”

—A.C.



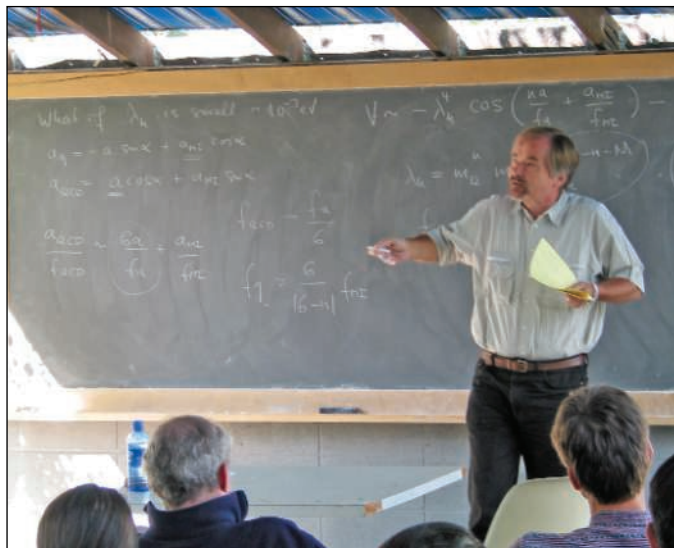
high-energy physics laboratory, CERN, near Geneva. The LHC should start collecting data in 2007, and many physicists believe it will produce the particles predicted by a theory called supersymmetry, which grew out of string theory and which assumes that for every type of particle we've seen, there exists a heavier "superpartner." Spotting those particles wouldn't prove string theory correct—string theory implies supersymmetry, but not the other way around—but they would give theorists more to work with. (Not observing those particles wouldn't necessarily sink string theory either, as they could simply be too massive to be produced at the LHC.)

Some theorists have even speculated that a few of string theory's extra dimensions might be wound loosely enough to be detected at the new particle smasher. If those dimensions are big enough, matter and energy might disappear into them when high-energy particles collide.

Meanwhile, other researchers are tackling an entirely different problem: They're trying to use string theory to explain the accelerating expansion of the universe. In 1998, astronomers detected the cosmic speedup by studying distant stellar explosions called supernovae. The observations suggested that something is stretching spacetime. And that's precisely what Einstein had in mind 80 years earlier when he dreamt up a space-stretching energy called the "cosmological constant." Although Einstein later abandoned the idea, the cosmological constant now appears to be real, and string theorists hope to calculate its value.

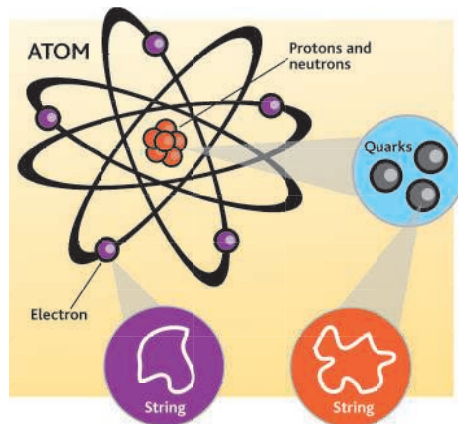
But that's not going to be easy, says Shamit Kachru, a string theorist at Stanford University in California. Most theorists assume that the cosmological constant is the energy trapped in the vacuum of empty space, which isn't zero because, thanks to the uncertainty principle, particles keep flitting in and out of existence. Basic string theory calculations yield vacuum energies that are many, many orders of magnitude too big.

Moreover, each way of winding the extra dimensions corresponds to a different version of the vacuum. Work on moduli stabilization suggests that there are a whopping 10^{300} different stable vacua, and theorists have no way to choose among them. String theorists now talk of a vast, cratered "landscape" in which each dimple corresponds to a possible vacuum. "If this picture is correct," Kachru says, "then it's unlikely that we'll explain the cosmological constant in a simple way."



En plein air. Hans-Peter Nilles of the University of Bonn, Germany, lectures in a classroom set up in the center's grape arbor.

Facing that landscape, some researchers are questioning what it will mean to make calculations and predictions. "In string theory as we know it, we can give up on making *unique* predictions because there are just so many vacua," says Scott Thomas, a particle theorist at Stanford University. Some, such as Thomas, favor measuring the statistical properties of the landscape and making more probabilistic predictions. A few prefer analyses that rely on the "anthropic principle," which essentially says that the cosmological constant can only have a value consistent with our own



Harmony. Elementary particles may be strings vibrating in different ways.

existence. Many seem to hope that some new principle or idea will point the way out of the conceptual wilderness.

Revolutions 3, 4, 5, ...

Even if they don't pay off immediately, renewed efforts to connect string theory to data are beneficial, researchers say. Such work opens lines of communication, says Eva Silverstein, a string theorist at Stanford

University and the Stanford Linear Accelerator Center in Menlo Park, California. "There was a period when there was an almost ethnic conflict between string theorists and phenomenologists," she says. "The situation is a lot healthier now."

Nevertheless, tensions still exist. For example, many string theorists point to the discovery of the accelerating expansion of the universe as the observation that gives them the best chance for making a connection with data. However, Raby, the particle theorist from Ohio State, says that for decades particle physics has provided far more data of far greater detail. "Since 1975, we've had a huge amount of information that everybody

has ignored," Raby says.

Even as some researchers struggle to connect string theory to experimental data, the theory itself continues to grow more complicated and mysterious. Ten years ago, researchers knew of five distinct types of string theory, which differed in, for example, whether the strings had to be closed loops. But in 1995, Edward Witten of the Institute for Advanced Study in Princeton, New Jersey, argued that all of them were different approximations of a single underlying theory he dubbed M-theory. It possesses yet another dimension and is filled not just with strings but with two-dimensional membranes and "branes" of three or more dimensions as well.

This "second string revolution" reassured string theorists that they were all working on the same thing. But in some ways it leaves them even farther from their goal of a single, definite theory of the physical world. No one knows what M-theory really is. And no one can say when theorists are likely to find out. "How many more string revolutions will we need?" Caltech's Schwarz wonders. "I don't know, but I think we'll need many more."

But that's probably acceptable to most of the researchers at the workshop, who seem genuinely pleased just to participate in such a grand pursuit. In the evening, they gather in the courtyard to grill steaks and hamburgers and to share a beer or a glass of wine. After dinner, the younger crowd engages in a spirited game of volleyball. Night falls, and a black bear wanders into the parking lot. Some people rush into the nearest building to get away from it; others rush out to glimpse the ursine intruder fleeing into the nearby sage and scrub. Its inky form quickly dissolves into the darkness like a phantom—or the dream of the ultimate theory.

—ADRIAN CHO

CREDITS (TOP TO BOTTOM): A. CHO/SCIENCE; K. BUCKHEIT/SCIENCE

What Can NIH Do for Physicists?

Biomedical scientists hope to convince U.S. politicians that more funding for the physical sciences and engineering eventually will save lives, too

What's the best way to share a meal with an 800-pound gorilla? Physicists, mathematicians, and engineers may have a chance to answer that question if federal legislators and agency officials embrace a campaign to expand the research menu at the National Institutes of Health (NIH).

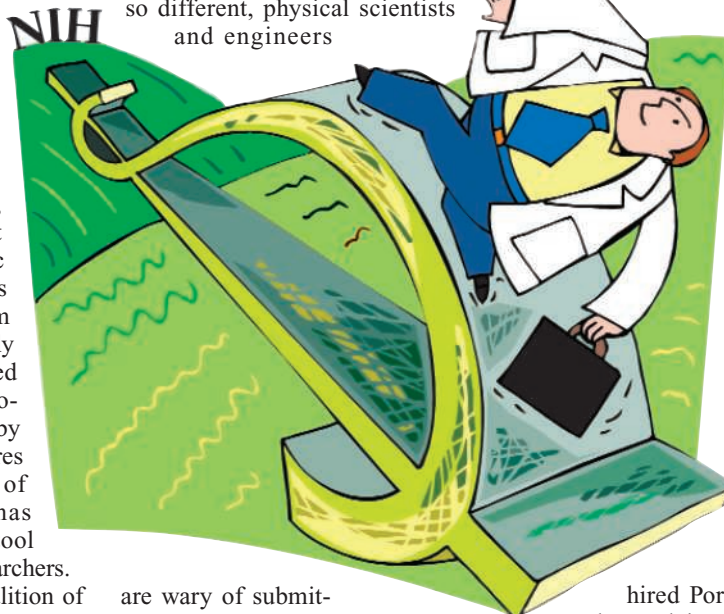
NIH dominates U.S. academic research, and the recent 5-year doubling of its budget (now \$28 billion a year) has accentuated the gap between federal support for the life and physical sciences. But NIH's growth has slowed to a crawl, leaving biomedical scientists casting about for ways to reignite interest in their discipline within Congress and the White House. At the same time, life scientists are worried that inadequate funding for basic research in the physical sciences and engineering could deprive them of discoveries that could ultimately benefit human health. An oft-cited example is nuclear magnetic resonance, a technology developed by physicists to see chemical structures that, 30 years later in the form of magnetic resonance imaging, has become an essential diagnostic tool for physicians and biomedical researchers.

The answer, according to a coalition of a dozen scientific societies, is a campaign called "Bridging the Sciences." Earlier this month, more than 100 scientists and officials from several U.S. research agencies met in suburban Maryland to discuss ways that NIH could make a bigger contribution to nonbiomedical sciences and vice versa. The meeting satisfied a directive Congress inserted into three spending bills, at the urging of the coalition, asking NIH "to discuss what needs to be done to encourage progress in the physical sciences that will provide support and underpinning for future advances in the life sciences." The coalition also has hired ex-Representative John Porter, a former chair of the House panel that controls NIH's budget and a longtime friend of biomedical research, to figure out how best to sell the idea to Congress and the executive branch.

Participants at the daylong public meeting had no trouble identifying obstacles. The biggest one, they said, was the vast difference between how physical and life sci-

tists define and tackle the intellectual challenges they face. "If Boeing designed airplanes the way that biologists conduct experiments," said Ken Dill, a biophysicist at the University of California, San Francisco, and one of three co-chairs of the meeting, "they'd take 1000 fuselages, stick wings on them in a random pattern, and then see which planes flew and which ones crashed."

Because their world view is so different, physical scientists and engineers



are wary of submitting research proposals to NIH, explained mathematician Tony Chan, dean of physical sciences at the University of California, Los Angeles. "The way life scientists talk is not the way mathematicians think," says Chan, who says his colleagues assume that their ideas won't be well received. Physical scientists also worry about being treated as second-class citizens, he adds. "We don't want to be called upon just to solve a problem that a biologist is having. We want to be involved from the start" in planning collaborative, interdisciplinary projects.

Cultural differences aren't the only barriers, however. Participants said the rigid departmental boundaries in academia devalue the contributions that faculty make to fields outside their discipline. The narrow reward system affects everything from how students are educated to how tenure decisions are made. Scientists outside biomedicine are also hampered by the conservative nature of the NIH peer-review sys-

tem, they noted, as well as the agency's relatively meager support for technology in service of basic science. The incompatibility of data sets from different disciplines also lowers the potential number of collaborations between the physical and life sciences, according to participants.

Organizers of the 9 November conference had hoped to go beyond fault finding and get scientists to imagine what could be achieved if NIH adopted a broader view of its research mission. The participants rose to the occasion, coming up with a list of so-called grand challenges. They included broad investigations into the basis of life and disease and the physical principles underlying the behavior of complex

biological systems, as well as more targeted efforts to develop systems that would allow living creatures to survive on the moon or new ways to deploy therapeutic agents against chronic diseases.

Conference organizers deliberately avoided asking scientists to put a price tag on their suggestions. However, all agreed that more government funding was needed. "To do it right, we'll need new money," says co-chair Claire Fraser, president of The Institute for Genomic Research in Rockville, Maryland.

For that, the coalition has hired Porter. "You look for a vehicle," he explained. In legislative parlance, that means inserting language into an existing bill affecting a relevant agency. Possible candidates, Porter suggested, would be a bill reauthorizing NIH programs, a similar measure reauthorizing NASA, or one of the many spending bills that Congress approves each year. The coalition initially proposed targeting the National Institute of Biomedical Imaging and Bioengineering, the newest of NIH's 22 institutes. But Dill now says that an NIH-wide effort, or even an interagency initiative, might be a better idea.

Dill and his colleagues will summarize the results of the conference before briefing top officials from NIH and the National Science Foundation (NSF) next month. Asked about the first fruits of the project, Dill says, "I'd like to see something happen next year." NSF's Bruce Hamilton says only that the report "will be the basis for further discussions."

—JEFFREY MERVIS

X-ray Source Produces a Glimmer of Hope

What do you do with a secondhand synchrotron? Two physicists had the idea of making it a gift to the troubled Middle East, where a home for it is now rapidly taking shape

ALLAN, JORDAN—The tawny hills around this village 30 kilometers north of Amman are fringed with pine, olive, and oak trees. Here, among shepherd boys tending sheep and goats, an unlikely building is taking shape. It will soon house one of the most advanced scientific instruments in the region, a synchrotron light source called SESAME, which is designed to allow researchers from across the Middle East to probe the shapes of proteins and the atomic structure of new materials.

The project, which began when physicists rescued a Berlin synchrotron from the scrap yard in 1997, seemed far-fetched to some but is fast becoming a reality. In April, SESAME (Synchrotron Light for Experimental Science and Applications in the Middle East) became a self-governing UNESCO organization when Israel joined Jordan, Egypt, Turkey, Bahrain, and Pakistan as the sixth official member. Two more, the Palestinian Authority and Iran, are in the process of joining.

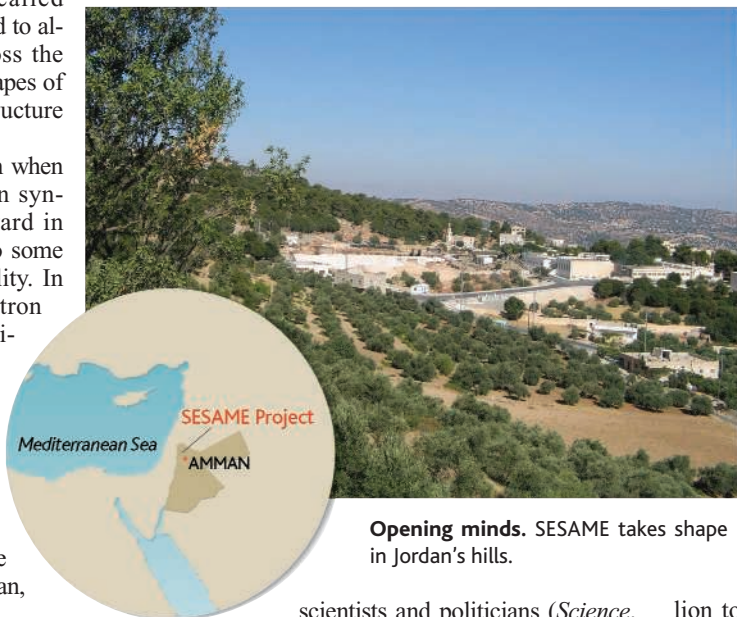
At the building site, donated by Jordan's government, the foundations are laid and walls are starting to rise. And last month, more than 90 scientists gathered in Turkey for SESAME's latest users' meeting to discuss the research they hope to do once the machine comes on line.

A synchrotron light source is a particle accelerator that propels electrons in a circle at close to the speed of light. The electrons give off intense beams of ultraviolet and x-ray light as they curve around the ring, and researchers use the light for everything from fundamental physics to microscopy of biological samples.

SESAME was the brainchild of physicists Herman Winick of the Stanford Synchrotron Radiation Laboratory in Palo Alto, California, and Gustav-Adolf Voss of DESY, Germany's particle physics lab in Hamburg. Both scientists were advising the German government on the building of a new synchrotron source, BESSY II, in Berlin, when Winick discovered that its predecessor, BESSY I, would be sold for scrap. "That was like a

knife in my heart," he says. BESSY I had been a groundbreaking machine, he adds, "and it was still in huge overdemand."

Winick wondered if it couldn't be reassembled somewhere else, with a few updates and modifications. His proposal quickly gained support from European and Middle Eastern



Opening minds. SESAME takes shape in Jordan's hills.

scientists and politicians (*Science*, 25 June 1999, p. 2077). In the hopeful days following the Oslo accords between Israel and the Palestinians, supporters argued that the machine would not only aid scientific development but also enable scientists to work together and build personal ties. Germany quickly agreed to donate the disassembled BESSY I, and in 2000, delegates from participating countries chose the Jordanian site.

Not everyone was convinced it would work. "I am one of the people who thought the project would never get off the ground," admits Zehra Sayers, a biophysicist at Sabanci University in Istanbul who now heads SESAME's Scientific Committee. But she soon changed her mind. "I could see how quickly it was moving and how much effort people were willing to put in," she says.

Support from Jordan has been particularly crucial to the project's early success, Winick says. The country's King Abdullah II has been a personal and enthusiastic supporter. He learned of the project in 1999, when he met briefly with Herwig Schopper,

former director of the CERN particle physics lab near Geneva, Switzerland, and UNESCO's Maurizio Iaccarino, who were touring the region to build support for SESAME. "As soon as the meeting was finished, the king asked me to prepare a letter [requesting to join] on the spot," says Khaled Toukan, Jordan's research and education minister, who serves as the acting director of SESAME.

The Allan site in Jordan also had a geographical advantage. Scientists in Istanbul can reach Amman in a 2-hour flight, Sayers notes. And, in theory, it's a 2-hour drive for scientists from Israel and the West Bank. But Israel's current military crackdown has brought long waits at checkpoints, and that 70-kilometer trip can take more than 6 hours now. The Israeli and Jordanian governments have promised to streamline travel for SESAME users, says Moshe Deutsch of Bar Ilan University in Ramat Gan, Israel.

SESAME's main challenge now is to secure promised funding from the European Union. Member countries' contributions cover the day-to-day costs, but updating the machine requires outside funds. The E.U. has promised \$12 million to upgrade the synchrotron from 0.8 to 2.5 GeV, but bureaucratic delays are holding up the final agreement. Once the E.U. money comes through, supporters hope that the United States and Japan will pitch in on the estimated \$10 million to \$15 million needed to build beamlines, the equipment that aims and focuses the x-rays onto the experiments.

Although SESAME won't produce its first x-rays until 2008, it is already fulfilling part of its mission, Sayers says. The project has sent more than two dozen scientists from the region to train at existing synchrotron sources. That effort has been a bit too successful, she adds: "The places [where] they were working have all offered them permanent jobs."

And, despite the dramatic increase in violence in the region, participants say SESAME provides a small glimmer of hope. "A synchrotron has a different kind of sociology," says Sayers. "It is a suitable project for the area, to bring people of different cultures together." Eliezer Rabinovici of the Hebrew University in Jerusalem agrees. "Politics is left for the coffee breaks or the evenings," he says. "As a string theorist, I work on parallel universes. I was always curious about what a parallel universe was like, and now I know. I'm living in one when I go to SESAME meetings." —GRETCHEN VOGEL

Head Games Show Whether Dinos Went on Two Legs or Four

Your mother was right: Posture matters. For dinosaurs, it's one of the most basic features that paleontologists—and exhibit designers—want to know. In Denver, a trio of paleontologists presented a broad survey of dinosaurs and showed that the shape of the inner ear canals can reveal whether a dinosaur stood upright or walked on all fours. The approach is great, says Donald Henderson, who studies dinosaur biomechanics at the University of Calgary in Alberta, Canada. “It’s a completely independent, objective source of evidence.”

There’s no doubt, of course, that the massive, thick-legged sauropods kept four feet on the ground. Or that *Tyrannosaurus rex*, with its shrimpy arms, walked upright. But for other creatures, the picture has not always been so clear. The duck-billed dinosaurs, such as *Edmontosaurus* for example, had strong legs and were sometimes reconstructed as being bipedal, sometimes quadrupedal. To make their various cases, paleontologists have traditionally looked at limb proportions and other aspects of anatomy, such as joint articulation.

The inner ear offers another way to examine posture and locomotion (*Science*, 31 October 2003, p. 770). With three semicircular canals oriented at right angles to each other, the inner ear helps keep the head oriented. The canals are lined with hairs that detect the sloshing of fluid inside them, which the brain analyzes to reveal how the head is moving. Graduate students Justin Sipla and Justin Georgi and paleontologist Catherine Forster, all at Stony Brook University in New York, have been peering into dinosaur skulls

with computed-tomography scanning to reconstruct ancient postures.

After examining 19 taxa from all the major groups of dinosaurs, they identified a distinct difference between bipeds and quadrupeds. In those that walked upright, such as the birdlike *Dromaeosaurus*, the anterior semicircular canal—which detects dipping of the head—was enlarged vertically relative to the posterior canal. That was not the case in four-footed dinosaurs, such as *Chasmosaurus*, a relative of *Triceratops*. “The correlation between the size of the anterior semicircular canal and posture was really nice,” Henderson says. The researchers speculate that the reason for expanding the canal—which makes it more sensitive—is that the head of a biped experiences greater downward accelerations while moving and must coordinate with the neck muscles to remain stable.

Next, the team analyzed taxa for which posture had been debated. As for *Edmontosaurus*, its ear resembled those of known quadrupeds—backing up recent inferences. And a scan of *Anchisaurus* confirmed that the closest relatives to sauropods, the prosauropods, were bipedal. The team plans to investigate when and how transitional forms in these groups began to evolve quadrupedality. Sipla says that since the talk, other paleontologists have been offering skulls for the project: “For a grad student, that’s a dream come true.”

DENVER, COLORADO—Almost 1000 paleontologists and enthusiasts met here from 3 to 6 November for the 64th annual meeting of the Society of Vertebrate Paleontology.

Reconstructing posture can be a slippery business, cautions Robert Reisz of the University of Toronto in Ontario, Canada. “But as long as we can get hard data, like the shape of the semicircular canals, then we’re more confident about our interpretations,” he says. That prospect alone will make paleontologists sit up straight.

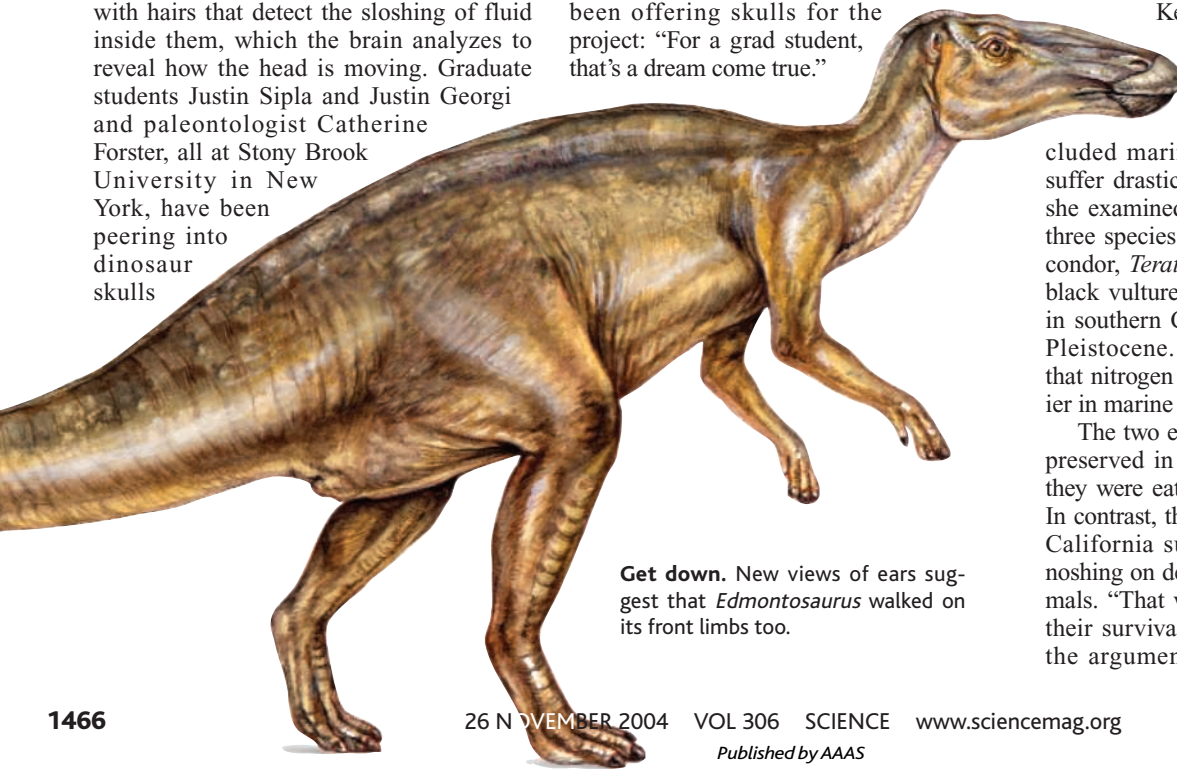
Antiextinction Tip: Eat to Live

A cosmopolitan diet may have helped the California condor avoid the fate of many other large scavenging birds 12,000 years ago, a paleontologist reported at the meeting.

The late Pleistocene was a difficult time for large animals in North America. Climate was changing, and human hunters had marched into the continent. Although the ultimate cause of the extinction of the mammoths and other large herbivores is still debated, it’s clear that their demise had drastic effects that cascaded through food webs. Saber-toothed cats and other predators went extinct as well, as did many kinds of vultures, including *Teratornis merriami*—the largest flighted bird ever, with a wingspan of 3 meters or more. Yet the California condor pulled through.

Kena Fox-Dobbs of the University of California, Santa Cruz, hypothesized that the reason might be that condors had broader diets that included marine mammals, which did not suffer drastic extinctions. To test the idea, she examined the isotopes in the bones of three species of fossil birds: the California condor, *Teratornis*, and the extinct western black vulture—all of which were common in southern California until the end of the Pleistocene. Ecologists have established that nitrogen and carbon isotopes are heavier in marine organisms.

The two extinct scavengers had isotopes, preserved in bone collagen, that indicated they were eating carcasses of land animals. In contrast, the condor bones from southern California suggested that they were also nosing on dead seals and other marine animals. “That wide dietary niche was key to their survival,” Fox-Dobbs says. Boosting the argument, condor fossils from New



Get down. New views of ears suggest that *Edmontosaurus* walked on its front limbs too.



Sushi lover. The California condor may owe its survival to its diverse diet.

Mexico and Florida indicate that the birds had terrestrial diets—and didn't survive there. (Food from the ocean would have been less plentiful in Florida, which lacks the currents that bring nutrients up from the sea floor off California.)

"It's a novel study," says paleontologist John Alroy of the National Center for Ecological Analysis and Synthesis in Santa Barbara, California. "As far as paleontological evidence goes, it's pretty convincing." The broader diet could explain why condors were able to survive despite the loss of many large animals. "To hang on for 12,000 years, you've got to be doing something right."

Timing Complicates History of Horses

It's a classic story of evolution. About 18 million years ago in North America, horses, camels, and other groups of herbivores independently evolved high-crowned cheek teeth. This condition, called hypsodonty, has long been considered a response to a changing environment: During this time, the Miocene Epoch, the climate was cooling, and grasses—which contain abrasive silica—began to spread and replace leafy woodlands. Tall teeth that last longer would have provided an immediate advantage.

The tale is not so straightforward, it turns out. At the meeting, Caroline Strömberg of the Swedish Museum of Natural History in Stockholm reported that it took 4 million years after the grass began to dominate the Great Plains for hypsodonty to appear—a puzzling lag. "It really does raise questions," says Christine Janis of Brown University. Yet not all was quiet on the western front: Janis and colleagues pre-

sented evidence that at about this time horses were developing legs more efficient at moving, which may have allowed them to range more widely for tender grass in the open landscape. Strömberg charted changes in vegetation by examining the tiny bits of silica, called phytoliths, contained in grasses, palms, and many other kinds of plants. She collected 99 samples from rocks across the central Great Plains, spanning roughly 31 million years (from the middle Eocene, through the Oligocene and Miocene) until about 9 million years ago. The relative amounts of various kinds of phytoliths revealed whether the habitat was open grassland resembling the modern savanna, woodland, or forest. The work paints the first high-resolution picture of vegetation for this time period. "It's an excellent, well-constrained study," says Bruce MacFadden of the University of Florida, Gainesville.

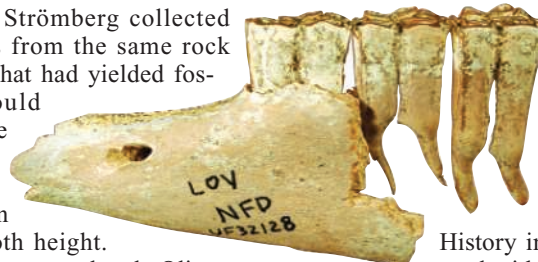
Because Strömberg collected the samples from the same rock formations that had yielded fossils, she could compare the changes in vegetation with known shifts in tooth height.

In the late Eocene and early Oligocene, the area was forested. Grasses replaced the trees in the central Great Plains by at least 22 million years ago, but full-blown hypsodonty didn't take root in horses for another 4 million years. "This is a significant lag," Strömberg says. "It weakens the argument for coevolution, in lockstep, of horses and grasses."

Then why the lag? One possible reason could be that there was weak or no pressure

to adapt to the new vegetation. But Strömberg points out that when the savanna first appeared, the closest relative to hypsodont horses, which belong to the genus *Parahippus*, evolved slightly higher teeth than its ancestors had. It may also be that some animals compensated by learning new behaviors to cope, such as feeding on grasses only in the spring, when they are tender, as red deer do.

Clues may come from elsewhere in the skeleton. Janis and Manuel Mendoza and Paul Errico of the University of Rhode Island have examined horses' limbs, for example. During the Miocene, horses and camels were evolving longer limbs, but apparently not to escape accelerating predators—which evolved longer limbs some 20 million years later. Instead, Janis proposed, the limbs first evolved to be more efficient at walking. In a preliminary analysis, Janis meas-



Delayed. High-crowned teeth took a while to evolve to resist gritty food.

ured the limbs of fossil horses at the American Museum of Natural History in New York City. Compared with their ancestors, the advanced horses of the Miocene had knees and ankles with features suggesting that the limbs would have been more constrained to move in a fore and aft plane and hence more efficiently. "I think they're increasing their foraging radius," Janis says. High-crowned teeth might not be the only way to make life on the grasslands less of a grind.

—ERIK STOKSTAD

Snapshots From the Meeting

Tetrapod ancestor. Researchers from the Academy of Natural Sciences in Philadelphia, Pennsylvania, the University of Chicago, Illinois, and Harvard University unveiled what may turn out to be the most significant fossil reported at the meeting: a lobe-finned fish that belongs to the group most closely related to four-legged vertebrates, known as tetrapods. "It may be an *Archaeopteryx*-quality transitional fossil," says Per Ahlberg of Uppsala University in Sweden. A complete skull and shoulder girdle, as well as two partial skulls, were found in roughly 380-million-year-old rocks on southern Ellesmere Island, Canada. It is only the third member known from this group, called the elpistostegids. The specimen will likely yield important insights in the evolution of tetrapods, Ahlberg predicts.

Precocious flyers. Birds and bats don't start flying until they're almost full grown. At the meeting, researchers from Humboldt University in Berlin and the University of London argued that pterosaurs were different, taking to wing at just 5% of adult mass. The pair studied variously sized individuals of *Pterodactylus kochi* and found that young ones had about the same aerodynamic proportions as adults, presumably suitable for takeoff. A recently described pterosaur embryo, complete with wing membranes, has also been interpreted as ready to fly. This could indicate that pterosaurs didn't need parental care.

—E.S.

Something in the Water

Scientists have long puzzled over what killed the animals that became the superbly preserved 47-million-year-old fossils recovered over the past few decades from the Messel Lake deposits in Germany. A team at the University of Bonn suspects that toxic algae did them in.

The fossils from the World Heritage Site of Messel near Darmstadt show astonishing diversity, from dog-sized primitive horses to birds, bats, beetles, and plants. Especially mysterious is the presence of birds and bats, which might have been expected to fly away from noxious volcanic gases previously invoked as the likely cause of death.

Now paleontologist Wighart von Koenigswald and colleagues think they have the answer. They observed that an unusually high proportion of specimens of the primitive horse *Propalaeotherium* (five out of 50) were pregnant mares. And there were five obvious pairs of *Allaeochelys* turtles. All this suggested a link between early summer reproduction and death in the lake. The Messel sediments are oil-rich muds made up of alternating fine layers of limestone and algae. Comparison with other deposits indicates that the algal layers were created by abundant blooms of cyanobacteria, normally present in low numbers but which sometimes take over surface waters and release toxins when nitrogen levels are high. "Animals drinking such poisoned water die almost instantly," observes Koenigswald's team. The authors, whose report is in the latest issue of *Paläontologische Zeitschrift*, say the presence of toxins is difficult to prove. But it's a "provocative new model for the death of the Messel mammals," says Yale University paleontologist Derek Briggs. "It should stimulate new research to detect any correlation between death assemblages and cyanobacterial blooms."



Pregnant mare with fetus.

Fear as Action

Much research has been conducted on how the human brain responds to facial expressions. A new Harvard brain-scan study suggests that reactions to scary bodily

involved in movement and action representation. This combination "may constitute a mechanism for fear contagion" as well as for action in response to fear—that is, fleeing—the authors observe.

De Gelder notes that because most research on emotions looks at faces, not bodies, scientists have assumed that amygdala activation is specific to fearful faces. This study suggests that "a more holistic view of visual processing" is needed, says cognitive scientist Pawan Sinha of the Massachusetts Institute of Technology, who adds that the brain "appears to be more flexible and opportunistic" in how it picks up fear messages than previously realized.

De Gelder says studies on the relation between emotion and movement could offer insights into movement disorders that also feature emotional disturbances, such as Parkinson's and Huntington's.

Gulf Oil Decline in Sight

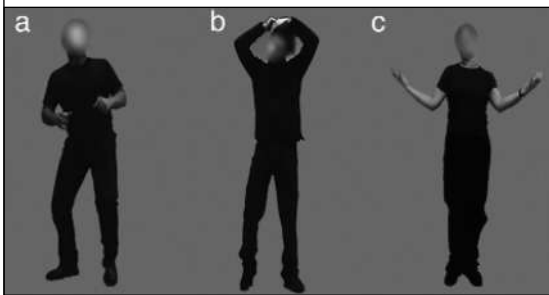
The price of a barrel of crude is way up, and government officials say incentives implemented by the Bush Administration in 2001 will soon be boosting production in the Gulf of Mexico. But despite the incentives, oil production in the Gulf may start to decline within the next 6 years, according to a new forecast from the Department of the Interior.

Total U.S. oil production peaked in 1970, but drillers have been driving up production in the Gulf, the country's top oil-producing area, by pushing into ever-deeper waters. Now companies are poised to extract the last drops. According to a new forecast by Interior's Minerals Management Service (MMS), Gulf production should surge by almost 50% by the end of the decade as industry reaches for oil beneath "ultradeep" (more than 1500 meters) waters and from more than 9 kilometers beneath the shallow sea floor. But that surge will be short-lived, says MMS, and Gulf production is likely to decline after 2011.

That's sharply at variance with the outlook espoused by the U.S. Department of Energy, which recently forecast that total U.S. oil output would hold steady through 2025. The projected Gulf peak—at 2.3 million barrels a day, or a quarter of total U.S. oil production—is the kind of sign that pessimistic oil analysts expect to see as world oil production peaks in the coming decade and the era of cheap oil comes to an end.

Image not available for online use.

Gulf of Mexico oil rig



Fearful (a), neutral (b), and happy (c) poses.

gestures involve not only the emotional brain but the motor areas as well.

Psychologist Beatrice de Gelder and colleagues at Harvard Medical School in Boston selected 24 photographs of actors in gestures that were fearful, happy, or emotionally neutral. They then blurred the faces so subjects' brains would only react to bodies. In a 16 November paper appearing online in the *Proceedings of the National Academy of Sciences*, the researchers report that whereas happy gestures only spurred activity in the visual cortex, the fearful ones revved up not only emotional centers, such as the amygdala, but also areas

Edited by Yudhijit Bhattacharjee

AWARDS

Math prizes. A request for a letter of recommendation led to a major mathematical discovery and earned



Cambridge University's Ben Green one of three 2004 research awards from the Clay Mathematics Institute.

"I asked [mathematician Terence Tao] for a reference for a job application," says Green, who had met Tao during a stint at Princeton University in 2001. "He said, 'Yes, of course, ... and I've been thinking about such and such.'" The conversation pulled Green and Tao into a close collaboration. The two soon solved a famous conjecture about the prime numbers: They showed that for any given number n , there are

an infinite number of evenly spaced progressions of primes that are n numbers long (*Science*, 21 May, p. 1095).

Green, 27, wins a 2-year fellowship and a sculpture. (Tao won a Clay award last year for other work.) The other two winners this year are Gérard Laumon and Bao-Châu Ngô of the University of Paris-Sud, honored for their work in algebra.

Mental health prize. Child psychiatrist Jonathan Picker has won the first Sidney Baer Prize for mental health research from the National Alliance for Research on Schizophrenia and Depression. Picker, a researcher at Harvard Medical School's McLean Hospital in Belmont, Massachusetts, wins the \$40,000 prize for his work examining the role of genetic and environmental risk factors in the development of schizophrenia.

Bioinformatics award. Biochemist Amos Bairoch of the Swiss Institute of Bioinformatics in Geneva has won the \$88,000 Latsis Prize from the European Science Foundation.

CHECKING IN

In the war zone. Behavioral ecologist Peter Smallwood misses doing fieldwork. But he doesn't really mind that his new job keeps him tied to a desk. That's because Smallwood is serving a 1-year stint in Baghdad as the new director of the Interim Iraqi Center for Science and Industry, which hopes to find employment for scientists and engineers from Saddam Hussein's weapons programs (*Science*, 25 June, p. 1884).

Since arriving in September, Smallwood has encouraged the Iraqi scientists to think creatively about how they can apply their skills to civilian projects. "Under the regime, you did exactly what you were told and nothing else," he says. One vehicle will be a fellowship program in which applicants must submit detailed proposals. He hopes by the end of the year to have 120 scientists on contract, with a long-term goal of helping 500 find new livelihoods.

The 43-year-old Smallwood is on leave from the University of Richmond in Virginia. And although he no longer has the chance to commune with nature, he says that "finding a praying mantis here in Baghdad one day totally made my day."



CELEBRITIES

Household name.

Women sitting down to breakfast will soon get tips on how to combat heart disease in a cereal promotion that features a New York City cardiologist. Starting in January, boxes of Wheat Chex and Multi-Grain Chex will deliver a public-service message from Nieca Goldberg, chief of women's cardiac care at Lenox Hill Hospital in New York City, as part of a public-service campaign sponsored by General Mills.



It's not Goldberg's first venture into popular culture: Earlier this year she worked with script writers for the soap opera *One Life to Live* in a plot line involving a female character with heart disease.

JOBS

Culture shift. An American molecular biologist has become the first woman to direct the Friedrich Miescher Institute in Basel, Switzerland. Next month Susan Gasser will take the reins of the 34-year-old biomedical research institute, funded by pharmaceutical giant Novartis. She succeeds Denis

Monard, who has served as interim director since 2002.

Gasser, now a professor at the University of Geneva, hopes to aggressively develop the careers of young group leaders, who she says do not receive enough attention.



Hans Hengartner, a biologist at the Swiss Federal Institute of Technology in Zurich, says Gasser has what it takes to connect the academic and pharmaceutical worlds. "She is outspoken, and she is a leader," he says.

Gasser, 49, has lived in Switzerland since moving there as a graduate student in 1979.

Got any tips for this page? E-mail people@aaas.org

CREDITS (TOP TO BOTTOM): ROBERT SHAPIRO; MARK GERMANN/COURTESY OF THE CLAY MATHEMATICS INST.; FMI; SOURCE: PETER SMALLWOOD

Letters to the Editor

Letters (~300 words) discuss material published in *Science* in the previous 6 months or issues of general interest. They can be submitted through the Web (www.submit2science.org) or by regular mail (1200 New York Ave., NW, Washington, DC 20005, USA). Letters are not acknowledged upon receipt, nor are authors generally consulted before publication. Whether published in full or in part, letters are subject to editing for clarity and space.

Using Stimulants in Children with ADHD

WE READ WITH GREAT INTEREST JENNIFER Couzin's article "Pediatric study of ADHD drug draws high-level public review" (News of the Week, 20 Aug., p. 1088), which describes "heated debate among pediatricians and bioethicists" over the ethics of a study proposing to evaluate the effects of stimulant medication in typically developing children. As one pediatrician and bioethicist stated in the article, "I can see why people are struggling... you're actually giving [children] a psychoactive drug."

This cautious approach toward use of stimulant medication in typically developing children is dramatically different from the relatively uninhibited use of stimulant medication for children with attention deficit hyperactivity disorder (ADHD). Many pediatricians, psychologists, and psychiatrists now believe that stimulant medication should be the first and often only treatment for ADHD (1), and, as a result, use of stimulant medication to treat children with ADHD has increased substantially in the past few decades (2), with recent estimates indicating that more than 7% of elementary school children are medicated daily (3).

Shouldn't there be at least as much concern about giving a psychoactive drug to children with ADHD—typically for years—as there is about giving a single dose of the same substance to children without ADHD? After all, Rapoport's studies in the 1980s, mentioned in Couzin's article, demonstrated that stimulants have equivalent effects in ADHD and normal children, suggesting that stimulant medication should only be administered when absolutely necessary and after other treatment approaches have been tried.

We do not believe that stimulant medication for ADHD should never be used. Rather, it should be used cautiously and only after other, less invasive treatments have been tried. DANIEL A. WASCHBUSCH¹ AND WILLIAM E. PELHAM JR.²
¹Department of Psychology, Dalhousie University, Halifax, NS B3H 4J1, Canada. ²Center for Children & Families, State University of New York at Buffalo, 3435 Main Street, Buffalo, NY 14214–3093, USA.

References

1. MTA Cooperative Group, *Arch. Gen. Psychiatry* **56**, 1073 (1999).
2. M. Olfson, S. C. Marcus, M. M. Weissman, P. S. Jensen, *J. Am. Acad. Child Adolesc. Psychiatry* **41**, 514 (2003).
3. A. S. Rowland et al., *Am. J. Publ. Health* **92**, 231 (2002).

Outbreak of West Nile Virus in North America

THE REPORT "EMERGING VECTORS IN THE *Culex pipiens* complex" by D. M. Fonseca et al. (5 Mar., p. 1535) advances sweeping extrapolations concerning mosquito blood-feeding behavior and West Nile virus (WNV) transmission. These findings led Fonseca to conclude (1) that a European introduction of Nearctic mosquitoes could "radically change the dynamics of WNV in Europe" and to state "[t]his is a plea for more control of the movements of these disease vectors."

Fonseca et al. find that certain microsatellite markers distinguish Palearctic from Nearctic *C. pipiens* and interpret this observation as supporting the idea that the former feeds solely on birds and the latter indiscriminately on birds and mammals. Cited references (2, 3), however, permit no such suggestion, while other publications (4–13) indicate that Nearctic *C. pipiens* seek hosts no differently than do Palearctic forms. Their epidemiological interpretation of this analysis, therefore, is incorrect.

The most reasonable explanation for the relative severity of WNV in the United States rests on the novelty of the event and the pathogenicity of the introduced strain. Until recently, Nearctic birds remained nonimmune against this virus and had not adapted to its presence. In addition, other more effective vectors, such as *C. tarsalis*, transmit WNV in many intensely affected Nearctic sites (14). This report, therefore, fails to explain the unique features of the American WNV outbreak and cannot justify imposition of European quarantine measures against American mosquitoes.

- A. SPIELMAN,¹ T. G. ANDREADIS,²
C. S. APPERSON,³ A. J. CORNEL,⁴
J. F. DAY,⁵ J. D. EDMAN,⁴ D. FISH,⁶
L. C. HARRINGTON,⁷
A. E. KISZEWSKI,¹ R. LAMPMAN,⁸
G. C. LANZARO,⁴ F.-R. MATUSCHKA,⁹
L. E. MUNSTERMANN,⁶ R. S. NASCI,¹⁰
D. E. NORRIS,¹¹ R. J. NOVAK,⁸
R. J. POLLACK,¹ W. K. REISEN,⁴
P. REITER,¹² H. M. SAVAGE,¹⁰
W. J. TABACHNICK,⁵ D. M. WESSON¹³

¹Harvard University, Boston, MA 02115, USA. ²Connecticut Agriculture Experiment Station, New Haven, CT 06504, USA. ³North Carolina State University, Raleigh, NC 27695, USA. ⁴University of California, Davis, CA 95616, USA. ⁵University of Florida, Vero Beach, FL 32962, USA. ⁶Yale University, New Haven, CT 06520, USA. ⁷Cornell University, Ithaca, NY 14853, USA. ⁸Illinois Natural History Survey, Champaign, IL 61820, USA. ⁹Humboldt University, 10099 Berlin, Germany. ¹⁰Centers for Disease Prevention and Control, Fort Collins, CO 80522, USA. ¹¹Johns Hopkins Bloomberg School of Public Health, Baltimore, MD 21205, USA. ¹²Pasteur Institute, 75724 Paris Cedex 15, France. ¹³Tulane University, New Orleans, LA 70118, USA.

References

1. D. MacKenzie, "Hybrid mosquitoes blamed for U.S. West Nile disease," *NewScientist.com*, 5 March 2004 (available at www.newscientist.com/news/news.jsp?id=ns99994748).
2. A. G. Richards, *Entomol. News* **52**, 211 (1941).
3. A. Spielman, *Ann. N.Y. Acad. Sci.* **951**, 220 (2001).
4. C. Apperson et al., *J. Med. Entomol.* **39**, 777 (2002).
5. C. Apperson et al., *Vector-Borne Zoonot. Dis.* **4**, 71 (2004).
6. W. Crans, *Proc. N.J. Mosq. Exterm. Assoc.* **51**, 51 (1964).
7. G. Eklis, *J. N.Y. Entomol. Soc.* **79**, 190 (1972).
8. R. Hayes, *Mosq. News* **21**, 179 (1961).
9. A. D. Hess, R. O. Hayes, *Am. J. Trop. Med. Hyg.* **19**, 327 (1970).
10. L. A. Magnarelli, *Am. J. Trop. Med. Hyg.* **26**, 547 (1977).
11. R. Nasci, J. Edman, *J. Med. Entomol.* **6**, 493 (1981).
12. C. Tempelis et al., *Am. J. Trop. Med. Hyg.* **16**, 111 (1967).
13. C. Tempelis, *J. Med. Entomol.* **11**, 635 (1975).
14. D. R. O'Leary et al., *Vector-Borne Zoonot. Dis.* **4**, 61 (2004).

Response

CITING STUDIES WHERE ONLY U.S. SPECIMENS were examined, Spielman et al. state that Nearctic and Palearctic *Culex pipiens* "seek hosts no differently." On the basis of the combined evidence of our genetic analyses and host preference studies performed in the United States, Europe, Africa, and the Middle East, we propose that they do.

Image not available for online use.

Colored scanning electron micrograph of a *Culex pipiens* mosquito.

LETTERS

In our Report, we used a panel of 8 highly polymorphic microsatellite loci to demonstrate that the two previously known forms of *Cx. pipiens* in Northern Europe [*Cx. pipiens* form (f.) “pipiens” and f. “molestus”] (1) are genetically distinct and do not interbreed there. We also demonstrated that all U.S. populations examined contain many individuals with hybrid genetic signatures (“pipiens” x “molestus”) alongside specimens with a “pipiens” signature. No hybrid signatures were seen in Northern European populations, although a few hybrids were detected in Southern France in late summer. Spielman *et al.* do not contest these findings.

European *Cx. pipiens* f. “pipiens” have been found to feed overwhelmingly on birds (2, 3) and ignore humans (4). We showed that populations of *Cx. pipiens* f. “molestus” from Northern Europe have the same genetic signature as North African and Middle Eastern populations that feed almost exclusively on mammals (2, 5), especially humans (5). These data support the hypothesis that there are two genetically distinct forms of *Cx. pipiens* in northern Europe that differ radically in their host preference.

In contrast, references (4–13) in the Spielman *et al.* Letter show that although birds are preferred by U.S. *Cx. pipiens*, 38% of the blood meals in a northeastern population were from mammalian sources (over 10% human) (6). Thus, U.S. *Cx. pipiens*, although mostly preferring birds, includes many individuals that will bite mammals. This is consistent with our finding that the U.S. populations examined have individuals with a hybrid signature (“pipiens” x “molestus”) alongside individuals with a “pipiens” signature.

Because human cases of West Nile virus (WNV) require vectors willing to bite birds and then mammals, we proposed that hybrids of the two behavioral forms contributed to the unique features of the U.S. outbreak (7). The demonstrated different geographic distribution of forms and hybrids within *Cx. pipiens* and the concordance of hybrid status and reports of host preference make the summary dismissal of our epidemiological interpretation by Spielman *et al.* premature, to say the least. The combined evidence led us also to state that the introduction of U.S. *Cx. pipiens* hybrids “has the potential to radically change the dynamics of WNV in Europe,” but we did not advocate the imposition of quarantine measures against U.S. mosquitoes. Introduced disease vectors can, however, have large health, economic, and ecological impacts. The traffic of insecticide-resistant mosquitoes (8) has rendered powerful insecticides useless, and

diseases transmitted by introduced mosquitoes threaten ecosystems [bird malaria, avian pox (9), WNV (10)], as well as human populations [yellow fever (11), dengue (12), WNV (13)]. This was the drive behind the statements made by D. M. Fonseca to the *New Scientist*.

The novelty and pathogenicity of WNV to U.S. birds are almost certainly important factors in the U.S. epidemic, but WNV would remain a bird or wildlife disease without vectors willing to bite birds and then humans. Indeed, *Cx. tarsalis* is considered a good vector of arboviruses to humans because it shifts from a predominantly bird feeder to mammal feeder during the breeding season (14). Such a clear pattern in host preference has not been found in U.S. *Cx. pipiens*, which instead show a high degree of geographic variation in host preference (6, 14) consistent with a heterogeneous hybrid ancestry.

The complexity of forms in *Cx. pipiens* has long been debated (15) and it is clear that the ability to identify *Cx. pipiens* populations differing in host preference and physiology is needed for informed epidemiological studies. Combining classical field and laboratory methodology with new technologies like those used in our study offers a way forward.

DINA M. FONSECA,^{1,6} NUSHA KEYGHOBADI,²
COLIN A. MALCOLM,³ FRANCIS SCHAFFNER,⁴
MOTOYOSHI MOGI,⁵ ROBERT C. FLEISCHER,⁶
RICHARD C. WILKERSON⁷

¹The Academy of Natural Sciences, 1900 Benjamin Franklin Parkway, Philadelphia, PA 19103, USA.

²Okanagan University College, Kelowna, BC V1V 1V7, Canada. ³School of Biological Sciences, Queen Mary, University of London, London E1 4NS, UK. ⁴Adege, EID Méditerranée, 34184 Montpellier Cedex 4, France. ⁵Saga Medical School, Nabeshima 5-1-1, Saga 849-8501, Japan.

⁶Genetics Program, Smithsonian Institution, 3001 Connecticut Avenue, NW, Washington, DC 20008-0551, USA. ⁷Walter Reed Army Institute of Research, 503 Robert Grant Avenue, Silver Spring, MD 20910-7500, USA.

References

1. R. E. Harbach, B. A. Harrison, A. M. Gad, *Proc. Entomol. Soc. Wash* **86**, 521 (1984).
2. A. Gabinaud *et al.*, *Cah. Orstom Sér. Ent. Méd. Parasitol.* **23**, 123 (1985).
3. T. G. Jaenson, *Med. Vet. Entomol.* **4**, 221 (1990).
4. P. S. Cranston, C. D. Ramsdale, K. R. Snow, G. B. White, "Keys to the adults, male hypopygia, fourth instar larvae and pupae of British mosquitoes (Culicidae) with notes on their ecology and medical importance" (Publication 48, Freshwater Biological Association, Ambleside, Cumbria, UK 1987).
5. J. H. Zimmerman, H. A. Hanafi, M. M. Abbassy, *J. Med. Entomol.* **22**, 82 (1985).
6. C. S. Apperson *et al.*, *Vector Borne Zoonot. Dis.* **4**, 71 (2004).
7. C. G. Hayes, *Ann. N.Y. Acad. Sci.* **951**, 25 (2001).
8. M. Raymond, A. Callaghan, P. Fort, N. Pasteur, *Nature* **350**, 151 (1991).
9. T. L. Benning, D. LaPointe, C. T. Atkinson, P. M. Vitousek, *Proc. Natl. Acad. Sci. U.S.A.* **99**, 14246 (2002).

10. R. G. McLean, S. R. Ubico, D. Bourne, N. Komar, *Curr. Top. Microbiol. Immunol.* **267**, 271 (2002).
11. P. Van der Stuyft *et al.*, *Lancet* **353**, 1558 (1999).
12. J. G. Rigau-Perez, D. J. Gubler, A. V. Vorndam, G. G. Clark, *J. Travel Med.* **4**, 65 (1997).
13. B. P. Granwehr *et al.*, *Lancet Infect. Dis.* **4**, 547 (2004).
14. C. H. Tempelis, *J. Med. Entomol.* **11**, 635 (1975).
15. E. B. Vinogradova, *Culex pipiens pipiens Mosquitoes: Taxonomy, Distribution, Ecology, Physiology, Genetics, Applied Importance and Control* (Pensoft, Moscow, 2000).

Mouse Biology at Monterotondo

GRETCHEN VOGEL'S ARTICLE ON THE European Molecular Biology Laboratory (EMBL) Programme at Monterotondo ("Institute sparks an Italian Renaissance in mouse biology," *News Focus*, 8 Oct., p. 217) was a well-deserved recognition of the success of this new branch of EMBL. Regrettably, the other parties that share credit for the success of Monterotondo were not mentioned. EMBL would not have succeeded if it were the only research entity on the Adriano Buzzati-Traverso campus at Monterotondo. The Consiglio Nazionale della Ricerca (CNR), through its Institute of Cell Biology (IBC) led by Glauco Tocchini-Valentini, has been an essential partner, inviting and hosting EMBL, providing an active scientific environment, sharing space and equipment, and solving a myriad of minor and major problems. CNR-IBC also operates EMMA-Monterotondo (the European Mutant Mouse Archive). Further credit is due to the pioneer teams of Klaus Rajewsky, Walter Witke, and Ulrich Kalinke, who, within strict budgetary constraints, created the nucleus of EMBL-Monterotondo. Rajewsky, the first director, brought conditional mutagenesis to the campus (an approach still central to the research of the EMBL groups), and encouraged the complementary development of powerful, RNA-based methods by IBC. The CNR/EMBL partnership created an atmosphere that justified increased funding by the EMBL member states in 2000, which was essential for the recruitment and success of Nadia Rosenthal and her group leaders. The lessons are of broader significance, too. The important shared goal of EMBL-Monterotondo, to promote internationalization of the Italian research landscape, cannot be achieved unilaterally. The recipe for success includes recruiting outstanding and dedicated staff, but also mutually respectful interaction and fruitful cooperation with local colleagues.

FOTIS C. KAFATOS

Director General, EMBL, Meyerhofstrasse 1, 69117 Heidelberg, Germany.

Beauty, Art, and Foreplay?

THE REVIEW BY V. S. RAMACHANDRAN OF THE book *The Psychology of Art and the Evolution of the Conscious Brain* by Robert L. Solso ("Beauty or brains?", *Books et al.*, 6 Aug., p. 779), in which Ramachandran states that "Art, in other words, is visual foreplay before the final climax of recognition," inspired the following light verse:

Art

Now I know why in painting school
The naked model is the rule:
To educate the artist's eye
And stimulate libido
For Art is simply how you try
In sex to have your say
So when Picasso painted girls
It's clear what he was doing
For all the bright and slashing whirls
It was just a prelude to his... wooing.

MARTIN GRAYSON

82 Vallywood Road, Cos Cob, CT 06807, USA.

CORRECTIONS AND CLARIFICATIONS

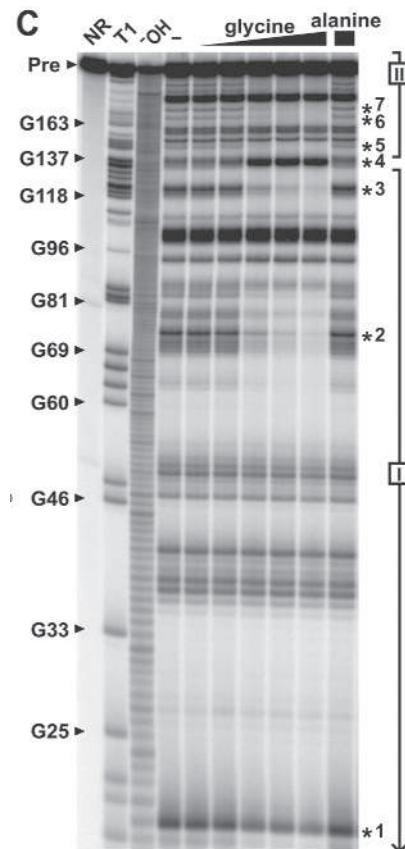
News of the Week: "New research commissioner caught in controversy's wake" by G. Vogel (5 Nov., p. 959). Janez Potočnik is European Commissioner from Slovenia, not Slovakia.

Reports: "A glycine-dependent riboswitch that uses cooperative binding to control gene expression" by M. Mandal *et al.* (8 Oct., p. 275). There was an error introduced into Fig. 1C during production. Several numbers and asterisks moved when the graphic was adjusted. The corrected figure is shown to the right.

Books *et al.*: "Culture and commerce in a seafood bazaar" by S. Gudeman (17 Sept., p. 1716). The text in the review's second paragraph should have read "Tsukiji, Theodore Bestor's study..." and "At the Tsukiji market in 1996, nearly 6 billion dollars of seafood changed hands..."

News Focus: "In mass extinction, timing is all" by R. A. Kerr (17 Sept., p. 1705). The image should have been credited to Joshua Feinberg, University of California, Berkeley.

Reports: "Population-level HIV declines and behavioral risk avoidance in Uganda" by R. L. Stoneburner and D. Low-Beer (30 Apr., p. 714). The citation on page 716 to reference 40 (R. L. Stoneburner, D. Low-Beer, *Int. J. Epidemiol.*, in press) should instead have been reference 14: R. Stoneburner, D. Low-Beer, paper presented at the XIII International Conference on AIDS, Durban, South Africa, July 2000. Reference 40 should be deleted in both the text and the references, as the paper will not be published in the *Int. J. Epidemiol.*



TECHNICAL COMMENT ABSTRACTS

COMMENT ON "Enhanced Open Ocean Storage of CO₂ from Shelf Sea Pumping"

Wei-Jun Cai, Minhan Dai

Thomas *et al.* (Reports, 14 May 2004, p. 1005) extrapolated a regional observation at a northern temperate marginal sea and speculated that continental shelves uptake atmospheric carbon dioxide by 0.4 Pg C year⁻¹ globally. Such a global extrapolation is premature, because observations from shelves located at lower latitudes suggest differently.

Full text at www.sciencemag.org/cgi/content/full/306/5701/1477c

RESPONSE TO COMMENT ON "Enhanced Open Ocean Storage of CO₂ from Shelf Sea Pumping"

Helmuth Thomas, Yann Bozec, Khalid Elkalay, Hein J. W. de Baar

The comment by Cai and Dai misrepresents previous studies and purports to caution against the common practice of worldwide extrapolation. The basis for our extrapolation was clearly outlined for the reader in our study. Previously, the lead author of the comment published just such an extrapolation based on the lower latitude South Atlantic Bight system being an annual carbon dioxide sink, unless split arbitrarily and erroneously.

Full text at www.sciencemag.org/cgi/content/full/306/5701/1477d

Comment on "Enhanced Open Ocean Storage of CO₂ from Shelf Sea Pumping"

In a well-designed North Sea study, Thomas *et al.* (1) found that atmospheric carbon dioxide (CO₂) was absorbed by continental shelf water and was eventually exported into the North Atlantic Ocean. The work confirmed preliminary observations in the same area (2, 3) and provided support for the continental shelf pump hypothesis (4, 5). Thomas *et al.* then extrapolated "the CO₂ uptake by the North Sea to the global scale" and inferred a net oceanic uptake of atmospheric CO₂ by coastal oceans of 0.4 Pg C year⁻¹. A previous global extrapolation based on limited observations in the East China Sea (ECS) suggested an even greater air-sea CO₂ flux of 1.0 Pg C year⁻¹ in the world's continental shelf (4). We are concerned with such extrapolations of regional studies to the global scale without cautioning readers that no current consensus exists on this issue.

Although most shelf CO₂ measurements have thus far revealed that shelves are sinks of atmospheric CO₂, these shelves are located in mid-latitude zones that experience strong spring blooms and substantial seasonal changes [i.e., the North Sea (50°N to 61°N) (1, 2), the Gulf of Biscay (42°N to 52°N) (2), the ECS (25°N to 38°N) (4, 6), and the Mid-Atlantic Bight (35.5°N to 41°N) (7)]. They absorb atmospheric CO₂, as evidenced by very low sea surface partial pressure of CO₂ (*p*CO₂) during planktonic bloom seasons. To sustain this uptake, absorbed CO₂ must be exported to the open ocean as organic and inorganic carbon under favorable shelf export conditions, especially in winter. The "continental shelf CO₂ pump hypothesis" was proposed to describe such circumstances (4). However, the shelves listed above represent only a small fraction of global shelf area (8) and may not be representative of global continental shelves. The North Sea, for example, is characterized by massive input from the land.

A recent report from the U.S. South Atlantic Bight (SAB) (27°N to 35°N) provided the first example of a major source of annual CO₂ to the atmosphere (9). The *p*CO₂ signal in the SAB is high during spring and summer and low during winter, which is the opposite of the trend observed in the North Sea and Gulf of Biscay (1, 2). Elsewhere, the shelf and upper slope area of the northern South China Sea (SCS) (20°N to 22°N) also act as an annual CO₂ source to

the atmosphere (10). Thus, it is clear that not all margins are a sink for atmospheric CO₂.

Margins are the most heterogeneous areas of the world's oceans, with potentially very different magnitudes of physical and biogeochemical mechanisms. Sea surface *p*CO₂ may differ because of latitudinal differences as well as differences related to oceanographic settings. The Arctic and subarctic shelves may be CO₂ sinks (11–13). The shelves vary from strong to weak CO₂ sinks in the temperate areas (1–7). Farther south in the SAB and in the SCS, the shelves are sources of CO₂ to the atmosphere (9, 10). The tropical and subtropical shelves and marginal seas are most likely sources of CO₂ to the atmosphere, driven by either the high annual surface temperature, the lack of a strong spring bloom, inputs from marshes (9) and mangroves (14), or reef formation.

Margins dominated by coastal upwelling are complex in that they receive deep water with high levels of both inorganic nutrient and CO₂. Although precise annual fluxes are difficult to define for these shelves, it again appears that the low-latitude shelves act as CO₂ sources (15, 16), whereas those at mid to high latitudes act as CO₂ sinks (17–19). However, these systems have a rather small total area (8). Large river plumes may be a strong sink of atmospheric CO₂ but, aside from the Amazon system, they represent a limited surface area compared with the surrounding waters that often appear as CO₂ sources (20, 21).

We are thus still at a stage of uncertainty about the magnitude of air-sea CO₂ exchange because of both the heterogeneous nature of ocean margins and the lack of spatial and temporal coverage of *p*CO₂ data. High- and low-latitude continental shelves have clearly not been sufficiently studied, and they deserve more attention in future research. The mechanisms that govern the net sink/source term and the magnitude of CO₂ exchange also require a more accurate understanding. Although the continental shelf pump hypothesis needs the scrutiny of further multidisciplinary field research, it is fair to suggest that low-latitude margins are not favorable for CO₂ absorption, in contrast to the case in mid- and high-latitude margins.

We laud the effort to explore the global significance of continental shelves in the ocean

carbon cycle (1, 4, 5) but are less confident in the global extrapolation of these studies. Atmospheric CO₂ uptake by continental shelves may have been overestimated given the latitudinal difference of air-sea exchange in marginal seas.

Wei-Jun Cai

*Department of Marine Sciences
University of Georgia
Athens, GA 30602, USA
E-mail: wcai@uga.edu*

and

*Key Laboratory of Marine
Environmental Science
Xiamen University
Ministry of Education
Xiamen 361005, China*

Minhan Dai

*Key Laboratory of Marine
Environmental Science
Xiamen University
Ministry of Education
Xiamen 361005, China*

References and Notes

- H. Thomas, Y. Bozec, K. Elkayal, *Science* **304**, 1005 (2004).
- M. Frankignoulle, A. V. Borges, *Global Biogeochem. Cycles* **15**, 569 (2001).
- S. Kempe, K. Pegler, *Tellus* **43B**, 224 (1991).
- S. Tsunogai, S. Watanabe, T. Sato, *Tellus* **51B**, 701 (1999).
- A. Yool, J. R. Fasham, *Global Biogeochem. Cycles* **15**, 831 (2001).
- S.-L. Wang, C.-T. A. Chen, G.-H. Hong, *Cont. Shelf Res.* **20**, 525 (2000).
- M. D. DeGrandpre, G. D. Olbu, C. M. Beatty, *Deep-Sea Res.* **49**, 4355 (2002).
- J. J. Walsh, *On the Nature of Continental Shelves* (Academic Press, San Diego, CA, 1988).
- W.-J. Cai, Z. Wang, Y. Wang, *Geophys. Res. Lett.*, **30**, 1849; <http://dx.doi.org/10.1029/2003GL017633>.
- M. Dai *et al.*, unpublished. Average air-sea CO₂ efflux in northern SCS was 7 mmol CO₂ m⁻² d⁻¹ in the summer and 1 to 3 mmol CO₂ m⁻² d⁻¹ in the spring and fall in the offshore shelf and upper slope. On a cruise in February 2004, we observed a net CO₂ influx in this region of -2.2 mmol CO₂ m⁻² d⁻¹, representing wintertime conditions; however, this will not change the net direction of air-sea CO₂ flux on an annual basis.
- L. G. Anderson, D. Dyrssen, E. P. Jones, *J. Geophys. Res.* **95C**, 1703 (1990).
- M. Murata, T. Takizawa, *Cont. Shelf Res.* **23**, 753 (2003).
- L. A. Codispoti, G. E. Friederich, D. W. Hood, *Cont. Shelf Res.* **5**, 133 (1986).
- A. V. Borges *et al.*, *Geophys. Res. Lett.* **30**, 1558 (2003); <http://dx.doi.org/10.1029/2003GL017143>.
- N. Lefevre *et al.*, *J. Geophys. Res.* **107**, 3055 (2002); <http://dx.doi.org/10.1029/2000JC000395>.
- C. Goyet *et al.*, *Deep-Sea Res.* **45**, 609 (1998).
- A. V. Borges, M. Frankignoulle, *Global Biogeochem. Cycles* **16**, 1020 (2002); <http://dx.doi.org/10.1029/2000GB001385>.
- A. van Geen *et al.*, *Deep-Sea Res.* **47**, 975 (2000).
- B. Hales, L. Bandstra, T. Takahashi, *Newsl. of Coastal Ocean Processes*, issue 17 (2003).
- J. F. Terner, C. Oudot, A. Dessier, *Mar. Chem.* **68**, 183 (2000).
- W.-J. Cai, *Geophys. Res. Lett.* **30**, 1032 (2003); <http://dx.doi.org/10.1029/2002GL016312>.
- This work has been supported by NSF grants OCE9982133 and OCE0425153 and NSF-China grants 40228007 and 90211020. We thank L. R. Pomeroy, G. T. F. Wong, and C. S. Hopkins for discussions.

29 June 2004; accepted 26 August 2004

Response to Comment on “Enhanced Open Ocean Storage of CO₂ from Shelf Sea Pumping”

The comment by Cai and Dai (1) recognizes the good design of our high-resolution carbon cycle study in the North Sea (2) but purports to caution against the common practice of extrapolating regional results to a global scale. We argue that the comment (1) is invalid on all counts and is a misleading representation of previous work (2–5). Indeed, in the comment, Cai and Dai target not only our *Science* paper (2) but also earlier work in another journal by Tsunogai *et al.* (6)—a 5-year-old study whose authors lack the opportunity to respond in this forum.

We surveyed the North Sea for four consecutive seasons (2). During each of the four cruises, we obtained ~23,000 measurements of the partial pressure of CO₂ (*p*CO₂) in surface waters and the atmosphere, and vertical profiles of dissolved inorganic carbon (DIC) at 97 stations. This high spatial resolution allowed for the most accurate estimate of the net annual air-sea flux of CO₂ for a coastal sea to date. Extrapolating from the North Sea (1.89% of all coastal seas), the net annual influx of CO₂ in worldwide coastal seas would be on the order of 20% of the overall net uptake by the oceans (assuming that all coastal seas behave like the North Sea). Similar global extrapolations have been made from studies in the Gulf of Biscay (4), East China Sea (ECS) (6, 7), and the salt-marsh-dominated margin system of the South Atlantic Bight (SAB) (5). All of these studies demonstrate a net annual uptake of atmospheric CO₂ and transport into the open ocean and therefore provide strong support for the continental shelf CO₂ pump hypothesis. They also demonstrate that it is common practice to place a regional study in wider (4) or global (5–7) context. In addition, the overview references provided in our study [notes 3 to 5 in (2)] allow the reader to assess our extrapolation.

The North Sea study (2) did not confirm preliminary observations in the same area (3, 4), as mistakenly stated in (1). The extrapolation of the Gulf of Biscay Study (4) to all European continental shelves ignored the undersampled North Sea. The pioneering North Sea study (3) in May to June 1986 used ~1000 calculated *p*CO₂ values [substantially fewer, as well as with considerably different *p*CO₂ values, than our May 2002 survey (2)],

and yielded a 6-week flux estimate, which differs greatly from the May 2002 survey and which has been extrapolated (3) to six warm months but not to an annual net flux value.

The concerns raised by Cai and Dai (1) about extrapolating a regional study to the global scale (1) contradict similar extrapolations made in previous work (6, 7), including the SAB study by the lead author of the current comment (5). The SAB study by Cai *et al.* (5) involved five repeats of only one shelf transect, which had first been extrapolated along the margin. It is important to note that there is inherent uncertainty in assumed along-margin uniformity. Next, the extrapolated shelf-wide DIC export rate (2.6 Mt C year⁻¹) was combined with rates somehow obtained in the salt marshes, into an overall budget [figure 3 in (5)] and then again extrapolated at a global scale to an annual net export rate of DIC into the deep ocean of 0.6 Gt C year⁻¹. This value was compared with the annual net value of 1.5 Gt C year⁻¹ extrapolated from another coastal sea (ECS) (6) and with the overall net annual uptake by the world oceans of 2 Gt C year⁻¹. Cai *et al.* (5) admitted that large uncertainty may be involved in the global extrapolation (their study was based on two successive extrapolations) but in the end suggested that “ocean carbon sequestration can proceed effectively through the absorption of atmospheric CO₂ by marsh grasses and the subsequent export to the open ocean.”

Cai and Dai (1) also mistakenly isolate the shelf part of the overall salt-marsh-dominated margin system as the first published example of a coastal margin acting as a net source of atmospheric CO₂. [It is not the first example; see (8)]. The SAB is obviously one system in which intense CO₂ fixation in the salt marsh causes massive organic loading of the shelf, which in turn drives net annual CO₂ outgassing from the open shelf. Despite loss of CO₂ to the atmosphere, the overall system still acts as a net annual sink of CO₂ and exports DIC into the deep ocean. Thus, the high *p*CO₂ values at the shelf [up to 1200 parts per million (ppm); see figure 1 in (5)] are intrinsic to this salt-marsh-dominated margin system and akin to the *p*CO₂ (up to 750 ppm) observed in the Scheldt River plume (8). Only if all the salt marshes were dammed off could the SAB shelf component be presented as a system on its own. If that were the case, however, the

high *p*CO₂ values at the shelf would disappear immediately. In due course, the modest autotrophic CO₂ fixation on the open shelf would drive a continental shelf pump, albeit at a more modest pace than nowadays.

Classical upwelling systems initially show CO₂ supersaturation in the newly upwelled waters and later act as strong CO₂ exporters to the deep ocean through the biological pump supported by upwelled nutrients (9–12). Depending on the balance between the CO₂ upwelling supply and the biological pump, these upwelling systems may act as either an annual source or an annual sink of CO₂. This is not dependent on latitude as suggested in (1); indeed, the largest upwelling system in the world is the Southern Ocean at high latitude (13). In a well-known study of mangrove systems in Papua New Guinea, the Bahamas, and India (14), the usual global extrapolation was made, which implied a global annual CO₂ release of 0.05 Pg C year⁻¹. Although this is a substantial amount, it is still an order of magnitude lower than the extrapolated global continental shelf uptake of 0.4 Pg C year⁻¹ from our North Sea study (2).

In conclusion, we believe that the comment by Cai and Dai (1) raises a non-issue, has made several invalid claims and wrongly cites previous studies of ocean uptake of atmospheric CO₂, and purports to caution about the common practice of global extrapolation. (2–5). Moreover, it confuses classical upwelling systems with a speculative latitudinal dependence of the CO₂ gas exchange in marginal seas and the enhanced open ocean storage of CO₂ from shelf sea pumping.

Helmuth Thomas

Royal Netherlands Institute for Sea Research
Department of Marine Chemistry and Geology
P.O. Box 59, 1790 AB Den Burg,
Netherlands
and Department of Oceanography
Dalhousie University
Halifax, Canada B3H 4J1
E-mail: helmuth.thomas@dal.ca

Yann Bozec

Khalid Elkalay

Hein J. W. de Baar

Royal Netherlands Institute for Sea Research

References and Notes

1. W.-J. Cai, M. Dai, *Science* **306**, 1477 (2004); www.sciencemag.org/cgi/content/full/306/5701/1477c.
2. H. Thomas, Y. Bozec, K. Elkalay, H. J. W. de Baar, *Science* **304**, 1005 (2004).
3. S. Kempe, K. Pegler, *Tellus* **43B**, 224 (1991).
4. M. Frankignoulle, A. V. Borges, *Global Biogeochem. Cycles* **15**, 569 (2001).
5. W.-J. Cai, Z. A. Wang, Y. Wang, *Geophys. Res. Lett.* **30**, 3-1 (2003).

TECHNICAL COMMENT

6. S. Tsunogai, S. Watanabe, T. Sato, *Tellus* **51B**, 701 (1999).
7. S.-L. Wang, C.-T. A. Chen, G.-H. Hong, C.-S. Chung, *Continental Shelf Res.* **20**, 525 (2000).
8. A. V. Borges, M. Frankignoulle, *Biogeochemistry* **59**, 41 (2002).
9. A. van Geen *et al.*, *Deep-Sea Res. II* **47**, 975 (2000).
10. N. Lefèvre *et al.*, *J. Geophys. Res.* **107**, 3055 (2002); <http://dx.doi.org/10.1029/2000JC000395>.
11. C. Goyet *et al.*, *Deep-Sea Res. I* **45**, 609 (1998).
12. R. Lendt, H. Thomas, A. Hupe, V. Ittekkot, *J. Geophys. Res.* **108**, 15-1 (2003).
13. J. M. J. Hoppema, *Global Planet. Change* **40**, 219 (2004).
14. A. V. Borges *et al.*, *Geophys. Res. Lett.* **30**, 12-1 (2003).
15. This work was supported by the Research Council for Earth and Life Sciences (ALW) of the Netherlands Organisation for Scientific Research (NWO).

23 July 2004; accepted 2 November 2004

Weighing the Evidence

Marc Mangel

A better understanding of evidence will always be important in science. At my university, for example, the Center for Informal Learning and Schools (1) brings together students and post-docs from the natural and social sciences. Topics they continually discuss include what constitutes data, what is evidence, and how is evidence used to draw conclusions.

The goal of *The Nature of Scientific Evidence* is to help answer those questions. To do so, Mark Taper (an ecologist at Montana State University) and Subhash Lele (a statistician at the University of Alberta) have drawn authors from the fields of ecology, statistics, and philosophy. The choice of ecology as the illustrative science is a good one, because ecology has strong traditions in both the discovery of new knowledge and the application of that knowledge to important problems of society. The chapters are grouped in five sections: “Scientific Process”; “Logics of Evidence”; “Realities of Nature”; “Science, Opinion, and Evidence”; and “Models, Realities, and Evidence.” Each chapter is followed by commentary, typically from two individuals, and a rejoinder by the author. The volume is aimed toward students as well as established scientists, statisticians, and philosophers. It reaches its target: there is something in it for everyone.

As might be expected of an edited volume, the technical level of the chapters varies considerably. Some of the mathematically easiest material (introductory in nature, where statistical symbols are explained) appears late in the book. There are many big ideas, but they are scattered around and one needs to work through (or at least, as Solly Zuckerman reputedly said, hum through) the technical details in order to get to them. As in most edited volumes, there is too much repetition. However, the book is a rare find: a source that could be used in graduate seminars in statistics, philosophy, or biology if the chapters are suitably chosen. It is brimming with ideas.

The reviewer is in the Department of Applied Mathematics and Statistics, University of California, Santa Cruz, CA 95064, USA. E-mail: msmangel@ams.ucsc.edu

A number of broad themes, including the definition of the scientific process and the structure of scientific knowledge, weave throughout the text. Evidence enters science in a variety of ways. Contributor Richard Royall has noted elsewhere (2) that given a set of observations, one may ask: What should I believe? What should I do? And how should I interpret the observations as evidence? The third question can be split and distilled to, What do the observations tell me about the truth of the hypothesis being considered? and What do they tell me about the hypothesis’s predictive accuracy? The topic of whether we are seeking the truth (which, it appears, statisticians are more likely to believe) or increasingly better understanding of reality (which scientists are more likely to believe) also appears in many chapters.

The operational issues center on the conflict between frequentist and Bayesian approaches to statistics, approaches that differ primarily in their notions of the relationship between data and hypotheses and in their treatments of prior information. The authors, like most statisticians and statistically oriented scientists, assume that it is necessary to choose between these two paradigms, instead of asking for the virtues of each that will help us gain a better understanding of the world. I would guess that most scientists are facultative Bayesians. They find frequentist statistics troubling because it often does not tell scientists what they really want to know; the trouble with Bayesian statistics is that the

prior is described as “subjective,” with all that this charged word connotes. At times the writing is vituperative (making it kind of fun to read), with Bayesians and frequentists attacking one another with well-known saws. But saws only cut, not build. One contributor notes that “statistics today is a conceptual and theoretical mess,” and the treatment of Bayesian and frequentist statistics in the volume does little to help solve that problem. Thus, the two schools of statistical thought, while battling among themselves (in a kind of last-statistician-standing showdown), let scientists down. Perhaps not unexpectedly, John Hammersley once wrote, “Scientists have learned to expect everything from

mathematicians short of actual help” (3).

Philosophers can help scientists understand the operation of science. In her chapter, Deborah Mayo summarizes the philosophical foundation of frequentist statistics in a précis of her earlier book (4), but the volume lacks a comparable treatment of the philosophical foundations of Bayesian statistics [as in (5)]. A philosophy of evidence should be inclusive. In addition to providing statements of evidence, it should show how to generalize, model, and use or discard data as well as how to deal with contradictory data. Unfortunately, the contributors offer little discussion of how one makes the trade-off between a firm philosophical foundation and gaining a deeper understanding of the natural world, especially for nonreductionist questions. The chapters that are the most oriented toward scientific problems are also those that have the least statistics.

The volume would have been improved by the inclusion of one illustrative problem, treated by both methods, that shows the weaknesses, strengths, and commonalities of each approach to evidence. However, frequentists and Bayesians agree on the general conclusions that evidence is comparative and that data may support one hypothesis over another (their argument is in quantifying that support) but the support for a single hypothesis cannot be quantified. At the philosophical level, most contributors would agree that although we will never know the truth, we might reach increasingly better understanding of nature. Scientists tend not to reject a theory that has some explanatory power or predictive power, even if it fails in other cases, when there is no alternative theory available (they’d have nothing to do). At the scientific level, most would agree that we need to carefully choose a model—or models, so that we can compare multiple models with the data—and know what assumptions are being made, so that we can separate the useful models from the others. At the statistical level, especially in these days of easy computing, we need to really understand the statistics that we are using.

The Nature of Scientific Evidence is far from perfect, but the volume is valuable and important. It deserves a read by everyone.

References and Notes

1. The center is a partnership among the University of California Santa Cruz; King’s College London; and the Exploratorium, San Francisco; www.exploratorium.edu/cils.
2. R. M. Royall, *Statistical Evidence: A Likelihood Paradigm* (Chapman and Hall, London, 1997).
3. J. M. Hammersley, *Bull. Inst. Math. Appl.* **10**, 235 (1974).
4. D. G. Mayo, *Error and the Growth of Experimental Knowledge* (Univ. Chicago Press, Chicago, 1996).
5. C. Howson, P. Urbach, *Scientific Reasoning: The Bayesian Approach* (Open Court, La Salle, IL, 1989).

The Nature of Scientific Evidence Statistical, Philosophical, and Empirical Considerations

Mark L. Taper and
Subhash R. Lele, Eds.

University of Chicago Press,
Chicago, 2004. 585 pp. \$85,
£59.50. ISBN 0-226-78955-
1. Paper, \$30, £21. ISBN 0-
226-78957-8.

ENVIRONMENT

What's Been Going On in the Woods

Michael Williams

No one who has visited the Harvard Forest and Museum at Petersham, Massachusetts, can have any doubt that forests are dynamic entities. Although the museum's realistic dioramas of the forest at various times during the last 200 years are striking enough, a walk through the forest itself is stunning. You enter a gloomy yet awe-inspiring grove of tall, mature trees that must, you think, have been there forever. It seems like the forest primeval, until you come across stone walls and the shells of stone dwellings with large trees growing through and out of them. And then it dawns on you that

Forests in Time
The Environmental
Consequences
of 1,000 Years
of Change in
New England

David R. Foster and
John D. Aber, Eds.

Yale University Press,
New Haven, CT, 2004.
491 pp. \$45, £35. ISBN
0-300-09235-0.

these are the field boundaries and houses of the hard-bitten pioneer farmers of New England, most of which were abandoned in the early 19th century. One can well see how the ruins of the Mayan civilization lay hidden under the Yucatan jungle for hundreds of years. Such scenes are a potent correction to our preconceptions and sensibility about a pristine "nature." They starkly illustrate that the past is essential to understanding present conditions, the roles of humans in fashioning the landscape, and the importance of history in deepening our knowledge of ecology. To understand the forest landscape here, or indeed anywhere, is to embark upon an exciting interplay between the humanities and natural sciences.

Forests in Time could be called a biography of the Harvard Forest and, with variations, of the forest of all New England, where before circa 1850 forest cover declined to about 40 percent of the landscape and has since reverted to between 60 and 90 percent.

The reviewer is at the School of Geography and the Environment, University of Oxford, Mansfield Road, Oxford, OX1 3TB, UK. E-mail: Michael.williams@geog.ox.ac.uk

Bill McKibben has called this rebirth of the forest "the great environmental story of the United States, and in some ways of the whole world" (1). Whether or not one agrees with him, the fact remains that in the block of mainly forested states in the eastern half of the country (from Minnesota to Louisiana and east) farmland has been reverting to forest at a rate approaching a net increase of one million acres a year since 1910. It is one of the greatest environmental stories of the 20th century.

David Foster (director of the Harvard Forest) and John Arbor (an ecologist at the University of New Hampshire) have done an excellent job bringing together 20 contributions, from over 50 authors, that tell the story of Harvard Forest and the wider New England forest with all its variety and complexity through time. The individual chapters synthesize and discuss a wealth of material from the primary literature, and a "Bibliographic Essay" at the end of the book provides a useful, concise guide to their contents.



Sprouting back. This Harvard Forest diorama depicts the vigorous growth of hardwoods (circa 1930) established after the clear-cutting of the old-field white pines.

The first three chapters are all necessary scene-setting in the broadest sense, but many readers will probably find the book's second section the most immediately appealing. "The Environmental and Human History of New England," the volume's longest chapter, discusses long-term climatic and vegetational changes, natural disturbances (such as hurricanes, pests, and pathogens), the impacts of Native Americans and fire, the history of land use and landscape transformation, present-day changes, and introduced pests and species.

Two subsequent chapters explore the effects of these processes on tree species at the regional and forest-stand levels. A third, on wildlife dynamics, documents the decline of, for example, moose, gray wolf, beaver, and cougar; the rise of coyote; and the resurgence of beaver and black bear.

The remaining chapters provide more technical details of the science—dealing, among other things, with plant composition, soil warming, atmospheric exchanges, and nitrogen saturation—but are all eminently readable. A particularly fascinating discovery is that the growing forests sequester far greater amounts of carbon than had been suspected. When extrapolated to consider regrowth throughout the developed world over the last century, this finding has important implications for the global warming–Koyoto debate that are often ignored. Aber’s brief, final chapter, “The Long Lens of History,” offers a useful summary of some of

the major conclusions and implications.

With few exceptions the contributions are readily accessible to the reader, who is aided by a wealth of diagrams, tables, and photographs. Tight editing has ensured uniform terminology and a pleasing coherence of the varied parts.

Besides refining our ideas about “nature,” ecology, and interdisciplinary research, what else can we learn from this set of essays? First, current forests are not stable or natural but are partially, if not largely, human artifacts. Not only has the extent of the forest changed radically over intervals as short as a few decades (let alone centuries), but so has its composition (with the effects depending on the sort and timing of disturbance). Complex natural and human disturbance regimes complicate our traditional view of succession dynamics. Consequently, the concept of a pristine, pre-Contact landscape frozen in time and space as a sort of base

point from which to measure anthropogenic (usually European immigrant) change—so beloved of romantics, environmentalists, and even some anthropologists—is simply a fiction. This has important policy implications for environmental impact assessment studies. Third, the forest performs important atmospheric functions that compensate to some extent for the deleterious anthropogenic emissions.

But above all, we become aware of how much more interdisciplinary research reveals of the truth than narrowly based disciplinary research in the natural sciences. For that alone, *Forests in Time* provides an important and timely addition to a growing literature that documents change and, by implication, underlines our responsibilities to that thing out there that we call “nature.”

Reference

1. B. McKibben, *Atl. Mon.* 275, 61 (April, 1995).

NOTA BENE: EXHIBITS

Tricking Our Vision

For centuries, the public has been entertained through the use of optical tricks and devices, culminating in today’s billion-dollar movie industry. The beginnings were modest by today’s standards: The earliest magic lanterns could display just one shadow image, though this was often enough to frighten viewers of these “lanterns of fear.” The exhibition *Eyes, Lies and Illusions* brings together numerous original devices and images, many of which continue to fascinate and amaze. It is largely drawn from

the personal collection of the German experimental filmmaker Werner Nekes.

Rather than charting a historical or scientific path, the curators group material into somewhat artificial categories such as “Shadowplay” and “Deceiving the Mind.” They also try to bring together modern art and historical artifacts, with mixed success. But despite these perhaps inevitable problems, the exhibition is a wonderful journey into the past. In the very first room, I was captivated by an excerpt from Lotte Reiniger’s *The Adventures of Prince Achmed* (1926), one of the first feature-length animated films. Reiniger used hand-cut silhouettes to create scenes of haunting beauty, grace, and refinement that continue to have a strong appeal today.

Several rooms feature some version of the peep box. Perspective boxes with several layers of cut-out images, similar to a miniature theatre stage, came into fashion in the 18th century. Other peep boxes used images that changed with the illumination,

revealing hidden features or changing scenes from day to night. One exhibit wall displays, lit from behind, some 30 transparent prints—hand-colored and perforated to provide peep-box views of scenes from around the world.

On the roof of the gallery, a camera obscura—essentially a lens in a hole in the wall of a dark room—projects onto the wall an inverted image of buses and other traffic crossing the Thames. Despite the mechanism’s simplicity, the projected image is surprisingly sharp and colorful. Similar devices were used to “conjure up” images and also led the way to the development of the photographic camera.

Although even some of the earliest magic lanterns could display a short series of images, animation began in earnest in the 19th century, when Eadweard Muybridge, Etienne-Jules Marey, and Ottomar Anschütz devised various techniques to capture motion. Muybridge used a row of cameras consecutively triggered by a passing horse to analyze its gallop, whereas Marey used just one camera to record many images (initially 12, later 30 and more) per second on the same negative, which allowed the detailed study of human motion. Anschütz developed early projection devices—called *Schnellseher* (literally “fast viewer”)—to display these sequences of images. Thus the scene was set for the cinema.

Today, we use sophisticated optical equipment every day. Nevertheless, the devices of past centuries, however simple they appear to be, can still capture the imagination. (As I watched, every visitor approaching two distorting mirrors, originally displayed in an optician’s waiting room in the 1840s, began to smile and fool around to see the reflection change.) *Eyes, Lies and Illusions* has something for anyone interested in the art, history, or science of optics. Unfortunately, the accompanying catalog cannot capture the show’s most important aspect—the direct interaction with the original devices. There is thus no substitute for going to see this fascinating exhibition.

—JULIA FAHRENKAMP-UPPENBRINK

Eyes, Lies and Illusions

Werner Nekes and Marina Warner, curators

Hayward Gallery, South Bank Centre, London. Through 2 January 2005. www.hayward.org.uk

Eyes, Lies and Illusions Drawn from the Werner Nekes Collection

by Laurent Mannoni, Werner Nekes, and Marina Warner

Hayward Gallery, London, 2004. Paper, 240 pp. £24.95. ISBN 1-85332-244-X.



Line Describing a Cone. Anthony McCall’s 1973 film installation with 16mm projector and hazer (shot at the Whitney Museum, New York, 2002).

Why Ordinary People Torture Enemy Prisoners

Susan T. Fiske, Lasana T. Harris, Amy J. C. Cuddy

As official investigations and court-martial continue, we are all taking stock of the events at Abu Ghraib last year. Initial reactions were shock and disgust. How could Americans be doing this to anyone, even Iraqi prisoners of war? Some observers immediately blamed “the few bad apples” presumably responsible for the abuse. However, many social psychologists knew that it was not that simple. Society holds individuals responsible for their actions, as the military court-martial recognizes, but social psychology suggests we should also hold responsible peers and superiors who control the social context.

Social psychological evidence emphasizes the power of social context; in other words, the power of the interpersonal situation. Social psychology has accumulated a century of knowledge about how people influence each other for good or ill (1). Meta-analysis, the quantitative summary of findings across a variety of studies, reveals the size and consistency of such empirical results. Recent meta-analyses document reliable experimental evidence of social context effects across 25,000 studies of 8 million participants (2). Abu Ghraib resulted in part from ordinary social processes, not just extraordinary individual evil. This Policy Forum cites meta-analyses to describe how the right (or wrong) social context can make almost anyone aggress, oppress, conform, and obey.

Virtually anyone can be aggressive if sufficiently provoked, stressed, disgruntled, or hot (3–6). The situation of the 800th Military Police Brigade guarding Abu Ghraib prisoners fit all the social conditions known to cause aggression. The soldiers were certainly provoked and stressed: at war, in constant danger, taunted and harassed by some of the very citizens they were sent to save, and their comrades were dying daily and unpredictably. Their morale suffered, they were untrained for

the job, their command climate was lax, their return home was a year overdue, their identity as disciplined soldiers was gone, and their own amenities were scant (7). Heat and discomfort also doubtless contributed.

The fact that the prisoners were part of a group encountered as enemies would only exaggerate the tendency to feel spontaneous prejudice against outgroups. In this context, oppression and discrimination are synonymous. One of the most basic princi-



ples of social psychology is that people prefer their own group (8) and attribute bad behavior to outgroups (9). Prejudice especially festers if people see the outgroup as threatening cherished values (10–12). This would have certainly applied to the guards viewing their prisoners at Abu Ghraib, but it also applies in more “normal” situations. A recent sample of U.S. citizens on average viewed Muslims and Arabs as not sharing their interests and stereotyped them as not especially sincere, honest, friendly, or warm (13–15).

Even more potent predictors of discrimination are the emotional prejudices (“hot” affective feelings such as disgust or contempt) that operate in parallel with cognitive processes (16–18). Such emotional reactions appear rapidly, even in neuroimag-

ing of brain activations to outgroups (19, 20). But even they can be affected by social context. Categorization of people as interchangeable members of an outgroup promotes an amygdala response characteristic of vigilance and alarm and an insula response characteristic of disgust or arousal, depending on social context; these effects dissipate when the same people are encountered as unique individuals (21, 22).

According to our survey data (13, 14), the contemptible, disgusting kind of outgroup—low-status opponents—elicits a mix of active and passive harm: attacking and fighting, as well as excluding and demeaning. This certainly describes the Abu Ghraib abuse of captured enemies. It also fits our national sample of Americans (14) who reported that allegedly contemptible outgroups such as homeless people, welfare recipients, Turks, and Arabs often are attacked or excluded (14).

Given an environment conducive to aggression and prisoners deemed disgusting and subhuman (23), well-established principles of conformity to peers (24, 25) and obedience to authority (26) may account for the widespread nature of the abuse. In combat, conformity to one’s unit means survival, and ostracism is death. The social context apparently reflected the phenomenon of people trying to make sense of a complex, confusing, ambiguous situation by relying on their immediate social group (27). People rioted at St. Paul’s Church, Bristol UK, in 1980, for example, in conformity to events they saw occurring in their immediate proximity (28). Guards abuse prisoners in conformity with what other guards do, in order to fulfill a potent role; this is illustrated by the Stanford

The authors are respectively Professor of Psychology and two doctoral students, Psychology and Neuroscience; Princeton University, Princeton NJ 08544–1010, USA. E-mail: sfiske@princeton.edu; lharris@princeton.edu; acuddy@princeton.edu

Prison Study, in which ordinary college students, randomly assigned to be full-time guards and prisoners in a temporary prison, nevertheless behaved respectively as abusers and victims (29). Social psychology shows that, whatever their own good or bad choices, most people believe that others would do whatever they personally chose to do, a phenomenon termed false consensus (30, 31). Conformity to the perceived reactions of one's peers can be defined as good or bad, depending on how well the local norms fit those of larger society.

As every graduate of introductory psychology should know from the Milgram studies (32), ordinary people can engage in incredibly destructive behavior if so ordered by legitimate authority. In those studies, participants acting as teachers frequently followed an experimenter's orders to punish a supposed learner (actually a confederate) with electric shock, all the way to administering lethal levels. Obedience to authority sustains every culture (33). Firefighters heroically rushing into the flaming World Trade Center were partly obeying their superiors, partly conforming to extraordinary group loyalty, and partly showing incredibly brave self-sacrifice. But obedience and conformity also motivated the terrorist hijackers and the Abu Ghraib guards, however much one might abhor their (vastly different) actions. Social conformity and obedience themselves are neutral, but their consequences can be heroic or evil. Torture is partly a crime of socialized obedience (34). Subordinates not only do what they are ordered to do, but what they think their superiors would order them to do, given their understanding of the authority's overall goals. For example, lynching represented ordinary people going beyond the law to enact their view of the community's will.

Social influence starts with small, apparently trivial actions (in this case, insulting epithets), followed by more serious actions (humiliation and abuse) (35–37), as novices overcome their hesitancy and learn by doing (38). The actions are always intentional, although the perpetrator may not be aware that those actions constitute evil. In fact, perpetrators may see themselves as doing a great service by punishing and/or eliminating a group that they perceive as deserving ill treatment (39).

In short, ordinary individuals under the influence of complex social forces may commit evil acts (40). Such actions are human behaviors that can and should be studied scientifically (41, 42). We need to understand more about the contexts that will promote aggression. We also need to understand the basis for exceptions—why, in

the face of these social contexts, not all individuals succumb (43). Thus, although lay-observers may believe that explaining evil amounts to excusing it and absolving people of responsibility for their actions (44), in fact, explaining evils such as Abu Ghraib demonstrates scientific principles that could help to avert them.

Even one dissenting peer can undermine conformity (24). For example, whistle-blowers not only alert the authorities but also prevent their peers from continuing in unethical behavior. Authorities can restructure situations to allow communication. For example, CEOs can either welcome or discourage a diversity of opinions. Contexts can undermine prejudice (1). Individual, extended, equal-status, constructive, cooperative contact between mutual outgroups (whether American blacks and whites in the military or American soldiers and Iraqi civilians) can improve mutual respect and even liking. It would be harder to dehumanize and abuse imprisoned Iraqis if one had friends among ordinary Iraqis. A difficult objective in wartime, but as some Iraqis work alongside their American counterparts, future abuse is less likely. The slippery slope to abuse can be avoided. The same social contexts that provoke and permit abuse can be harnessed to prevent it. To quote another report [(45), p. 94]: "All personnel who may be engaged in detention operations, from point of capture to final disposition, should participate in a professional ethics program that would equip them with a sharp moral compass for guidance in situations often riven with conflicting moral obligations."

References and Notes

- S. T. Fiske, *Social Beings* (Wiley, New York, 2004).
- F. D. Richard, C. F. Bond, J. J. Stokes-Zoota, *Rev. Gen. Psychol.* **7**, 331 (2003).
- B. A. Bettencourt, N. Miller, *Psychol. Bull.* **119**, 422 (1996).
- M. Carlson, N. Miller, *Sociol. Soc. Res.* **72**, 155 (1988).
- M. Carlson, A. Marcus-Newhall, N. Miller, *Pers. Soc. Psychol. Bull.* **15**, 377 (1989).
- C. A. Anderson, B. J. Bushman, *Rev. Gen. Psychol.* **1**, 19 (1997).
- A. Taguba, "Article 15-6. Investigation of the 800th Military Police Brigade," accessed 30 June 2004 from www.npr.org/iraq/2004/prison_abuse_report.pdf
- B. Mullen, R. Brown, C. Smith, *Eur. J. Soc. Psychol.* **22**, 103 (1992).
- B. Mullen, C. Johnson, *Br. J. Soc. Psychol.* **29**, 11 (1990).
- J. Duckitt, in *Advances in Experimental Social Psychology*, M. P. Zanna, Ed. (Academic Press, New York, 2001).
- When their own mortality is salient, as in wartime, people particularly punish those from outgroups seen to threaten basic values (12).
- S. Solomon, J. Greenberg, T. Pyszczynski, *Curr. Dir. Psychol. Sci.* **9**, 200 (2000).
- S. T. Fiske, A. J. Cuddy, P. Glick, J. Xu, *J. Person. Soc. Psychol.* **82**, 878 (2002).
- A. J. Cuddy, S. T. Fiske, P. Glick, "The BIAS map: Behaviors from intergroup affect and stereotypes," unpublished manuscript (Princeton University, Princeton, NJ, 2004).
- L. J. Heller, thesis, Princeton University, 2002.
- H. Schütz, B. Six, *Int. J. Intercult. Relat.* **20**, 441 (1996).
- J. F. Dovidio et al., in *Stereotypes and Stereotyping*, C. N. Macrae, C. Stangor, M. Hewstone, Ed. (Guilford, New York, 1996).
- C. A. Talaska, S. T. Fiske, S. Chaiken, "Predicting discrimination: A meta-analysis of the racial attitudes-behavior literature," unpublished manuscript (Princeton University, Princeton, NJ, 2004).
- A. J. Hart et al., *Neuroreport* **11**, 2351 (2000).
- E. A. Phelps et al., *J. Cogn. Neurosci.* **12**, 729 (2000).
- Neuroimaging data represent college student reactions to photographs of outgroup members. These data should not be interpreted to mean that such reactions are innate or "wired in"; they result from long-term social context (9) and vary depending on short-term social context (46).
- M. E. Wheeler, S. T. Fiske, *Psychol. Sci.*, in press.
- J. P. Leyens et al., *Eur. J. Soc. Psychol.* **33**, 703 (2003).
- R. Bond, P. B. Smith, *Psychol. Bull.* **119**, 111 (1996).
- S. Tanford, S. Penrod, *Psychol. Bull.* **95**, 189 (1984).
- J. Tata et al., *J. Soc. Behav. Pers.* **11**, 739 (1996).
- J. C. Turner, *Social Influence* (Brooks/Cole, Pacific Grove, CA, 1991).
- S. D. Reicher, *Eur. J. Soc. Psychol.* **14**, 1 (1984).
- C. Haney, C. Banks, P. Zimbardo, *Int. J. Criminol. Penol.* **1**, 69 (1973).
- B. Mullen et al., *J. Exp. Soc. Psychol.* **21**, 262 (1985).
- B. Mullen, L. Hu, *Br. J. Soc. Psychol.* **27**, 333 (1988).
- S. Milgram, *Obedience to Authority* (Harper & Row, New York, 1974).
- T. Blass, *J. Appl. Soc. Psychol.* **29**, 955 (1999).
- H. C. Kelman, in *The Politics of Pain: Torturers and Their Masters*, R. D. Crelinsten, A. P. Schmidt, Eds. (Univ. of Leiden, Leiden, NL, 1991).
- A. L. Beaman et al., *Pers. Soc. Psychol. Bull.* **9**, 181 (1983).
- A. L. Dillard, J. E. Hunter, M. Burgoon, *Hum. Commun. Res.* **10**, 461 (1984).
- E. F. Fern, K. B. Monroe, R. A. Avila, *J. Mark. Res.* **23**, 144 (1986).
- E. Staub, *Pers. Soc. Psychol. Rev.* **3**, 179 (1999).
- A. Bandura, *Pers. Soc. Psychol. Rev.* **3**, 193 (1999).
- L. Berkowitz, *Pers. Soc. Psychol. Rev.* **3**, 246 (1999).
- J. M. Darley, *Pers. Soc. Psychol. Rev.* **3**, 269 (1999).
- A. G. Miller, Ed., *The Social Psychology of Good and Evil* (Guilford, New York, 2004).
- Although social context matters more than most people think, individual personality also matters, in accord with most people's intuitions: Social Dominance Orientation (SDO) describes a tough-minded view that it is a zero-sum, dog-eat-dog world, where some groups justifiably dominate other groups. People who score low on SDO tend to join helping professions, be more tolerant, and endorse less aggression; they might be less inclined to abuse. People choosing to join hierarchical institutions such as the military tend to score high on SDO, in contrast (47). Right-Wing Authoritarianism (RWA) entails conforming to conventional values, submitting to authority, and aggressing as sanctioned by authority. People who score low on RWA would be less prone to abuse. (48) High SDO and RWA both predict intolerance of outgroups, social groups outside one's own.
- A. G. Miller, A. K. Gordon, A. M. Buddie, *Pers. Soc. Psychol. Rev.* **3**, 254 (1999).
- J. R. Schlesinger, H. Brown, T. K. Fowler, C. A. Homer, J. A. Blackwell Jr., *Final Report of the Independent Panel to Review DoD Detention Operations*, accessed 8 November 2004, from www.informationclearinghouse.info/article6785.htm
- L. T. Harris, S. T. Fiske, unpublished data.
- J. Sidanius, F. Pratto, *Social Dominance: An Intergroup Theory of Social Hierarchy and Oppression* (Cambridge Univ. Press, New York, 1999).
- B. Altemeyer, *Enemies of Freedom: Understanding Right-Wing Authoritarianism* (Jossey-Bass, San Francisco, 1988).

10.1126/science.1103788

A Higher Order of Silence

Adone Mohd-Sarip and C. Peter Verrijzer

During the development of multicellular organisms, a single fertilized egg gives rise to a plethora of specialized cell types, which are the building blocks of distinct tissues. Because virtually all the cells in our body contain an identical genome, it is the discriminative reading of the genetic information that determines whether a cell is a muscle, skin, or nerve cell. In order to have the “right cell” at the “right place,” it is essential that a chosen cellular gene expression program be maintained throughout cell division. Failures in cellular memory or epigenetic control can lead to serious developmental defects and diseases such as cancer. Research over the past decade has made clear that the regulated compaction of genomic DNA into chromatin is fundamental to keeping a gene turned “on” in one cell lineage but turned “off” in another. Two reports on pages 1571 and 1574 of this issue provide intriguing new insights into how this might be achieved (1, 2).

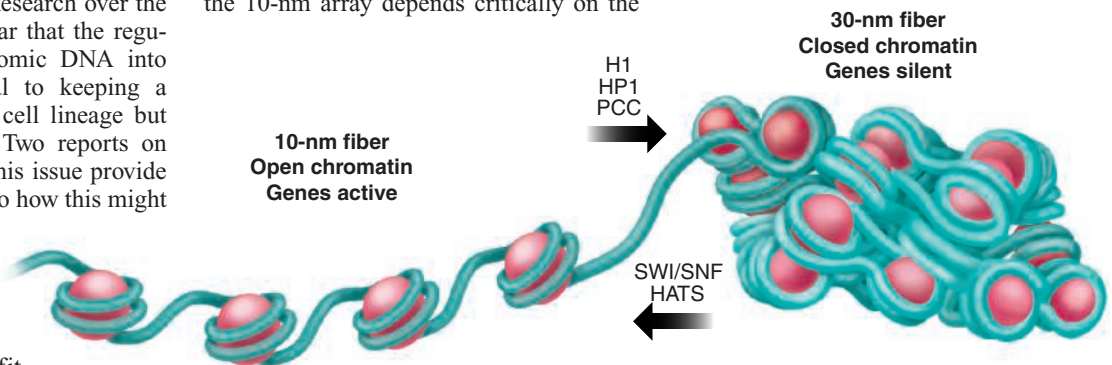
The packaging of DNA into chromatin allows the DNA of human cells (about 2 m in length if stretched out) to fit into a nucleus with a diameter of only 10 μm . The basic repeat element of chromatin is the nucleosome, which consists of 147 base pairs (bp) of DNA wrapped 1.7 times around an octamer of histone proteins (two copies each of core histones H2A, H2B, H3, and H4). Core histones contain a trihelical histone fold domain that mediates histone-histone and histone-DNA binding, as well as unstructured amino-terminal tail domains that are subjected to extensive covalent modifications. Nucleosomes, connected by about 20 to 60 bp of linker DNA, form a 10-nm “beads-on-a-string” array, which can be compacted further into a “30-nm” chromatin fiber (see the figure) (3, 4). Whereas the three-dimensional structure of the nucleosome is known in exquisite detail (5), the structure of the higher order 30-nm chromatin fiber is poorly understood.

One basic issue is the arrangement of

the nucleosomes within the 30-nm fiber. Two classes of model have been proposed: (i) the “one-start helix” in which nucleosomes, connected by bent linker DNA, are arranged linearly in a higher order helix; and (ii) the “two-start helix” in which nucleosomes, connected by straight linker DNA, zigzag back and forth between two adjacent helical stacks. To distinguish between these two competing models of higher order chromatin folding, Dorigo and co-workers (1) developed an ingenious experimental approach using a fully defined *in vitro* system to generate regular nucleosomal arrays. Further compaction of the 10-nm array depends critically on the

shows that local interactions between nucleosomes can drive self-organization into a higher order chromatin fiber.

But what is the physiological relevance of higher order chromatin? Notably, the buffer conditions promoting formation of a 30-nm chromatin fiber reflect the *in vivo* environment better than do those that yield a 10-nm fiber. One basic premise of chromatin regulation is that genes are silenced through compaction of chromatin, which reduces the accessibility of DNA. In contrast, gene expression may require the “opening up” of chromatin. The Polycomb group (PcG) of gene repressors and the trithorax group (trxG) of gene activators are two antagonistic classes of proteins that may act through modulation of chromatin structure (6–8). Together, these factors maintain the gene expression patterns of key developmental regulators and hence are crucial players in cellular differentia-



Regulated chromatin folding directs gene expression. A parsimonious model illustrating the transition from a 10-nm “beads-on-a-string” open chromatin formation to the next level of chromatin organization: the compacted 30-nm chromatin fiber. Depicted is one possible form of the chromatin fiber produced by a “two-start helix.” Folding or unfolding of the chromatin fiber affects the accessibility of DNA to regulatory factors, which control gene expression. Whereas gene silencing factors such as the PCC complex, HP1, and H1 stabilize higher order chromatin folding, gene activators such as the SWI/SNF remodeling complexes and histone acetyl transferases (HATS) initiate chromatin unfolding.

base of the histone H4 amino-terminal tails, believed to contact the histone H2A/H2B dimer of the neighboring nucleosome. Indeed, disulfide cross-links between a pair of cysteine residues that replaced selected amino acids in histone H4 and H2A stabilized the higher order chromatin structure. Next, Dorigo *et al.* digested the linker DNA connecting adjacent nucleosomes within the cross-linked compacted chromatin. Analysis of the length of the nucleosome stacks, now solely connected by internucleosomal cross-links, revealed a two-start rather than a one-start organization. This conclusion was corroborated by electron microscopy. In addition to important structural insights, this study

tion, stem cell renewal, and cancer. The trxG group includes members of the SWI/SNF family of adenosine triphosphate (ATP)-dependent chromatin remodeling factors, which use energy derived from ATP hydrolysis to open up chromatin. Conversely, *in vivo* studies suggest that PcG repression reduces DNA accessibility, but how this is achieved remains unclear (6–9).

In their study, Francis *et al.* (2) used electron microscopy to visualize the compaction of a nucleosomal array promoted by a core polycomb complex, named PCC. It will be of interest to determine whether PCC-induced compacted chromatin forms a bona fide two-start 30-nm fiber. One

The authors are in the Department of Biochemistry, Erasmus Medical Center, Rotterdam, Netherlands. E-mail: c.verrijzer@erasmusmc.nl

PCC complex compacts about three nucleosomes, which suggests that each complex might contact multiple nucleosomes and bring them closer together. Removal of the unstructured histone tails by the protease trypsin did not affect chromatin compaction by PCC; hence, these tails may not be required. Histone tail modifications may, however, contribute to the recruitment of PCC in vivo (10). Furthermore, it remains possible that the base of the H4 tail, which is important for internucleosome association, was not completely removed by trypsin treatment. One subunit of PCC, named PSC, appears to be particularly critical; a region of PSC that is essential in vivo is also important for chromatin compaction in vitro.

The term “higher order chromatin” is

frequently used, or abused, to explain epigenetic effects on gene expression, but what it refers to in molecular terms has not been well defined. The Dorigo *et al.* study provides a first glimpse of chromatin folding at the next level beyond the nucleosomal array. Meanwhile, the Francis *et al.* findings support the notion that PCC creates compacted chromatin domains that silence genes. These studies emphasize that higher order folding is an intrinsic attribute of the nucleosomal array used by gene regulatory factors. Silencing factors such as PCC, HP1, or the linker histone H1 appear to act, albeit through different mechanisms, by stabilizing the internucleosome interactions that drive higher order folding. Conversely, gene activation by SWI/SNF chromatin remodelers and histone acetyl

transferases is likely to involve destabilization of the 30-nm fiber. The dissection of the diverse mechanisms by which chromatin folding is regulated will be central to understanding the molecular basis of cellular memory.

References

1. B. Dorigo *et al.*, *Science* **306**, 1571 (2004).
2. N. J. Francis *et al.*, *Science* **306**, 1574 (2004).
3. T. J. Richmond, J. Widom, in *Chromatin Structure and Gene Expression*, S. C. R. Elgin, J. L. Workman, Eds. (Oxford Univ. Press, Oxford, 2000), pp. 1–23.
4. P. J. Horn, C. L. Peterson, *Science* **297**, 1824 (2002).
5. K. Luger *et al.*, *Nature* **389**, 251 (1997).
6. T. Mahmoudi, C. P. Verrijzer, *Oncogene* **20**, 3055 (2001).
7. L. Ringrose, R. Paro, *Annu. Rev. Genet.* **38**, 413 (2004).
8. J. A. Simon, J. W. Tamkun, *Curr. Opin. Genet. Dev.* **12**, 210 (2002).
9. D. P. Fitzgerald, W. Bender, *Mol. Cell. Biol.* **21**, 6585 (2001).
10. L. Wang *et al.*, *Mol. Cell* **14**, 637 (2004).

PHYSICS

What Is Dark Matter Made Of?

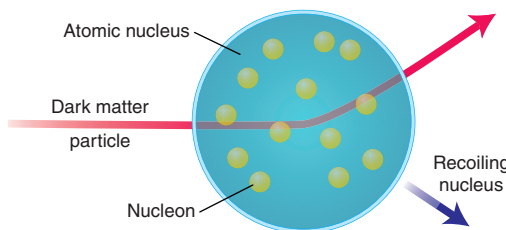
Konstantin Zioutas, Dieter H. H. Hoffmann, Konrad Dennerl, Thomas Papaevangelou

Astrophysical observations reveal that galaxies and clusters of galaxies are gravitationally held together by vast halos of dark (that is, nonluminous) matter. Theoretical reasoning points to two leading candidates for the particles that may make up this mysterious form of matter: weakly interacting massive particles (WIMPs) and axions. Particle accelerators have not yet detected either of the two particles, but recent astrophysical observations provide hints that both particles may exist in the universe, although definitive data are still lacking. Dark matter need not consist exclusively of only one of these two types of particles.

Precise measurements of the cosmic microwave background have shown that dark matter makes up about 25% of the energy budget of the universe; visible matter in the form of stars, gas, and dust only contributes about 4%. However, the nature of dark matter remains a mystery. To explain it, we must go beyond the standard model of elementary particles and look toward more exotic types of particles.

One such particle is the neutralino, a WIMP that probably weighs as much as

1000 hydrogen atoms (henceforth, we refer to the neutralino as a generic WIMP). Neutralinos are postulated by supersymmetric models, which extend the standard model to higher energies. To date, no neutralinos have been created in particle accelerators, but in the future they may be produced in the world’s most powerful particle



Detection of neutralinos. Neutralinos can be detected directly with underground detectors through their elastic scattering on nuclei. The energy deposited by the recoiling nucleus (large circle) is expected to provide the direct signature.

accelerator, the Large Hadron Collider currently being built at CERN. A recent precise measurement of the magnetic dipole moment of the muon favors the existence of new particles such as neutralinos.

Another possibility for the direct detection of neutralinos is to seek evidence for the tiny nuclear recoils produced by interactions between neutralinos (created when the universe was very young and very hot) and atomic nuclei (see the first figure). Because such interactions are rare and the effects small, they can only be detected in experiments that are conducted under-

ground, where the high-energy cosmic radiation is suppressed by several orders of magnitude.

Astrophysical observations could provide indirect evidence for neutralinos. On astrophysical scales, collisions of neutralinos with ordinary matter are believed to slow them down. The scattered neutralinos, whose velocity is degraded after each collision, may then be gravitationally trapped by objects such as the Sun, Earth, and the black hole at the center of the Milky Way galaxy, where they can accumulate over cosmic time scales. Such dense agglomerates could therefore yield an enhanced signal for the postulated neutralinos of cosmic origin.

Another possible signal may come from collisions between two neutralinos, which are believed to result in pairwise annihilation of the neutralinos in dense condensates of such particles. This process would be highly energetic, with energies of billions of electron volts (eV)—much higher than the energy of solar neutrinos, which does not exceed tens of millions of eV. The neutrinos resulting from neutralino annihilation should carry a distinct signature that could

be observed with neutrino telescopes designed to search for dark matter of this kind. Neutrinos (for example, from annihilating neutralinos deep within the solar core) are the only particles associated with neutralino annihilation or decay that are likely to escape from their place of birth.

Recently, the gamma-ray spectrometer on the European Space Agency’s INTEGRAL satellite has provided evidence for a “fountain” of antimatter electrons (that is, positrons) that are being ejected from some object near the galactic center, presumably a black hole. The data indicate that some

K. Zioutas is at the Physics Department, University of Thessaloniki, 52114 Thessaloniki, Greece, and at CERN, 1211 Geneva 23, Switzerland. D. H. H. Hoffmann is at the Institut für Kernphysik, TU-Darmstadt, Schlossgartenstr. 9, 64289 Darmstadt, Germany. K. Dennerl is at the Max-Planck-Institut für Extraterrestrische Physik, Giessenbachstraße, 85748 Garching, Germany. Th. Papaevangelou is at CERN, 1211 Geneva 23, Switzerland. E-mail: hoffmann@physik.tu-darmstadt.de

10^{43} positrons per second are annihilated from the galactic center region (1). This process requires an energy input of several thousand times the energy output of the Sun. The observation has been interpreted as possible evidence for a population of annihilating or decaying, relatively light, dark matter particles with a rest energy (which is equivalent to the rest mass of the particle) of ~ 1 million to 100 million eV in the galactic center. This result must be reconciled with the lack of evidence for such a particle in particle accelerators.

At much higher energies, the terrestrial High Energy Stereoscope System (HESS) telescope has observed a continuous emission of γ -rays (2), which might be a signature of annihilating WIMPs in the core of the Milky Way (3). But their energy (at least 12,000 times the rest mass of the hydrogen atom) is much higher than that expected from supersymmetric models, leaving room for dark matter particles that are even more exotic than those considered to date. Further observations are required to substantiate this remarkable initial observation, whose origin is unknown.

The other dark matter particle candidate is the axion. This particle has also not been discovered directly, but there is some indirect evidence for its existence. It has been proposed in order to reconcile the expected properties of the strong interaction—the force that binds quarks (the building blocks of neutrons and protons) together—with recent measurements.

At the heart of the problem lies the so-called charge-parity symmetry. (Charge conjugation symmetry implies that the laws of physics are unchanged if every particle is replaced by its antiparticle, whereas parity symmetry means that the physics of any process should be the same for the mirror image of that process. When the two are combined, one not only reverses the spatial direction but also replaces matter with antimatter.) Theoretical reasoning suggests that the strong interaction should violate charge-parity symmetry. But the measured upper limit of the electric dipole moment of the neutron is some nine orders of magnitude smaller than expected for a strong interaction that violates charge-parity symmetry. To reconcile theory and experiment, Peccei and Quinn proposed a model that requires the existence of a new particle, the axion (4, 5).

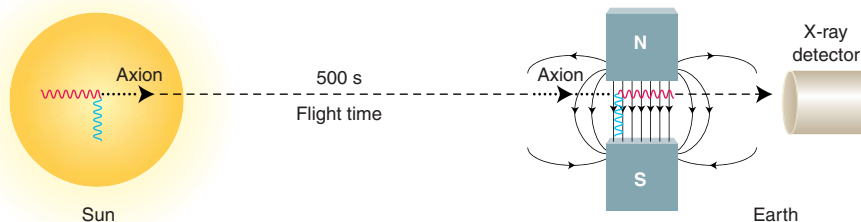
On the basis of theoretical reasoning, astrophysical observations, recent cosmological observations, and negative results from various earthbound direct experimental searches, the purported neutral axion must have a rest mass of between 1 millionth of an eV and a few eV. Attempts to detect axions use their proposed interaction

with a magnetic field, which results in its conversion to a photon. Thus, axions left over from the Big Bang epoch can be detected with a resonant cavity inside a strong magnetic field, where their presence would be indicated by excess microwave photons with an energy equal to the axion rest mass (6).

Besides the ubiquitous nonrelativistic dark matter axions (which are relics from an early era of our universe), large amounts of relativistic axions could be produced inside stars through conversion of thermal photons in the electric field of the atomic nuclei (see the second figure) (7, 8). When these relativistic axions escape from a star like our Sun, energy dissipates from the stellar core. They can be converted back to photons in a magnetic field and should therefore be detectable as an excess of photons when the magnet is pointed toward the celestial axion source. The ongoing CAST experiment at CERN (9) searches directly

These massive axions provide a possible explanation for a wide range of puzzles in astrophysics. A very small fraction of such axions does not escape from the gravitational field of the Sun (their place of birth) and can accumulate in orbits around the Sun over cosmic times. This gravitational capture is completely different from that discussed above for neutralinos. The radiative decay of such relatively short-lived trapped axions can give rise to self-heating of the solar atmosphere; this process may explain various mysterious observations from the Sun and beyond, such as the origin of the extremely hot (>1 million K) solar corona, which has long puzzled scientists (11, 12). This scenario can be directly verified with the use of a large-volume chamber to search for the spontaneous decay of short-lived axions to two x-rays.

Unfortunately, such decay x-rays from accumulated relatively short-lived trapped



Detection of solar axions. Axions are believed to be created in the hot solar core via the interaction between a thermal photon (red horizontal wave) and a virtual photon (blue vertical wave) near atomic nuclei. In a magnetic field, the axion is converted back to a photon (red horizontal wave). Detection of the latter by an x-ray detector would provide direct evidence for solar axions.

for solar axions by pointing a Large Hadron Collider dipole test magnet toward the Sun at sunrise and sunset. Thanks to the powerful magnet and the installed x-ray focusing mirrors (which reduce noise), the detection sensitivity is considerably improved relative to previous experiments of this kind.

Beyond the three spatial dimensions of our everyday experience, more spatial dimensions have been proposed to resolve some of today's greatest physics mysteries (such as why the gravitational force is so feeble). These extra dimensions are believed to change the behavior of certain particles, such as axions, drastically. For example, conventional axions created in the hot solar core are believed to have a tiny rest mass (less than about 0.001% of the rest mass of the electron). But within the framework of large extra dimensions (10, 11), the same particles will appear to be quite massive (about 1% of the electron rest mass), with a total energy (kinetic energy and rest mass) of up to ~ 10 keV; however, their lifetime is relatively short ($\sim 10^{20}$ s) (10, 11).

axions create a “ghost plasma,” heating the Sun’s (or any other) real plasma and complicating its interpretation. However, other phenomena in the galactic center and in galaxy clusters may fit the axion scenario. First, there should be no hot diffuse plasma in the galactic center, because it could not remain gravitationally bound to the galactic disk (13); the diffuse hard x-ray energy spectrum from the galactic center is also of unknown origin, because there is no known class of sources that are sufficiently numerous, bright, and hot to produce it (14). Second, observations from the intercluster medium in galaxy clusters require some kind of additional gas physics (15–18), because the dependence of its x-ray luminosity on temperature contradicts the conventional laws of physics; in addition, the observed excess entropy of the intercluster hot plasma needs some as yet unknown nongravitational processes.

All these processes could be explained by exotic dark matter particles that undergo radiative decay and emit hard x-rays in the process. Also, the total masses of galaxy

clusters derived from gravitational lensing and x-ray data sometimes differ by up to a factor of 2 (17, 18), providing a further indication that our picture of these largest cosmological objects is not complete. Therefore, care should be taken before using the x-ray emission from the dark matter-dominated galaxy clusters to derive cosmological distances (19).

The astrophysical observations discussed here indicate that axions and neutralinos may have been abundantly produced in the early universe and/or inside stars. These two types of particles remain the favorite candidates for dark matter and other celestial phenomena. As ever more sensitive detectors are built, more defini-

tive evidence for or against neutralinos and axions should become available. Existence of one does not preclude existence of the other: The dark matter in the universe may contain both of these particles, as well as many other, as yet unforeseen ones.

References and Notes

1. P. Jean *et al.*, *Astron. Astrophys.* **407**, L55 (2003).
2. F. Aharonian *et al.*, *Astron. Astrophys.* **425**, L13 (2004).
3. R. Irion, *Science* **305**, 763 (2004).
4. R. D. Peccei, H. R. Quinn, *Phys. Rev. Lett.* **38**, 1440 (1977).
5. R. D. Peccei, H. R. Quinn, *Phys. Rev. D* **16**, 1791 (1977).
6. R. Bradley *et al.*, *Rev. Mod. Phys.* **75**, 777 (2003).
7. G. G. Raffelt, *Phys. Rep.* **333–334**, 593 (2000).
8. G. G. Raffelt, *Annu. Rev. Nucl. Part. Sci.* **49**, 163 (1999).
9. CERN Axion Solar Telescope (<http://cast.web.cern.ch/CAST>).

10. L. DiLella, A. Pilaftsis, G. Raffelt, K. Zioutas, *Phys. Rev. D* **62**, 125011 (2000).
11. L. DiLella, K. Zioutas, *Astropart. Phys.* **19**, 145 (2003).
12. K. Zioutas, K. Dennerl, L. DiLella, D. H. H. Hoffmann, Th. Papaevangelou, *Astrophys. J.* **607**, 575 (2004).
13. K. Ebisawa, Y. Maeda, H. Kaneda, S. Yamauchi, *Science* **293**, 1633 (2001).
14. M. P. Muno *et al.*, *Astrophys. J.* **613**, 326 (2004).
15. C. Day, *Phys. Today* **56**, 16 (March 2003).
16. S. Peng Oh, *Mon. Not. R. Astron. Soc.* **353**, 468 (2004).
17. I. G. McCarthy, A. Babul, G. P. Holder, M. L. Balogh, *Astrophys. J.* **591**, 515 (2003).
18. I. G. McCarthy, G. P. Holder, A. Babul, M. L. Balogh, *Astrophys. J.* **591**, 526 (2003).
19. A. Cho, *Science* **304**, 1092 (2004).
20. We thank Ch. Eleftheriadis, Y. Semertzidis, and S. Vasotto for their assistance. Supported by the Bundesministerium für Forschung und Technologie, the General Secretariat for Research and Technology (Greece), and CERN.

ECOLOGY

Oh the Locusts Sang, Then They Dropped Dead

Richard S. Ostfeld and Felicia Keesing

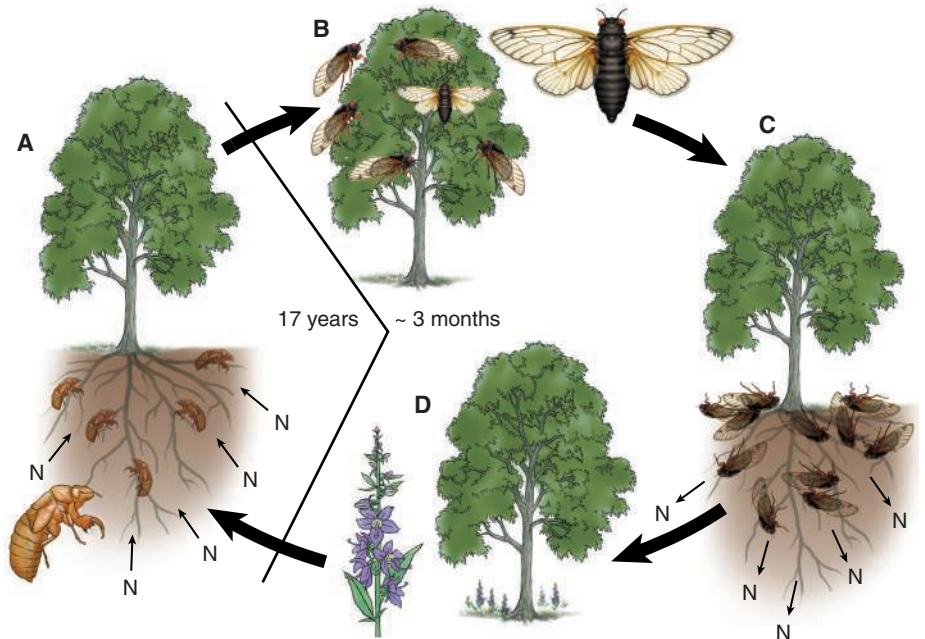
The Bob Dylan song “Day of the Locusts” refers to the cacophony from the 1970 emergence of 17-year cicadas (*Magicicada* spp.), which happened to coincide with his acceptance of an honorary degree from Princeton University. These cicadas, which dutifully reappeared aboveground in 1987 and then again this year, are a quintessential case of a resource pulse—a transient, multiannual episode of resource superabundance. On page 1565 of this issue, Yang (1) describes the ramifying impacts that massive pulses of cicada carcasses have on forest soils, microbial biomass, nitrogen availability, and reproductive success of understory plants.

Resource pulses typically are associated with reproductive events in plants, such as synchronized heavy seed production (mast-seeding) within populations of oaks or bamboos, and even more spectacularly, across dozens of genera of paleotropical dipterocarp trees (2). Plant populations that synchronize seed production achieve high reproductive success because seed predators can only consume a fraction of the hyperabundant resource (“predator satiation”) (3), and most of the escapees ger-

minate. Similarly, so many periodical cicadas are involved in the dissonant mating swarms that their predators—principally birds—can consume no more than 15% of the peak numbers (4). The remainder die after reproducing and drop to the forest floor.

Although much is known about the evolutionary causes of synchronized reproductive events, only recently have ecologists begun to analyze the consequences of resource pulses for ecosystems (5). The predominant type of resource pulse—mast seeding—occurs in grasses, annual forbs, shrubs, and trees, across at least four continents and from deserts to tropical rain forests. Generalist consumers—often rodents—are the most immediate beneficiary of this superabundant resource, and they respond with population outbreaks of their own. These rodent irruptions, in turn, result in severe impacts on their alternate prey, such as songbird eggs (6), their avian

Enhanced online at www.sciencemag.org/cgi/content/full/306/5701/1488



A 17-year pulse of nitrogen from cicada carcasses. (A) For 17 years, cicada nymphs feed on tree xylem, slowly incorporating belowground nitrogen (N) absorbed by the tree’s roots. (B) Upon emergence, adult cicadas mate and lay eggs within a several-week period, and then die and drop to the forest floor. (C) The accumulated nitrogen in their carcasses is released after a burst of activity by microbial decomposers. (D) This spike of available soil nitrogen leads to increased nitrogen content and seed size of the American bellflower (*C. americanum*), an understory plant.

The authors are in the Institute of Ecosystem Studies, Millbrook, NY 12545, USA. F. Keesing is also in the Biology Department, Bard College, Annandale-on-Hudson, NY 12504, USA. E-mail: rostfeld@ecostudies.org

CREDIT: TAINA LUTWAK

and mammalian predators (7), and their parasites and pathogens (5, 8). In these cases, the pulsed resource is quickly converted into consumer biomass, and the direct and indirect consequences for ecosystems follow this consumer pathway.

The research by Yang demonstrates a new pathway by which resource pulses can affect ecosystems—through the action of decomposers (1). Unlike seeds, which germinate following escape from predation, periodical cicadas die and rot. These insects are a high-quality fertilizer indeed (about 10% nitrogen), delivered at a rate of up to 0.5 kg m⁻². Within a month of a simulated cicada irruption, biomass of both fungal and bacterial decomposers in the soil increased dramatically, and this in turn resulted in a tripling of soil ammonium, and a more-than-doubling of soil nitrate concentration. As with other fertilizers, the cicada-induced flush of soil nutrients ultimately boosted nitrogen concentration and seed mass in the American bellflower (*Campanulastrum americanum*), an understory plant.

Periodical cicada nymphs spend 16-plus years attached to tree roots sucking on xylem (9), resulting in a persistent, long-term deflection of soil-derived nitrogen from leaves into insect biomass. Upon emergence, the cicadas then transport this stolen nitrogen aboveground. From there, a

little ends up in avian or mammalian consumer tissue, and another fraction goes to cicada egg production, but most becomes fertilizer, first for soil microbes and then for understory plants like bellflowers. Because the nitrogen-enriched bellflower tissues die and decompose themselves, the trees would seem to be the ultimate recipients of the prodigal nitrogen's return underground (see the figure).

Analyzing radial tree-ring growth of oaks within the geographic ranges of 13-year and 17-year cicadas, Koenig and Liebhold (10) found a ~4% decrease in tree growth during the year of emergence, which they attributed to the damage caused by oviposition wounds in twigs. However, some of Koenig and Liebhold's analyses also demonstrated a ~1% increase in tree radial growth during the first 4 years after emergence, for which they had no explanation. The fertilization effect of cicada carcasses reported by Yang might account for this apparently compensatory stimulation of growth after emergence.

Spectacular resource pulses like the emergence of periodical cicadas constitute one of the more obvious demonstrations that ecological systems rarely exist in equilibrium states, but instead are in constant flux. By tracing the responses of populations or entire trophic levels to resource pulses, ecologists can assess the extent to

which resources versus consumers control abundance or biomass—in other words, whether control is bottom-up or top-down. They can also determine the strength and nature of interconnections between species or trophic levels. A trophic cascade occurs when top-down effects permeate through three or more trophic levels (11), and we suggest that the cicada-decomposer-plant system, which represents the penetrance of bottom-up effects through three trophic levels, be considered a “trophic fountain.” The bottom-up metaphor, of course, refers to the effects of lower trophic levels on higher ones. In a more physical sense of the metaphor, Yang's work demonstrates how organisms and materials flow inexorably from bottom to top and back again.

References

1. L. H. Yang, *Science* **306**, 1565 (2004).
2. L. M. Curran, M. Leighton, *Ecol. Monogr.* **70**, 101 (2000).
3. D. H. Janzen, *Ann. Rev. Ecol. Syst.* **2**, 465 (1971).
4. K. S. Williams, K. G. Smith, F. M. Stephen, *Ecology* **74**, 1143 (1993).
5. R. S. Ostfeld, F. Keesing, *Trends Ecol. Evol.* **15**, 232 (2000).
6. K. A. Schmidt, R. S. Ostfeld, *Ecology* **84**, 406 (2003).
7. B. Jedrzejewska, W. Jedrzejewski, *Predation in Vertebrate Communities: The Białowieża Primeval Forest as a Case Study* (Springer, New York, 1998).
8. T. L. Yates *et al.*, *BioScience* **52**, 989 (2002).
9. J. White, C. E. Strehl, *Ecol. Entomol.* **3**, 323 (1978).
10. W. D. Koenig, A. M. Liebhold, *Can. J. For. Res.* **33**, 1084 (2003).
11. M. L. Pace, J. J. Cole, S. R. Carpenter, J. F. Kitchell, *Trends Ecol. Evol.* **14**, 483 (1999).

PLANETARY SCIENCE

Nothing Simple About Asteroids

Erik Asphaug

Twelve years ago, scientists obtained the first close look at asteroids, when the Galileo mission en route to Jupiter acquired high-resolution images of Gaspra and Ida (1, 2). Since then, much has changed but little has solidified. Even following a year-long rendezvous by NASA's NEAR Shoemaker orbiter at asteroid Eros (see first and second figures) (3), asteroid science remains at a crossroads. The surface remote sensing and imaging techniques applied to date have yet to resolve a single fundamental question of asteroid geophysics or chemistry. A detailed new model for asteroid seismology, reported by Richardson *et al.* on page 1526 of this issue (4), shows how acoustic reverberations from impacts can cause asteroid topography to flatten, diffusing small-scale features and erasing small craters. Like other recent

models (5), this work also illustrates how seismological experiments—akin to those conducted by Apollo astronauts on the Moon—may soon reveal information about the structure and evolution of comets and asteroids.

Asteroids are famously menacing, and the movie script requires them to be tamed or destroyed. The hazard posed by asteroids has focused minds, but their essence is the more interesting question. Asteroids are not mere rocks; their own self-gravitation, however minuscule, is central to their evolution (6). Nor are they planets: Most asteroids are undifferentiated (never melted) precursors to planets, or fragments of these. Others are

fragments of differentiated planet precursors that were catastrophically disrupted long ago. Most are very porous, spin rapidly, and are irregular in shape, suggesting a tumultuous history. Contradictory attempts have been made to correlate their visible and infrared colors to the confusing taxonomy of meteorites.

As for asteroid geophysics, the most basic terminology is undecided. Conflicting definitions exist for terms such as regolith,



Eros: the best studied asteroid. This image of the 33 by 13 by 13 km near-Earth object, with dimensions of 33 by 13 by 13 km³, was taken on 28 January 2001 by the NEAR Shoemaker orbiter.

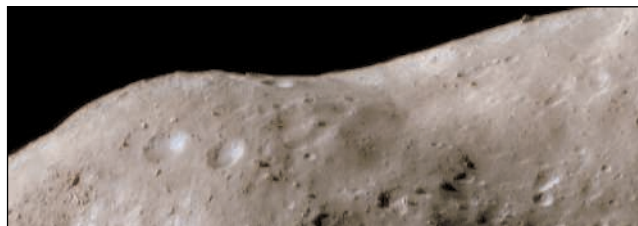
rubble pile, contact binary, comet, asteroid, and even planet. (The largest known asteroid, Ceres, a target of NASA's Dawn mission, has a diameter of 930 km and is arguably a planet if Pluto is one).

Help with understanding asteroids, when it comes, will be in the form of orbiters that image the inner structure of an asteroid, and landed experiments including sample returns. Seismomechanical probes of the deep interior can also reveal how regolith (planetary soil) behaves under microgravitational conditions. These experiments will not only solve one of the most interesting and important puzzles in planetary science; they will also tell us how to tame any dangerous rogue asteroid.

Advanced concepts for asteroid exploration are making important headway. The most ambitious asteroid mission to date is Hayabusa, the Japanese spacecraft en route to 25143 Itokawa, a near-Earth asteroid with a diameter of 0.5 km. When it reaches Itokawa in mid-2005, Hayabusa will touch the surface and fire a small bullet to knock grains into a canister for return to Earth. Before leaving the asteroid, Hayabusa will deploy a low-cost microrobot called MINERVA (see the third figure) that will hop across the surface and return pictures from tiny cell-phone cameras. After MINERVA investigates the asteroid, Hayabusa will return to Earth with its precious cargo.

MINERVA will not perform any seismology, but it was Hayabusa Project Scientist Akira Fujiwara who invented the concept of asteroid seismology in 1991. Fujiwara showed how impact stresses from the largest impact event on Phobos could be related to the geometry of the asteroid's global fractures (7). (Phobos is the innermost satellite of Mars and probably a captured asteroid.)

Two- and three-dimensional impact hydrocodes (6)—that is, numerical simulations of collisions into realistic asteroid shapes, sizes, and materials—were later used to re-



Near-Earth Landscape. This false-color image of Eros was taken by NEAR on 16 October 2000 while orbiting 54 km above the asteroid. In pale brown areas, the surface is believed to be reddened and darkened by the solar wind and by micrometeorite impacts. In white or blue areas, fresher materials are exposed from the subsurface on steep slopes.

late the largest craters on a given asteroid to the geologic features observed by spacecraft. For example, a series of parallel faults on asteroid Ida is evidence that Ida is probably a shattered monolith. Asteroid Mathilde exhibits no distant effects from its half-dozen impacts, and is thus probably a rubble pile.

As Richardson *et al.* point out, different asteroid structures have different reverberations; the frequency response of a fractured medium mainly depends on its internal fracture geometry. Asteroid seismology is thus well suited for inverse modeling—using measured reverberations to tell us what is inside.

But performing seismology in deep space, on a body with extraordinarily little gravity, whose surface may consist of highly mobile, statically charged dirt, presents significant challenges. How does one an-

chor a geophone or a seismic source into bedrock, or into dust, in microgravity? Hayabusa's poking and prodding might lead the way. One idea is to use an impact penetrator that buries its way into the surface. But the escape velocity of an asteroid is very low: If MINERVA hops faster than about 20 cm/s it risks leaving Itokawa. A penetrator could bounce off, never to return. The Rosetta spacecraft, which is en route to Comet 67/P Churyumov-Gerasimenko, will attempt anchoring with harpoons in 2014. Just letting a seismic payload come to rest on the comet's surface is another possibility—it is not ideal for seismology, but in terms of deployment is no different from how Hayabusa will drop off bright target markers to Itokawa's surface for navigation. An orbiting spacecraft could drop a handful of identical "pods" onto the surface, each with an accelerometer and an explosive charge. Detonating one by one, the pods would conduct a series of multipath seismological experiments (8).

By coupling impact hydrocodes to seismic evolution models, Richardson *et al.* have set the stage for a detailed geomorphological understanding of small planetary bodies. They begin with the assumption that the asteroid Eros (see the first two figures) consists of a few megablocks in close contact, and otherwise resembles the Moon in its seismological properties. Their results are consistent with the absence of small craters on Eros, but do reverberations of a fraction of a millimeter per second, in

microgravity, really trigger geomorphic diffusion? Electrical or granular cohesion might resist it. Another possible explanation for the lack of small craters is electrostatic levitation, leading to the rise and fall of dust, filling in the hollows and creating "ponds" (9). Alternatively, small meteoroids may be winnowed by solar radiation forces before they can impact Eros, so that small craters are never created (10). Or, small grains may work their way down in thermal cycles, leaving large boulders stranded like Brazil nuts at the surface in a granular convection that degrades the loose terrain (11).

On the basis of existing evidence—including the lack of a clear picture of how the original cosmic



Asteroid robot. Hayabusa is en route to investigate Itokawa, a rocky near-Earth asteroid with a diameter of ~500 m, in 2005. In this illustration by A. Ikeshita, the small robotic probe MINERVA (Micro-/Nano- Experimental Robot Vehicle for Asteroid) is seen to the lower right. A navigation target marker is also seen deployed, aiding the spacecraft in acquiring its small sample.

sediment would solidify as intact rocks—there is no compelling reason to abandon alternative models for the interior of Eros, including that of a compacted fine-grained silt that experiences faults and fissures like any clod of dirt. A dirt-clod model for Eros and similar asteroids is defensible: It can explain why the spectral characteristics of the most abundant meteorites on Earth differ from those of the most abundant asteroids in near-Earth space, because ejected dirt clumps could not survive a meteorite's brutal fate during ejection from their parent asteroid and entry through Earth's atmosphere. Common meteorites would have to come from stronger parent asteroids.

These are exciting times for asteroid science, but one wonders how long they can go on without an unambiguous founda-

tion. Understanding asteroids is central to understanding how planets emerged from the primordial swarm of planetesimals. Asteroids also show us how fundamental geophysical processes—such as geomorphology, impact cratering, and granular mechanics—behave in a microgravity environment. And certainly, the challenge of diverting a hazardous asteroid will require some knowledge of asteroid geology (12), unless we are to go shooting in the dark when that time comes.

References and Notes

1. M. J. S. Belton *et al.*, *Science* **257**, 1647 (1992).
2. M. J. S. Belton *et al.*, *Science* **265**, 1543 (1994).
3. J. Veverka *et al.*, *Science* **289**, 2088 (2000).
4. J. E. Richardson, H. J. Melosh, R. Greenberg, *Science* **306**, 1526 (2004).
5. J. D. Walker, W. F. Huebner, *Adv. Space Res.* **33**, 1564 (2004).

6. E. Asphaug, E. Ryan, M. Zuber, in *Asteroids III*, W. F. Bottke Jr., A. Cellino, P. Paolicchi, R. P. Binzel, Eds. (Univ. of Arizona Press, Tucson, AZ, 2002), pp. 463–484.
7. A. Fujiwara, *Icarus* **89**, 384 (1991).
8. D. J. Scheeres *et al.*, 34th Lunar and Planetary Science Conference, 17 to 21 March 2003, League City, TX, abstract 1444 (see www.lpi.usra.edu/meetings/lpsc2003/pdf/1444.pdf).
9. M. S. Robinson, P. C. Thomas, J. Veverka, S. Murchie, B. Carcich, *Nature* **413**, 396 (2002).
10. J. F. Bell, 32nd Lunar and Planetary Science Conference, 12 to 16 March 2001, Houston, TX, abstract 1964 (see www.lpi.usra.edu/meetings/lpsc2001/pdf/1964.pdf).
11. E. Asphaug, P. J. King, M. R. Swift, M. R. Merrifield, 32nd Lunar and Planetary Science Conference, 12 to 16 March 2001, Houston, TX, abstract 1708 (see www.lpi.usra.edu/meetings/lpsc2001/pdf/1708.pdf).
12. M. Belton, T. H. Morgan, N. Samarasinha, D. K. Yeomans, Eds., *Mitigation of Hazardous Comets and Asteroids* (Cambridge Univ. Press, Cambridge, UK, 2004).
13. Support from the NASA Planetary Geology and Geophysics Program and the NASA Discovery Data Analysis Program is gratefully acknowledged.

EVOLUTION

Epistasis in RNA Viruses

Yannis Michalakis and Denis Roze

If you cross two black guinea pigs you may get several albino pups. This could happen, for example, if the boar and sow are both heterozygous at the *C* locus for the *c^a* allele, which prevents the production of the pigment melanin. Guinea pig fur color is determined by many genes, but the *C* locus strongly affects the expression of these genes in homozygous *c^a* individuals. The *C* locus is said to be epistatic because it affects the expression of genes at other loci. Developmental biology is replete with examples of epistatic gene interactions. On the other hand, evolutionary biology is desperately searching for them. Two recent studies—by Sanjuán *et al.* in a recent issue of *Proceedings of the National Academy of Sciences U.S.A.* (1) and by Bonhoeffer *et al.* on page 1547 of this issue (2)—report analyses of epistatic gene interactions in RNA viruses and discuss their relevance to viral recombination.

Epistatic interactions are important in evolutionary biology almost whenever multilocus genetics matter. The recent explosion of interest in epistatic interactions is epitomized by publication of a book devoted to the topic (3). Regarding his doctoral work on guinea pig fur color and its determination, Wright has admitted that this study was one of four factors that led him to propose his “shifting balance theory” of adaptive landscapes (4). Epistatic interactions are al-

so prominent in studies of speciation and reproductive isolation (5). And, inevitably, they are central to the evolution of genetic recombination (see the figure) (6).

There are very few examples of epistatic gene interactions in evolutionary biology, principally because of the difficulties inherent in performing such studies. One either needs to know all the genes determining a trait, which is typically rare in evolutionary biology, or one needs to conduct relatively laborious breeding experiments. Moreover, the relation between the trait's value and its fitness benefit is crucial and must be at least partly known. It is not surprising, therefore, that the few examples of epistasis in evolution come from microorganisms. The two new RNA virus studies provide measures of epistatic gene interactions allowing fresh insights into their effects on evolution (1, 2).

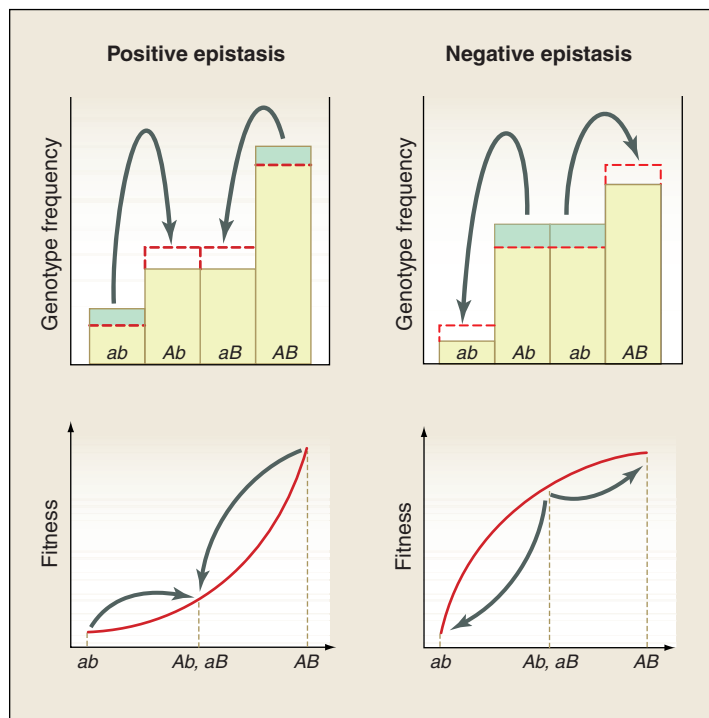
In their new work, Sanjuán and colleagues (1) examined vesicular stomatitis virus (VSV), which does not exhibit recombination. They analyzed a set of single-nucleotide mutations generated by directed mutagenesis. The individual fitness effects of these mutations, deleterious or beneficial, were previously established (7). The authors now report the fitness effects of pairs of mutations that are either deleterious or beneficial when single. Remarkably, singly beneficial mutations when paired exhibit negative epistasis, whereas singly deleterious mutations when paired exhibit positive epistasis. In both cases, the mutation pairs act antagonistically: Their combined effect is less than that expected from their individual effects.

In a related study, Bonhoeffer and colleagues present evidence for positive epistasis in another RNA virus, human immunodeficiency virus 1 (HIV-1) (2). These authors examined the evolution of recombination in HIV-1, which unlike VSV is known to recombine frequently. If recombination in HIV-1 had been selected for because of gene interactions, then epistasis between pairs of genes should be slightly negative (see the figure). Surprisingly, Bonhoeffer and colleagues report that gene interactions in HIV-1 exhibit positive epistasis.

Their data come from an impressive analysis of the amino acid sequences of the protease and the major part of the reverse transcriptase of HIV-1 derived from 9466 patient samples. These retroviral samples were obtained from HIV-1-infected patients undergoing drug therapy. The authors then analyzed the fitness benefits conferred by these two proteins. Briefly, genes encoding the two viral proteins were introduced into NL4-3, a molecular HIV clone that can undergo only one replication cycle. Fitness of the viral progeny was measured in vitro by comparing the number of progeny produced by these constructs to that produced by the NL4-3 clone. The presence of epistasis was tested in two ways: (i) by analyzing the relation between the logarithm of fitness and number of mutations differentiating each sample from the reference clone; and (ii) by examining the fitness of pairs of di-allelic polymorphic sites for which all four possible combinations were observed. The effects of mutations at other loci were averaged. Both methods revealed positive epistasis in HIV-1.

In the results from the second method used by Bonhoeffer and co-workers, epistasis spanned negative and positive values,

The authors are at Génétique et Evolution des Maladies Infectieuses, UMR CNRS IRD 2724, Montpellier Cedex 5, France. E-mail: yannis.michalakis@mpl.ird.fr; denis.roze@mpl.ird.fr



Evolution of recombination between two selected loci. Genotypes *ab*, *Ab*, *aB*, and *AB* have relative fitnesses 1 , $1 + s$, $1 + s$, and $(1 + s)^2 + e$, where e is a measure of epistasis. Positive epistasis generates an excess of extreme genotypes [(top left) dashed lines correspond to linkage equilibrium]. Recombination tends to reduce this excess by re-creating intermediate genotypes (arrows) that are less fit on average (bottom left). This effect selects against recombination. Furthermore, recombination decreases the variance in fitness, which reduces the efficiency of selection and also selects against recombination. Negative epistasis (right) generates an excess of intermediate genotypes, which is reduced by recombination (arrows). Because extreme genotypes are less fit on average, this selects against recombination. However, recombination now increases the variance in fitness, thus increasing the efficiency of selection and resulting in selection for recombination. Theoretical models show that the benefits of recombination in terms of increased variance in fitness are stronger than the cost in terms of average fitness when epistasis is negative and sufficiently weak (15). Two other terms often used in the literature are “synergistic” and “antagonistic.” Synergistic (“work together”) means that combinations of mutations have stronger effects than those expected from the effects of the individual mutations. Thus, synergism among mutations results in positive epistasis for beneficial mutations and negative epistasis for deleterious mutations (“makes things better when things are good, and worse when they’re bad”). Antagonistic (“struggle against”) means that combinations of mutations have weaker effects than those expected from the effects of the individual mutations. Thus, antagonism among mutations results in negative epistasis for beneficial mutations and positive epistasis for deleterious mutations (“makes things worse when they are good, and better when they are bad”).

the mean being positive. When only mutations that give rise to strong effects were considered, an even larger mean value for positive epistasis was obtained. Interestingly, these mutations are known to have arisen in response to drug therapy. Unfortunately, Bonhoeffer *et al.*'s second method—which a priori could be compared to the analysis of Sanjuán *et al.* (1)—did not examine whether epistasis was positive or negative when the mutations involved were singly deleterious or singly beneficial (after averaging over the genetic background) (8). Given that most of the HIV-1 isolates had a lower fitness than that exhibited by the NL4-3 HIV clone, we conclude that epistasis between deleterious mutations is positive (antagonistic) in HIV-1.

Why should that be the case? Epistasis between loci, like dominance between different alleles at a given locus, could be viewed as either the result of evolution or the unavoidable consequence of the way organisms function. For example, the metabolic control theory of deleterious mutations affecting enzyme activities predicts that epistasis will be either synergistic or antagonistic depending on whether the mutations in question affect the same enzyme (always synergistic) or not. If the mutations affect different enzymes, the nature of epistasis will depend on whether selection acts to maximize metabolic flux (antagonistic) or the concentration of an intermediate in the pathway (partly synergistic), or to optimize either the flux or the quantity of metabolic product (mostly synergistic) (9).

We do not know of any models explicitly addressing the question of the evolution of epistasis. Models of the evolution of genetic robustness, however, provide some basis for discussion (10). Organisms with high mutation rates, such as RNA viruses, are expected to evolve flat fitness landscapes, meaning that they comprise many genotypes with equal or almost equal fitness (11, 12). This kind of fitness landscape should lead to negative epistasis for deleterious mutations (synergistic) (13), and also negative epistasis for beneficial mutations (antagonistic).

Environmental variation as a factor affecting whether epistasis is negative or positive has only been touched on. In a simulation study of the effects of deleterious mutations on bacteriophage T7 growth, severe deleterious mutations were always found to interact antagonistically, whereas the interactions between mildly deleterious mutations depended on the quality of the environment. In rich environments, the mutations were also antagonistic, but in poor environments they were synergistic (14). It is difficult to generalize and extrapolate the results of this study to other organisms, which may have different metabolic activities and live in different environments. This study, however, underlines that the effect of the environment on epistasis deserves more attention, both theoretically and experimentally. Future studies should complement our understanding of how and whether a particular kind of epistasis is dependent on the environment.

The Sanjuán *et al.* and Bonhoeffer *et al.* studies show that the pattern of epistasis in RNA viruses is not compatible with current genetic theories of sexual reproduction and recombination, which assume that mutations affecting fitness exhibit negative epistasis. Given that VSV exhibits no recombination, perhaps this is not a big problem. In contrast, HIV-1 recombines frequently and Bonhoeffer and colleagues propose that it may do so to repair single-strand breaks in the RNA genome. This and the fact that VSV and HIV-1 are subject to exceptionally high mutation rates caution us against extrapolating results obtained with these simple organisms. Nevertheless, their contribution to our understanding of evolution remains invaluable.

References and Notes

1. R. Sanjuán, A. Moya, S. F. Elena, *Proc. Natl. Acad. Sci. U.S.A.* **101**, 15376 (2004).
2. S. Bonhoeffer, C. Chappay, N. T. Parkin, J. M. Whitcomb, C. J. Petropoulos, *Science* **306**, 1547 (2004).
3. J. B. Wolf, E. D. I. Brodie, M. J. Wade, Eds., *Epistasis and the Evolutionary Process* (Oxford Univ. Press, New York, 2000).
4. S. Wright, *J. Anim. Sci.* **46**, 1192 (1978).
5. S. Gavrillets, *Fitness Landscapes and the Origin of Species* (Princeton Univ. Press, Princeton, NJ, 2004).
6. S. P. Otto, T. Lenormand, *Nature Rev. Genet.* **3**, 252 (2002).
7. R. Sanjuán, A. Moya, S. F. Elena, *Proc. Natl. Acad. Sci. U.S.A.* **101**, 8396 (2004).
8. There are obviously infinitely many ways in which to analyze such a rich data set.
9. E. Szathmáry, *Genetics* **133**, 127 (1993).
10. C. O. Wilke, C. Adami, *Mutat. Res.* **522**, 3 (2003).
11. C. O. Wilke, J. L. Wang, C. Ofria, R. E. Lenski, C. Adami, *Nature* **412**, 331 (2001).
12. P. Schuster, J. Swetina, *Bull. Math. Biol.* **50**, 635 (1988).
13. J. A. de Visser *et al.*, *Evol. Int. J. Org. Evol.* **57**, 1959 (2003).
14. L. You, J. Yin, *Genetics* **160**, 1273 (2002).
15. N. H. Barton, *Genet. Res.* **65**, 123 (1995).

INTRODUCTION

Common Signaling Themes

The Connections Maps, *Science's* freely accessible database of information on signal transduction featured at *Science's* online Signal Transduction Knowledge Environment (STKE), continues to grow. This issue of *Science* features Viewpoints in which authorities who have constructed new Connections Map pathways provide overviews of the biological and medical processes that are regulated and briefly look ahead to future developments.

That signaling mechanisms are shared across distantly related organisms is readily apparent. Alonso and Stepanova (p. 1513) describe signaling by ethylene, a gaseous plant hormone that regulates processes such as seed germination and fruit ripening. Receptors for ethylene are similar to two-component histidine kinases, common signaling machines in bacterial cells. Ethylene signals are also apparently modulated by a mitogen-activated protein kinase (MAPK) cascade, a signaling module present in eukaryotic organisms from yeast to humans. As Gfeller and Farmer describe (p. 1515), the plant immune system is regulated by jasmonates, fatty acid derivatives somewhat like vertebrate prostaglandins. Much remains to be defined in the jasmonate pathways, including the jasmonate receptor.

In other pathways, many components are known and can be connected in complicated networks. Investigation is turning to fascinating questions of how a limited set of similar or even identical components is assembled in different ways in distinct cell types to control completely different biological responses. The MAPK cascade (a series of protein kinases sequentially activated by phosphorylation) also acts in three distinct signaling pathways in yeast: a pheromone sensing pathway (Wang and Dohlman, p. 1508), a pathway that monitors extracellular osmotic conditions (Westfall *et al.*, p. 1511), and a nutrient-sensitive pathway that converts yeast into a connected filamentous form (Truckses *et al.*, p. 1509). These pathways even share one identical member of the MAPK cascade, yet specificity is normally faithfully maintained.

In humans, fibroblast growth factor receptors (FGFRs) and epidermal growth factor receptors (EGFRs) are receptor tyrosine kinases that control cell proliferation and cell death and are implicated in common debilitating diseases (Schlessinger, p. 1506). These receptors share similar signaling machinery (including MAPK cascades), but the components are wired together in distinct ways that may change the amplitude, duration, and localization of signals in the cell. Vivier *et al.* (p. 1517) describe signaling in deadly lymphocytes known as natural killer cells that provide a first line of defense against infection in mammals. Again, the ubiquitous MAPK cascade crops up. The immunologist's challenge is to understand a system where both stimulatory and inhibitory receptors exist and signals may spread from one to multiple receptors.

Eiden notes in his Editorial (p. 1437) that knowledge management has become critical as efforts proceed to decipher biological regulatory mechanisms and manipulate them for beneficial effect. Mapping the connections and providing enhanced access to information about pathways and components may be the easy part. Using assembled knowledge to decipher how signals vary in time and space, and how subtle differences in network wiring and possible dynamic changes in connectivity produce fine regulation that is robust to all sorts of insults and perturbations, will likely require the best tools we can muster—and then some.

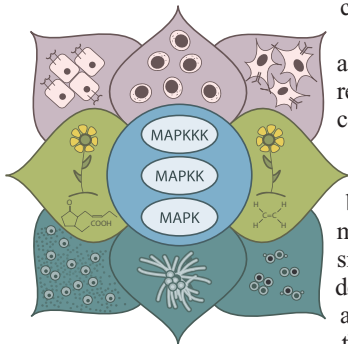
L. BRYAN RAY, ELIZABETH M. ADLER, NANCY R. GOUGH

CONTENTS

VIEWPOINTS

- 1506 Common and Distinct Elements in Cellular Signaling via EGF and FGF Receptors**
J. Schlessinger
- 1508 Pheromone Signaling Mechanisms in Yeast: A Prototypical Sex Machine**
Y. Wang and H. G. Dohlman
- 1509 Jekyll and Hyde in the Microbial World**
D. M. Truckses, L. S. Garrenton, J. Thorner
- 1511 When the Stress of Your Environment Makes You Go HOG Wild**
P. J. Westfall, D. R. Ballon, J. Thorner
- 1513 The Ethylene Signaling Pathway**
J. M. Alonso and A. N. Stepanova
- 1515 Keeping the Leaves Green Above Us**
A. Gfeller and E. E. Farmer
- 1517 Natural Killer Cell Signaling Pathways**
E. Vivier, J. A. Nunès, F. Vély

See also Editorial on page 1437 and links to related pathways at www.sciencemag.org/sciext/cellsignaling/.



Science

Common and Distinct Elements in Cellular Signaling via EGF and FGF Receptors

Joseph Schlessinger*

Signaling pathways that are activated by epidermal growth factor (EGF) or fibroblast growth factor (FGF) receptors have been identified and compared (detailed Connections Maps are available at *Science's* Signal Transduction Knowledge Environment). Both receptors stimulate a similar complement of intracellular signaling pathways. However, whereas activated EGF receptors (EGFRs) function as the main platform for recruitment of signaling proteins, signaling through the FGF receptors (FGFRs) is mediated primarily by assembly of a multidocking protein complex. Moreover, FGFR signaling is subject to additional intracellular and extracellular control mechanisms that do not affect EGFR signaling. The differential circuitry of the intracellular networks that are activated by EGFR and FGFR may affect signal specificity and physiological responses.

The human genome contains 59 genes that encode 20 distinct families of receptor tyrosine kinases (RTKs) (1). In response to stimulation by specific ligands, RTKs regulate a great diversity of cellular processes (2), including cell survival, proliferation and differentiation, cell metabolism, and cell migration. Dysfunctions in RTKs and their signaling pathways have been linked to diabetes, atherosclerosis, severe developmental pathologies, and various cancers (3). The EGF receptor (EGFR) family comprises four members designated EGFR, ErbB2, ErbB3, and ErbB4 (4). The intrinsic protein tyrosine kinase (PTK) activities of these receptors and their abilities to recruit and activate intracellular signaling pathways are controlled by members of the EGF family of growth factors. Although certain members of the EGFR family can be activated by several EGF family members (e.g., EGFR), others do not directly bind any ligand (e.g., ErbB2) or are devoid of intrinsic PTK activity (e.g., ErbB3). Therefore, the action of ErbB3 and ErbB2 are dependent upon combinatorial interactions with other members of the EGFR family that are stimulated by EGF, transforming growth factor α (TGF- α), heparin-bound EGF (HB-EGF), or other EGF family members (4).

The fibroblast growth factor receptor (FGFR) family also comprises four RTKs designated FGFR1, FGFR2, FGFR3, and FGFR4 (5). An important hallmark of FGFRs is that the diversity of this RTK family is controlled by alternative RNA splicing, resulting in the generation of multiple splice variants (6) in the extracellular domains that exhibit distinct tissue expression patterns and differential ligand-binding characteristics toward the

22 known FGFs. Consequently, a single *Fgfr* gene can encode two receptors that exhibit different FGF-binding characteristics (6) and that are expressed in different tissues (i.e., mesenchyme, epithelium).

In this Viewpoint, we compare key features underlying the action of EGFRs and FGFRs that may lead to their unique pleiotropic responses and physiological roles. This comparison may provide insights into one of the key open questions in cell signaling, that is, how signaling specificity is generated following stimulation of a common complement of signaling pathways by a given RTK.

Before ligand stimulation, intramolecular interactions within the extracellular domains of each of the EGF and FGF receptors maintain the two receptors in an inactive monomeric state (7). Both receptors are activated by ligand-induced dimerization, tyrosine autophosphorylation, and stimulation of their intrinsic PTK activities (2). Moreover, similar repertoires of intracellular signaling pathways are stimulated by both RTKs (2). Yet, inspection of the various steps involved in the action of the two receptors shows that signaling through FGFR involves additional layers of control that take place both inside and outside the cell.

EGFR is activated by the binding of one type of ligand molecule (i.e., EGF, TGF- α) (2, 4); in contrast, the activation of FGFR involves two different ligands, FGF and heparan sulfate proteoglycan (HSPG), that act together to activate FGFRs (2, 8). The binding of each ligand alone is insufficient for stabilization of FGFR dimerization, a prerequisite for tyrosine autophosphorylation and stimulation of the intrinsic PTK activity. HSPG increases the binding affinity of FGF to FGFR and stabilizes FGFR dimerization and activation. Furthermore, it is thought that FGF bound to HSPG in the extracellular matrix may provide a store of FGF molecules.

Comparison of EGFR and FGFR signaling pathways that are summarized in the STKE Connection Maps (9, 10) shows that, for the most part, a similar repertoire of signaling proteins are recruited and activated by the two receptors. Yet, the regulation of the signaling pathways by FGFR is less direct, involving additional layers of control. In the case of EGFR, tyrosine autophosphorylation sites on the receptor function as the main platform for recruitment of signaling components that are activated by EGF signaling (2, 11). In addition, some signaling pathways are activated by accessory proteins that are tyrosine phosphorylated by EGFR (Fig. 1). In contrast, a docking protein (FRS2) that is tyrosine phosphorylated by FGFR (12) recruits the lion's share of the signaling components that are activated by FGF stimulation, and only a few signaling pathways are activated by direct interactions with the FGFR (Fig. 1).

Tyrosine autophosphorylation sites located in the C terminus of EGFR (13) function as binding sites for the adaptor proteins Grb2, Nck, and Shc; for phospholipase C γ (PLC- γ); and for the transcription factor, STAT1 (9). Grb2 molecules are recruited by EGFR directly and indirectly through tyrosine-phosphorylated Shc, leading to the activation of the Ras-mitogen-activated protein kinase (MAPK) cascade (9, 14). Recruitment to the membrane and tyrosine phosphorylation enhance the enzymatic activity of PLC- γ , leading to the formation of two second messengers, diacylglycerol (DAG) and inositol 1,4,5-trisphosphate (IP $_3$). IP $_3$ releases Ca $^{2+}$ from internal stores, which in turn acts in concert with DAG to translocate protein kinase C (PKC) to the cell membrane and stimulate its enzymatic activity (9). PKC then phosphorylates and regulates the activity of many proteins, including EGFR; phosphorylation of a threonine residue (Thr 654) in the juxtamembrane domain modulates EGF binding affinity and kinase activity of the EGFR (15). Nck may link the EGFR with the actin cytoskeleton (9), and tyrosine phosphorylation of STAT1 leads to transcription of genes that regulate cell cycle arrest (9). In addition, EGF stimulates a cell survival pathway mediated by phosphoinositide 3-kinase (PI3K) and the protein kinase Akt (16) by an indirect mechanism in which tyrosine phosphorylation of the docking protein Gab1 or ErbB3 by EGFR leads to recruitment and activation of PI3K.

Department of Pharmacology, Yale University School of Medicine, New Haven, CT 06520, USA.

*To whom correspondence should be addressed.
E-mail: joseph.schlessinger@yale.edu

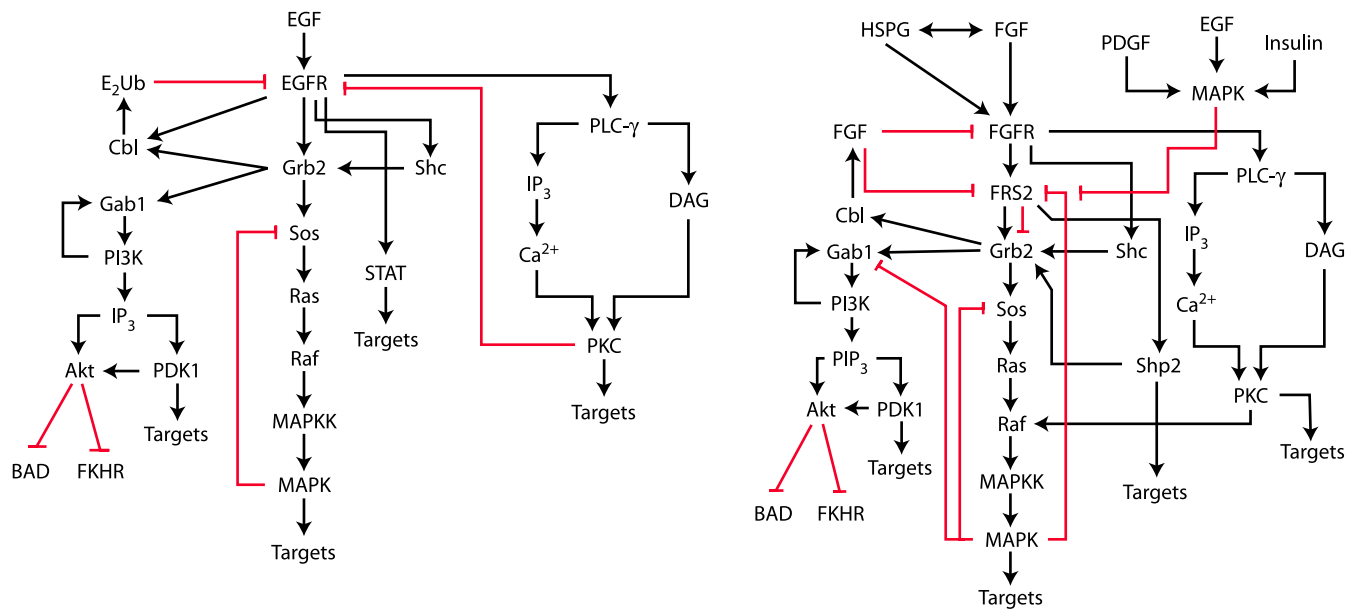


Fig. 1. Cell signaling by EGF or FGF receptors. An abbreviated version of signaling by EGFR (left) and FGFR (right). Detailed description is presented in STKE Connections Maps (9, 10). Stimulatory and inhibitory stimuli are depicted in black and red, respectively. Abbreviations: HSPG,

heparan sulfate proteoglycan; E₂Ub, ubiquitin-conjugating enzyme; IP₃, inositol 1,4,5-triphosphate; PIP₃, phosphatidylinositol 3,4,5-trisphosphate. Additional abbreviations are in the text and in the Connections Maps (9, 10).

Although the signaling pathways activated by FGFRs substantially overlap with those activated by EGFRs, the pathways are activated through the formation of a multi-docking protein complex induced by tyrosine phosphorylation. Tyrosine phosphorylation of FRS2 leads to recruitment of four Grb2 molecules directly and two Grb2 molecules indirectly through tyrosine phosphorylation of the protein tyrosine phosphatase Shp2 in complex with FRS2. Grb2 molecules bound to FRS2 recruit the nucleotide exchange factor SOS, leading to the activation of the Ras-MAPK signaling cascade. In addition, Grb2 recruits the docking protein Gab1, which is tyrosine phosphorylated by FGFR, leading to recruitment and activation of the PI3K-Akt cell survival pathway (16, 17).

Differences in the mechanisms of negative regulation between FGFR and EGFR are also apparent, despite involving similar regulatory elements. The ubiquitin ligase Cbl interacts with EGFR directly and indirectly through Grb2, promoting ubiquitination and degradation of EGFR (18). Grb2, bound to Cbl, does not interact directly with FGFR but, rather, binds to tyrosine-phosphorylated FRS2, promoting ubiquitination and degradation of FRS2 and FGFR (19). FRS2 is also the site of an additional negative-feedback

loop from MAPK, which is absent in the EGFR pathway. The binding of tyrosine-phosphorylated Sprouty to the SH2 domain of Grb2 sequesters Grb2 and prevents its binding to the activated EGFR or FRS2, causing attenuation of the Ras-MAPK cascade in EGF and FGF signaling (18, 20). However, it was proposed that Sprouty may play a bimodal negative and positive role in regulation of signaling through EGF and other RTKs (20).

Although both EGFR and FGFR stimulate a similar repertoire of canonical intracellular signaling pathways, signaling by FGFR is more complex and subject to additional control mechanisms. The less stringent control of EGFR activity may explain why overexpression of EGFR and ErbB2 occurs frequently in different cancers (3). If signaling pathways are viewed as components of intracellular networks, the specificity generated by an intracellular network may be affected by layers of control that may influence signal duration, signal amplitude, and spatial localization of key regulatory elements. In addition, inhibitory signals promoted by cross talk between RTKs (21); by protein phosphatases, receptor endocytosis, and degradation; and by other negative-feedback mechanisms may also

affect signal specificity and biological outcome (22).

References and Notes

- G. Manning *et al.*, *Science* **298**, 1912 (2002).
- J. Schlessinger, *Cell* **103**, 211 (2000).
- P. Blume-Jensen, T. Hunter, *Nature* **411**, 355 (2001).
- R. N. Jorissen *et al.*, *Exp. Cell Res.* **284**, 31 (2003).
- M. C. Naski, D. M. Ornitz, *Front. Biosci.* **3**, D781 (1998).
- T. Miki *et al.*, *Proc. Natl. Acad. Sci. U.S.A.* **89**, 246 (1992).
- J. Schlessinger, *Science* **300**, 750 (2003).
- D. M. Ornitz *et al.*, *Mol. Cell. Biol.* **12**, 240 (1992).
- J. Schlessinger, Epidermal Growth Factor Receptor Pathway. *Sci. STKE* (Connections Map, as seen November 2004), http://stke.sciencemag.org/cgi/cm/stkecm;CMP_14987.
- J. Schlessinger, Fibroblast Growth Factor Receptor Pathway. *Sci. STKE* (Connections Map, as seen November 2004), http://stke.sciencemag.org/cgi/cm/stkecm;CMP_15049.
- T. Pawson, P. Nash, *Science* **300**, 445 (2003).
- Y. R. Hadari *et al.*, *Proc. Natl. Acad. Sci. U.S.A.* **98**, 8578 (2001).
- J. Schlessinger, A. Ullrich, *Neuron* **9**, 383 (1992).
- G. L. Johnson, R. Lapadat, *Science* **298**, 1911 (2002).
- C. Cochet *et al.*, *J. Biol. Chem.* **259**, 2553 (1984).
- L. C. Cantley, *Science* **296**, 1655 (2002).
- B. Lamothe *et al.*, *Mol. Cell. Biol.* **24**, 5657 (2004).
- H. Waterman *et al.*, *EMBO J.* **21**, 303 (2002).
- A. Wong *et al.*, *Proc. Natl. Acad. Sci. U.S.A.* **99**, 6684 (2002).
- H. J. Kim, D. Bar-Sagi, *Nat. Rev. Mol. Cell Biol.* **5**, 441 (2004).
- I. Lax *et al.*, *Mol. Cell* **10**, 709 (2002).
- J. D. Jordan *et al.*, *Cell* **103**, 193 (2000).
- J. Bonner-Stewart assisted in the preparation of the online STKE Pathways. J.S. is supported by NIH grant RO1-AR051448-01 and funds from the Ludwig Institute for Cancer Research.

Pheromone Signaling Mechanisms in Yeast: A Prototypical Sex Machine

Yuqi Wang and Henrik G. Dohlman*

The actions of many extracellular stimuli are elicited by complexes of cell surface receptors, heterotrimeric guanine nucleotide-binding proteins (G proteins), and mitogen-activated protein (MAP) kinase complexes. Analysis of haploid yeast cells and their response to peptide mating pheromones has produced important advances in our understanding of G protein and MAP kinase signaling mechanisms. Many of the components, their interrelationships, and their regulators were first identified in yeast. Current analysis of the pheromone response pathway (see the Connections Maps at *Science's* Signal Transduction Knowledge Environment) will benefit from new and powerful genomic, proteomic, and computational approaches that will likely reveal additional general principles that are applicable to more complex organisms.

All cells have the capacity to sense and discriminate among various environmental stimuli and to then generate an appropriate intracellular response. One common mechanism for detecting and transmitting extracellular signals uses cell surface receptors coupled to intracellular heterotrimeric guanine nucleotide-binding proteins (G proteins). Human G protein-coupled receptors (GPCRs) mediate responses to light, odor, taste, hormones, and neurotransmitters. Prominent examples include receptors for epinephrine, histamine, and serotonin. Drugs such as β -adrenergic receptor blockers (which bind epinephrine receptors), antihistamines, and serotonin-reuptake inhibitors are among the most widely prescribed drugs. Even in the simplest eukaryotes, GPCRs regulate fundamental processes such as cell motility, development, and sexual reproduction. Clearly, a detailed understanding of G protein signaling is important for understanding human disease as well as basic cellular physiology.

The budding yeast *Saccharomyces cerevisiae* has proven indispensable in elucidating the mechanisms of G protein and mitogen-activated protein (MAP) kinase signaling (1). A combination of genetic, biochemical, and molecular biological analysis of the response of haploid yeast cells to their peptide mating pheromones has established basic principles of G protein signaling and regulation. Examples include the identification of monoubiquitination as a signal for receptor endocytosis (2, 3), definitive demonstration of a positive signaling role for G protein $\beta\gamma$ subunits (4), the first discovery of three-tiered structure of the MAP kinase module (5), development of the concept of a kinase-

scaffold protein (6), and the first demonstration that regulator of G protein signaling (RGS) proteins desensitize the G proteins (7).

The yeast pheromone response begins with GPCRs at the plasma membrane (Fig. 1). Two haploid cell types, known as MAT α and MAT α , each secrete small peptide pheromones, called α factor and α factor, respectively.

The α factor binds to a specific receptor (Ste2) on MAT α cells, whereas α factor binds to a distinct receptor (Ste3) on MAT α cells. The pheromone receptors activate a G protein heterotrimer consisting of an α subunit (Gpa1) and a $\beta\gamma$ subunit dimer (Ste4-Ste18). Upon activation, the G protein subunits dissociate, and the signal is then transmitted and amplified through multiple effector proteins that bind to G $\beta\gamma$. Cellular responses ultimately include changes in cytoskeletal structure that lead to polarized cell growth, induction of new gene transcription, changes in nuclear architecture, arrest of cell cycle progression in the G₁ phase, and finally cell fusion (mating) to form the α/α diploid. Polarized cell growth is required

to establish the site for cell fusion (plasmogamy). New gene transcription is required to produce, for example, proteins that mediate cell adhesion. Growth arrest is required to synchronize the cell cycles of the two mating partners. Nuclear changes are required in preparation for nuclear fusion (karyogamy) and the completion of diploid zygote formation.

A major target of the G $\beta\gamma$ -transmitted signal is a MAP kinase cascade. In this route, a MAP kinase kinase kinase (Ste11) phosphorylates and activates a MAP kinase kinase (Ste7). Ste7 phosphorylates and activates two MAP kinases, Kss1 and Fus3. Genetic analysis indicates that Fus3 acts primarily in the mating pathway leading to haploid cell fusion, whereas Kss1 acts primarily in the invasive or "pseudohyphal" growth pathway

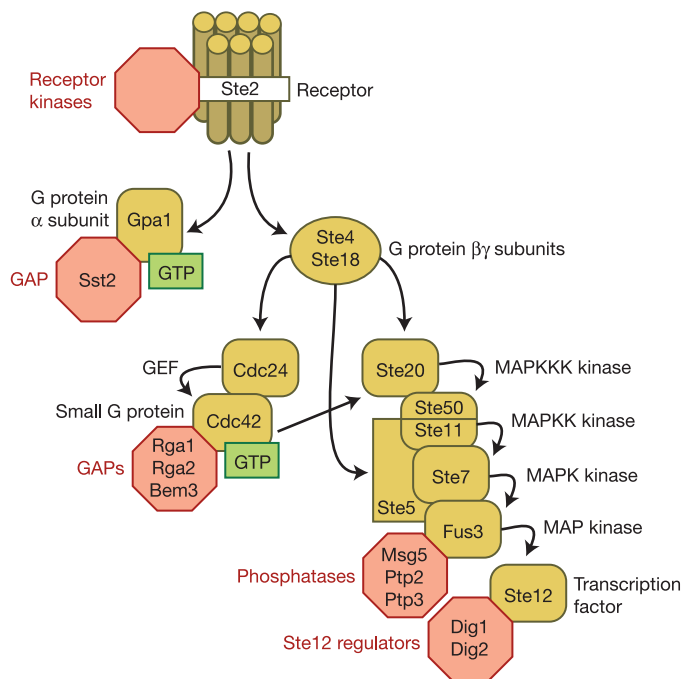


Fig. 1. Components of the pheromone response pathway in yeast. Pheromone (α factor in this case) binds to a cell surface receptor (Ste2) that in turn promotes GTP binding to the G protein α subunit (Gpa1). GTP triggers dissociation of α from the G protein $\beta\gamma$ subunits (Ste4 and Ste18). Free $\beta\gamma$ activates a downstream signaling cascade through the guanine nucleotide exchange factor Cdc24, the protein kinase Ste20, and the kinase scaffold protein Ste5. The MAP kinase Fus3 phosphorylates and activates the transcription factor Ste12, resulting in new gene transcription. Additional components modulate signaling, including receptor kinases, GTPase-accelerating proteins (GAPs) (Sst2, Rga1, Rga2, and Bem3), MAP kinase phosphatases (Msg5, Ptp2, and Ptp3), an activator of Ste11 (Ste50), and inhibitors of Ste12 (Dig1 and Dig2). Some components are omitted for clarity.

Department of Biochemistry and Biophysics, University of North Carolina, Chapel Hill, NC 27599-7260, USA.

*To whom correspondence should be addressed. E-mail: hdohlman@med.unc.edu

in nitrogen-starved cells (8, 9). It is likely that Fus3 and Kss1 normally act separately, but either can function in the absence of the other. In haploid yeast cells, a major fraction of the proteins that make up the MAP kinase cascade (Ste11, Ste7, and Fus3) is bound to a scaffold protein called Ste5. Upon activation, G β can bind to Ste5, where it evidently induces a conformational change in the protein (10). In this context, the Ste5-Ste11-Ste7-Fus3 assembly can be regarded as an effector complex. This scaffolded arrangement presumably allows for more efficient signaling and possibly protects against inappropriate cross talk with the other MAP kinases in yeast.

Another G β effector critical for mating is Cdc24, a guanine nucleotide exchange factor for Cdc42 (11). Cdc42 is a member of the Ras superfamily of small guanosine triphosphatases (GTPases) and specifically regulates actin rearrangements that lead to polarized cell growth and morphogenesis. In yeast, Cdc42 is required for budding in dividing cells and for the formation of a projection that protrudes from the cell after pheromone-triggered cell cycle arrest. This mating projection is where many signaling proteins are concentrated and where cell fusion begins. Cdc42 may also regulate transcription and cell division through its binding to the p21-activated protein kinase Ste20 (12).

Analysis of the yeast mating pathway has provided insights into signal desensitization. A property of signal-response systems in general, and of G protein-coupled receptors in particular, is that prolonged stimulation leads to an attenuated response. At a cellular and molecular level, desensitization typically results from feedback inhibition events that serve to dampen further signaling. Receptors are well known as targets of desensitization, but the first insight that G proteins are also subject to desensitization occurred through analysis of *SST2* (super-sensitive to pheromone) mutations in yeast

(7). Genetic disruption of *SST2* allows cells to respond to doses of pheromone that are roughly two orders of magnitude lower than those detected by normal cells. *SST2* mutants also prevent recovery from pheromone-induced growth arrest, even if the ligand is removed. Homologs of *Sst2* exist in higher eukaryotes and were renamed RGS proteins and shown to accelerate G protein GTPase activity, thus leading to subunit reassociation (1).

Yeast will surely continue to be an attractive and appropriate model for the study of G protein and MAP kinase signaling. The yeast pheromone signaling pathway is structurally and functionally similar to hormone and neurotransmitter signaling pathways in mammals; the G protein and kinase components in particular share extensive sequence similarity with their mammalian counterparts. Yeast is unequaled as a tool for genetic analysis. Its ability to grow stably as a haploid is useful for studying gene mutations that are recessive. Homologous recombination in yeast is useful for studying the physiological function of proteins, through gene replacement and gene disruption. Indeed, yeast is the only system in which nearly every open reading frame has been deleted (13), organized into microarrays (14), fused to fluorescent marker proteins (15), affinity-tagged (16), and purified (17). Consequently it is now possible to study gene function, gene transcription, protein localization, and intermolecular associations in a systematic manner and on a genome-wide scale.

Although our understanding of pheromone signaling is very sophisticated, substantial challenges remain. Little is known about how genes that are essential for viability contribute to pheromone responses. Pathway components probably undergo multiple posttranslational modifications, and technologies to identify the chemical nature and location of those modifications remain nascent. Perhaps the most

challenging of all will be the establishment of accurate and quantitative models of the pheromone-response pathway (18). A complete understanding of any cellular process requires models that accurately predict behavior in response to cellular perturbations. Achieving this goal will require a full accounting of every signaling component and every enzymatic reaction, both in cellular space and over time. Newly available genomics and proteomics tools, such as the yeast pheromone response pathway Connections Map at *Science's* Signal Transduction Knowledge Environment (STKE) (19), will facilitate these efforts, but they will also require new and coordinated efforts by biologists, chemists, mathematicians, and computer scientists.

References and Notes

- H. G. Dohlman, J. W. Thorner, *Annu. Rev. Biochem.* **70**, 703 (2001).
- L. Hicke, H. Riezman, *Cell* **84**, 277 (1996).
- A. F. Roth, N. G. Davis, *J. Cell Biol.* **134**, 661 (1996).
- M. Whiteway *et al.*, *Cell* **56**, 467 (1989).
- Z. Zhou, A. Gartner, R. Cade, G. Ammerer, B. Errede, *Mol. Cell Biol.* **13**, 2069 (1993).
- K. Y. Choi, B. Satterberg, D. M. Lyons, E. A. Elion, *Cell* **78**, 499 (1994).
- H. G. Dohlman, D. Apaniesk, Y. Chen, J. Song, D. Nusskern, *Mol. Cell Biol.* **15**, 3635 (1995).
- J. Zeitlinger *et al.*, *Cell* **113**, 395 (2003).
- D. M. Truckses, L. S. Garrenton, J. Thorner, *Science* **306**, 1509 (2004).
- C. Sette, C. J. Inouye, S. L. Stroschein, P. J. Iaquina, J. Thorner, *Mol. Cell Biol.* **11**, 4033 (2000).
- Z. S. Zhao, T. Leung, E. Manser, L. Lim, *Mol. Cell Biol.* **15**, 5246 (1995).
- L. Leberer, D. Dignard, D. Harcus, D. Y. Thomas, M. Whiteway, *EMBO J.* **11**, 4815 (1992).
- E. A. Winzeler *et al.*, *Science* **285**, 901 (1999).
- G. Giaever *et al.*, *Nature* **418**, 387 (2002).
- W. K. Huh *et al.*, *Nature* **425**, 686 (2003).
- S. Ghaemmaghami *et al.*, *Nature* **425**, 737 (2003).
- E. Phizicky, P. I. Bastiaens, H. Zhu, M. Snyder, S. Fields, *Nature* **422**, 208 (2003).
- D. Endy, R. Brent, *Nature* **409**, 391 (2001).
- H. G. Dohlman, Pheromone Signaling Pathways in Yeast. *Sci. STKE* (Connections Map, as seen November 2004), http://stke.sciencemag.org/cgi/cm/stkecm;CMP_13999.

VIEWPOINT

Jekyll and Hyde in the Microbial World

Dagmar M. Truckses, Lindsay S. Garrenton, Jeremy Thorner*

Fungi are nonmotile organisms that obtain carbon from compounds in their immediate surroundings. Confronted with nutrient limitation, the yeast *Saccharomyces cerevisiae* undergoes a dimorphic transition, switching from spherical cells to filaments of adherent, elongated cells that can invade the substratum. A complex web of sensing mechanisms and cooperation among signaling networks (including a mitogen-activated protein kinase cascade, cyclic adenosine monophosphate-dependent protein kinase, and 5'-adenosine monophosphate-activated protein kinase) elicits the appropriate changes in physiology, cell cycle progression, cell polarity, and gene expression to achieve this differentiation. Highly related signaling processes control filamentation and virulence of many human fungal pathogens.

For both the layperson and the molecular biologist, the most familiar fungal cell is baker's yeast (*S. cerevisiae*). This budding

yeast has become a valuable model for examining the eukaryotic way of life at the molecular level. Although relatively benign,

S. cerevisiae has shed light on fundamental mechanisms in fungal pathogenesis because it adopts two distinct morphologies: a spherical or ovoid (yeastlike) form, which proliferates by budding, and a filamentous form. For fungal pathogens, such as *Candida albicans*, the ability to undergo this dimorphic transition is strongly correlated

Division of Biochemistry and Molecular Biology, Department of Molecular and Cell Biology, University of California, Berkeley, CA 94720-3202, USA.

*To whom correspondence should be addressed. E-mail: jeremy@socrates.berkeley.edu

with invasion of host tissue and virulence (1, 2).

On rich medium, *S. cerevisiae* proliferates as separate spherical cells. However, in response to nitrogen limitation (3), the cells become thin and oblong, and after a daughter buds, it remains adherent and connected end-to-end with its mother, resembling a link in a sausage string (Fig. 1). Elucidating the signaling pathways necessary to elicit such filamentous growth has led to insights about how cells respond to different stimuli and how they share components with other signaling pathways yet evoke unique responses that are physiologically appropriate.

As our Connections Map on *Science's* Signal Transduction Knowledge Environment (4) indicates, the switch from budding to pseudohyphal growth in *S. cerevisiae* is controlled by at least three signaling modalities (5). Each input involves the action of different classes of protein kinases. The core of one pathway is a three-tiered mitogen-activated protein kinase (MAPK) cascade (6). Each kinase catalyzes the transfer of phosphate from adenosine 5'-triphosphate (ATP) to serine, threonine, or tyrosine residues in the next kinase, which provides for switchlike amplification of signal propagation. The MAPK cascade operates in concert with a second input that acts by means of cyclic adenosine monophosphate (cAMP)-dependent protein kinase (PKA) (7), best studied in yeast for its role in glucose metabolism in vegetatively growing cells. When the supply of glucose is exhausted, a third input that acts through 5'-AMP-activated protein kinase (AMPK) ensures continued robust filamentous growth on fermentation end products and other nonglucose carbon sources (8, 9). AMPK (Snf1) may act upstream of or in conjunction with the action of the atypical protein kinases, Tor1 and Tor2 (10, 11).

The MAPK module is stimulated by two small guanosine triphosphatases (GTPases) anchored at the plasma membrane, Ras2 and Cdc42. How nutrient limitation promotes conversion of Ras2 and Cdc42 to their active (GTP-bound) state is not understood; however, Cdc42 acts downstream of Ras2. One role of Cdc42 is to activate a p21-activated protein kinase (PAK), Ste20. Ste20 then phosphorylates and activates the first kinase (Ste11) in the MAPK cascade, which in turn phosphorylates the next kinase (Ste7). These gene products are designated *ste* (for sterile), because they were first identified as required for the signaling that induces haploid yeast cells to mate. Once activated by Ste7, the MAPK (Kss1) phosphorylates two transcriptional repressors, Dig1 and Dig2, in the nucleus, which derepresses the transcription

factor, Ste12 (12). Ste12 is targeted to the promoters of genes required for filamentous growth in a complex with a second transcription factor, Tec1 (13).

How does the signal get transmitted from the plasma membrane to the nucleus? Membrane-bound, activated Cdc42 binds to a specific sequence [Cdc42/Rac interactive binding (CRIB) motif] in the initiating kinase Ste20. Membrane association of Ste20 is enhanced by a scaffold protein, Bem1, that is membrane-tethered through its phosphoinositide-binding PX domain and interacts with Pro-rich motifs in Ste20 through tandem SH3 domains. The encounter of activated Ste20 with its substrate, the kinase Ste11, is ensured, given that Cdc42 also binds to Ste50, an adaptor protein that is tightly bound to Ste11. Also, Ste11 associates with a membrane-localized osmosensor, Sho1, and with a MAPK kinase (Pbs2) that is itself bound to Sho1 (14). Conse-

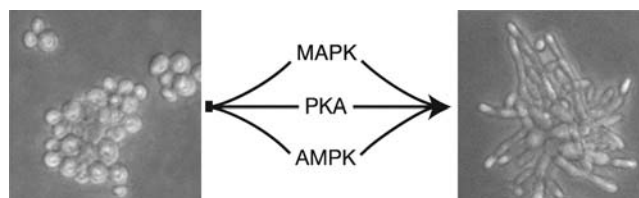


Fig. 1. The switch from budding (left) to pseudohyphal growth (right) in *S. cerevisiae* is controlled by at least three signaling inputs: Kss1, a MAPK; Tpk2, a PKA catalytic subunit isoform; and Snf1, a yeast ortholog of AMPK.

quently, Ste11 gets phosphorylated and activated when Ste20 has been activated. Presumably, dissociation of Ste11 from the membrane permits it to encounter its target in the cytosol, the kinase Ste7. Ste7 forms tight complexes with Kss1, the third kinase in the MAPK cascade, through a MAPK-docking motif at the N terminus of Ste7 (15).

Kss1 also gets phosphorylated and activated, albeit only transiently, when a yeast cell responds to the peptide pheromone that induces mating (16). Yet, pheromone stimulation does not lead to a filamentous growth response. Pathway specificity is maintained, in part, because pheromone response channels the Ste11- and Ste7-dependent signals to a different MAPK, Fus3. Also, activated Fus3 phosphorylates Tec1 at a specific site (which is not a target of Kss1), marking Tec1 for ubiquitin-mediated degradation. The absence of Tec1 prevents expression of the bank of genes necessary for filamentous growth. Embarking on one course of action by the cell limits the other options open to it in a simple and straightforward fashion, which has enormous ramifications for understanding what developmental biologists call “commitment” to a particular cell fate during differentiation in multicellular organisms.

In addition to triggering the MAPK cascade, activated Ras2 stimulates adenylate cyclase (Cyr1), an integral membrane enzyme that converts ATP to cAMP (17), thus increasing the intracellular cAMP concentration. Binding of cAMP to the regulatory subunit (Bcy1) of PKA releases the three catalytic subunit isoforms (Tpk1, Tpk2, and Tpk3) from inhibition, thereby enhancing their activity and perhaps affecting their relative concentrations in the nucleus. Despite their similarity (67 to 76% identity), only Tpk2 is required to fully activate the filamentous growth response, whereas Tpk3 (but not Tpk1) has an inhibitory role. Tpk2 phosphorylates the transcription regulators, Flo8 and Sfl1. Sfl1 antagonizes Flo8-promoted expression of *FLO11*, which encodes the flocculin required for the cell-cell and cell-substratum adhesion necessary for filamentation. Phosphorylation by Tpk2 promotes Flo8 binding to and activation of the *FLO11* promoter and, at the same time, relieves Sfl1-mediated repression by prohibiting its dimerization and DNA binding. Likewise, AMPK (Snf1) promotes sustained *FLO11* expression by blocking two other repressors (Nrg1 and Nrg2).

Diploid yeast initiate filamentous growth when deprived of nitrogen. Haploid yeast undergo a similar dimorphic switch (dubbed “invasive growth”) but only when glucose is limiting. In either instance, the MAPK cascade and PKA are involved. How do yeast sense a decrease in the nitrogen or glucose supply? An ammonium permease (Mep2) (18) has been implicated in the former process, but whether its function is coupled to Ras2 activation is unclear. Nitrogen limitation causes increased expression of the *GPR1* gene, which encodes a heterotrimeric GTP-binding protein (G protein)-coupled receptor that associates with a G protein α subunit, Gpa2 (19). The ligands for Gpr1 include glucose itself (20). Activated Gpa2 stimulates adenylate cyclase and promotes filamentous growth through PKA but does not need Ras2 to do so. Just as mammalian adenylate cyclase is activated directly by $G_{\alpha s}$, Gpa2 may stimulate the cyclase Cyr1. Apparent $G\beta$ subunits for Gpa2 (Gpb1/Krh2 and Gpb2/Krh1) and a candidate $G\gamma$ subunit (Gpg1) have been found. These proteins act as negative regulators of PKA signaling, possibly by sequestration of Gpa2, but action on other targets has not been ruled out.

Two integral membrane proteins, Sho1 and Msb2 (perhaps in a complex), are necessary for Kss1 (MAPK) activation under conditions that promote filamentous growth, and Msb2 interacts directly with activated (GTP-bound) Cdc42 (21). Both Sho1 and Msb2 also provide stimulatory inputs in

response to hyperosmotic stress. These new insights do not yet reveal what is sensed by Sho1 and Msb2, nor how Ras2 and Cdc42 become activated, to evoke filamentous growth. Interestingly, Msb2 strongly resembles a class of mammalian membrane-anchored glycoproteins, called mucins, implicated in metazoan cell signaling (22). Clearly, more will be learned about environmental and nutrient sensing, integration of signaling pathways, and signaling specificity in complex networks by continued study of the filamentous growth process in yeast.

References and Notes

1. C. Sanchez-Martinez, J. Perez-Martin, *Curr. Opin. Microbiol.* **4**, 214 (2001).

2. P. Sudbery, N. Gow, J. Berman, *Trends Microbiol.* **12**, 317 (2004).
3. C. J. Gimeno, P. O. Ljungdahl, C. A. Styles, G. R. Fink, *Cell* **68**, 1077 (1992).
4. D. M. Truckses, L. S. Garrenton, J. Thorner, *Filamentous Growth Pathway in Yeast. Sci. STKE* (Connections Map, as seen November 2004), http://stke.sciencemag.org/cgi/cm/stkecm;CMP_14554.
5. M. Gagliano, F. F. Bauer, I. S. Pretorius, *FEMS Yeast Res.* **2**, 433 (2002).
6. H. U. Mösch, *Contrib. Microbiol.* **5**, 185 (2000).
7. C. A. D'Souza, J. Heitman, *FEMS Microbiol. Rev.* **25**, 349 (2001).
8. S. P. Palecek, A. S. Parikh, S. J. Kron, *Microbiology* **148**, 893 (2002).
9. S. Kuchin, V. K. Vyas, M. Carlson, *Biochem. Soc. Trans.* **31**, 175 (2003).
10. P. Bertram *et al.*, *Mol. Cell. Biol.* **22**, 1246 (2002).
11. J. R. Rohde, M. E. Cardenas, *Curr. Top. Microbiol. Immunol.* **279**, 53 (2004).
12. J. G. Cook, L. Bardwell, S. J. Kron, J. Thorner, *Genes Dev.* **10**, 2831 (1996).

13. H. D. Madhani, G. R. Fink, *Science* **275**, 1314 (1997).
14. A. Zarrinpar, R. P. Bhattacharyya, M. P. Nittler, W. A. Lim, *Mol. Cell* **14**, 825 (2004).
15. L. Bardwell, J. Thorner, *Trends Biochem. Sci.* **21**, 373 (1996).
16. Y. Wang, H. G. Dohlman, *Science* **306**, 1508 (2004).
17. J. M. Gancedo, *FEMS Microbiol. Rev.* **25**, 107 (2001).
18. B. Magasanik, *Eukaryot. Cell* **2**, 827 (2003).
19. Y. Xue, M. Batlle, J. P. Hirsch, *EMBO J.* **17**, 1996 (1998).
20. K. Lemaire, S. Van de Velde, P. Van Dijk, J. M. Thevelein, *Mol. Cell* **16**, 293 (2004).
21. P. J. Cullen *et al.*, *Genes Dev.* **18**, 1695 (2004).
22. K. L. Carraway, V. P. Ramsauer, B. Haq, C. A. Carothers Carraway, *Bioessays* **25**, 66 (2003).
23. Research in the Thorner laboratory on this subject is supported by the NIH (GM-21841 and CA-09041). We thank J. Heitman, G. Sprague, S. Kron, and members of the Thorner laboratory for helpful comments.

VIEWPOINT

When the Stress of Your Environment Makes You Go HOG Wild

Patrick J. Westfall, Daniel R. Ballon, Jeremy Thorner*

When exposed to increased dissolved solute in their environment (hyperosmotic stress), all eukaryotic cells respond by rapidly activating a conserved mitogen-activated protein kinase cascade, known in budding yeast *Saccharomyces cerevisiae* as the high osmolarity glycerol (HOG) pathway. Intensive genetic and biochemical analysis in this organism has revealed the presumptive osmosensors, downstream signaling components, and metabolic and transcriptional changes that allow cells to cope with this stressful condition. These findings have had direct application to understanding stress sensing and control of transcription by stress-activated mitogen-activated protein kinases in mammalian cells.

Cells must constantly adapt their physiology to respond to changing environmental conditions and stimuli. These adjustments are frequently achieved by signal transduction pathways that result in the activation of protein kinases of the conserved mitogen-activated protein kinase (MAPK) family (1). After initial response and propagation of the signal and once cells are adapted to the altered condition, the signaling machinery is deactivated. One environmental stress is exposure to a milieu containing a dissolved solute concentration that is sufficiently high to compromise cell turgor pressure (2). To adapt to hyperosmotic conditions, cells can produce various small molecules that increase the total intracellular solute concentration, thereby pro-

viding osmotic stabilization. The budding yeast *Saccharomyces cerevisiae*, for example, produces the solute, glycerol, and thus the

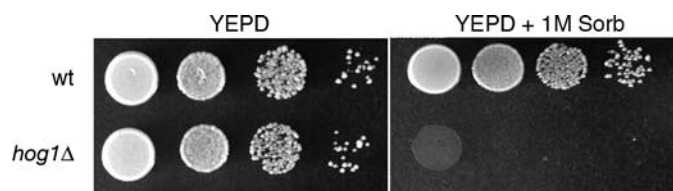


Fig. 1. The requirement for the Hog1 MAPK for cell survival under hyperosmotic conditions is illustrated by plating serial 10-fold dilutions of wild-type (wt) cells and an otherwise isogenic derivative lacking the *HOG1* gene (*hog1Δ*) on normal rich medium (YEPD) or on the same medium containing 1 M sorbitol, as indicated.

Division of Biochemistry and Molecular Biology, Department of Molecular and Cell Biology, University of California, Berkeley, CA 94720-3202, USA.

*To whom correspondence should be addressed. E-mail: jeremy@socrates.berkeley.edu

signal transduction network necessary to achieve this end is called the high osmolarity glycerol (HOG) pathway. It includes a MAPK cascade that leads to phosphorylation and activation of the MAPK, Hog1 (its mammalian homolog is the stress-activated MAPK, p38) (3) (Fig. 1). Response to hyperosmotic stress has revealed multiple levels of complex regulation.

HOG Signaling

As our STKE Connections Map (4) indicates, there are two discrete branches of the HOG pathway that can lead to the phosphorylation and activation of the MAPK kinase (MAPKK) Pbs2 and its cognate MAPK, Hog1 (5). In the first branch, two plasma membrane proteins provide the input. Sho1 (an integral membrane protein with four transmembrane segments) may be a turgor and heat sensor (6), and Msb2 (a mucin-like protein with a single transmembrane segment) may serve as a gauge of plasma membrane-cell wall connectivity (7). Sho1 and Msb2 physically interact. Maximal stimulation through this branch in response to hyperosmotic conditions requires both Sho1 and Msb2 and leads to activation of the membrane-associated Rho family guanine triphosphatase (GTPase) Cdc42 through GTP binding. Cdc42, in turn, binds to and stimulates the protein kinase, Ste20 (8). How Sho1 and Msb2 stimulate production of GTP-bound Cdc42 is not known, but the C-terminal cytosolic tail of Msb2 itself binds activated Cdc42 (7). Cdc42 is tethered to the plasma membrane by a C-terminal geranylgeranyl substituent. Thus, GTP-bound Cdc42 also recruits Ste20 to the plasma membrane. The target of Ste20 is the MAPK kinase kinase (MAPKKK), Ste11. Ste11 is positioned at the plasma membrane by direct association with the cytosolic tail of Sho1 (9); by direct association with the

MAPKK Pbs2, which is itself anchored to Sho1 (10); and, lastly, through interaction with Cdc42 mediated by the adaptor protein Ste50. Once activated, Ste11 phosphorylates and activates the MAPKK Pbs2. This mechanism results in Hog1 activation in response to strongly hyperosmotic conditions (for example, 0.5 to 1.0 M NaCl). The activation pathway for mammalian p38 resembles this Sho1- and Msb2-dependent branch (11).

The second branch leading to phosphorylation and activation of Pbs2 occurs upon less severe hyperosmotic shifts (for example, 0.125 to 0.25 M NaCl) and involves another transmembrane protein, Sln1, which serves as an osmosensor. Sln1 has protein-histidine kinase activity and is situated at the head of a phospho-relay cascade (Sln1 → Ypd1 → Ssk1) akin to the so-called two-component signaling systems first described in prokaryotic cells (12). Under isoosmotic conditions, Sln1 is autophosphorylated and transfers the phosphate group to an intermediate protein, Ypd1, which in turn transfers the phosphate group to an aspartate residue on the response regulator protein, Ssk1 (13). Ssk1 binding to the MAPKKs Ssk2 and Ssk22 is required for their function. However, only the unphosphorylated form of Ssk1 binds to and activates Ssk2 and Ssk22 (14). Hence, Sln1-dependent phosphotransfer to Ssk1 blocks activation of Ssk2 and Ssk22. Under osmotic stress, Sln1 no longer undergoes autophosphorylation, phosphate is not transferred to Ssk1, and Ssk2 and Ssk22 are stimulated. Although Ssk2 and Ssk22 seem redundant for their ability to initiate HOG signaling by phosphorylating Pbs2, Ssk2 has an additional role in the recovery of the actin cytoskeleton after osmotic shock. All three MAPKKs (Ste11, Ssk2, and Ssk22) phosphorylate Pbs2, and activated Pbs2 phosphorylates Hog1 on both a Thr and a Tyr residue.

Dual phosphorylation of Hog1 occurs within minutes of exposing cells to hyperosmotic conditions. Initial exposure to high salt causes nonspecific dissociation of many proteins from chromatin. Activated Hog1 first provides short-term protection for the transcriptional capacity of the cell by phosphorylating both a Na⁺-H⁺ antiporter (Nha1) and a potassium channel (Tok1) in the plasma membrane, thereby stimulating Na⁺ efflux (15). Hog1-stimulated Na⁺ ejection allows proteins to reassociate with DNA. Hog1 action also affects translation and cell cycle progression. In addition, phosphorylation of Hog1 promotes its nuclear import, apparently mediated by the karyopherin Nmd5 (16). Once inside the nucleus, activated Hog1 leads to increased expression of ~600 genes (17).

Nuclear Hog1 interacts with various transcriptional activators and repressors. A transcriptional repressor complex (Sko1/Tup1/Ssn6) is bound to the promoters of many of the genes that undergo increased transcription in response to hyperosmotic stress. Activated Hog1 binds to and phosphorylates Sko1, modifying its association with Tup1-Ssn6 and allowing recruitment of the SAGA and Swi/Snf chromatin-modifying and remodeling complexes, thereby inducing gene expression (18). Under conditions of severe salt stress (1 M NaCl), Sko1 gets exported from the nucleus; curiously this translocation is not Hog1-dependent but depends instead on the action of cyclic adenosine monophosphate-dependent protein kinase. Various stressful conditions, including hyperosmotic stress, induce the expression of genes controlled by two highly related, zinc finger-containing transcriptional activators, Msn2 and Msn4. Nuclear Hog1 binds to Msn2-Msn4 at the promoters of certain stress-responsive genes, which in turn recruits another transcriptional activator, Hot1, to the same complexes. At other loci, like the promoter of the *GPD1* gene, Hot1 is bound constitutively and independently of Msn2-Msn4 interactions. In this case, nuclear Hog1 binds to and phosphorylates Hot1, promotes recruitment of yet another transcriptional activator, Msn1, and associates with components of the general transcription machinery. All of these actions are necessary for optimal transcription of this gene (19). *GPD1* encodes the glycerol 3-phosphate dehydrogenase essential for glycerol production, which converts triose phosphate (namely, dihydroxyacetone phosphate) and NADH to glycerol-3-phosphate and nicotinamide adenine dinucleotide (NAD⁺). Lastly, there is evidence that Hog1 also promotes expression of the genes under its control by recruiting the Rpd3-Sin3 histone deacetylase complex and thereby remodeling in some unique way the chromatin structure around the promoters to which Hog1 is targeted (20).

By about 20 to 30 min after osmotic shock, concomitant with onset of glycerol production and restoration of osmotic balance, Hog1 is dephosphorylated and exported from the nucleus via the karyopherin, Xpo1 (16). Multiple phosphoprotein phosphatases, some phospho-Tyr-specific (Ptp2 and Ptp3) and some phospho-Thr-specific (Ptc1, Ptc2, and Ptc3), maintain low basal levels of Hog1 activity and down-regulate Hog1 after its activation. The Ssk2 (and Ssk22) activator Ssk1 is degraded in a ubiquitin- and proteasome-dependent manner during the adaptation process (21). However, further increase of the external solute concentration elicits rephosphorylation and nu-

clear reentry of Hog1 with kinetics nearly identical to those seen in the initial response, suggesting that the Sho1-dependent branch may be the primary input in this situation.

Intriguing mechanistic questions remain about operation of the HOG pathway. How changes in external solute concentration are perceived by the osmosensors remains undetermined, although the fact that Sho1 is activated by heat suggests that it may undergo a conformational change. Three different MAPK modules in *S. cerevisiae*—pheromone response, filamentous growth, and one branch of the HOG pathway—all activate the same MAPKKK, Ste11. How specificity is maintained in propagation of the signals from Ste11 remains unclear. Indeed, in the absence of either Pbs2 or Hog1, osmotic stress does lead to activation of Ste7 and Fus3, the MAPKK and MAPK of the pheromone response pathway, and induction of genes normally only expressed in response to mating pheromone (22). Understanding signaling specificity of this sort may shed light on how cells adapt to chronic stress conditions and how to lessen the impact of diseases that arise from adventitious activation of one pathway by another.

References and Notes

1. M. C. Gustin, J. Albertyn, M. Alexander, K. Davenport, *Microbiol. Mol. Biol. Rev.* **62**, 1264 (1998).
2. S. Hohmann, *Microbiol. Mol. Biol. Rev.* **66**, 300 (2002).
3. J. Han, J. D. Lee, L. Bibbs, R. J. Ulevitch, *Science* **265**, 808 (1994).
4. P. J. Westfall, D. R. Ballon, J. Thorner, High Osmolarity Glycerol (HOG) Pathway in Yeast. *Sci. STKE* (Connections Map, as seen November 2004), http://stke.sciencemag.org/cgi/cm/stkecm;CMP_14620.
5. E. de Nadal, P. M. Alepuz, F. Posas, *EMBO Rep.* **3**, 735 (2002).
6. A. Winkler *et al.*, *Eukaryot. Cell* **1**, 163 (2002).
7. P. J. Cullen *et al.*, *Genes Dev.* **18**, 1695 (2004).
8. D. C. Raitt, F. Posas, H. Saito, *EMBO J.* **19**, 4623 (2000).
9. A. Zarrinpar, R. P. Bhattacharyya, M. P. Nittler, W. A. Lim, *Mol. Cell* **14**, 825 (2004).
10. T. Maeda, M. Takekawa, H. Saito, *Science* **269**, 554 (1995).
11. M. T. Uhlik *et al.*, *Nat. Cell Biol.* **5**, 1104 (2003).
12. F. Posas *et al.*, *Cell* **86**, 865 (1996).
13. J. M. Lu, R. J. Deschenes, J. S. Fassler, *Eukaryot. Cell* **2**, 1304 (2003).
14. F. Posas, H. Saito, *EMBO J.* **17**, 1385 (1998).
15. M. Proft, K. Struhl, *Cell* **118**, 351 (2004).
16. P. Ferrigno, F. Posas, D. Koepf, H. Saito, P. A. Silver, *EMBO J.* **17**, 5606 (1998).
17. S. M. O'Rourke, I. Herskowitz, *Mol. Biol. Cell* **15**, 532 (2004).
18. M. Proft, K. Struhl, *Mol. Cell* **9**, 1307 (2002).
19. P. M. Alepuz, E. de Nadal, M. Zapater, G. Ammerer, F. Posas, *EMBO J.* **22**, 2433 (2003).
20. E. De Nadal *et al.*, *Nature* **427**, 370 (2004).
21. N. Sato, H. Kawahara, A. Toh-e, T. Maeda, *Mol. Cell Biol.* **23**, 6662 (2003).
22. S. M. O'Rourke, I. Herskowitz, *Genes Dev.* **12**, 2874 (1998).
23. Research in the Thorner laboratory on this subject is supported by NIH (GM-21841 and GM-68343). We thank F. Posas, H. Saito, S. Hohmann, G. Ammerer, and members of the Thorner laboratory for helpful comments.

The Ethylene Signaling Pathway

Jose M. Alonso* and Anna N. Stepanova

Plants use a structurally very simple gas molecule, the hydrocarbon ethylene, to modulate various developmental programs and coordinate responses to a multitude of external stress factors. How this simple molecule generates such a diverse array of effects has been the subject of intense research for the past two decades. A fascinating signaling pathway, with classical as well as novel plant-specific signaling elements, is emerging from these studies. We describe the four main modules that constitute this signaling pathway: a phosphotransfer relay, an EIN2-based unit, a ubiquitin-mediated protein degradation component, and a transcriptional cascade. The canonical and *Arabidopsis* ethylene signaling pathways in the Signal Transduction Knowledge Environment Connections Maps provide a complete panoramic view of these signaling events in plants.

Several signaling molecules with hormone-like functions have been identified in plants, the simplest of all being ethylene. Despite its structural simplicity, this gaseous hormone plays a critical role in the regulation of developmental programs throughout the plant life cycle and serves as a major response mediator to various environmental signals (1–3). Seed germination, cell elongation, fertilization, fruit ripening, seed dispersal, defense against pathogens, and response to external stress factors are among the essential processes regulated by ethylene (2, 4). A combination of genetic, biochemical, and molecular approaches is uncovering this remarkable signaling pathway in plants (5). Although the initial hunt for the major elements of the ethylene pathway was performed in the model plant *Arabidopsis thaliana*, identification and functional analysis of the corresponding genes in other plant species uncovered a high degree of conservation of this signaling cascade in the plant kingdom (6). The general components of the pathway are described in (7); a more detailed view focusing on *Arabidopsis* is presented in (8).

The first prerequisite for any signaling molecule to be functional is the existence of a detection system to precisely monitor its levels. The specific recognition of ethylene by a receptor protein presents uncommon challenges because of the extreme structural simplicity of this hormone and the consequent small number of possible interaction points between the signal molecule and its receptor. In plants, this challenge is met by a family of endoplasmic reticulum (ER)-localized ethylene receptors that share sequence similarity with the bacterial two-component histidine kinases. The particular physicochemical properties of the ethylene gas allow it to freely diffuse through the membranes and the cytoplasm, eliminating the need for an active

transporter system to deliver the ligand to its receptors in the ER. The required high binding affinity and specificity of the ethylene receptors is achieved with the help of a copper cofactor associated with the hydrophobic ligand-binding pocket of the receptor molecule (9–11). Mutations in the hydrophobic domain of any of the five *Arabidopsis* receptors—ETR1, ETR2, EIN4, ERS1, and ERS2—result in dominant ethylene insensitivity of the corresponding mutant plants (12, 13). Interestingly, some of these mutations abolish ethylene binding, which suggests that in the absence of the hormone, the receptors actively repress the ethylene response (14). Conclusive evidence for the negative regulatory role of the receptors was obtained from the analysis of loss-of-function mutants (15). Lack of phenotypes in the single loss-of-function receptor mutants indicated a high degree of functional redundancy among the receptors, whereas the constitutive activation of the ethylene response in double, triple, and quadruple loss-of-function mutants confirmed the role of the receptors as repressors of this signaling pathway (15).

In contrast with the ethylene-binding domain, the histidine and receiver domains of the receptors are not conserved across the five family members. Only ETR1 and ERS1 contain a canonical histidine kinase moiety, and the receiver domain is completely absent in ERS1 and ERS2 (12). The role of these two domains in ethylene signal transduction remains controversial. Analysis of the gain- and loss-of-function mutants suggests that although all of the receptors can sense ethylene, only the histidine kinase domain of ETR1 and ERS1 can transduce the signal to the downstream components. On the other hand, the essential role of the histidine kinase is by itself questionable, because the expression of a kinase-dead version of ETR1 in the double hypomorphic mutant *etr1 ers1* is capable of restoring the normal ethylene response (16). Furthermore, ERS1 and all of the type II receptors (ERS2, ETR2, and EIN4) have recently been shown to possess a serine kinase activity

in vitro, thus suggesting an alternative, histidine kinase-independent mechanism to transduce the phosphorylation signal from the receptors to the downstream components (17). The in vivo roles of both the histidine and the serine kinase activities need to be tested in sensitive assays using new receptor mutants harboring mutations in the kinase domain.

Almost nothing is known about the role of the receiver domain in the receptor function. Along with the kinase domain, it participates in the protein-protein interaction between the receptor and yet another negative regulator of the pathway: CTR1, a Raf-like serine-threonine kinase (18). This interaction is important not only for the activation of CTR1 by the receptors, but also for its proper subcellular localization in the ER (19). Both null and kinase-dead CTR1 mutant alleles result in the constitutive activation of ethylene responses, indicating the negative regulatory role of CTR1 and suggesting that the kinase activity is important for the function of this protein in plants (20, 21). It is not yet understood how the ETR1-CTR1 complex inactivates EIN2, the positive component of the pathway that genetically works downstream of CTR1. Studies in both *Arabidopsis* and *Medicago* suggested that a mitogen-activated protein kinase (MAPK) cascade might be involved in this step of the pathway (22). Considering all of the data available to date, a mechanistic model has been proposed (Fig. 1) in which the receptors are active in the absence of ethylene and stimulate the negative regulator CTR1, which in turn shuts off the ethylene pathway. Binding of ethylene to the receptors relieves this CTR1-mediated blockage by rendering the receptors (and hence CTR1) inactive (15). Awaiting final confirmation is the possibility that CTR1 regulates the activity of EIN2 by inactivating a MAPK cascade comprising SIMKK and MPK6.

The complete ethylene insensitivity of loss-of-function *ein2* mutants indicates the critical role this protein plays in the ethylene response. Despite the sequence similarity of EIN2 to the NRAMP family of metal ion transporters, no biochemical function has been assigned to EIN2 (23). The ability of high levels of the EIN2 C terminus to constitutively activate the ethylene response suggests that this unique domain of the protein participates in the transduction of the signal to the downstream components, whereas the NRAMP-like domain may sense the upstream signals (23). The mechanism by which the ethylene signal is transduced from CTR1 to EIN2, and the

Department of Genetics, North Carolina State University, Raleigh, NC 27695, USA.

*To whom correspondence should be addressed. E-mail: jmalonso@unity.ncsu.edu

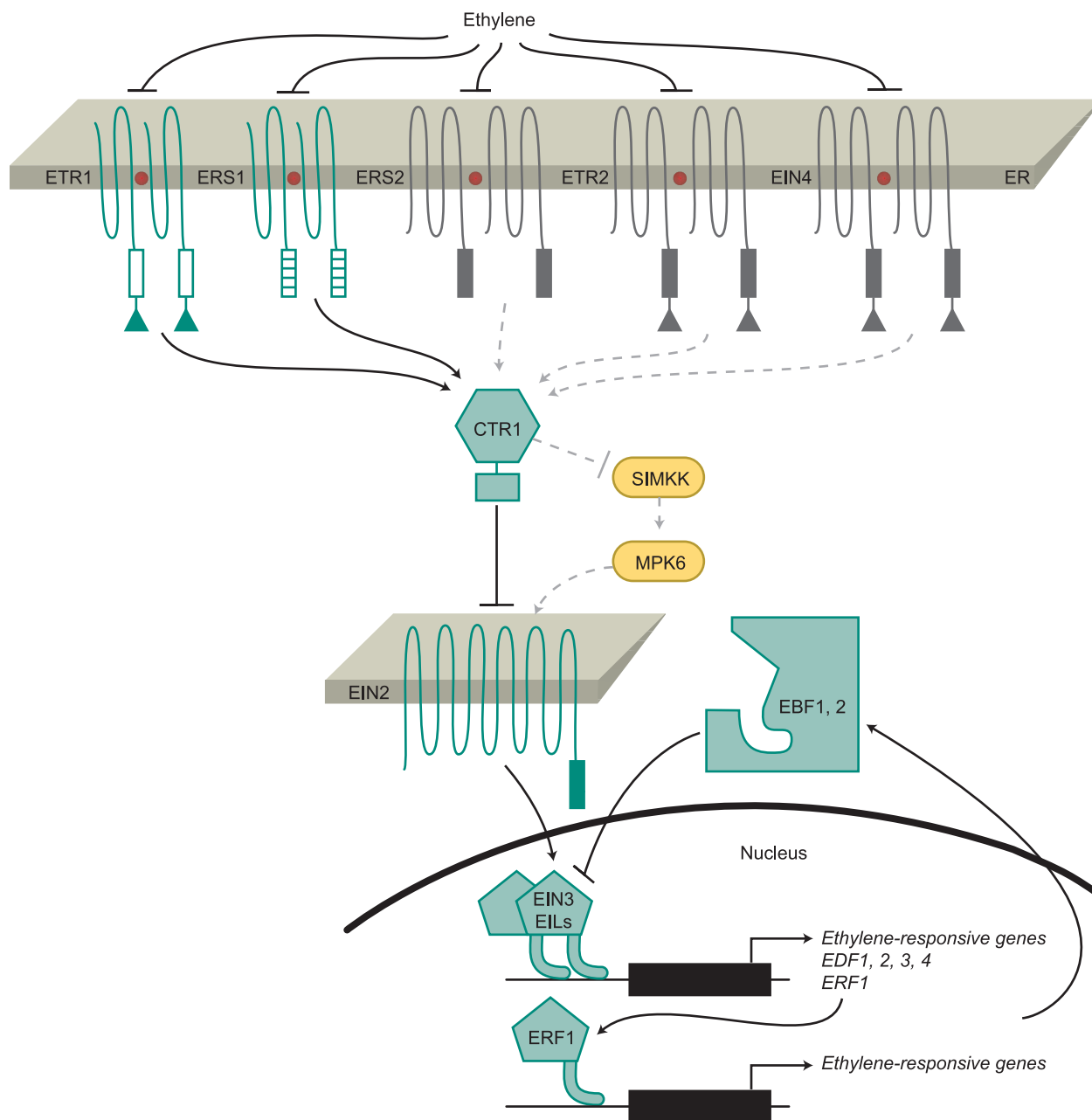


Fig. 1. Representation of the ethylene signal transduction pathway. Ethylene is perceived by a family of receptors located in the ER membrane. Binding of ethylene to the hydrophobic pocket of the receptors is mediated by a copper cofactor. The receptors physically interact with the Raf-like kinase CTR1. Binding of ethylene to the receptors results in the inactivation of both receptors and CTR1, causing derepression of a positive regulatory molecule, EIN2. A MAPK cascade (yellow) may be involved in the signal trans-

duction between CTR1 and EIN2. By an unknown mechanism, a positive signal is then transmitted from EIN2 to the transcription factors EIN3/EILs, resulting in the stabilization and, consequently, accumulation of the EIN3/EIL proteins in the nucleus, where they induce transcription of *ERF1*, *EDF1*, *2*, *3*, *4*, and other ethylene-regulated genes as the first step in a transcriptional cascade that unleashes the downstream ethylene responses. The levels of EIN3 are regulated by two F-box proteins, EBF1 and 2, whose transcription is inducible by ethylene.

question of how EIN2 activates the EIN3 family of transcription factors, remain two of the most intriguing aspects of ethylene signaling.

The ethylene signal arrives at the nucleus through EIN3, a plant-specific transcription factor that belongs to a small gene family (24). Although there are five other *EIN3*-like genes (*EILs*) in *Arabidopsis*, the nearly complete ethylene insensitivity of the *ein3 eil1* double mutant suggests that the rest of the *EILs* may have a marginal role in the response to high

levels of ethylene used in the typical ethylene response assays (25). The marked reduction in the ethylene sensitivity of plants harboring mutations in these transcription factors also highlights the critical role of transcription in ethylene responses. Modulation of the *EIN3* activity by ethylene is achieved, at least in part, through the control of EIN3 protein levels (26, 27). The direct interaction between EIN3 and two F-box proteins (EBF1 and EBF2), the phenotypic analysis of loss- and gain-

of-function *ebf* mutants, and the results of pharmacological studies clearly implicate an SCF (SKP1/cullin/F-box protein) E3 ubiquitin ligase complex and the proteasome in the regulation of EIN3 protein levels (26–28). The ethylene-mediated modification of EIN3, EBFs, or both that prevents EIN3 from being targeted for degradation remains unknown. The stabilization of EIN3 by ethylene results in the transcriptional activation of hundreds of genes (29). The search for direct targets of

EIN3 resulted in the identification of *ERF1*, a gene encoding a member of the EREBP family of transcription factors whose expression is rapidly induced by ethylene in an EIN3-dependent manner and whose promoter harbors an EIN3-binding site (30). In addition to being regulated by EIN3, *ERF1* is also induced by jasmonate and is likely to represent a point of interaction between the response pathways of these two hormones (31). Additional putative targets of EIN3 have been identified among other members of the EREBP family of transcription factors. Four genes, *EDF1* to *EDF4*, that encode proteins with two distinct plant-specific DNA-binding domains, AP2 (a feature common to all EREBP family members) and B3, have been found to be rapidly induced by ethylene and to control a subset of ethylene responses (29). A transcriptional cascade acting downstream of EIN3 offers the opportunity not only to explain the diversity of ethylene effects but also to integrate ethylene with other signaling pathways.

Ethylene signal transduction and its crosstalk with other signals remain an exciting topic

of current research in plants. It is foreseeable that the ethylene field will continue to expand and offer many interesting discoveries as the existing gaps in the pathway are filled in.

References and Notes

1. F. Abeles, P. Morgan, M. Saltveit, *Ethylene in Plant Biology* (Academic Press, San Diego, CA, 1992).
2. P. R. Johnson, J. R. Ecker, *Annu. Rev. Genet.* **32**, 227 (1998).
3. A. Mattoo, J. Suttle, *The Plant Hormone Ethylene* (CRC Press, Boca Raton, FL, 1991).
4. K. L. Wang, H. Li, J. R. Ecker, *Plant Cell* **14** (suppl.), S131 (2002).
5. H. Guo, J. R. Ecker, *Curr. Opin. Plant Biol.* **7**, 40 (2004).
6. H. J. Klee, *Plant Physiol.* **135**, 660 (2004).
7. A. N. Stepanova, J. M. Alonso, *Sci. STKE* (Connections Map, as seen November 2004), http://stke.sciencemag.org/cgi/cm/stkecm;CMP_13899.
8. A. N. Stepanova, J. M. Alonso, *Sci. STKE* (Connections Map, as seen November 2004), http://stke.sciencemag.org/cgi/cm/stkecm;CMP_14238.
9. T. Hirayama, J. M. Alonso, *Plant Cell Physiol.* **41**, 548 (2000).
10. A. B. Bleeker, *Trends Plant Sci.* **4**, 269 (1999).
11. A. B. Bleeker, H. Kende, *Annu. Rev. Cell Dev. Biol.* **16**, 1 (2000).
12. J. Hua et al., *Plant Cell* **10**, 1321 (1998).
13. H. Sakai et al., *Proc. Natl. Acad. Sci. U.S.A.* **95**, 5812 (1998).
14. F. I. Rodriguez et al., *Science* **283**, 996 (1999).
15. J. Hua, E. M. Meyerowitz, *Cell* **94**, 261 (1998).
16. W. Wang, A. E. Hall, R. O'Malley, A. B. Bleeker, *Proc. Natl. Acad. Sci. U.S.A.* **100**, 352 (2003).
17. P. Moussatche, H. J. Klee, *J. Biol. Chem.*, in press; published online 9 September 2004 (10.1074/jbc.M403100200).
18. K. L. Clark, P. B. Larsen, X. Wang, C. Chang, *Proc. Natl. Acad. Sci. U.S.A.* **95**, 5401 (1998).
19. Z. Gao et al., *J. Biol. Chem.* **278**, 34725 (2003).
20. J. J. Kieber, M. Rothenberg, G. Roman, K. A. Feldmann, J. R. Ecker, *Cell* **72**, 427 (1993).
21. Y. Huang, H. Li, C. E. Hutchison, J. Laskey, J. J. Kieber, *Plant J.* **33**, 221 (2003).
22. F. Ouaked, W. Rozhon, D. Lecourieux, H. Hirt, *EMBO J.* **22**, 1282 (2003).
23. J. M. Alonso, T. Hirayama, G. Roman, S. Nourizadeh, J. R. Ecker, *Science* **284**, 2148 (1999).
24. Q. Chao et al., *Cell* **89**, 1133 (1997).
25. J. M. Alonso et al., *Proc. Natl. Acad. Sci. U.S.A.* **100**, 2992 (2003).
26. H. Guo, J. R. Ecker, *Cell* **115**, 667 (2003).
27. T. Potuschak et al., *Cell* **115**, 679 (2003).
28. J. M. Gagne et al., *Proc. Natl. Acad. Sci. U.S.A.* **101**, 6803 (2004).
29. J. M. Alonso et al., *Science* **301**, 653 (2003).
30. R. Solano, A. Stepanova, Q. Chao, J. R. Ecker, *Genes Dev.* **12**, 3703 (1998).
31. O. Lorenzo, R. Piqueras, J. J. Sanchez-Serrano, R. Solano, *Plant Cell* **15**, 165 (2003).
32. We thank R. Franks for critical reading of the manuscript. Supported by NCSU and NSF.

VIEWPOINT

Keeping the Leaves Green Above Us

Aurélie Gfeller and Edward E. Farmer*

The plant immune system relies to a great extent on the highly regulated expression of hundreds of defense genes encoding antimicrobial proteins, such as defensins, and antiherbivore proteins, such as lectins. The expression of many of these genes is controlled by a family of mediators known as jasmonates; these cyclic oxygenated fatty acid derivatives are reminiscent of prostaglandins. The roles of jasmonates also extend to the control of reproductive development. How are these complex events regulated? Nearly 20 members of the jasmonate family have been characterized. Some, like jasmonic acid, exist in unmodified forms, whereas others are conjugated to other lipids or to hydrophobic amino acids. Why do so many chemically different forms of these mediators exist, and do individual jasmonates have unique signaling properties or are they made to facilitate transport within and between cells? Key features of the jasmonate signal pathway have been identified and include the specific activation of E3-type ubiquitin ligases thought to target as-yet-undescribed transcriptional repressors for modification or destruction. Several classes of transcription factor are known to function in the jasmonate pathway, and, in some cases, these proteins provide nodes that integrate this network with other important defensive and developmental pathways. Progress in jasmonate research is now rapid, but large gaps in our knowledge exist. Aimed to keep pace with progress, the ensemble of jasmonate Connections Maps at the Signal Transduction Knowledge Environment describe (i) the canonical signaling pathway, (ii) the *Arabidopsis* signaling pathway, and (iii) the biogenesis and structures of the jasmonates themselves.

The importance of the jasmonate pathway, in a nutshell, is that it plays a central role in maintaining the balance between biomass in the green and red kingdoms, between plants and animals. Plants unable to synthesize or perceive jasmonates are highly susceptible to a wide range of herbivores and pathogens (1, 2), because the pathway regulates the expression of a plethora of inducible defense-related genes. For example, within 3 to 5 hours of insects'

feeding on leaves, the levels of hundreds of transcripts change, and of these, 67 to 84% are estimated to be under the control of the jasmonate pathway (3). In addition, and depending on the plant species in question, jasmonate signaling components can control the development and/or function of entire defensive structures, such as trichomes (4) or extrafloral nectaries (5). The biological roles of jasmonates extend to reproductive development. Here, dif-

ferences between species are apparent. Unlike *Arabidopsis*, in which mutations that impair jasmonate perception have a particularly high impact on male fertility, similar mutations in tomato have a much greater effect on female fertility (4). The pathway even boasts its own novel organelle; the wound-stimulated biogenesis of endoplasmic reticulum (ER) bodies is jasmonate-dependent (6), although functions for this new structure have yet to be defined.

Jasmonates are small lipid derivatives. Discounting enantiomeric variants, about 20 naturally occurring jasmonates have been described. This growing family is presented at the Jasmonate Biochemical Pathway at STKE (7). Several members of the jasmonate family may have discrete roles as signals. In *Arabidopsis*, jasmonic acid (JA) is necessary for the expression of a number of genes, whereas cyclopentenone jasmonates may regulate others (7). Furthermore, the *Arabidopsis* JASMONIC ACID RESISTANT 1 (JAR1) protein is an ATP-dependent JA-amino synthetase that conjugates JA to hydrophobic amino acids, in particular, isoleucine (Ile) (8). The *jar1* mutation renders root growth less sensitive to exoge-

Gene Expression Laboratory, Plant Molecular Biology, University of Lausanne, Biology Building, 1015 Lausanne, Switzerland.

*To whom correspondence should be addressed. E-mail: edward.farmer@unil.ch

nous JA and increases susceptibility to certain opportunistic root pathogens without affecting male fertility, a process that, nevertheless, requires JA synthesis. JA-Ile may be an endogenous regulator and, if so, would be the first example of a biologically active hormone conjugate. Nevertheless, the possibility remains that OPDA and/or JA also act as regulatory ligands.

Two Connections Maps describing jasmonate signal transduction elements are maintained at STKE: A canonical pathway (9) presents progress in plants in general, whereas the *Arabidopsis* signal pathway (10) is dedicated to this model organism. Little is known about early steps in jasmonate signaling, but several important papers have highlighted rapidly executed jasmonate-triggered events in the plasma membrane. In one of these reports, patch-clamping of stomatal guard cells revealed that methyl jasmonate promoted K⁺ efflux, a process necessary for stomatal closure (11). Further downstream in the signaling pathway, several key components have been identified. This recent progress will soon put us in a position to estimate the “greenness” of the pathway (Fig. 1), i.e., how many jasmonate signal-transducing components are from protein families that have expanded in the plant lineage?

Jasmonates function through a signal pathway that is branched below a central processor that is, arguably, essential for all well-characterized JA responses, the CSN/SCF^{COI1} complex (12). The jasmonate-specific component of this complex, the F-box protein COI1, can be regarded as a “pale green protein,” be-

cause it is a member of a ubiquitous eukaryotic protein family that has been greatly expanded in plants. This complex appears to function early in the perception of jasmonates, and no genes functioning between JA and COI1 have yet been characterized. SCF itself is a ubiquitin E3-ligase thought to target transcriptional repressors. These presumed targets have yet to be identified, but one COI1-interacting protein is a histone deacetylase (12). A new genetic element important for the correct repression of a pool of jasmonate-responsive genes has emerged. The COS1 gene (13) encodes an enzyme that operates in the penultimate step of riboflavin biosynthesis. Riboflavin, or its immediate precursor, appears to be a necessary component in the correct repression of some jasmonate-regulated genes.

Thanks to recent work from a number of groups, we now have a better view of the transcription factors (TFs) operating in the jasmonate pathway. This emerging picture has a green tint. Some AP-2-domain TFs regulate jasmonate-dependent gene expression; the most recently reported is ERF1 in *Arabidopsis* (14). AP-2 domain TFs are unique to plants, and this is also the case for WRKY TFs including WRKY70, a TF that integrates signals from the jasmonate and salicylate pathways (15). A third class of TFs involved in jasmonate responses in vegetative tissues, the MYC class, is represented by MYC2 in *Arabidopsis* (16) and by JAMYC2 and JAMYC10 in tomato (17). *Arabidopsis* MYC2 activates wound-response genes in a jasmonate-

dependent manner and also represses some ethylene-response genes (16, 17). These MYC TFs are basic helix-loop-helix (bHLH) proteins, members of a large family in eukaryotes that has expanded in the plant kingdom. A fourth type of transcription factor encoded by the *BOTRYTIS SUSCEPTIBLE 1* gene is strongly implicated in jasmonate signaling: *BOS1* encodes an R2R3MYB protein (18).

The jasmonate field is clearly moving fast in several directions. A large number of laboratories are engaged in genetic approaches to define more signaling components. There is great interest, as well as a great deal to learn about early signaling events. How are jasmonates moved into and out of cells? How and which jasmonates are perceived? Does CSN/SCF^{COI1} target transcriptional repressors and, if so, what is their nature? We can now expect to see a larger variety of genetic screens, some based on natural variation in responses to jasmonates. Genes controlling reproductive processes through the pathway must be identified. At the biochemical level, the quest to discover and understand the roles of new jasmonate adducts and esterified jasmonates is continuing apace. These results will rapidly be applied to the study of jasmonate signaling in nature, and increased emphasis on multi-trophic interactions can be expected. When more elements functioning in jasmonate signaling are identified, we will be able to see the true color of the pathway at the molecular level. *Science's* STKE should prove a valuable tool with which to compare the evolutionary architecture of the jasmonate pathway to the other key signal pathways that shape, protect, and define the plant kingdom.

References

1. J. S. Thaler, B. Owen, V. J. Higgins, *Plant Physiol.* **135**, 530 (2004).
2. A. Kessler, R. Halitschke, I. T. Baldwin, *Science* **305**, 665 (2004).
3. P. Reymond *et al.*, *Plant Cell* **16**, 3132 (2004).
4. L. Li *et al.*, *Plant Cell* **16**, 126 (2004).
5. M. Heil, *J. Ecol.* **92**, 527 (2004).
6. I. Hara-Nishimura, R. Matsushima, *Curr. Opin. Plant Biol.* **6**, 583 (2003).
7. R. Liechti, E. E. Farmer, Jasmonate Biochemical Pathway. *Sci. STKE* (Connections Map, as seen November 2004), http://stke.sciencemag.org/cgi/cm/stkecm;CMP_7361.
8. P. Staswick, I. Tiryaki, *Plant Cell* **16**, 2117 (2004).
9. R. Liechti, A. Gfeller, E. E. Farmer, Jasmonate Signaling Pathway. *Sci. STKE* (Connections Map, as seen November 2004), http://stke.sciencemag.org/cgi/cm/stkecm;CMP_13820.
10. R. Liechti, A. Gfeller, E. E. Farmer, *Arabidopsis* Jasmonate Signaling Pathway. *Sci. STKE* (Connections Map, as seen November 2004), http://stke.sciencemag.org/cgi/cm/stkecm;CMP_13931.
11. N. H. Evans, *Plant Physiol.* **131**, 8 (2003).
12. A. Devoto *et al.*, *Plant J.* **32**, 457 (2002).
13. S. Xiao *et al.*, *Plant Cell* **16**, 1132 (2004).
14. O. Lorenzo, R. Piqueras, J. J. Sanchez-Serrano, R. Solano, *Plant Cell* **15**, 165 (2003).
15. J. Li, G. Brader, E. T. Palva, *Plant Cell* **16**, 319 (2004).
16. O. Lorenzo, J. M. Chico, J. J. Sanchez-Serrano, R. Solano, *Plant Cell* **16**, 1938 (2004).
17. M. Boter, O. Ruiz-Rivero, A. Abdeen, S. Prat, *Genes Dev.* **18**, 1577 (2004).
18. T. Mengiste, X. Chen, J. Salmeron, R. Dietrich, *Plant Cell* **15**, 2551 (2003).



Fig. 1. In nature, the balance between biomass in plants and animals favors the plants, in part because of their robust defense systems, many of which depend on the jasmonate pathway. An emerging question is whether the evolutionary architecture of this signal pathway is as “green” as the plants it protects?

Natural Killer Cell Signaling Pathways

Eric Vivier,^{1*} Jacques A. Nunès,² Frédéric Vély³

Natural killer (NK) cells are lymphocytes of the innate immune system that are involved in the early defenses against foreign cells, as well as autologous cells undergoing various forms of stress, such as microbial infection or tumor transformation. NK cell activation is controlled by a dynamic balance between complementary and antagonistic pathways that are initiated upon interaction with potential target cells. NK cells express an array of activating cell surface receptors that can trigger cytolytic programs, as well as cytokine or chemokine secretion. Some of these activating cell surface receptors initiate protein tyrosine kinase (PTK)-dependent pathways through noncovalent associations with transmembrane signaling adaptors that harbor intracytoplasmic ITAMs (immunoreceptor tyrosine-based activation motifs). Additional cell surface receptors that are not directly coupled to ITAMs also participate in NK cell activation. These include NKG2D, which is noncovalently associated to the DAP10 transmembrane signaling adaptor, as well as integrins and cytokine receptors. NK cells also express cell surface inhibitory receptors that antagonize activating pathways through protein tyrosine phosphatases (PTPs). These inhibitory cell surface receptors are characterized by intracytoplasmic ITIMs (immunoreceptor tyrosine-based inhibition motifs). The tyrosine-phosphorylation status of several signaling components that are substrates for both PTKs and PTPs is thus key to the propagation of the NK cell effector pathways. Understanding the integration of these multiple signals is central to the understanding and manipulation of NK cell effector signaling pathways.

Natural killer (NK) cells are lymphocytes of the innate immune system that are involved in early defenses against both allogeneic (nonself) cells and autologous cells undergoing various forms of stress, such as infection with viruses, bacteria, or parasites or malignant transformation. NK cells act by means of direct cytotoxic attack on their targets or by producing a large array of cytokines and chemokines. The latter approach contributes to initiation of the antigen-specific immune response, making NK cells an important link between innate and adaptive immunity. Although NK cells do not express classical antigen receptors of the immunoglobulin family, such as the antibodies produced by B cells or the T cell receptor expressed by T cells, they are equipped with various receptors whose engagement allows them to discriminate between target and nontarget cells. Only a minority of these receptors, such as the natural cytotoxicity receptors (NCRs), are NK cell specific. Most are also found on other hematopoietic cells, particularly T cells. NK cells have been instrumental in revealing a general theme in cell activation, which is that effector cell func-

tion results from a dynamic equilibrium between multiple and sometimes opposing pathways that can be simultaneously engaged (1, 2). Integration of these numerous inputs culminates in a graded NK cell response—in other words, cytotoxicity and/or cytokine production. Furthermore, analysis of various mouse mutant models as well as blocking experiments using panels of monoclonal antibodies against human NK cells have revealed that NK cell natural cytotoxicity is a very robust effector function, which can be triggered through apparently similar or redundant signaling pathways. We focus here on NK signaling pathways that are dependent on protein tyrosine kinase activation, as well as on the equilibrium between excitatory and inhibitory signals.

NK cells express several cell surface activating complexes that are formed by noncovalent association between distinct transmembrane ligand-binding and signaling adaptor polypeptides. Most signaling adaptor polypeptides, such as killer cell-activating receptor-associated protein [KARAP, also called DNAX-activating protein of 12 kD (DAP12)], FcR γ , and CD3 ζ , contain one or three ITAMs (immunoreceptor tyrosine-based activation motifs; YxxL/Ix₆₋₈YxxL/I, where x is any amino acid), whereas another one, DAP10, contains a YxxM motif, where x is any amino acid (Fig. 1). All of these adaptor molecules contain a transmembrane aspartic acid residue, whose negative charge is required for oligomer formation. We will concentrate on these oligomeric activating

complexes, because their modular design appears to represent an evolutionarily conserved architecture common to several signaling pathways (for example, B cell receptor, T cell receptor, Toll-like receptors, and cytokine—as well as growth factor receptor-mediated signaling pathways). This oligomeric architecture allows plasticity in the composition of the receptor, so that it can be readily adapted to mediate disparate responses (3).

In human NK cells, these receptors include the low-affinity Fc γ receptor CD16 (Fc γ RIIIA), which enables recognition of antibody-coated target cells and thus antibody-dependent cell cytotoxicity (ADCC) and cytokine production. CD16 couples to the ITAM-bearing polypeptides CD3 ζ and FcR γ , as do the NKp46 and NKp30 NCRs (4). In addition, NK cells express the ITAM-bearing adaptor KARAP/DAP12, which associates with activating killer-cell Ig-like receptors (KIR-S), the NCR NKp44, and the activating receptors for human leukocyte antigen E (HLA-E), namely the CD94-NKG2C and the CD94-NKG2E heterodimers (4). There are many differences between human and mouse NK cell surface receptors. In the mouse, NK cells express CD16 in association with FcR γ , as well as activating Ly49, the mouse NKG2D-S isoform, and CD94 heterodimers that associate with KARAP/DAP12. In a manner reminiscent of T cell receptor- and B cell receptor-mediated signaling pathways, engagement of NK cell ITAM-bearing receptors activates “first line” protein tyrosine kinases (PTKs) of the Src family (such as p56lck and p59fyn), which phosphorylate ITAMs on tandem tyrosine residues, thereby leading to the recruitment and activation of “second line” tandem-SH2 PTKs of the Syk family (such as Syk and ZAP70). Various transmembrane adaptors (such as linker of activated T cells, LAT) and cytosolic adaptors [such as SH2 domain-containing leukocyte phosphoprotein of 76 kD (SLP-76) and SH3-binding protein 2 (3BP2)] then enter into the signaling pathway. These adaptors play an important role in integrating and propagating the signals that lead to cell activation. Indeed, a major function of LAT resides in its capacity to provide multiple tyrosine-phosphorylation docking sites for the SH2 domains of intracellular signaling molecules (such as cytosolic adaptor proteins), thereby targeting them to the inner leaflet of the plasma membrane. In T cells, numerous signaling molecules bind to LAT either directly through SH2 domains [for

¹Centre d'Immunologie de Marseille-Luminy, INSERM-CNRS-Univ. Méditerranée, Campus de Luminy, Case 906, 13288 Marseille cedex 09, France.

²Institut de Cancérologie de Marseille, INSERM UMR 599, 13009 Marseille, France. ³INSERM U608-Univ. Méditerranée, Faculté de Pharmacie, 13005 Marseille, France.

*To whom correspondence should be addressed. E-mail: vivier@ciml.univ-mrs.fr

example, Grb2, Gads, Grap, PLC- γ 1 (phospholipase C- γ 1), PI3K (phosphatidylinositol 3-kinase), Cbl-b, 3BP2, and Shb] or indirectly, through other adaptor molecules (for example, SLP-76, Sos, Itk, Vav, Nck, SLAP-130, and SKAP55) (5). LAT thus acts as a scaffold for the organization of macromolecular T cell signalosome complexes. In NK cells, LAT is tyrosine phosphorylated following direct contact with target cells and stimulation of CD16. Among the various downstream LAT signaling partners described in T cells, only PLC- γ 1 has been reported to directly interact with the phosphorylated form of LAT in activated human NK cells (6), but other possible associations have not been studied in these cells. Despite the apparent wiring conservation between ITAM-dependent signaling pathways in T cells and NK cells, no drastic alterations of NK cell

development have been described in mice deficient in the ITAM-bearing polypeptides, p56lck, Syk-family members, LAT, or SLP-76, in contrast to the major impairment in T cell development observed in these mutant mice. These results thus reveal that the pathways involved in NK and T cell development are markedly different. As far as NK cell effector function is concerned, only Syk^{-/-}ZAP70^{-/-} NK cells present notable signaling defects in ADCC as well as in cytokine secretion (7). These results initially suggest that ITAM-bearing polypeptides, p56lck, LAT, or SLP-76 might play redundant roles in the initiation and propagation of NK cell effector programs. However, NK cells use distinct combinations of receptors (and thus distinct proximal signaling pathways) to induce cytotoxicity or produce cytokines when encountering distinct target cells.

Therefore, a definitive statement about the involvement of NK signaling components must await a more extensive analysis of NK cell effector function when triggered through a large panel of cell surface receptors.

NK cells also express NKG2D, a cell surface receptor that is noncovalently associated with the DAP10 (DNAX-activating protein of 10 kD) transmembrane adaptor polypeptide. The proximal DAP10 signaling pathway includes Grb-2, PLC- γ 2, SLP-76, and PI3K (8), and several features distinguish it from ITAM-dependent signaling pathways. First, DAP10 signaling is independent of Syk-family protein tyrosine kinases (8). Second, it has been shown in the mouse that DAP10 is coupled to the Rac-Cdc42 family exchange factor Vav1, whereas ITAM-bearing polypeptides couple to its relatives Vav2 and Vav3 (9). Third, DAP10 signals appear sufficient to trigger mouse NK

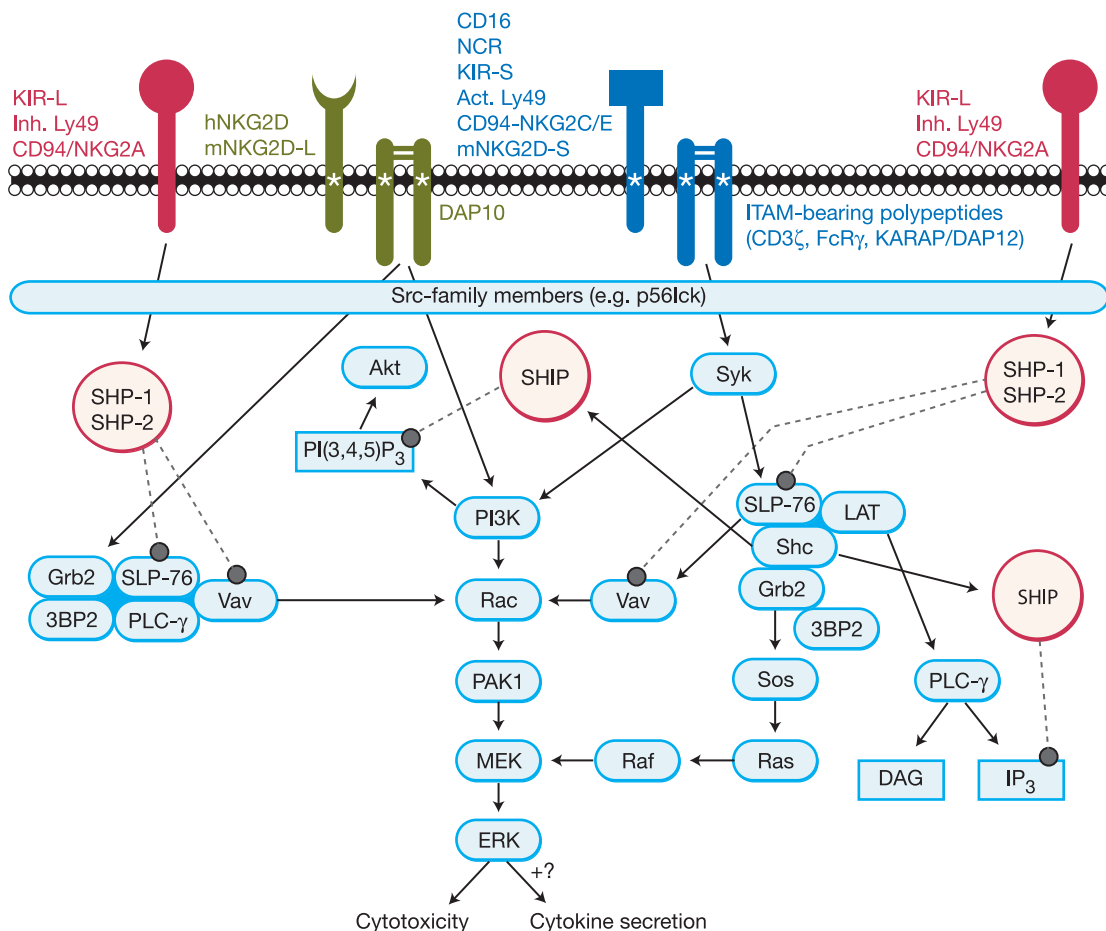


Fig. 1. NK cell effector signaling pathways. Oligomeric activating receptors, which include ITAM-bearing molecules (red) or DAP10 (green), as well as inhibitory MHC class I-specific receptors (blue), are represented. h, human; m, mouse. Asterisks indicate the presence of a transmembrane charged amino acid. KIR-S are activating killer cell Ig-like receptors with a short intracytoplasmic domain and no intrinsic signaling properties, whereas KIR-L are inhibitory receptors with an intracytoplasmic ITIM. In the mouse, but not in humans, two alternative spliced forms of NKG2D coexist: Whereas NKG2D-L associates with DAP10, NKG2D-S can associate with both DAP10 and KARAP/DAP12 (3). The link between DAP10 and SLP-76 is not fully characterized but could occur by way of Grb2 (5). The signaling pathways leading to cytokine secretion appear to be strictly dependent on ITAM-bearing receptors, but their precise delineation remains to be completed. The substrates for SHP-1 and SHP-2 tyrosine phosphatases downstream of ITIM-bearing molecules include Vav1. For additional details, refer to STKE Connections Maps (http://stke.sciencemag.org/cgi/cm/stkecm;CMP_13625 and http://stke.sciencemag.org/cgi/cm/stkecm;CMP_14358).

cell cytotoxicity against certain tumor cell lines but insufficient for inducing cytokine secretion (e.g., interferon- γ). In contrast, ITAM-dependent signals can trigger both cytotoxicity and cytokine secretion (3, 7).

Both ITAM-dependent signaling and DAP-10–dependent signaling seem to converge on a common NK cell cytotoxicity pathway. This common pathway involves the activation of Rac, which sequentially leads to activation of the mitogen-activated protein kinase (MAPK) extracellular signal-regulated kinase (ERK) by way of p21-activated kinase (PAK) and mitogen-activated or extracellular signal-regulated protein kinase (MEK) (10), culminating in the redistribution of intracytoplasmic granules and their exocytosis at the interface between the NK cell and its target (Fig. 1). The intracytoplasmic signaling molecule 3BP2 might be a common integrator for both DAP10- and ITAM-dependent cytotoxic pathways. Indeed, 3BP2 act as a positive regulator of NK cell-mediated cytotoxicity and couples to both Vav1 and Vav2 (11). Nonetheless, it remains clear that cytotoxicity and cytokine secretion depend on distinct signaling pathways (8).

A major finding resulting from the study of NK cell signal transduction has been the elucidation of inhibitory pathways that control NK cell effector function (12, 13). NK cells express cell surface receptors, such as the human killer cell inhibitory receptor-L (KIR-L) and mouse Ly49, that transduce inhibitory signals upon engagement with their major histocompatibility complex (MHC) class I ligands. In contrast to oligomeric ITAM-dependent receptors, inhibitory

receptors are monomeric and express one or more intracytoplasmic immunoreceptor tyrosine-based inhibition motifs (ITIMs; I/S/T/LxYxxL/V). Upon tyrosine phosphorylation, ITIMs recruit and activate the tandem SH2 protein tyrosine phosphatases SHP-1 and SHP-2 (12, 13). Inhibition by ITIM-bearing receptors of signaling mediated by ITAM-coupled receptors is saturable and proportional to the magnitude of engagement of both types of receptors by their ligands. Inhibitory and activating receptors thus act in concert, and coaggregation between activating and inhibitory receptors is required for inhibition to occur (14). A dynamic equilibrium is set between the “strength” of activating and inhibitory signals and is relayed by the level of tyrosine phosphorylation of critical signaling components (such as Vav1) that can serve as targets for both Syk-family protein tyrosine kinase and SHP-1 or SHP-2 protein phosphatases.

Many other receptors, including adhesion molecules, cytokine receptors, and Toll-like receptors, contribute to the dynamic balance between activating and inhibitory signals. In particular, β_2 integrin (LFA-1) signaling is coupled to perforin degranulation, as well as to the formation of NK cell–target cell conjugates through the Wiskott-Aldrich syndrome protein (WASp), a regulator of actin cytoskeleton (15, 16). Interestingly, WASp is also critically involved in both natural cytotoxicity and ADCC, exemplifying the cross talk between the signaling pathways that are initiated by distinct NK cell surface receptors (15). Another example of cross talk between apparently independent receptors has been recently described for the human NKp30,

NKp44, and NKp46 NCRs, in which the engagement of a single NCR (e.g., NKp46) results in the activation of the signaling cascades associated with the other NCRs (e.g., NKp30 and NKp44). NCRs thus appear to form a functionally coordinated activating molecular complex, possibly resulting in the amplification of activating signals (17). It remains necessary to find a way to quantify the “strength” of the multiple signals that are initiated in NK cells upon interaction with encountering cells and to understand how these inputs are integrated. Finally, the differential association of KARAP/DAP12 or DAP10 with mouse NKG2D at various stages of mature NK cell activation (3) suggests that during NK cell differentiation, the wiring of NK cell surface molecules can be variable, paving the way for future dissection of signaling pathways during NK cell development.

References

1. E. Tomasello, M. Blery, E. Vély, E. Vivier, *Semin. Immunol.* **12**, 139 (2000).
2. L. L. Lanier, *Curr. Opin. Immunol.* **15**, 308 (2003).
3. A. Diefenbach et al., *Nature Immunol.* **3**, 1142 (2002).
4. L. Moretta et al., *Eur. J. Immunol.* **32**, 1205 (2002).
5. R. L. Wange, *Sci. STKE* **2000**, re1 (2000).
6. D. Jevremovic et al., *J. Immunol.* **162**, 2453 (1999).
7. S. Zompi et al., *Nature Immunol.* **4**, 565 (2003).
8. D. D. Billadeau, J. L. Upshaw, R. A. Schoon, C. J. Dick, P. J. Leibson, *Nature Immunol.* **4**, 557 (2003).
9. M. Cella et al., *J. Exp. Med.* **200**, 817 (2004).
10. K. Jiang et al., *Nature Immunol.* **1**, 419 (2000).
11. D. Jevremovic, D. D. Billadeau, R. A. Schoon, C. J. Dick, P. J. Leibson, *J. Immunol.* **166**, 7219 (2001).
12. F. Vély, E. Vivier, *J. Immunol.* **159**, 2075 (1997).
13. E. O. Long, *Annu. Rev. Immunol.* **17**, 875 (1999).
14. M. Bléry et al., *J. Biol. Chem.* **272**, 8989 (1997).
15. A. Gismondi et al., *Blood* **104**, 436 (2004).
16. O. D. Perez, D. Mitchell, G. C. Jager, G. P. Nolan, *Blood* **104**, 1083 (2004).
17. R. Augugliaro et al., *Eur. J. Immunol.* **33**, 1235 (2003).

Science

Functional Genomics Web Site

- Links to breaking news in genomics and biotech, from *Science*, *ScienceNOW*, and other sources.
- Exclusive online content reporting the latest developments in post-genomics.
- Pointers to classic papers, reviews, and new research, organized by categories relevant to the post-genomics world.
- *Science's* genome special issues.
- Collections of Web resources in genomics and post-genomics, including special pages on model organisms, educational resources, and genome maps.
- News, information, and links on the biotech business.

www.sciencegenomics.org

Stokes Drag on a Sphere in a Nematic Liquid Crystal

J. C. Loudet,* P. Hanusse, P. Poulin

A sphere of radius R moving in a fluid of viscosity η experiences a Stokes drag force $F_S = 6\pi\eta Rv$, where v is the velocity of the sphere (1). For anisotropic liquids, an anisotropic drag force is predicted (2, 3). We experimentally determined the Stokes drag coefficients of a Brownian sphere immersed in a nematic liquid crystal phase. Unlike previous falling ball experiments (3), which can only yield an average viscous drag, we used video microscopy coupled with particle tracking routines (4) to quantitatively measure the anisotropic diffusion coefficients.

A nematic liquid crystal possesses an orientational order specified by a unit vector, \mathbf{n} , called the director (5). In the absence of any perturbation, the director field is uniformly aligned. The presence of a particle alters the orientational order of the nematic, which yields to elastic distortions and topological defects (6, 7).

We studied a binary mixture composed of a thermotropic nematic phase (E7, Merck) and an isotropic dispersed phase (silicone oil, Aldrich, a copolymer of dimethylsiloxane and methylphenylsiloxane). At high temperature, the mixture ($\phi_{E7} > 95$ weight percent, where ϕ is the weight fraction) forms an isotropic phase. When a sample is thermally quenched, the subsequent phase separation leads to the formation of isotropic droplets embedded in the nematic solvent (8). We focused on the early stages of the phase separation, when the small coarsening oil droplets exhibit the Saturn or surface ring configuration, in which a disclination line surrounds the sphere at its equator (Fig. 1A, inset) (8, 9). This configuration is stable against thermal fluctuations and has quadrupolar symmetry (7).

Working with very dilute suspensions ($\phi_{oil} \leq 0.6$ weight percent), these noninteracting quadrupoles, the diameters of which range from 1 to 2 μm , perform Brownian motion. Using video microscopy and particle tracking routines (4), we analyzed the Brownian

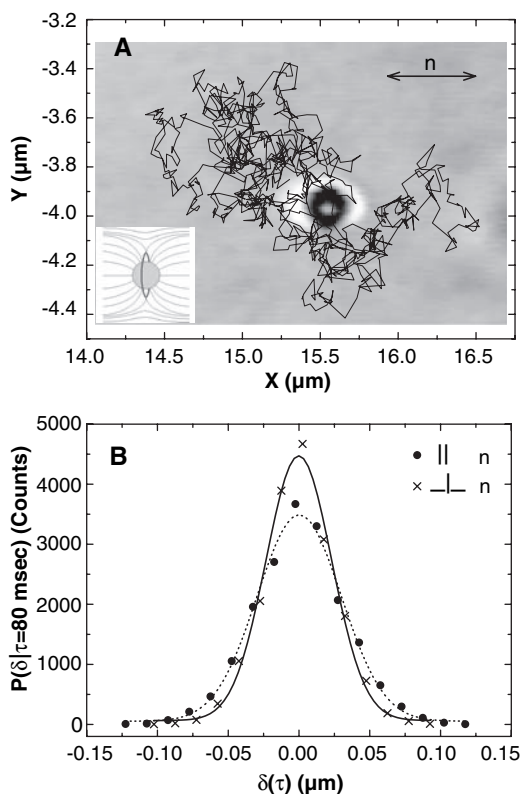


Fig. 1. (A) Brownian trajectory of a 1- μm -diameter droplet embedded in a nematic continuous phase. The time τ between two steps was 0.125 s. Background picture: The director around the drop exhibits the Saturn ring configuration (inset), and the black double arrow indicates the director alignment far from the particle. The particle size and the graph axes do not have the same scale. (B) Histograms of particle displacements along (\parallel) and perpendicular (\perp) to the director for $\tau = 0.08$ s from a sample of 18,000 trajectory steps. The solid and dotted lines are Gaussian fits.

fluctuations and determined the particle positions at regular time steps. A typical trajectory derived from 1000 snapshots is shown in Fig. 1A. The self-diffusion coefficient of a random walker is given by the Stokes-Einstein relation $D = k_B T / 6\pi\eta R$, where k_B is the Boltzmann constant and T the temperature (5). Stokes drag forces can therefore be computed, provided that D (and hence η) can be experimentally determined. Because the nematic phase has a rotational symmetry axis, the Brownian motion is governed by two independent diffusion coefficients, namely D_{\parallel} and D_{\perp} , which characterize the diffusion along and perpendicular to the director, respectively. They are given by $D_{\parallel/\perp} = k_B T / 6\pi\eta_{\parallel/\perp} R$, where η_{\parallel} and η_{\perp} are related to the intrinsic viscosity coefficients of the liquid crystal material (2, 3).

From the analysis of the Brownian fluctuations, it is possible to derive D_{\parallel} and D_{\perp} . The probability that a particle will diffuse a distance δ in the plane in time τ obeys the Gaussian distribution (5): $P(\delta|\tau) = P_0(\tau) \exp\left(-\frac{\delta^2}{\Delta^2(\tau)}\right)$, where $P_0(\tau)$ is a normalization constant and $\Delta(\tau)$ is the width of the distribution. Averaging over 18,000 trajectory steps, Fig. 1B shows the histograms of the particle displacements $\delta = |\mathbf{r}(t + \tau) - \mathbf{r}(t)|$, where $\mathbf{r}(t)$ refers to the distance of the particle's center of mass to the origin of time t , in both the x ($\parallel \mathbf{n}$) and y ($\perp \mathbf{n}$) directions. The histograms are well fitted by a Gaussian distribution the width of which, Δ , is directly related to D through $\Delta_{\parallel/\perp}^2 = 4D_{\parallel/\perp}\tau$. We see that $\Delta_{\parallel} > \Delta_{\perp}$, which implies that $D_{\parallel} > D_{\perp}$. It is therefore easier for the quadrupoles to diffuse along the director than perpendicular to it. From the values of $\Delta_{\parallel/\perp}$, we compute D_{\parallel} , D_{\perp} , and the anisotropy ratio D_{\parallel}/D_{\perp} (Table 1). These results are in fair agreement with recent Stokes drag calculations that take into account the distortions of the director field (2, 3).

References and Notes

- J. Happel, H. Brenner, *Low Reynolds Number Hydrodynamics* (Kluwer, Dordrecht, Netherlands, 1991).
- R. W. Ruhwandel, E. M. Terentjev, *Phys. Rev. E* **54**, 5204 (1996).
- H. Stark, D. Ventzki, *Phys. Rev. E* **64**, 031711 (2001).
- J. C. Crocker, D. G. Grier, *J. Coll. Interf. Sci.* **179**, 298 (1996).
- P. M. Chaikin, T. C. Lubensky, *Principles of Condensed Matter Physics* (Cambridge Univ. Press, Cambridge, 1995).
- P. Poulin, H. Stark, T. C. Lubensky, D. A. Weitz, *Science* **275**, 1770 (1997).
- H. Stark, *Phys. Rep.* **351**, 387 (2001).
- J. C. Loudet, P. Barois, P. Poulin, *Nature* **407**, 611 (2000).
- J. C. Loudet, P. Poulin, *Colloid Chemistry I* (Topics in Current Chemistry 226, Springer, Berlin, 2003).
- Supported by the CNRS, Aquitaine Region, and Bordeaux University.

16 July 2004; accepted 24 September 2004

Centre de Recherche Paul Pascal, CNRS, Avenue A. Schweitzer 33600, Pessac, France.

*To whom correspondence should be addressed. E-mail: loudet@crpp-bordeaux.cnrs.fr

Table 1. Diffusion coefficients and anisotropic ratios derived from experiments and simulations [see (3), values of liquid crystal 5CB] for a Saturn ring droplet of radius $R = 0.55 \mu\text{m}$.

Diffusion coefficients	Experiments	Simulations
D_{\parallel} ($10^{-3} \mu\text{m}^2/\text{s}$)	7.7	7.9
D_{\perp} ($10^{-3} \mu\text{m}^2/\text{s}$)	4.8	4.6
D_{\parallel}/D_{\perp}	1.6	1.72

Impact-Induced Seismic Activity on Asteroid 433 Eros: A Surface Modification Process

James E. Richardson,* H. Jay Melosh, Richard Greenberg

High-resolution images of the surface of asteroid 433 Eros revealed evidence of downslope movement of a loose regolith layer, as well as the degradation and erasure of small impact craters (less than ~ 100 meters in diameter). One hypothesis to explain these observations is seismic reverberation after impact events. We used a combination of seismic and geomorphic modeling to analyze the response of regolith-covered topography, particularly craters, to impact-induced seismic shaking. Applying these results to a stochastic cratering model for the surface of Eros produced good agreement with the observed size-frequency distribution of craters, including the paucity of small craters.

The Near Earth Asteroid Rendezvous (NEAR) Shoemaker mission to the asteroid 433 Eros revealed a heavily cratered surface, covered with a veneer of loose regolith and peppered with numerous boulders (Fig. 1A). This regolith layer displays evidence of downslope movement in several forms (1–4): debris aprons at the base of steep slopes, bright streaks of freshly exposed material on crater walls, the pooling of regolith in topographic lows, a large number of degraded craters, and a scarcity of craters less than ~ 100 m in diameter. One plausible explanation for these phenomena is seismic reverberation of the asteroid after impact events, which is potentially capable of destabilizing slopes, causing regolith to migrate downslope, and degrading or erasing small craters (1–5).

Impact-induced seismic shaking of an asteroid in the 1 to 100 km size range is an attractive mechanism for three reasons. First, the small volume of the asteroid keeps the concentration of seismic energy high even after the seismic energy injected by an impact has completely dispersed throughout the body (6). Second, the very low surface gravity of the asteroid (surface gravity $g_a \approx 10^{-3}$ to $10^{-5} g_{\text{earth}}$) permits small seismic accelerations to destabilize material resting on slopes (6), where destabilization begins at 0.2 to 0.5 g_a for loose regolith (7). Third, S-type asteroids such as Eros—composed of silicate rock, residing in a vacuum, and having an extremely low moisture content—should have very low seismic energy attenuation rates (8).

Lunar and Planetary Laboratory, University of Arizona, Tucson, AZ 85721, USA.

*To whom correspondence should be addressed. E-mail: jrjch@lpl.arizona.edu

We illustrate the first and second points above by equating the seismic energy injected by an impactor, which is a small fraction of the impactor's kinetic energy [seismic efficiency $\eta \approx 10^{-3}$ to 10^{-5} (9)], with the seismic energy necessary to produce accelerations that exceed $1 g_a$ throughout the asteroid and destabilize all slopes on the surface. We then solved for the minimum diameter of a stony projectile, traveling at a typical asteroid impact speed [$v_p = 5 \text{ km s}^{-1}$ (10)], that meets this

condition (Fig. 1B) (11). For an asteroid the size of Eros (mean diameter, ~ 17 km), the impactor size necessary to achieve global seismic accelerations of $1 g_a$ is quite small, ~ 2 m (0.5 to 10 m) in diameter: far smaller than the size of impactor that would disrupt the asteroid (1.1 to 1.6 km) (12, 13).

The availability of sufficient seismic energy, however, is not enough to show the efficacy of this mechanism: This requires a detailed analysis. The precursor for our work, like that of Cheng *et al.* (5), is a classic study of the seismic effects of impacts on lunar surface topography (14). Building upon this study, we investigated the process through five modeling steps: (i) finding the typical seismic reverberation signal generated by an impact, (ii) using this signal to synthesize generic impact seismograms for Eros, (iii) computing the response of regolith-covered slopes to these seismic vibrations, (iv) applying this downslope motion to the degradation and erasure of impact craters, and finally, (v) using these results to produce a model for the cratering record on the surface of the asteroid.

First, we found the typical seismic reverberation signal generated by an impact by using the finite differencing SALES-2 hydrocode (11, 15). Briefly accelerating individual cells in a numerical mesh at the impact point, we then monitored the resulting motion at selected seismograph points (Fig. 2A). The goal was

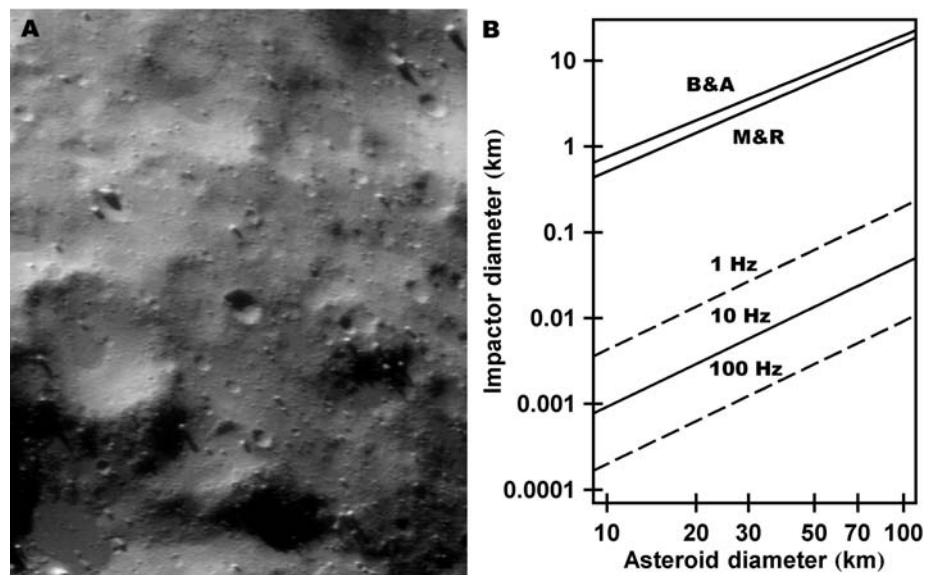


Fig. 1. (A) NEAR Shoemaker mission high-resolution image (width, 1.1 km; resolution, 6 m) of the surface of Eros, showing evidence for a regolith layer tens of meters thick and displaying slumping, the pooling of regolith in topographic lows, and small crater degradation (image no. 0154882617). (B) Lower curves: Minimum stony impactor diameter [$\eta = 10^{-4}$ (9), $v_p = 5 \text{ km s}^{-1}$ (10)], necessary to cause $1-g_a$ accelerations throughout the volume of a stony asteroid of given diameter, for seismic frequencies of $f = 1, 10,$ and 100 Hz . Alternatively, for $f = 10 \text{ Hz}$, these curves represent seismic efficiency values of $\eta = 10^{-6}, 10^{-4},$ and 10^{-2} , respectively. Upper curves: Minimum stony impactor diameter necessary to cause the disruption of a stony asteroid, calculated per Melosh and Ryan (M&R) and Benz and Asphaug (B&A) (12, 13).

to obtain the seismic reverberation signal from an impact into a highly fractured, heterogeneous target (Fig. 2B) typical of an asteroid body (16). This modeling showed that the frequency response of a fractured medium is primarily dependent upon the inherent fracture spacing rather than on the impactor diameter. We therefore chose a fracture structure that produced results consistent with impacts into the upper lunar crust (14, 17), which like Eros is highly fractured from long impact exposure (8). The resulting seismograms (Fig. 2B) had a frequency spectrum generally between 1 and 100 Hz, with a peak at about 10 to 20 Hz.

In principle, the same finite differencing methods could be used for the second step, the synthesis of generic seismograms for Eros, but the asteroid is too large for this method to be practical at sufficient frequency resolution.

Instead, we took advantage of Eros's highly fractured global structure (4, 18). Lunar seismic studies show that the dispersion of seismic energy in a fractured, highly scattering medium is a diffusion process, such that the seismic energy density ϵ in a fractured asteroid should obey the equation (8)

$$\frac{\partial \epsilon}{\partial t} = K_s \nabla^2 \epsilon - \frac{\omega \epsilon}{Q} \quad (1)$$

where t is the time, K_s is the seismic diffusivity, ∇^2 is the Laplacian operator, ω is the seismic frequency, and Q is a dissipation parameter (seismic quality factor). We solved Eq. 1 in Cartesian coordinates (11) and approximated the initial spatial energy distribution as a delta function—reasonable because the impactors considered

here are much smaller than the target asteroid. This solution was used to obtain a mean or “global average” seismic energy profile as a function of time for each impactor diameter (0.5 to 500 m). Local seismic effects, such as enhanced vibration close to the impact site or unusual effects due to the irregular shape of Eros, were not included.

The synthesis of a generic seismogram begins with the fraction of impactor energy that is converted to seismic energy [using $\eta = 10^{-4}$ (9)], then the division of this energy into frequency components in accordance with power spectra obtained from the hydrocode simulations. Moving through time, we used the solution to Eq. 1 to simulate the buildup of seismic energy by diffusion and the loss of seismic energy by attenuation for each frequency component, which were then combined using inverse Fourier analysis to produce a final seismogram level (Fig. 2, C and D). To be conservative, the assumed values of $Q = 2000$ and $K_s = 0.25 \text{ km}^2 \text{ s}^{-1}$ are about half of the values derived for the fractured lunar crust (8).

Next, we applied these synthetic seismograms to a numerical model of regolith resting on a variety of slopes under Eros gravity conditions. This was done using the Newmark slide-block method (14), which approximates the motion of a mobilized regolith layer by modeling the motion of a rigid block resting on an inclined plane (11). Computing the accelerations imparted to the block by gravity and the seismically shaken slope yielded an overall block (layer) displacement, with both hopping and sliding permitted. Although the model can include a regolith-layer shear strength (cohesion), as a first approach we assumed the layer was a uniform, noncohesive, Coulomb material, such as dry sand. This slide-block modeling showed that for Eros, global downslope motion on all slopes (2° to 30°) begins at impactor diameters of about 1 to 2 m, agreeing well with our previous analytical calculation of ~ 2 m. Figure 3A shows the resulting downslope volumetric flux per impact q_i as a function of slope ∇z (where z is elevation) for a portion of the impactor diameter range (5 to 50 m).

The motion represented in Fig. 3A is typical of nonlinear, disturbance-driven, downslope flow and is described by (19)

$$q_i = \frac{K_i \nabla z}{1 - \left(\frac{|\nabla z|}{S_c}\right)^2} \quad (2)$$

We used Eq. 2 to fit each downslope flux curve and determine the downslope diffusion constant per impact, K_i (Fig. 3B, solid circles), and the critical slope, S_c (20). These fits yielded a set of diffusion constants K_i as a function of impactor diameter D_p that follows power-law relationships that fall into two regimes: $D_p = 1$ to 4 m, where sliding occurs in stick-slip fashion, and $D_p > 4$ m,

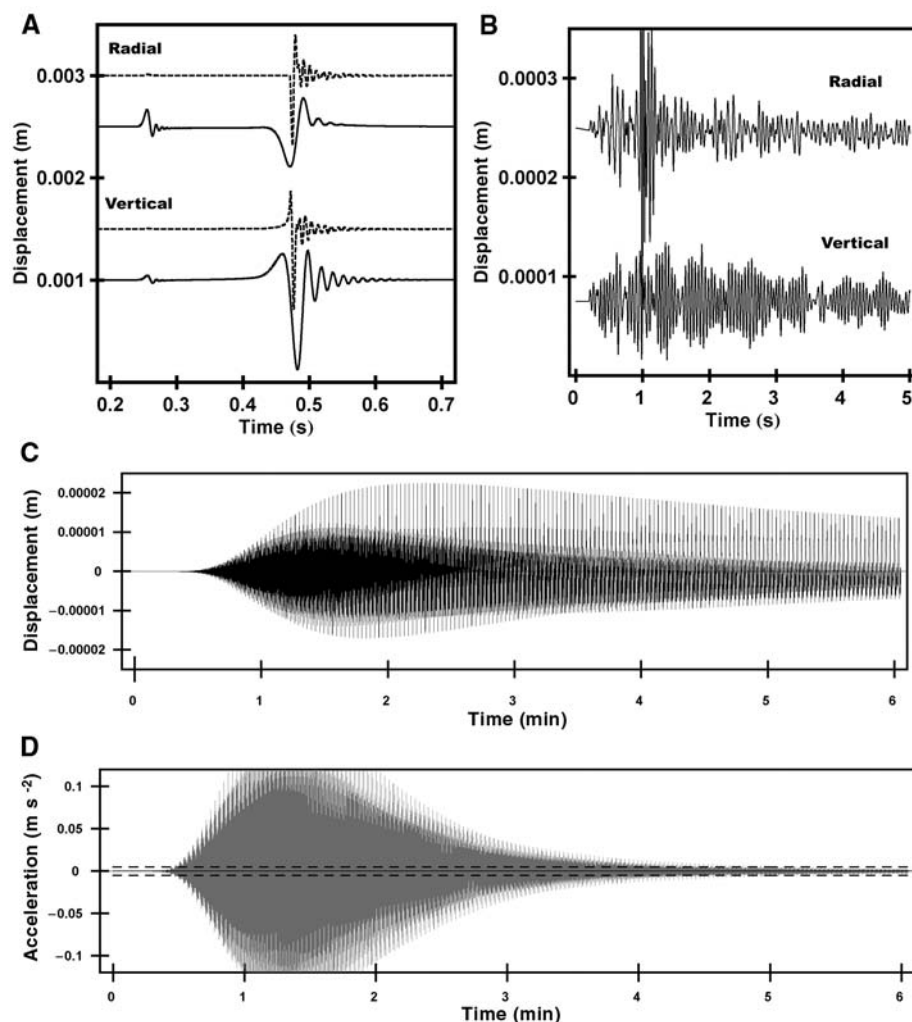


Fig. 2. (A) Theoretical (dashed) (29) and hydrocode-produced (solid) (15) surface seismograms at 0.5-km distance from an impact into a homogeneous half-space, showing a weak P -wave arrival (at 0.25 s) and strong Rayleigh wave arrival (at 0.5 s). (B) Hydrocode-produced surface seismograms at 90° away from an impact into a 1-km-diameter, fractured, spherical body. (C) The first 6 min of a synthetic seismogram for the far side of Eros after the strike of a 10-m stony impactor, showing an asymmetrical, mixed-phase reverberation signal. (D) The seismic accelerations (gray) for the seismogram shown in (C). The two dashed lines indicate the approximate surface gravity magnitude ($g_a \approx 5 \text{ mm s}^{-2}$), showing that seismic accelerations exceeding $1 g_a$ last for ~ 5 min after this impact.

where sliding occurs in continuous fashion (Fig. 3B, solid lines).

Next, we applied this downslope motion to the degradation and erasure of impact craters. If the slope is small, Eq. 2 becomes nearly linear with respect to slope ($q_i \approx K_i \nabla z$). This linearization permits us to use the results from the previous step in a model of topographic modification, described by a diffusion equation in terms of elevation z (21)

$$\frac{\partial z}{\partial t} = K_d \nabla^2 z \quad (3)$$

where K_d is a downslope diffusion constant per unit time. We solved Eq. 3 in cylindrical coordinates (11) and gave the initial topography the shape of an axially symmetric, fresh impact crater (22) with a depth to diameter (d/D) ratio of 0.2. This solution simulates the degradation (filling) of a crater because of seismic shaking (Fig. 3C), given our downslope diffusion constants. The most important term in the solution is a relaxation term

$$R = e^{-Khk^2}, \text{ where } K = \sum_{i=1}^n K_i \quad (4)$$

h is the mobilized regolith layer thickness, k is the spatial wave number, and n is the number of impacts. In our modeling, the crater was considered to be erased after six $1/e$ decays, $R = e^{-6} = 0.0025$, which gave a d/D ratio of 0.0005.

Our Bessel function form of the initial crater shape consists of a very narrow (Gaussian) range of spatial wave numbers k that peak at $k_0 = 4/D$. The point at which a crater becomes erased can be approximated by substituting k_0 for k in the relaxation term (Eq. 4) and equating the arguments $-6 = -Kh(4/D)^2$ to give

$$K \geq \frac{3D^2}{8h} \quad (5)$$

for the erased state. When applied to the solution to Eq. 3, this corresponds to a d/D ratio of 0.0041: at least twice as flat as what could reasonably be counted from NEAR images, $d/D = 0.01$ (4). Equation 5 thus permits an assessment of crater seismic damage, as downslope diffusion accumulates over time (through multiple impacts) until final crater erasure.

Finally, we used these results to model the evolution of the crater size-frequency distribution on Eros and show how seismic modification changes the overall crater population (11). This model uses Monte Carlo techniques (23) to populate a surface with craters as a function of time, allowing them to be obliterated by the effects of subsequent impacts: super-positioning, blanketing by impact ejecta, and seismic shaking. The modeled impactor population matches that of the main asteroid belt (24), where Eros has spent most of its lifetime (25). The resulting crater size-

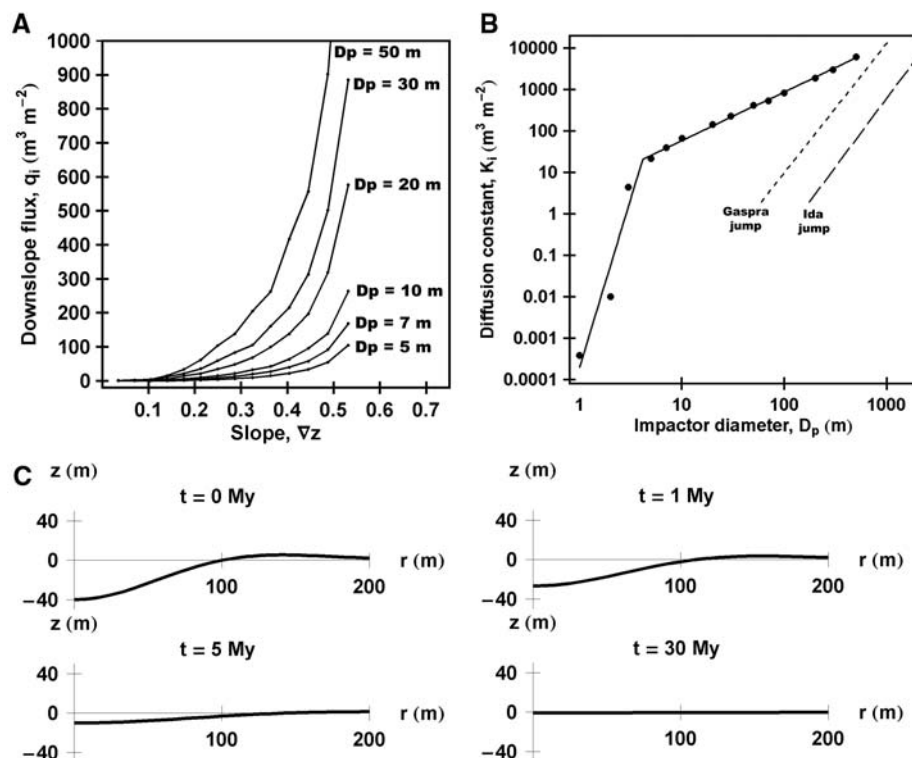


Fig. 3. (A) Newmark slide-block model results for six impactor sizes, plotting volumetric flux per impact q_i ($\text{m}^3 \text{m}^{-2}$) as a function of slope gradient ∇z and displaying the nonlinear relationship typical of disturbance-driven flow (19). (B) Downslope diffusion constants per impact K_i ($\text{m}^3 \text{m}^{-2}$) plotted as a function of impactor size D_p (m). Solid circles show the derived values from Eq. 2, and solid lines show a linear least squares fit to these points. These results are compared with the seismic “jump” distances reported by Greenberg *et al.* (27, 28), which were estimated from surface velocities on a homogeneous, spherical hydrocode model after impact. (C) Axial profile (in cylindrical coordinates) of a 200-m-diameter crater, plotted at four different times and showing its gradual erasure by impact-induced seismic shaking of an asteroid with the same volume and surface area as Eros. Complete erasure occurs at a crater age of about 30 Myr in a Main Belt impactor flux.

frequency distributions are shown in Fig. 4, in which the observed (3, 4) and modeled distributions are in good agreement at a Main Belt surface age of 400 ± 200 million years (My) (26).

The reduced numbers of small craters is a result of seismic erasure, causing lower equilibrium values than would otherwise be expected. This equilibrium point is a sensitive function of the assumed thickness of the mobilized regolith layer h (in Eq. 5). By varying this parameter, we found a best fit corresponding to $h \approx 0.1$ m, with actual values for h perhaps as high as a few meters. This thickness is considerably less than the estimates of an average regolith thickness of 20 to 40 m from the NEAR observations (4). We infer from this that much of the regolith layer possesses a depth-dependent porosity and cohesion gradient, perhaps due to compaction from seismic shaking. This would produce lower porosity and higher cohesion with increasing depth (4). Such a gradient was observed for the lunar regolith, causing the regolith to preferentially slide at shallow critical depths (14).

This modeling produces good agreement with the empirical observations, but there is

considerable uncertainty with regard to the asteroid’s actual seismic and regolith properties. We have based our results on values appropriate to the one impact-generated environment that has been studied in detail: the upper lunar crust. Even with these uncertainties, however, this work constrains these properties and effectively demonstrates the ability of impact-induced seismic shaking of Eros to destabilize slopes, cause regolith to migrate downslope, and degrade or erase small craters.

References and Notes

1. J. Veverka *et al.*, *Science* **292**, 484 (2001).
2. P. Thomas *et al.*, *Icarus* **155**, 18 (2002).
3. C. R. Chapman *et al.*, *Icarus* **155**, 104 (2002).
4. M. S. Robinson, P. C. Thomas, J. Veverka, S. L. Murchie, B. B. Wilcox, *Meteoritics* **37**, 1651 (2002).
5. A. F. Cheng, N. Izenberg, C. R. Chapman, M. T. Zuber, *Meteoritics* **37**, 1095 (2002).
6. M. J. Cintala, J. W. Head, J. Veverka, *Proc. Lunar Planet. Sci. Conf.* **9**, 3803 (1978).
7. T. W. Lambe, R. V. Whitman, *Soil Mechanics, SI Edition* (Wiley, New York, 1979), pp. 256–257.
8. A. M. Dainty *et al.*, *Moon* **9**, 11 (1974).
9. P. H. Schultz, D. E. Gault, *Moon* **12**, 159 (1975).
10. W. F. Bottke, M. C. Nolan, R. Greenberg, R. A. Kolvoord, *Icarus* **107**, 255 (1994).
11. Materials and methods are available as supporting material on Science Online.
12. H. J. Melosh, E. V. Ryan, *Icarus* **129**, 562 (1997).
13. W. Benz, E. Asphaug, *Icarus* **142**, 5 (1999).

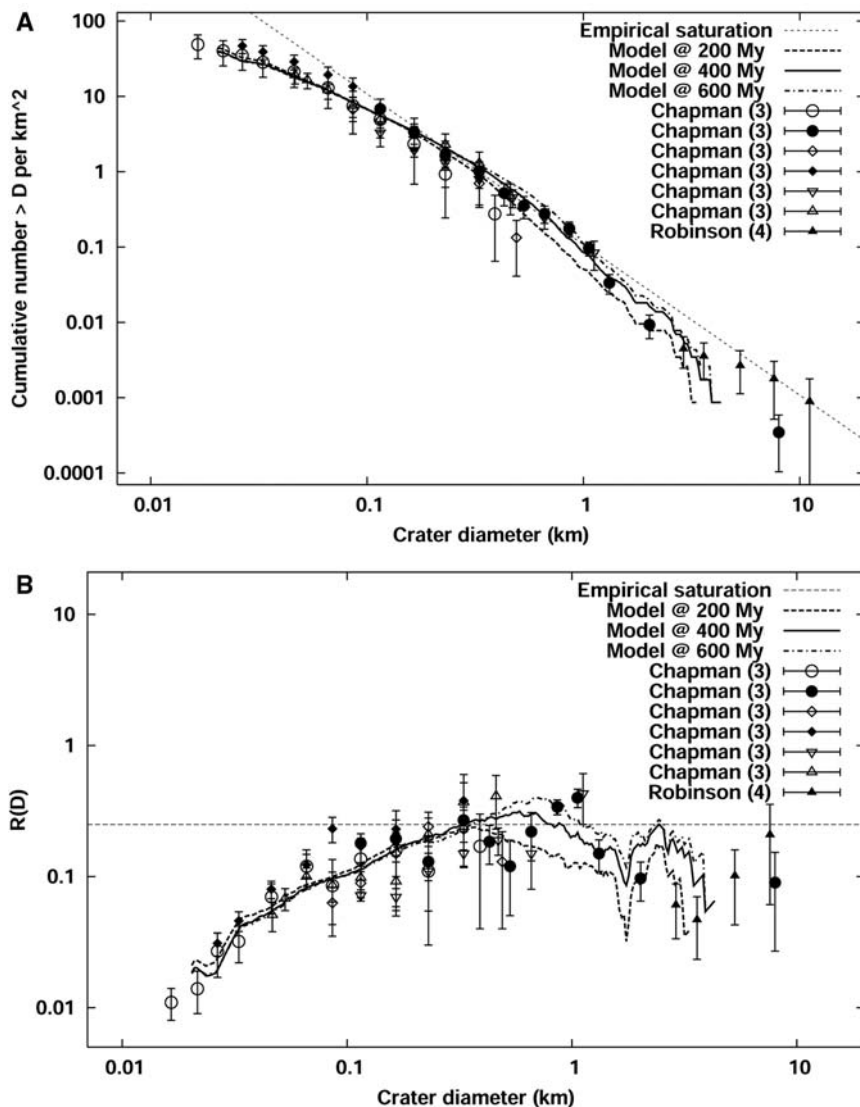


Fig. 4. (A) Cumulative and (B) relative size-frequency distribution plots (30) of Eros craters per square kilometer as a function of crater diameter, showing a favorable comparison between observed (3, 4) and modeled values after 400 ± 200 My (Main Belt surface age) (26). The low abundance of small craters is a result of seismic erasure, causing lower equilibrium values than would otherwise be expected (empirical saturation, thin dashed line). The symbols are the same as those listed in table 1 of (3).

14. N. Houston, J. Moriwaki, C. S. Chang, *Proc. Lunar Planet. Sci. Conf.* 4, 2425 (1973).
15. G. S. Collins, H. J. Melosh, J. V. Morgan, M. R. Warner, *Icarus* 157, 24 (2002).
16. D. C. Richardson, Z. M. Leinhardt, H. J. Melosh, W. F. Bottke, E. Asphaug, in *Asteroids III*, W. F. Bottke et al., Eds. (Univ. of Arizona Press, Tucson, AZ, 2002), pp. 501-516.
17. F. Duennebieber, G. H. Sutton, *J. Geophys. Res.* 79-29, 4365 (1974).
18. L. Prockter et al., *Icarus* 155, 75 (2002).
19. J. J. Roering, J. W. Kirchner, W. E. Dietrich, *Water Resour. Res.* 35-3, 853 (1999).
20. Under normal sliding conditions, the critical angle (the angle of stability) would be the one assigned to the layer in the model, $\mu_s = 0.7$, but because of the ballistic launching of the layer while in motion, this was better left as a free parameter in the fit, with values falling between 0.55 and 0.65 (near the assigned angle of repose, $\mu_d = 0.6$).
21. E. H. Culling, *J. Geol.* 68, 336 (1960).
22. H. J. Melosh, *Impact Cratering: A Geologic Process* (Oxford Univ. Press, New York, 1989), pp. 154-161.
23. W. H. Press, S. A. Teukolsky, W. T. Vetterling, B. P. Flannery, *Numerical Recipes in Fortran 77* (Cambridge Univ. Press, Cambridge, 1992), pp. 266-319.
24. D. O'Brien, thesis, University of Arizona (2004).
25. P. Michel, P. Farinella, C. Froeschle, *Astron. J.* 116, 2023 (1998).
26. This is neither an absolute age for Eros, because major impacts can potentially "reset" the asteroid surface record (27, 28), nor is it an accurate age for the current surface record, because the chaotic nature of Eros's orbit has exposed it to a highly variable impactor flux (25) rather than our assumed constant flux. At best, this surface age represents a lower limit, assuming that an average Main Belt impactor flux is at the high end of those to which Eros has actually been exposed.
27. R. Greenberg, M. C. Nolan, W. F. Bottke, R. A. Kolvoord, J. Veverka, *Icarus* 107, 84 (1994).
28. R. Greenberg et al., *Icarus* 120, 106 (1996).
29. H. Kanamori, J. W. Given, *Geophys. Res. Lett.* 10-5, 373 (1983).
30. A. Woronow et al., *Icarus* 37, 467 (1979).
31. We thank H. Kanamori (California Institute of Technology) for the use of his theoretical seismic code for Lamb pulse seismic sources, C. Chapman (Southwest Research Institute) for the use of his crater count data for Eros, and D. O'Brien (University of Arizona) for the use of his modeling results for the collisional history of the main asteroid belt. Supported by grant no. NAG5-12619 of NASA's NEAR Data Analysis Program and no. NAG5-11493 of NASA's Planetary Geology and Geophysics Program.

Supporting Online Material
www.sciencemag.org/cgi/content/full/306/5701/1526/DC1
 Materials and Methods

1 September 2004; accepted 15 October 2004

Periodic Mesoporous Dendrisilicas

Kai Landskron and Geoffrey A. Ozin*

We report the synthesis of a new class of materials called periodic mesoporous dendrisilicas. They are prepared from dendrimers with trialkoxysilyl groups at the outmost shell. Dendrimers of various cores and numbers of shells are used. The dendrisilica synthesis is based on acid- or base-catalyzed hydrolysis of the trialkoxysilyl groups and subsequent template-directed condensation of the dendrimers into an ordered template-dendrisilica nanocomposite. The template can be removed with organic solvents, producing a periodic mesoporous dendrisilica whose pore walls consist of interconnected dendrimer building blocks.

Ordered hierarchical composite structures are beginning to play a key role in the development of nanotechnology. The struc-

tures can be composed of organic and inorganic building blocks that are self-assembled into architectures with dimen-

sions spanning multiple length scales, akin to those in nature's biological systems (1, 2). Dendrimers are a class of nanomaterials that have a hyperbranched monodisperse polymer structure and an overall architecture that is well defined in terms of physical size and shape, internal porosity, and surface properties. This architecture enables dendrimers to be used as chemical sensors, drug delivery systems, and imaging and contrast agents (3, 4). Periodic

Materials Chemistry Research Group, Department of Chemistry, 80 St. George Street, University of Toronto, Toronto, Ontario M5S 3H6, Canada.

*To whom correspondence should be addressed. E-mail: gozin@chem.utoronto.ca

mesoporous silicas are a class of nanomaterials that have a structure based on a periodic arrangement of mesopores, and they are currently of interest for catalysis, separation science, and chemical sensing (5).

We describe a strategy that allows the integration of dendrimers and periodic mesoporous silica materials to create nanocomposite materials that we call periodic mesoporous dendrisilicas (PMDs). PMDs represent archetypes of ordered mesoporous materials with channel walls composed of interconnected dendrimer building blocks.

We have achieved this goal by using dendrimer building blocks functionalized with alkoxyisilyl groups at the outmost shell. We observed that the dendrimer building blocks undergo template-directed self-assembly in aqueous acid or base to form the PMD. The template was subsequently removed by solvent extraction, maintaining the structural integrity of the PMD (Fig. 1).

We chose the silsesquioxanes **1** and **2** (Scheme 1), which represent a first and second generation of carbosilane-type dendrimers, as the PMD precursors in our experiments. Tetravinylsilane and trichlorosilane in tetrahydrofuran with dihydrogenhexachloroplatinate as catalyst gave $\text{Si}[(\text{C}_2\text{H}_4)\text{SiCl}_3]_4$, which was then converted into **1** using ethanol (6, 7). The second-generation dendrimer **2** was prepared from $\text{Si}[\text{C}_2\text{H}_4\text{SiCl}_3]_4$ by first replacing the chloro groups by vinyl groups using vinylmagnesiumbromide, then subsequent hydrosilylation with HSiCl_3 (8), and finally ethanolysis of the hydrosilylation product $\text{Si}[\text{C}_2\text{H}_4\text{Si}(\text{C}_2\text{H}_4\text{SiCl}_3)_3]_4$. We also synthesized the molecule **3** (Scheme 1), which represents a first-generation dendrimer with a more complex core. It was synthesized analogously to **1** and **2**, starting from the commercially available compound bis-(triethoxysila)methane, $(\text{EtO})_3\text{SiCH}_2\text{Si}(\text{OEt})_3$. All precursors were obtained at high purity according to ^{13}C and ^1H nuclear magnetic resonance (NMR) data as well as electrospray mass spectrometry (9).

We demonstrated that the precursors **1**, **2**, and **3** can be co-assembled with surfactant mesophases in an aqueous solution to create the periodic mesoporous dendrisilicas PMD-1, PMD-2, and PMD-3. The preparation of PMD-1 used the NaOH base-catalyzed co-assembly of octadecyltrimethylammonium-bromide micelles with **1** to give an ordered surfactant-dendrisilica nanocomposite. The surfactant was removed by stirring in a hydrochloric acid-methanol solution to give PMD-1. Similarly, dendrimer **2** and dendrimer **3** were self-assembled into PMD-2 and PMD-3, respectively, using a triblock copolymer as template in an acidic sodium

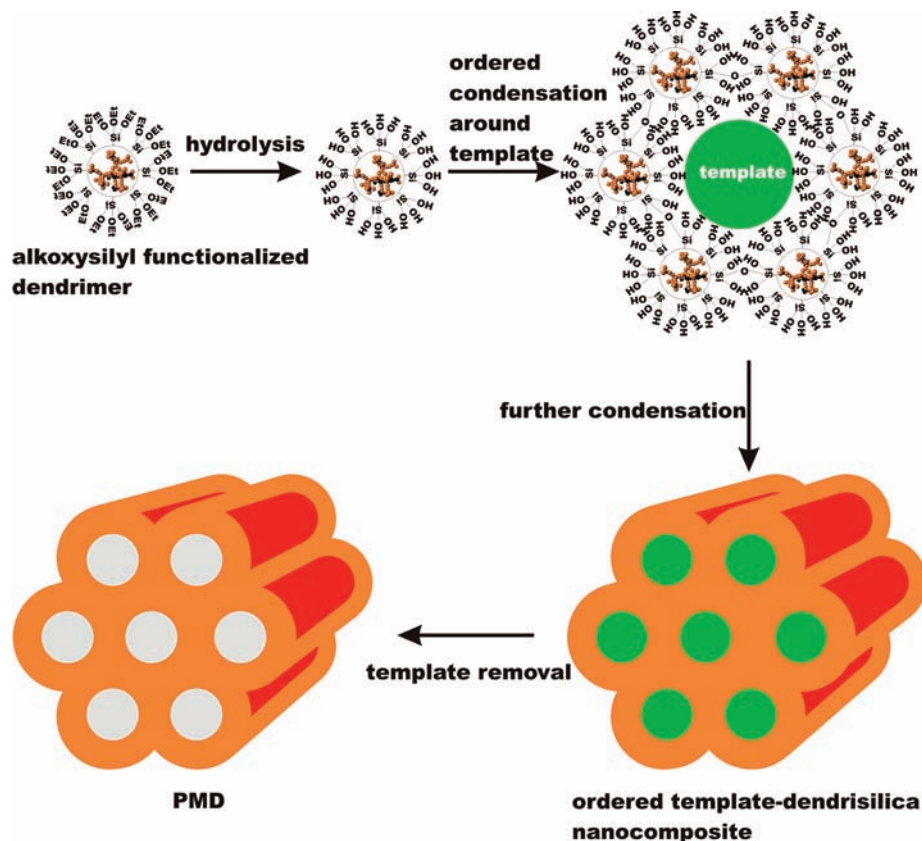


Fig. 1. Schematic illustration of the self-assembly of a PMD. A dendrimer functionalized with $\text{Si}(\text{OEt})_3$ groups at its outermost shell hydrolyzes and condenses around a surfactant template.

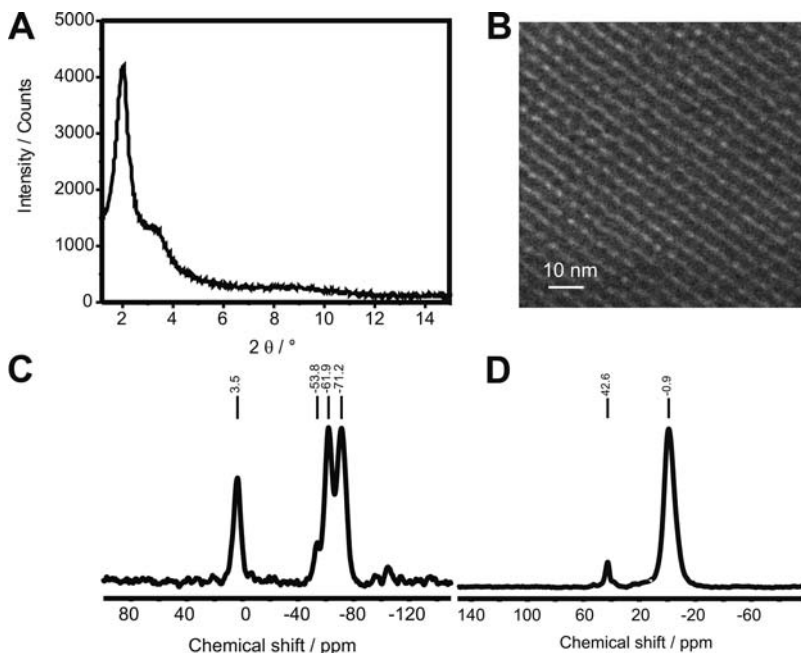


Fig. 2. (A) Powder x-ray diffraction pattern and (B) TEM images of the surfactant-extracted PMD-1. (C) ^{29}Si MAS NMR spectrum and (D) ^{13}C CP MAS NMR spectrum of the surfactant-extracted PMD-1.

chloride solution. The template was removed afterward with an acetone-hydrochloric acid solution (9).

Figure 2A shows the powder x-ray diffraction pattern of the surfactant-extracted PMD-1. The [100] reflection gives a d spac-

Fig. 3. Nitrogen adsorption data for the surfactant-extracted PMD-1. The diagram shows the type-IV N_2 isotherm with a BJH analysis of the mesopores (inset).

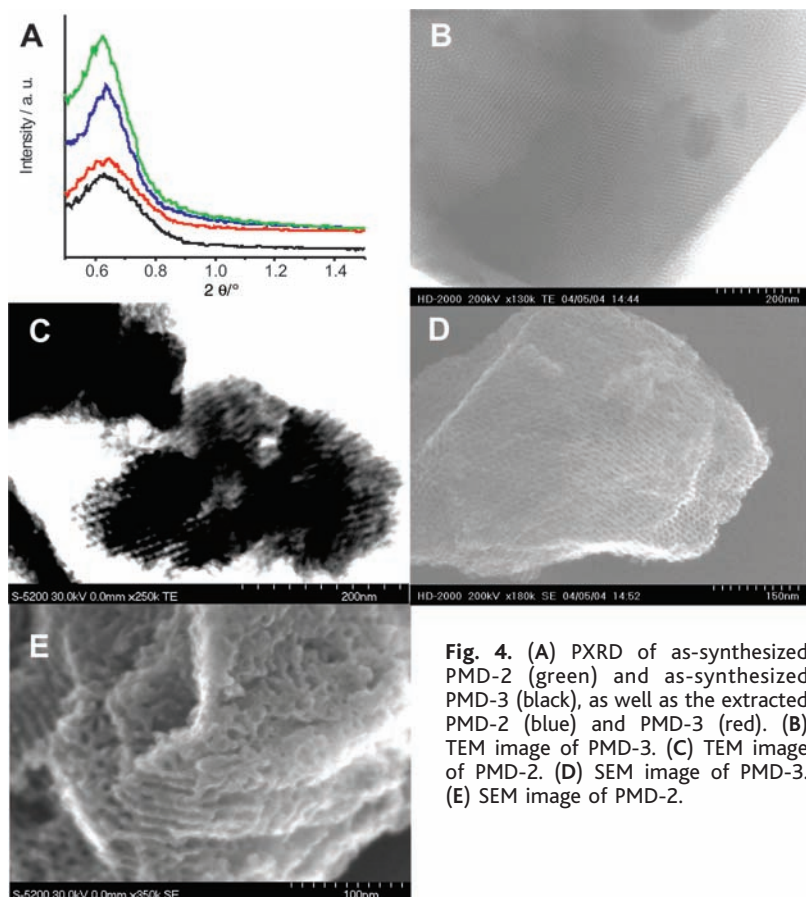
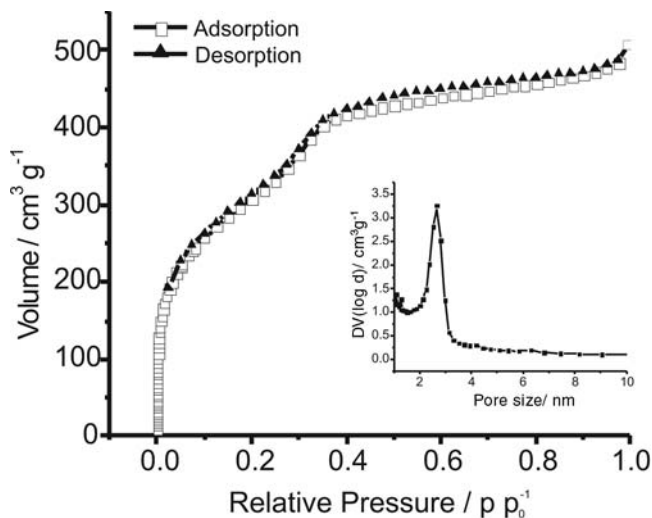


Fig. 4. (A) PXRD of as-synthesized PMD-2 (green) and as-synthesized PMD-3 (black), as well as the extracted PMD-2 (blue) and PMD-3 (red). (B) TEM image of PMD-3. (C) TEM image of PMD-2. (D) SEM image of PMD-3. (E) SEM image of PMD-2.

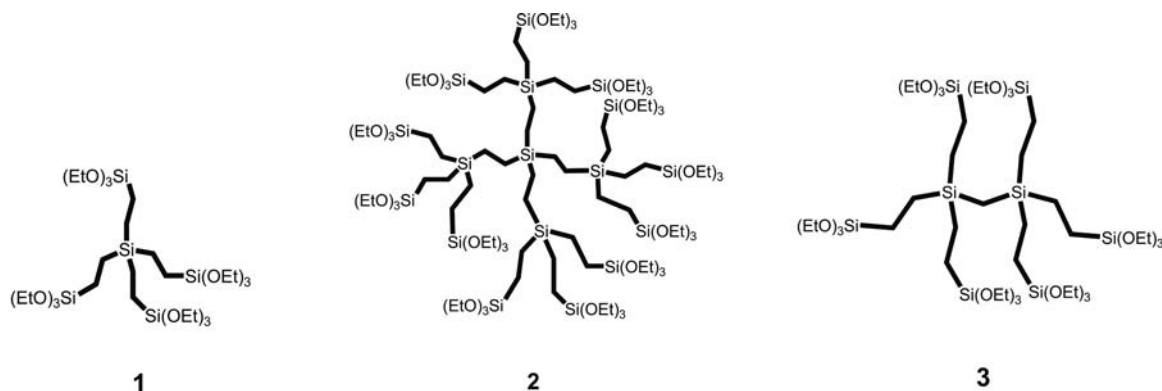
ing of 4.0 nm. Transmission electron microscope (TEM) images of the PMD-1 provided additional structural information, showing the presence of periodic arrays of parallel-aligned mesoscale channels with a spacing of ~ 4 nm. Mesopore and wall diameters are both ~ 2 nm (Fig. 2B). The ^{29}Si magic-angle spinning (MAS) NMR spectroscopy of PMD-1 showed that no significant Si–C bond cleavage occurred

during the synthesis. The surfactant-extracted material (Fig. 2C) showed four peaks at 3.5, 53.8, 61.9, and 71.2 parts per million (ppm). The signal at 3.5 ppm can be assigned to the SiC_4 building units of the dendrimer core, whereas the other signals represent tetrahedral units T_1 $\text{SiC}(\text{OSi})(\text{OH})_2$ (53.8 ppm), T_2 $\text{SiC}(\text{OSi})_2(\text{OH})$ (61.9 ppm), and T_3 $\text{SiC}(\text{OSi})_3$ (71.2 ppm). The integration of the SiC_4 and SiO_3C units revealed a

ratio of 1:3.9, which is close to the theoretical value of 1:4. The ^{13}C cross-polarization (CP) MAS NMR spectroscopy of the PMD indicated that full removal of the surfactant had occurred by showing a peak at -0.9 ppm. This value is typical for a CH_2CH_2 bridge between two Si atoms (10). A small signal at 42.8 ppm indicated some methoxylation of the silanol groups during the extraction process.

Nitrogen adsorption data for the powder form of PMD-1 show a diagnostic type IV isotherm with well-defined capillary condensation and very little hysteresis (Fig. 3). The Brunauer Emmett Teller (BET) surface area was found to be as high as $1102 \text{ m}^2 \text{ g}^{-1}$, and the mesopore diameter was about 2.5 nm, calculated by Barrett Joynes Halenda (BJH) methods (Fig. 3), and was close to that seen in TEM images (Fig. 2B). These adsorption data, together with the d spacing of 4.0 nm given by powder x-ray diffraction (PXRD), provide an independent estimate of the channel wall thickness equal to about 1.5 nm. This value corroborates the TEM-obtained diameter of the mesopores and the thickness of the channel walls. The small amount of hysteresis indicated that the pores were very uniform. The diameter of the building block was approximately 0.7 nm, assuming a tetrahedral conformation. These data indicate that the breadth of the channel wall was composed of just two condensed dendrimer building blocks, which were responsible for the above-mentioned structural stability.

The PXRD data and the TEM images of PMD-2 and PMD-3 (Fig. 4), with the PXRD data giving d spacings of 14.4 nm for PMD-2 and 14.1 nm for PMD-3, show that these materials can be reproducibly made with a high degree of mesostructural order. Furthermore, TEM images suggest pore sizes of about 8 nm and a pore wall thickness about 6 nm. ^{29}Si MAS NMR investigations showed two signals for the SiC_4 (11 ppm) and SiO_3C (59 ppm) building units for PMD-2 (10 and 58 ppm, respectively, for PMD-3). The integration of the signals revealed a molar ratio of 1:3.1, which is slightly higher than the theoretical value of 1:2.4. This result indicates that some of the SiC_4 units have transformed into SiO_3C units, most likely originating from some Si–C bond cleavage during synthesis. However, the NMR data suggest that the majority of the dendritic SiC_4 building units remain intact during self-assembly. Similarly, the integrals for PMD-3 showed a ratio of 1:4.1 instead of 1:3. No signals for SiO_4 units were observed in both materials, suggesting that the SiO_3C units of the outmost shell are hydrothermally more stable than the interior



Scheme 1.

SiC₄ units. The integral ratios were reproducible, with varying pulse delay times between 3 and 30 s, indicating that the ²⁹Si nuclei were sufficiently relaxed to give accurate integrals. Nitrogen isotherms demonstrated the ordered mesoporous nature of both PMD-2 and PMD-3 by showing typical type-IV isotherms. The BET surface areas were 775 m² g⁻¹ (PMD-2) and 767 m² g⁻¹ (PMD-3). The BJH analysis revealed a narrow pore size distribution with average pore sizes of 9.1 nm (PMD-2) and 8.2 nm (PMD-3), which is consistent with the TEM data.

References and Notes

1. I. W. Hamley, *Angew. Chem. Int. Ed. Engl.* **42**, 1692 (2003).
2. G. J. de A. A. Soler-Illia, C. Sanchez, B. Lebeau, J. Patarin, *Chem. Rev.* **102**, 4093 (2002).
3. G. R. Newkome, E. He, C. N. Moorefield, *Chem. Rev.* **99**, 1689 (1999).
4. M. Fischer, F. Vögtle, *Angew. Chem. Int. Ed. Engl.* **38**, 884 (1999).
5. C. T. Kresge, M. Leonowicz, J. C. Vartuli, J. S. Beck, *Nature* **359**, 710 (1992).
6. A. W. Van der Made, P. W. N. M. Van Leeuwen, *Chem. Commun.* 1400 (1992).
7. M. J. Michalczyk, W. J. Simonsick Jr., K. G. Sharp, *J. Organomet. Chem.* **521**, 261 (1996).
8. D. Seyferth, D. Y. Son, A. L. Rheingold, R. L. Ostrander, *Organometallics* **13**, 2682 (1994).

9. Materials and methods are available as supporting material on *Science Online*.
10. S. Inagaki, S. Guan, Y. Fukushima, T. Ohsuna, O. Terasaki, *J. Am. Chem. Soc.* **121**, 9611 (1999).
11. The authors thank Dr. N. Coombs for the TEM imaging. G.A.O. is Government of Canada Research Chair in Materials Chemistry. He is indebted to the Natural Sciences and Engineering Research Council of Canada for support of this work.

Supporting Online Material

www.sciencemag.org/cgi/content/full/306/5701/1529/DC1
Materials and Methods

26 August 2004; accepted 13 October 2004

A Reversible Synthetic Rotary Molecular Motor

José V. Hernández, Euan R. Kay, David A. Leigh*

The circumrotation of a submolecular fragment in either direction in a synthetic molecular structure is described. The movement of a small ring around a larger one occurs through positional displacements arising from biased Brownian motion that are kinetically captured and then directionally released. The sense of rotation is governed solely by the order in which a series of orthogonal chemical transformations is performed. The minimalist nature of the [2]catenane flashing ratchet design permits certain mechanistic comparisons with the Smoluchowski-Feynman ratchet and pawl. Even when no work has to be done against an opposing force and no net energy is used to power the motion, a finite conversion of energy is intrinsically required for the molecular motor to undergo directional rotation. Nondirectional rotation has no such requirement.

Molecular-level motors differ from their macroscopic counterparts not only in scale but in how environmental factors influence their operation. Macroscopic machines are generally unaffected by ambient thermal

energy, and a directional force must be applied to cause movement of each component. For molecular-sized motors, however, inertia is negligible and the parts are subject to random and incessant Brownian motion (1). Rather than fight this effect, biological motors use these random fluctuations in their mechanisms (2). For example, in F₁F₀-adenosine triphosphatase (ATPase), which spins the γ shaft counterclockwise (viewing F₁ from above) as proton-motive force

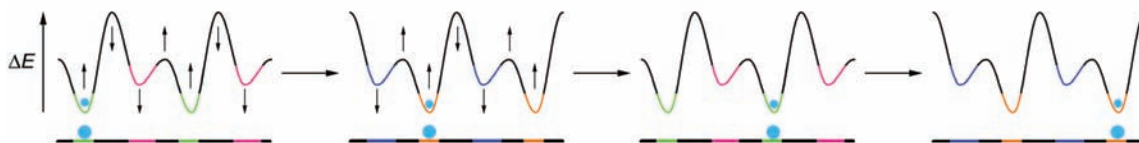
powers ATP production and clockwise if ATP is consumed to drive proton flow against a concentration gradient (3), Brownian motion drives both the power and exhaust strokes (2). Inspired by such biological motors and by Feynman's celebrated discussion (4) of the miniature ratchet and pawl first introduced (5) by Smoluchowski, efforts have been made to design molecules that exhibit directional control over submolecular rotary motion (6–10). Unidirectional rotation about single (11, 12), double (13–16), and mechanical (17) bonds has been achieved, but unlike F₁F₀-ATPase, these artificial motor molecules are only able to rotate in one direction but not the other. We now report on a molecular structure in which a fragment can be circumrotated in either direction, and we probe features of the underlying mechanism.

During the past decade, a number of remarkable theoretical formalisms have been developed using nonequilibrium statistical physics that explain how various types of fluctuation-driven transport can occur (18, 19). Underlying each of these Brownian ratchet or motor mechanisms are three components (20): (i) a randomizing element (21), (ii) an energy input to avoid falling foul of the Second Law of Thermodynamics (22, 23), and (iii) asymmetry in the energy or information potential in the dimension in which the motion occurs.

School of Chemistry, University of Edinburgh, The King's Buildings, West Mains Road, Edinburgh EH9 3JJ, UK.

*To whom correspondence should be addressed.
E-mail: David.Leigh@ed.ac.uk

Fig. 1. A flashing energy ratchet mechanism for Brownian particle transport along an oscillating potential energy surface.

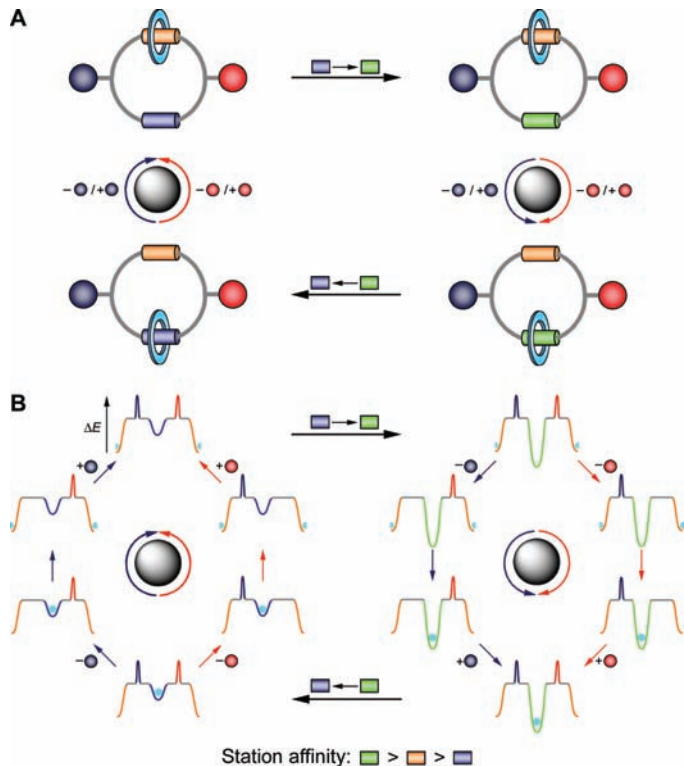


Such ratchet mechanisms not only account for the general principles behind biological motors (24–27) but have also been successfully applied to the development of transport and separation devices for mesoscopic particles and macromolecules, microfluidic pumping, the photoalignment of liquid crystals, and quantum and electronic applications (26, 28–31).

A flashing ratchet is a particular type of energy ratchet mechanism (25), a classic example of which consists in physical terms (Fig. 1) of an asymmetric potential energy surface (a periodic series of two different minima and two different maxima) along which a Brownian particle is directionally transported by sequentially raising and lowering each set of minima and maxima by changing the potential (for example, with an oscillating electric field and a charged particle). Catenanes and rotaxanes, molecules in which components are physically linked together but not connected by covalent bonds, are excellent systems with which to study characteristics of submolecular motion (8). The mechanical linkage inherently restricts certain degrees of freedom for the relative displacement of the interlocked components while simultaneously permitting large-amplitude motion in the allowed vectors. The way in which the principles of an energy ratchet can be applied to a catenane architecture is not to consider the whole structure as a molecular machine, but rather to view one macrocycle as a motor that transports a substrate—the other ring—directionally around itself. In its simplest manifestation, this gives rise to a [2]catenane such as **1** (Fig. 2) that should be able to unidirectionally rotate the smaller ring about the larger one in response to a series of chemical reactions.

There are several differences, however, between the flashing ratchet particle transport mechanism in Fig. 1 and the one applied to catenane **1** in Fig. 2: (i) The molecular system is cyclic, so the translational transport along a periodic energy potential becomes a directional rotation around a two-minima–two-maxima loop; (ii) only one energy minimum is varied for **1**, not both (which is sufficient to ensure that the energy difference between the two minima changes twice); and (iii) the single steps that simultaneously change minima depth and maxima height in the classical energy ratchet mechanism are separated into their thermodynamic and kinetic con-

Fig. 2. (A) Schematic illustration and (B) potential energy surface for the small light blue ring in a minimalist [2]catenane rotary molecular motor, **1**. The ring preferentially resides on one or other of the two binding sites (stations), represented by colored cylinders. The colored spheres are bulky groups, each of which sterically blocks one of the two tracks between the stations. The blue-to-green and green-to-blue transformations represent (balance-breaking) chemical reactions that change the binding affinity of a station for the small ring, providing a driving force for the ring to redistribute itself between the stations if it is able to be exchanged between them. Removal of a red or purple sphere (linking reaction) allows the ring to move between stations by a particular route. Reattachment of the sphere (unlinking reaction) ratchets the net transported quantity of rings.



stituents in the chemical system. Despite these differences, the physical principles behind the two mechanisms are the same.

In chemical terms, catenane **1** is a stimuli-responsive molecular shuttle (8, 32) with two routes (each of which can be independently blocked) that connect the two binding sites or “stations” for the small macrocycle (Fig. 3). To satisfy oneself that internal motion within a chemical structure can be described in terms of a stochastic transport mechanism, it is useful to consider how the net change of position occurs within a typical stimuli-responsive molecular shuttle (32). At equilibrium, the small macrocycle is distributed between two different stations (an asymmetric track) according to a Boltzmann distribution. An external trigger (the energy input) chemically modifies one binding site in such a way that the initially disfavored station becomes energetically more favorable for the macrocycle. Thermal fluctuations (the randomizing element) provide the energy required by the small macrocycle to sever its interactions with a station and set off on a Brownian walk

through which the new equilibrium position is established.

Catenane **1** was prepared as the *fum-E-1* (33) isomer according to Fig. 3 (34, 35). Net changes in the position or potential energy of the smaller ring were sequentially achieved by (i) photoisomerization to the maleamide ($\rightarrow mal-Z-1$) (36, 37); (ii) de-silylation/re-silylation ($\rightarrow succ-Z-1$); (iii) reisomerization to the fumaramide ($\rightarrow succ-E-1$); and finally, (iv) de-tritylation/re-tritylation to regenerate *fum-E-1*, the whole reaction sequence producing a net clockwise (as drawn in Fig. 3) circumrotation of the small ring about the larger one. Exchanging the order of steps (ii) and (iv) generated the equivalent counterclockwise rotation of the small ring. The time scales and number of reactions involved for directional rotation in **1** make it somewhat less practical than the methods previously developed for nonreversible synthetic rotary motors (11–17). Nevertheless, the chemistry is surprisingly robust and can be carried out as a direct sequence of reactions without purification at each stage, using resins to neutralize or remove excess re-

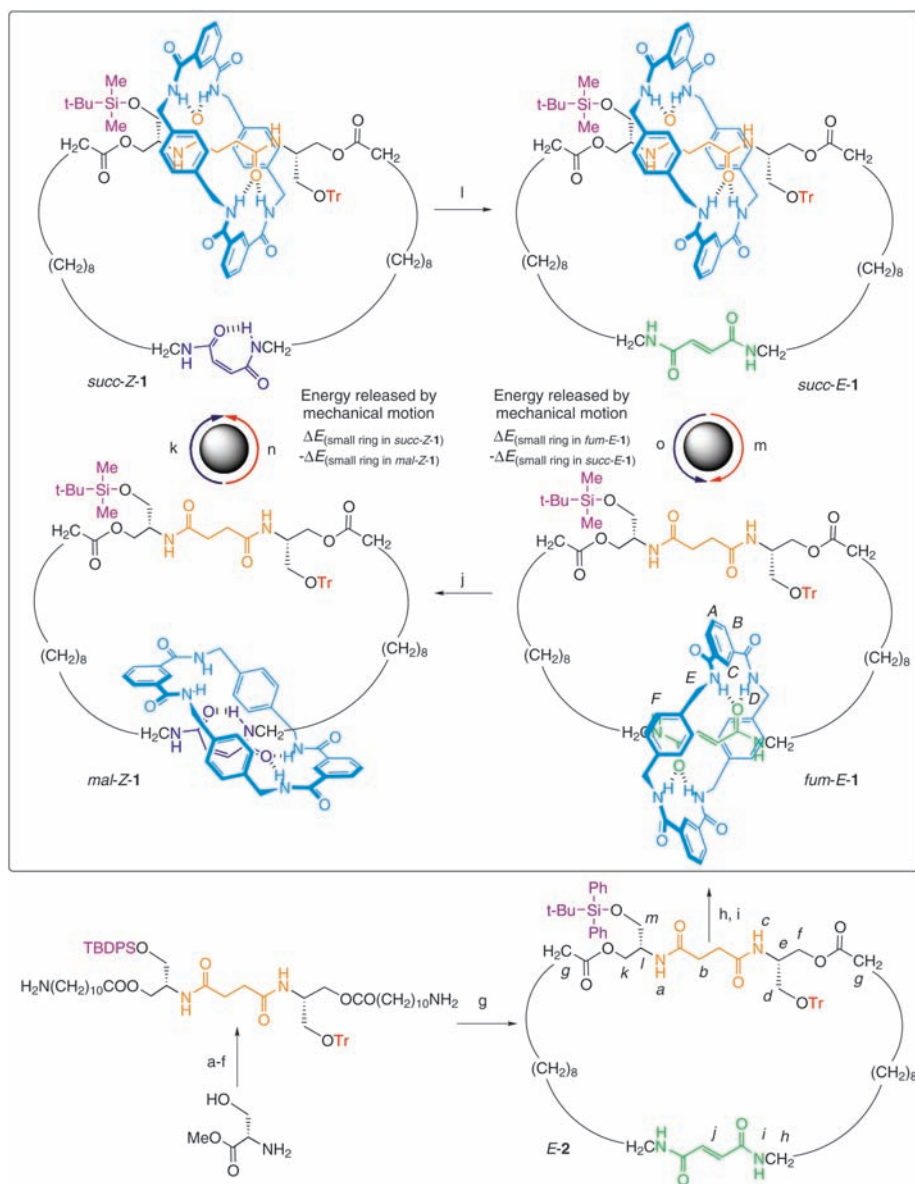


Fig. 3. Synthesis route and operation of reversible rotary motor **1**. Reagents and conditions (unless otherwise stated, reactions were carried out at room temperature and in CH_2Cl_2) were as follows: step a, succinyl chloride, triethylamine (Et_3N), and N,N -dimethylformamide (DMF) 0°C , 2 hours, 80%; step b, t -butyldiphenylsilyl chloride (TBDPSCl), NH_4NO_3 , DMF, 8 hours, 30%; step c, trityl chloride (TrCl), Bu_4NClO_4 , 2,4,6-collidine, CHCl_3 , 61°C , 2 hours, 86%; step d, NaBH_4 , LiCl, tetrahydrofuran and ethanol, 8 hours, 79%; step e, $\text{FmocNH}(\text{CH}_2)_{10}\text{CO}_2\text{H}$, dicyclohexylcarbodiimide (DCC), 1-hydroxybenzotriazole (HOBT), 4-(dimethylamino)pyridine, 8 hours, 85%; step f, Et_2NH , 8 hours, 73%; step g, fumaric acid, DCC, HOBT, CHCl_3 , 8 hours, 52%; step h, 8 equivalents of isophthaloyl dichloride, 8 equivalents of p -xylylenediamine, Et_3N , CHCl_3 , 3 hours, 30%; step i, tetrabutylammonium fluoride (TBAF), 20 min then cool to -10°C and add 2,4,6-collidine, t -butyldimethylsilyl triflate (TBDMSOTf), 40 min, overall 72%; step j, hv 254 nm, 5 min, 50%; step k, TBAF, 20 min then cool to -78°C and add 2,4,6-collidine, TBDMSOTf, 1 hour, overall 61%; step l, piperidine, 1 hour, $\sim 100\%$; step m, $\text{Me}_2\text{S}\cdot\text{BCl}_3$, -10°C , 10 min, and then TrCl, Bu_4NClO_4 , 2,4,6-collidine, 16 hours, overall 74%; step n, $\text{Me}_2\text{S}\cdot\text{BCl}_3$, -10°C , 15 min, then cool to -78°C and add 2,4,6-collidine, TrOTf, 5 hours, overall 63%; step o, TBAF, 20 min, then cool to -10°C and add 2,4,6-collidine, TBDMSOTf, 40 min, overall 76%. The above refer to preparative yields of isolated compounds. Net clockwise circumrotation was also achieved in one pot through the successive addition of reagents to *fum-E-1* in the following sequence (^1H NMR-determined percentage conversions are given in parentheses): step j, hv 254 nm, 5 min (50% *mal-Z-1* present); step k, 4 equivalents of TBAF, 20 min, cool to -78°C and add 30 equivalents of TBDMSOTf and 30 equivalents of 2,4,6-collidine, 30 min, then 60 equivalents of Wang resin, Dowex MR mixed bed ion-exchange resin and activated 4 Å molecular sieves, decant ($\sim 33\%$ *succ-Z-1* present); step l, 20 equivalents of piperidine, 1 hour, then Dowex MR mixed bed ion-exchange resin, decant ($\sim 33\%$ *succ-E-1* present); step m, 1 equivalent of $\text{Me}_2\text{S}\cdot\text{BCl}_3$, -10°C , 5 min, and then add 25 equivalents of 2,4,6-collidine and 20 equivalents of TrOTf, 1 hour ($\sim 90\%$ *fum-E-1* present; $\sim 28\%$ of the total molecules in the sample having undergone circumrotation). The chirality of **1** is present only for synthetic convenience.

agents and byproducts, with only modest reductions in yields indicated by ^1H nuclear magnetic resonance (NMR) spectroscopy.

Unlike the previously reported (17) [3]catenane rotor, which relied on the dynamics of model compounds to determine stimuli-induced unidirectional behavior, the sense of rotation in **1** was demonstrated directly by isolation of samples of the [2]catenane after each synthetic step and the position of the small ring unambiguously determined by ^1H NMR (Figs. 4 and 5). Shielding effects reveal the position of the small macrocycle in each of the four catenane isomers. Comparison of the spectrum of *fum-E-1* (Fig. 4A) with that of the macrocycle *E-2* (Fig. 4B) shows a downfield shift of the H_j protons of the fumaramide station but not the succinamide group (H_b) in the catenane. In contrast, *succ-E-1* (Fig. 4C) features a -1.3 parts per million difference in the H_b protons but little change in the signals of the fumaramide residue. The macrocycle is similarly located over the succinamide residue in *succ-Z-1* (see, for example, the shifts of H_b in Fig. 5, B and C). Finally, although the small ring does not spend too much time actually over the poorly binding maleamide station in *mal-Z-1* (as evidenced by the relatively small shift in H_j in Fig. 5A as compared to Fig. 5B), it is clearly trapped on the maleamide side of the silyl and trityl blocking groups because of the lack of shielding of the succinamide signals (H_b are unchanged between Fig. 5A and Fig. 5B) and some significant shielding observed for H_b .

Biological motors are too complex for the thermodynamic function of individual amino acid movements to be unravelled in detail. In contrast, the apparent simplicity of **1** and the minimalist nature of its design allow insight into the fundamental role that each part of the structure plays in the operation of the rotary machine.

The various chemical transformations perform two different functions: One pair (the linking/unlinking reactions, steps k and m or n and o in Fig. 3) modulates whether the small macrocycles can be exchanged between the two binding sites on the big ring (that is, allow the small macrocycle to become statistically balanced between the two binding sites according to a Boltzmann distribution); the second pair (balance-breaking reactions, steps j and l in Fig. 3) isomerize the olefin station (either $E \rightarrow Z$ or $Z \rightarrow E$), switching its binding affinity for the small macrocycle either on or off (37). By changing the relative binding affinities of the two stations in the large ring, each balance-breaking stimulus provides a driving force for redistribution of the small ring if it is able to move between the binding sites. In other words, the stations and blocking groups effectively disconnect the thermodynamic and kinetic components of detailed

balance (22, 23); the balance-breaking reactions control the thermodynamics and impetus for net transport by biased Brownian motion, and the linking/unlinking reactions largely (38) control the relative kinetics and ability to exchange. Raising a kinetic barrier also “ratchets” transportation, allowing the statistical balance of the small ring to be subsequently broken without reversing the preceding net transportation sequence. Lowering a kinetic barrier allows “escapement” of a ratcheted quantity of rings in a particular direction.

To obtain 360° rotation of the small ring about the large ring, the four sets of reactions must be applied in one of two sequences, each taking the following form: first a balance-breaking reaction; then a linking/unlinking step; then the second balance-breaking reaction; finally, the second linking/unlinking step. The direction of net rotation is determined solely by the way in which the balance-breaking and linking/unlinking steps are paired: an external input of information. The efficiency or yields of the reactions or the position of the ring at any stage (even if the machine makes a “mistake”) are immaterial to the direction in which net motion occurs, as long as the reactions continue to be applied in the same sequence. Although reversing the sequence of the four steps changes the pairings and so rotates the small ring in the opposite direction, reversing the entire sequence of six chemical reactions does not, because linking/unlinking operations are not commutative.

We finish the circumrotation reaction sequence with the same molecule, *fum-E-1*, that we started with (although a 360° rotation of one fragment has occurred), and the light-fueled balance-breaking reaction is reversed by a quantitative exoergic reaction, so no net energy is consumed to fuel the rotation. This is in one sense obvious, because the movement of the small ring takes place through Brownian motion and does not have to be powered; and in another somewhat surprising, because directional circumrotation of the small ring has occurred, which could be used to do external work—analogueous to the hypothetical lifting of a flea by the Smoluchowski-Feynman ratchet and pawl (4). However, if the [2]catenane does do work against an opposing force, the energy required is taken from the balance-breaking reactions. If the balance-breaking chemical reactions do not actually fuel the net rotation, is it really necessary to carry them out? At first glance it seems that the small ring in a [2]catenane such as **3** might undergo directional circumrotation without them (Fig. 6).

Let us consider the situation in which 100% of the small rings are initially located on the succinamide station closest to the blocking groups: 100% *succ1-3*. De-tritylation fol-

lowed by re-tritylation generates 50% *succ2-3* (and 50% remains as *succ1-3*). Treatment of this mixture with a de-silylation/re-silylation

sequence leads to a final product mixture, which again is 50% *succ1-3* and 50% *succ2-3*. However, half of the molecules that are now

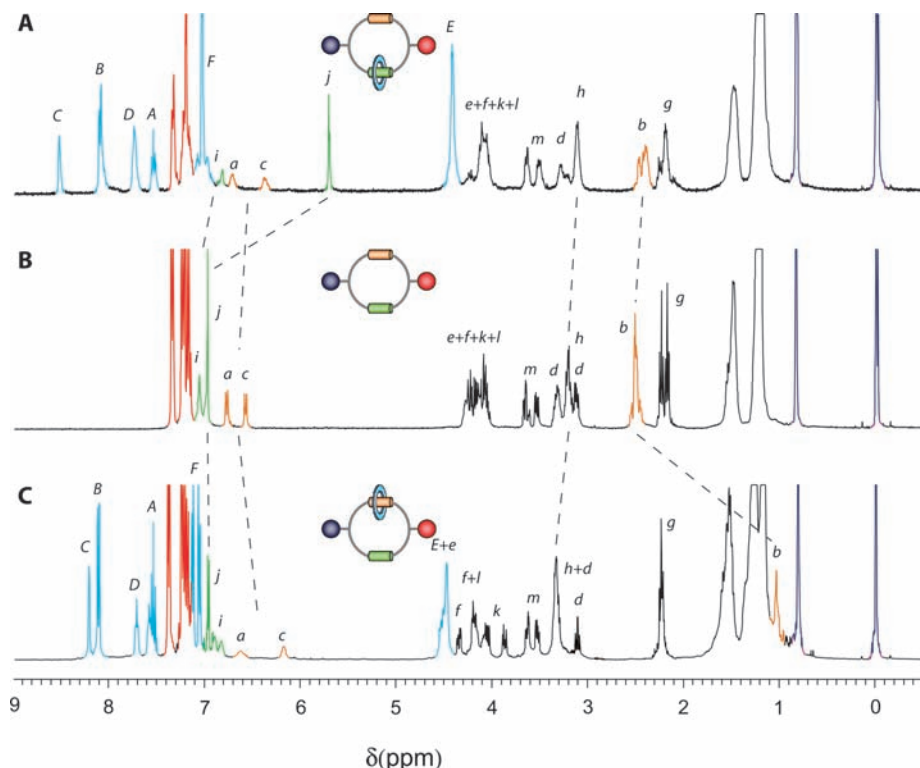


Fig. 4. ^1H NMR spectra (400 MHz, CDCl_3 , at 298 K) of (A) [2]catenane *fum-E-1*, (B) macrocycle *E-2*, and (C) [2]catenane *succ-E-1*. The color coding and lettering correspond to those shown in Fig. 3.

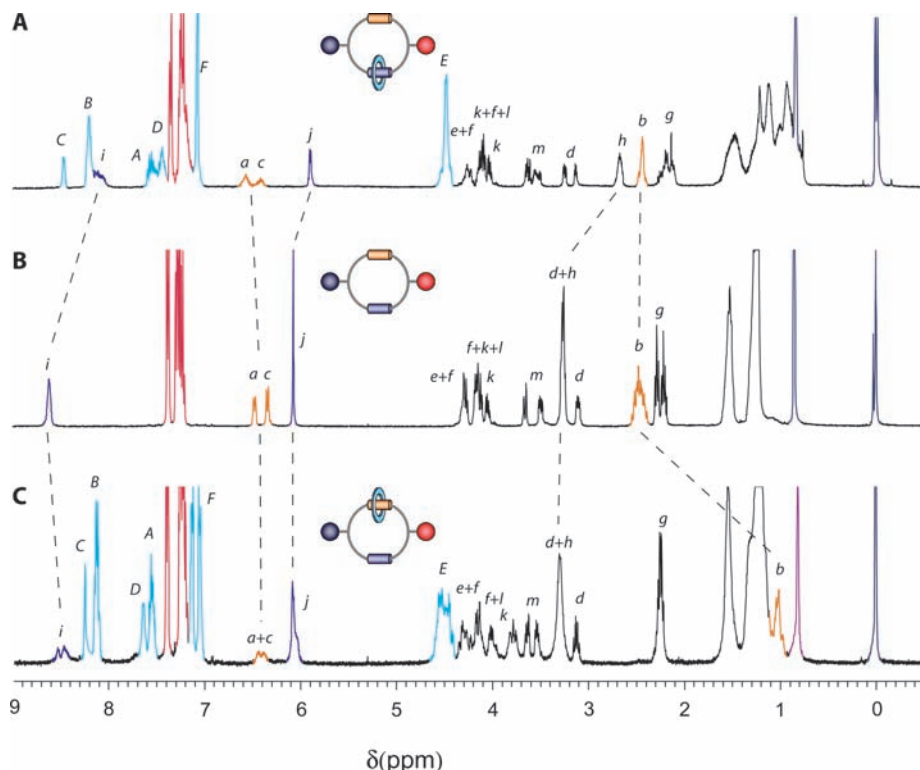


Fig. 5. ^1H NMR spectra (400 MHz, CDCl_3 , at 298 K) of (A) [2]catenane *mal-Z-1*, (B) macrocycle *Z-2*, and (C) [2]catenane *succ-Z-1*.

succ1-3 (25% of the total molecules) have undergone a 360° clockwise circumrotation of the small ring, and all of the *succ2-3* structures (50% of the total molecules) have undergone a 180° rotation of the small ring (half clockwise, half counterclockwise). The remaining 25% of total molecules have undergone no net positional change of the small ring, and so the average for the sample is a 90° clockwise rotation without applying any chemical reactions to change the relative values of the two stations' energy minima. When we apply the sequence of reactions for a second (or any subsequent) time, however, although 75% of the molecules again individually undergo partial or complete revolution of the small ring, no net rotation occurs in either direction over a bulk sample. The 50% of molecules that start as *succ1-3* give a net 90° clockwise rotation in response to the linking/unlinking sequence, and the 50% that start as *succ2-3* rotate an equivalent amount in a counterclockwise sense. A statistically significant number of catenane **3** molecules can only undergo net unidirectional rotation if the distribution of the small macrocycle between the binding sites is unbalanced at the start of the reaction sequence.

We can use some simple thermodynamic accountancy to calculate both the maximum amount of mechanical work that can be done by **1** and how much chemical energy has to be processed to cause directional motion of the small ring even if no work needs to be done against an opposing external force. The energy available to do work each time the small ring changes station equates to the macrocycle binding energy differences between the two sites (32). The light-fueled $E \rightarrow Z$ transformation allows up to $\Delta E_{(\text{small ring in succ-Z-1})} - \Delta E_{(\text{small ring in mal-Z-1})}$ to be performed during the subsequent linking step and the piperidine-catalyzed $Z \rightarrow E$ reaction permits a further $\Delta E_{(\text{small ring in fum-E-1})} - \Delta E_{(\text{small ring in succ-E-1})}$

(Fig. 3). Because $\Delta E_{(\text{small ring in succ-Z-1})} \sim \Delta E_{(\text{small ring in succ-E-1})}$, the maximum total mechanical work that can be performed by circumrotation is $\Delta E_{(\text{small ring in fum-E-1})} - \Delta E_{(\text{small ring in mal-Z-1})}$; that is, the difference in small ring binding affinity between the fumaramide and maleamide stations. It is interesting to note that the binding affinity of the intermediate station is irrelevant to the amount of work that can be carried out by the molecular motor.

A quantitative thermodynamic requirement for unidirectional rotation of the small ring is provided by the difference between the free energies of the sequence of reactions j, k, l, m carried out on *fum-E-1* and the same series of reactions applied to the macrocycle, *E-2*. The thermodynamics associated with the linking/unlinking steps cancel out (39). However, the $E \rightarrow Z$ isomerization step (step j) for the catenane is inherently more endothermic than the analogous reaction on the macrocycle because of the additional energy necessary to disrupt the hydrogen bond network of the small ring with the fumaramide station. The extra energy required to raise the potential energy of the transported particle (again, the difference in small ring binding energies of the fumaramide and maleamide stations) is returned to the thermal bath upon reisomerization to fumaramide and subsequent repositioning of the macrocycle. This requirement of extra energy to be processed by the system for the molecular machine to rotate directionally even when no work has to be done against an external force is once more reminiscent of the Smoluchowski-Feynman ratchet and pawl, which Feynman appreciated could be driven directionally by Brownian motion using heat flow between two thermal reservoirs; for example, by having the vanes attached to the shaft of the Feynman ratchet be hot and the wheel cold (40–42). We note that the amount of additional chemical energy that must be processed for directional rota-

tion to occur in the catenane is the sum of the energy differences that govern the Boltzmann distribution of the small ring between the binding sites at each stage; that is, the factor that determines the directional efficiency of the motor at constant temperature.

Mechanisms formulated from nonequilibrium statistical mechanics can be successfully used to design synthetic molecular motors such as **1**. In turn, the analysis of this deceptively simple molecule, particularly the separation of the kinetic and thermodynamic requirements for detailed balance, provides experimental insight into how and why an energy input is essential for directional rotation of a submolecular fragment by Brownian motion. Even though no net energy is used to power the motion, there has to be a particular amount of energy conversion for net rotation to be directional over a statistically significant number of molecules; a requirement that is absent if the equivalent motion is nondirectional (or, indeed, for directional rotation within a single molecule where balance is inherently broken). The quantity of energy conversion required to induce directionality has an intrinsic lower limit, corresponding exactly (and somewhat beautifully) to both the energy difference that determines the directional efficiency of rotation and the maximum amount of work that the motor can theoretically perform in a single cycle; there can be no perpetually unidirectionally rotating molecular structure of the second kind through such a mechanism. The factors that determine the sense of rotation in **1**, together with the requirement for finite energy conversion for directional rotation in circumstances when no work is done against an external force, illustrate how interplay between informational and thermodynamic laws governs directional Brownian rotation in molecular structures.

References and Notes

1. E. M. Purcell, *Am. J. Phys.* **45**, 3 (1977).
2. M. Schliwa, Ed., *Molecular Motors* (Wiley-VCH, Weinheim, Germany, 2003).
3. P. D. Boyer, *Angew. Chem. Int. Ed.* **37**, 2296 (1998).
4. R. P. Feynman, R. B. Leighton, M. Sands, *The Feynman Lectures on Physics* (Addison-Wesley, Reading, MA, 1963), vol. 1, chap. 46.
5. M. von Smoluchowski, *Physik. Zeitschr.* **13**, 1069 (1912).
6. T. R. Kelly, I. Tellitu, J. P. Sestelo, *Angew. Chem. Int. Ed. Engl.* **36**, 1866 (1997).
7. A. P. Davis, *Angew. Chem. Int. Ed.* **37**, 909 (1998).
8. V. Balzani, A. Credi, F. M. Raymo, J. F. Stoddart, *Angew. Chem. Int. Ed.* **39**, 3349 (2000).
9. M. F. Hawthorne et al., *Science* **303**, 1849 (2004).
10. C. P. Mandl, B. König, *Angew. Chem. Int. Ed.* **43**, 1622 (2004).
11. T. R. Kelly, H. De Silva, R. A. Silva, *Nature* **401**, 150 (1999).
12. T. R. Kelly, R. A. Silva, H. De Silva, S. Jasmin, Y. J. Zhao, *J. Am. Chem. Soc.* **122**, 6935 (2000).
13. N. Koumura, R. W. J. Zijlstra, R. A. van Delden, N. Harada, B. L. Feringa, *Nature* **401**, 152 (1999).
14. N. Koumura, E. M. Geertsema, M. B. van Gelder, A. Meetsma, B. L. Feringa, *J. Am. Chem. Soc.* **124**, 5037 (2002).

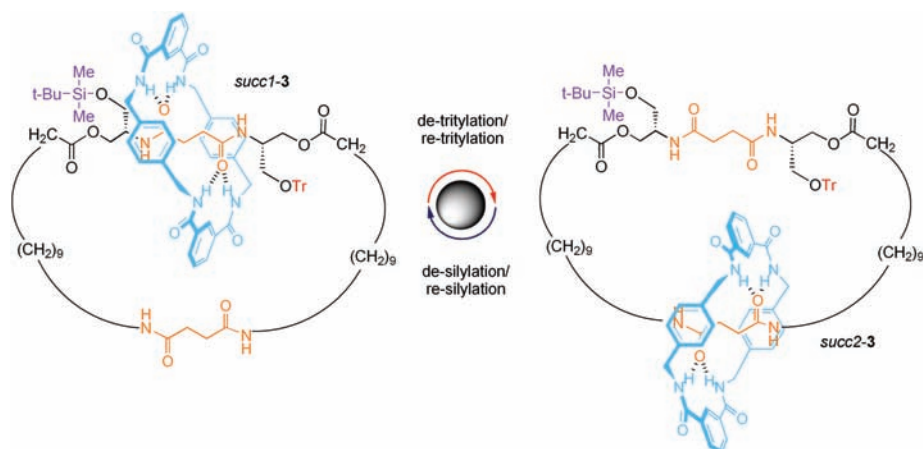


Fig. 6. Positional isomerism in a [2]catenane, **3**, with stations of degenerate binding energies.

15. M. K. J. ter Wiel, R. A. van Delden, A. Meetsma, B. L. Feringa, *J. Am. Chem. Soc.* **125**, 15076 (2003).
16. R. A. van Delden, M. K. J. ter Wiel, H. De Jong, A. Meetsma, B. L. Feringa, *Org. Biomol. Chem.* **2**, 1531 (2004).
17. D. A. Leigh, J. K. Y. Wong, F. Dehez, F. Zerbetto, *Nature* **424**, 174 (2003).
18. P. Reimann, *Phys. Rep.* **361**, 57 (2002).
19. J. M. R. Parrondo, L. Dinis, *Contemp. Phys.* **45**, 147 (2004).
20. R. D. Astumian, *Science* **276**, 917 (1997).
21. Randomizing influences other than Brownian motion can be used in ratchet mechanisms. For example, in quantum ratchets, quantum effects such as tunneling play this role.
22. The principle of detailed balance (23) tells us that no net task can be performed by the fluxional exchange of components at equilibrium, because transitions take place at the same rate in opposite directions. The structure of catenane 1 is remarkable in that it separates the kinetic (ability to exchange) and thermodynamic (impetus for net transport) requirements for detailed balance.
23. L. Onsager, *Phys. Rev.* **37**, 405 (1931).
24. R. D. Astumian, P. Hänggi, *Phys. Today* **55**, 33 (November 2002).
25. R. D. Astumian, I. Derényi, *Eur. Biophys. J.* **27**, 474 (1998).
26. Special issue on "Ratchets and Brownian Motors: Basics, Experiments and Applications," H. Linke, Ed., *Appl. Phys. A* **75**, 167 (2002).
27. G. Oster, H. Y. Wang, *Trends Cell Biol.* **13**, 114 (2003).
28. J. Rousselet, L. Salome, A. Ajdari, J. Prost, *Nature* **370**, 446 (1994).
29. L. P. Faucheux, L. S. Bourdieu, P. D. Kaplan, A. J. Libchaber, *Phys. Rev. Lett.* **74**, 1504 (1995).
30. J. S. Bader et al., *Proc. Natl. Acad. Sci. U.S.A.* **96**, 13165 (1999).
31. S. Matthias, F. Müller, *Nature* **424**, 53 (2003).
32. A. Altieri et al., *Angew. Chem. Int. Ed.* **42**, 2296 (2003).
33. The prefix indicates the position of the smaller macrocycle on the larger one.
34. Although catenane *fum-E-1* was originally prepared as its *O-t-butyl*diphenylsilyl (TBDPS) derivative, the steric bulk caused low yields during the re-silylation protocol of step k, so it was replaced with the smaller TBDMS group for all the directional rotation studies.
35. Materials and methods are available as supporting material on *Science* Online.
36. The photoisomerization reaction gives a 50:50 *E:Z* mixture in the photostationary state. No accompanying photodegradation or decomposition was detected (37).
37. F. G. Gatti et al., *Proc. Natl. Acad. Sci. U.S.A.* **100**, 10 (2003).
38. By raising or lowering the energy minima, the balance-

- breaking reactions intrinsically affect the kinetic barriers as well.
39. This is not quite as simple as the ΔG values of the forward and reverse covalent bond forming and breaking reactions canceling each other out. When unlinking takes place, the restriction in freedom of movement reduces the entropy of the small macrocycle in addition to the ΔG change associated with the chemical reaction; however, when linking occurs, the entropy increases by the same amount.
40. Certain aspects of Feynman's discussion of the ratchet and pawl as a motor have been shown to be flawed (41, 42).
41. J. M. R. Parrondo, P. Español, *Am. J. Phys.* **64**, 1125 (1996).
42. M. O. Magnasco, G. Stolovitzky, *J. Stat. Phys.* **93**, 615 (1998).
43. This work was supported by the Carnegie Trust (a scholarship to E.R.K.) and the European Union (a Marie Curie Fellowship to J.V.H.).

Supporting Online Material

www.sciencemag.org/cgi/content/full/306/5701/1532/DC1

Materials and Methods
Scheme S1

11 August 2004; accepted 8 October 2004

Three-Dimensional Hydrogen Microscopy in Diamond

P. Reichart,^{1*} G. Datzmann,¹ A. Hauptner,¹ R. Hertenberg,²
C. Wild,³ G. Dollinger^{1‡}

A microprobe of protons with an energy of 17 million electron volts is used to quantitatively image three-dimensional hydrogen distributions at a lateral resolution better than 1 micrometer with high sensitivity. Hydrogen images of a <110>-textured undoped polycrystalline diamond film show that most of the hydrogen is located at grain boundaries. The average amount of hydrogen atoms along the grain boundaries is $(8.1 \pm 1.5) \times 10^{14}$ per square centimeter, corresponding to about a third of a monolayer. The hydrogen content within the grain is below the experimental sensitivity of 1.4×10^{16} atoms per cubic centimeter (0.08 atomic parts per million). The data prove a low hydrogen content within chemical vapor deposition-grown diamond and the importance of hydrogen at grain boundaries, for example, with respect to electronic properties of polycrystalline diamond.

Diamond is a promising material for various applications. Although its chemical and mechanical properties have led already to widespread applications, its potential for electronic or optical application remains limited because of imperfections (1). The recently demonstrated high carrier mobility in single-crystal chemical vapor-deposited diamond (2) opens

perspectives for electronic devices in hostile, high-voltage, or high-temperature environments (3); diamond optics (4); radiation sensors (5); and particle detectors (6).

However, the production and characterization of high-quality diamond, especially for electronic devices, is a great challenge. Chemical vapor deposition (CVD), for example, is a well-established method (7) to synthesize high-quality diamond layers and opens the possibility for hetero- and homo-epitaxial growth of CVD diamond layers up to some mm thickness (8, 9). One main aim is to understand the origin of structural imperfections and impurities and to reduce or control these in order to improve the electronic and optical properties. The presence of hydrogen is known to influence these properties (10, 11). Depending on type and quality, average hydrogen concentrations were found from below the detection limits of

10^{17} atoms/cm³ up to about 10^{19} atoms/cm³ in the bulk of polycrystalline diamond layers (12). Also, several hydrogen-related complexes were identified (13–15). However, there is insufficient information about the quantity and the spatial distribution of these, and perhaps as-yet-unidentified, types of hydrogen-related defects. It is even unknown whether most of the hydrogen being detected in diamond is concentrated at grain boundaries, inclusions, and other extended defects or whether hydrogen is distributed homogeneously throughout the bulk at defects of atomic dimensions. The decrease of the hydrogen content with increasing size of the crystallites inside polycrystalline CVD diamond layers, as well as infrared (15) or electron spin resonance studies (16), indirectly indicate that most of the hydrogen is situated at grain boundaries. Another explanation, however, is that there is reduced defect density within the grains with growing film thickness. Information about the absolute quantity of hydrogen inside the grain compared with

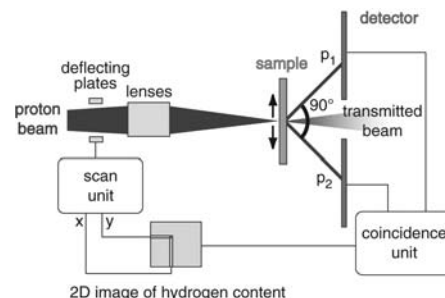


Fig. 1. Hydrogen analysis by pp scattering. The two protons emitted from a proton scattered at a hydrogen nuclei of the sample are detected in coincidence by a suitable detection system (25).

¹Physik Department E12, Technische Universität (TU) München, 85748 Garching, Germany. ²Department für Physik, Ludwig-Maximilians-Universität (LMU) München, 85748 Garching, Germany. ³Fraunhofer Institut für Angewandte Festkörperphysik, 79108 Freiburg, Germany.

*Present address: Microanalytical Research Centre, School of Physics, University of Melbourne, Victoria, 3010, Australia.

†To whom correspondence should be addressed. E-mail: p.reichart@ph.unimelb.edu.au

‡Present address: Angewandte Physik und Messtechnik, Universität der Bundeswehr München, 85577 Neubiberg, Germany.



Fig. 2. (A) Surface view of the unpolished polycrystalline CVD diamond sample. (B) Cross-sectional image of the original 500- μm -thick polished sample, showing the columnar structure of the diamond layer. Grain sizes increase with distance from the nucleation layer to about 50 μm wide

close to the surface. (C) Grain structure to clarify the structure of the diamond sample of (B). The dotted line marks the lower surface after polishing the sample from the back in order to perform hydrogen analysis.

those at the grain boundaries is needed to clear this question without doubt.

We concentrate here on the microscopic analysis of hydrogen distributions in CVD diamond. So far, it has been difficult to analyze hydrogen with the necessary sensitivity and lateral resolution to answer this question, despite several attempts to extend existing hydrogen analysis techniques to their limits (17–19). Therefore, a method was developed for sensitive three-dimensional hydrogen microscopy (20, 21) by using coincident elastic proton-proton (pp) scattering (22). The principle of this technique (Fig. 1) shows that a proton scatters with a hydrogen atom situated inside the sample. The two protons from this elastic pp-scattering reaction leave the scattering site with an angle of 90° to each other. Provided that the scattered protons have enough energy to leave the sample, the coincident detection with this signature is used to filter the pp reaction from all other scattering reactions, and one gets a nearly background-free hydrogen signal. A sensitivity better than 0.1 atomic parts per million (ppm) has been obtained (23). This method has been adopted at the proton microprobe SNAKE [superconducting nanoscope for applied nuclear (Kern) physics experiments] (24) of the Munich tandem accelerator by using protons with an energy of 17 MeV (25). It gives a lateral resolution of better than 1 μm , which is limited by the beam spot size of the microprobe (23). Depth information of several-micrometer resolution is obtained simultaneously from energy loss analysis of the scattered protons (26).

In order to solve the question on the distribution of hydrogen in diamond, we analyzed a high-quality, polycrystalline, $\langle 110 \rangle$ -textured CVD diamond layer (25, 27). The diamond has been deposited in a 6-kW microwave CVD reactor onto a 3-inch Si(100)-wafer at 820°C by using 1% methane in hydrogen gas at 160 mbar. An image of the as-grown surface obtained by optical microscopy (Fig. 2A) shows that the 111 facets of

individual grains have an average size of about 50 μm by 50 μm . The cross-sectional view (Fig. 2B) has been taken from the layer that was originally grown to about 500 μm in thickness and mechanically polished at the top surface in order to remove the faceted structure. The columnar crystallites establish from the nucleation layer at the substrate and grow as illustrated (Fig. 2C). As marked with the dotted line, the layer was mechanically polished from the back to get a freestanding sample. The end step of thinning was performed by a reactive ion etching process in oxygen plasma to get a layer 55 μm thick and grain boundaries nearly perpendicular to the surface. The resulting layer is thin enough that the scattered protons from pp scattering can be transmitted through it, and therefore hydrogen imaging becomes possible on that layer. By using atomic force microscopy, we determined a surface roughness of about 0.6 nm (root mean square) on an area of 2 μm by 2 μm .

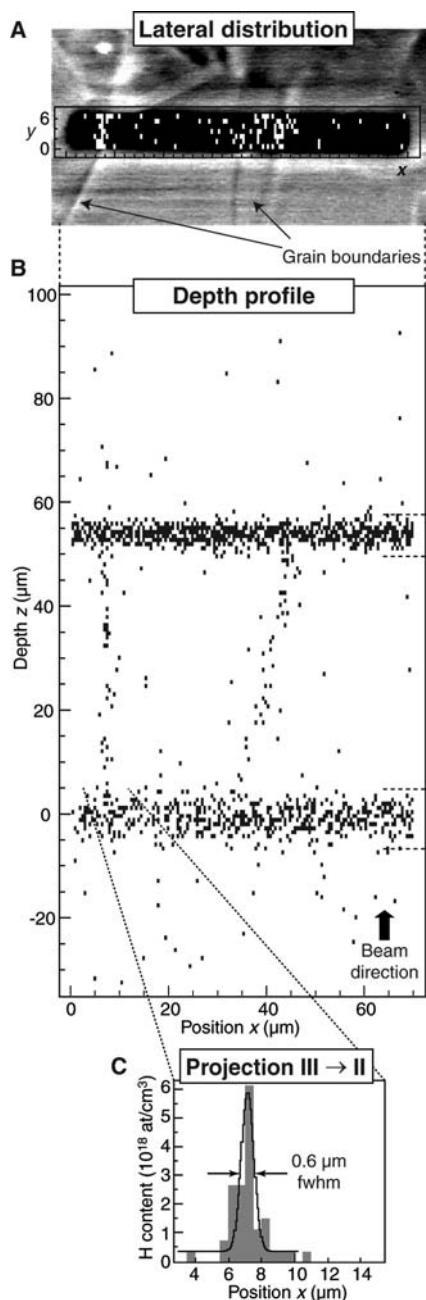
An optical phase contrast microscope picture of this layer in top view is shown (Fig. 3A) with the grain boundaries clearly visible. The black rectangle marks the 70- μm -long (x axis) and 7- μm -wide area (y axis) analyzed by the focused 17-MeV proton microbeam with a fluence of 6×10^{17} protons/ cm^2 . The beam dimensions were about 0.6 μm by 2.0 μm at a beam current of 54 pA or 3.4×10^8 protons/s. The analysis was performed at room temperature in a hydrocarbon-free scattering chamber at SNAKE at a vacuum pressure of 10^{-7} mbar. No significant change of the hydrogen content at the surface and in the bulk was observed during the analysis (23), although a blackening of the irradiation area arose because of defects created by the proton beam in the diamond layer.

The lateral hydrogen distribution as obtained from hydrogen microscopy is superimposed onto the optical image of Fig. 3A. The events from the front or back surface are disregarded in this spectrum in order to reveal the signal from the hydrogen inside the layer. One entry corresponds to about 6.5×10^7 H atoms. A sharp

accumulation of hydrogen events is visible on the left side, and a broader one on the right, both exactly correlated with the position of the visible structures in the optical image.

A clear view of the hydrogen distribution is given by the cross-sectional hydrogen distribution of the diamond layer (Fig. 3B). The two horizontal branches in the marked areas I-II and III-IV correspond to the hydrogen at the front and back surface of the diamond layer with a content of about $(7.2 \pm 0.4 \pm 1.4) \times 10^{15}$ H atoms/ cm^2 and $(11.3 \pm 0.4 \pm 2.2) \times 10^{15}$ H atoms/ cm^2 , respectively. The first error interval represents the statistical uncertainty; the second represents the systematic uncertainty. Ideal $\langle 110 \rangle$ surfaces do not reconstruct (28), and one expects about 2.2×10^{15} dangling bonds per cm^2 saturated with one hydrogen atom each. The larger hydrogen coverage reflects surface roughness and additional adsorption of water and hydrocarbon molecules as previously proposed (29). The widths of the two branches are caused by limited depth resolutions of 3 μm and 6 μm at the upper and lower surface, respectively (26). This depth resolution is sufficient to separate the hydrogen-rich surface from the low hydrogen content at depths between the marked points II and III. In Fig. 3B, the two hydrogen enhancements of the superimposed spectrum in Fig. 3A appear localized in lines running between the two surfaces. The left one is nearly perpendicular to the surface, whereas the right one is tilted by about 15° with respect to the surface normal. Therefore, we conclude that the right structure in the optical micrograph of Fig. 3A is a tilted grain boundary. For the left perpendicular grain boundary, the projection of the hydrogen content between II and III to the bottom of the diamond film is shown in Fig. 3C. It depicts a width of the hydrogen enhancement of only 0.6 μm and shows that the principle position resolution is at least as good as this value. The areal density of hydrogen at the grain interfaces is $(7.8 \pm 1.3 \pm 1.6) \times 10^{14}$ H atoms/ cm^2 for the left grain

Fig. 3. (A) Optical microscopy image of the irradiated diamond sample. With use of the optical phase contrast technique, the grain boundaries become visible. The dark rectangle marks the position of the analyzed area of $70\ \mu\text{m}$ by $7\ \mu\text{m}$. Superimposed is the lateral distribution of the detected hydrogen events without the hydrogen signal from the surfaces. (B) Scatter plot of filtered coincident pp-scattering events calibrated as a two-dimensional cross section of hydrogen distribution. The density of the points scales with the hydrogen content, and one entry corresponds to about 6.5×10^7 H atoms. The horizontal branches represent the hydrogen contamination at the surfaces. Corresponding to the position of the grain boundaries in the optical image, two significant enhancements of hydrogen inside the layer are detected. (C) The projection of the events in depths between II and III toward the x axis in (B) demonstrates the sharpness of the left hydrogen accumulation, showing a principle position resolution better than $0.6\ \mu\text{m}$.



boundary and $(8.5 \pm 1.3 \pm 1.7) \times 10^{14}$ H atoms/cm² for the right, respectively. This corresponds to about a third of a monolayer of hydrogen situated at each interface between the grains of the polycrystalline layer.

In order to get information on the hydrogen content within the grains, a second measurement has been performed on a single grain. The measured area is marked black in Fig. 4A, which does not contain any visible grain boundary. In accordance, no hydrogen enhancement is visible in the cross-sectional hydrogen distribution (Fig. 4B). One entry in the spectrum corresponds to 1.0×10^8 H atoms. Between the hydrogen enhancements at the surface, several counts are present, resulting in $(3.8^{+1.5}_{-1.3} \pm 0.4) \times 10^{16}$ H atoms/cm³.

However, above the upper and below the lower hydrogen surface layer, a similar density of detected events is visible. These events have to be attributed to accidental coincidence events that are not suppressed by the five-level filter procedure described in (23). They give a background level of $(4.2^{+1.5}_{-1.3} \pm 0.4) \times 10^{16}$ H atoms/cm³. At this background level, the hydrogen content is consistent with zero and an upper limit of $(1.2 \pm 0.4) \times 10^{16}$ H atoms/cm³ with use of the evaluation scheme of Feldman and Cousins at small signals (30). In terms of this statistical treatment, the background represents an experimental "sensitivity" of 1.7×10^{16} H atoms/cm³. Taking all measurements made up to now into account, the sensitivity of the microscopic

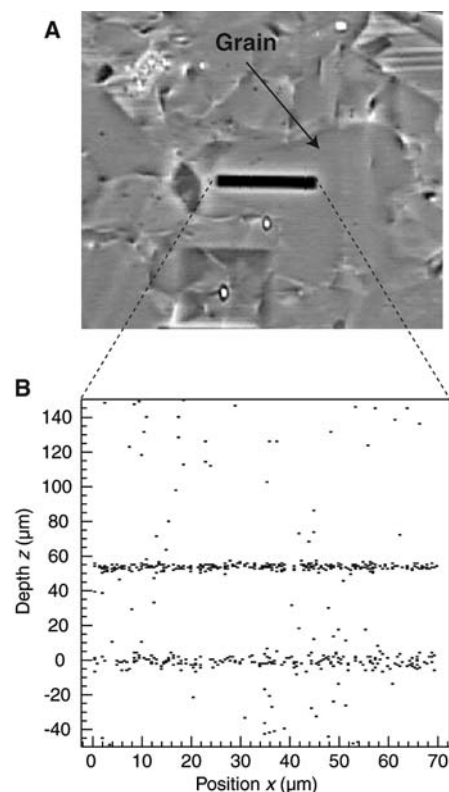


Fig. 4. (A) Optical-phase contrast microscopy image of the area around the black marked line scan ($70\ \mu\text{m}$ by $7\ \mu\text{m}$) within a single grain. (B) Cross section of the hydrogen distribution as a depth profile, with one event corresponding to 1.0×10^8 H atoms. No significant hydrogen enhancement is visible between the branches of the surface hydrogen, and the content is as large as the background by accidental coincidences. This results in an upper limit of 1.2×10^{16} H atoms/cm³ for the hydrogen content within the grain.

analysis reduces to 1.4×10^{16} H atoms/cm³ (0.08 atomic ppm hydrogen) (23).

Our results give further insight into the role of hydrogen with respect to electronic properties of diamond. One expects that the observed hydrogen at the grain boundaries saturates dangling bonds at the grain interfaces and therefore suppresses generation of charge carriers. The hydrogen-containing defects at the grain boundaries probably lead to traps for charge carriers as observed in ion beam-induced current measurements (31). At surfaces of some types of diamond, hydrogen bonding is related to p-type surface conductivity (32). Several models like the so-called transfer doping model (33) are used to describe this conductivity. Similar hydrogen-related doping effects at structural inhomogeneities like the grain interfaces may be proposed for electrical activity inside polycrystalline layers. However, the measured high specific bulk resistance of $\rho > 10^{13}$ ohm-cm of the analyzed sample excludes a doping efficiency similar to that on the diamond sur-

face. This fits with the transfer doping model, because it is conceivable that there would be no suitable molecules within the layer to contribute to the transfer doping process. The low content of hydrogen within the grain proves the potential of microwave CVD to grow high-quality diamond. The content is even well below the doping levels used for p and n doping of diamond and is, therefore, also in line with the high resistance of the studied sample.

References and Notes

- B. Dischler, C. Wild, Eds., *Low-Pressure Synthetic Diamond*, vol. 11 of *Springer Series in Materials Processing*, W. Michaeli, H. Warlimont, E. Weber, Eds. (Springer, Berlin, 1998).
- J. Isberg *et al.*, *Science* **297**, 1670 (2002).
- A. Vescan, I. Daumiller, P. Gluche, W. Ebert, E. Kohn, *Diamond Relat. Mater.* **7**, 581 (1998).
- E. Wörner, C. Wild, W. Müller-Sebert, P. Koidl, *Diamond Relat. Mater.* **10**, 557 (2001).
- C. Manfredotti *et al.*, *Nucl. Instrum. Methods A* **458**, 360 (2001).
- P. Bergonzo *et al.*, *Phys. Status Solidi (a)* **185**, 167 (2001).
- J. C. Angus, C. C. Hayman, *Science* **241**, 913 (1988).
- H. Kawarada *et al.*, *J. Appl. Phys.* **81**, 3490 (1997).
- C. Yan, Y. K. Vohra, H. Mao, R. J. Hemley, *Proc. Natl. Acad. Sci. U.S.A.* **99**, 12523 (2002).
- H. Kawarada, *Surf. Sci. Rep.* **26**, 205 (1996).
- A. M. Stoneham, in *The Properties of Natural and Synthetic Diamond*, J. E. Field, Ed. (Academic Press, New York, 1992), pp. 4–34.
- G. Dollinger, A. Bergmaier, C. M. Frey, M. Roesler, H. Verhoeven, *Diamond Relat. Mater.* **4**, 591 (1995).
- F. Fuchs, C. Wild, K. Schwarz, W. Müller-Sebert, P. Koidl, *Appl. Phys. Lett.* **66**, 177 (1995).
- C. Glover, M. E. Newton, P. Martineau, D. J. Twitchen, J. M. Baker, *Phys. Rev. Lett.* **90**, 185507 (2003).
- B. Dischler, C. Wild, W. Müller-Sebert, P. Koidl, *Physica B* **185**, 217 (1993).
- D. F. Talbot-Ponsonby *et al.*, *Phys. Rev. B* **57**, 2264 (1998).
- R. D. Maclear *et al.*, *Diamond Relat. Mater.* **8**, 1615 (1999).
- S. H. Connell *et al.*, *Diamond Relat. Mater.* **7**, 1714 (1998).
- R. Samlenski, C. Haug, R. Delto, C. Wild, R. Brenn, *Nucl. Instrum. Methods B* **190**, 324 (2002).
- D. Dujmić, M. Jakšić, N. Soić, T. Tadić, I. Bogdanović, *Nucl. Instrum. Methods B* **111**, 126 (1996).
- K. A. Sjöland *et al.*, *Nucl. Instrum. Methods B* **124**, 639 (1997).
- B. L. Cohen, C. L. Fink, J. H. Degnan, *J. Appl. Phys.* **43**, 19 (1972).
- P. Reichart *et al.*, *Nucl. Instrum. Methods B* **219**, 980 (2004).
- G. Datzmann *et al.*, *Nucl. Instrum. Methods B* **181**, 20 (2001).
- Materials and methods are available on Science Online.
- P. Reichart *et al.*, *Nucl. Instrum. Methods B* **197**, 134 (2002).

- C. Wild, N. Herres, P. Koidl, *J. Appl. Phys.* **68**, 973 (1990).
- F. Maier *et al.*, *Surf. Sci.* **443**, 177 (1999).
- A. Bergmaier, G. Dollinger, A. Aleksov, P. Gluche, E. Kohn, *Surf. Sci.* **481**, L433 (2001).
- G. J. Feldman, R. D. Cousins, *Phys. Rev. D* **57**, 3873 (1998).
- S. M. Hearne, D. N. Jamieson, E. Trajkov, S. Praver, J. E. Butler, *Appl. Phys. Lett.* **84**, 4493 (2004).
- C. E. Nebel *et al.*, *Appl. Phys. Lett.* **79**, 4541 (2001).
- F. Maier, M. Riedel, B. Mantel, J. Ristein, L. Ley, *Phys. Rev. Lett.* **85**, 3472 (2000).
- This work was supported by the Beschleunigerlaboratorium der LMU und TU München, as well as the German Bundesministerium für Bildung und Forschung. We thank T. Graf, WSI München, and L. Goergens; TU München, for the atomic force microscopy and x-ray diffraction measurements, as well as M. Schubert, LMU München, and A. Bergmaier; TU München, for data acquisition and programming support. Many thanks also to R. Lutter, O. Schaille, K. Steinberger, LMU München, and the whole accelerator team for their great assistance.

Supporting Online Material

www.sciencemag.org/cgi/content/full/306/5701/1537/DC1

Materials and Methods
Figs. S1 to S5
References and Notes

19 July 2004; accepted 7 October 2004

Probing Electronic Transitions in Individual Carbon Nanotubes by Rayleigh Scattering

Matthew Y. Sfeir,^{1*} Feng Wang,^{2*} Limin Huang,³
Chia-Chin Chuang,⁴ J. Hone,⁴ Stephen P. O'Brien,³
Tony F. Heinz,^{2,†} Louis E. Brus^{1,†}

Rayleigh scattering spectra were obtained from individual single-walled carbon nanotubes with the use of a laser-generated visible and near-infrared supercontinuum. This diagnostic method is noninvasive and general for nanoscale objects. The approach permits clear identification of excited states in arbitrary metallic and semiconducting nanotubes. We analyzed spectral lineshapes in relation to the role of excitonic effects and correlated the results with Raman scattering data on individual tubes. The nanotube structure remained the same over distances of tens of micrometers. Small nanotube bundles retained distinct Rayleigh spectroscopic signatures of their component nanotubes, thus allowing the probing of nanotube-nanotube interactions.

Single-walled carbon nanotubes (SWNTs) comprise a family of more than 200 structures characterized by different chiral angles and diameters, each having a distinct electronic structure that can be either metallic or semiconducting (*1*). This richness and diversity, which makes carbon nanotubes so

promising for various applications (*2–4*), poses a substantial challenge in characterization of specific SWNTs. A general optical characterization technique that permits noninvasive measurements of the electronic structure of an arbitrary individual nanotube has been lacking. Among existing techniques, vibrational spectra of individual SWNTs have been obtained from resonance Raman scattering (*5–7*). Although Raman excitation spectra provide some information on the electronic transitions, the requirement of tunable excitation and the weakness of the Raman signal make these experiments extremely challenging (*8*). Recent observations

of nanotube fluorescence, and the corresponding excitation spectra, have furthered the characterization of SWNTs (*9–11*). However, this approach is inherently limited to semiconducting nanotubes and its application is currently restricted to small-diameter tubes.

We use Rayleigh scattering spectroscopy to identify the electronic transitions of both metallic and semiconducting individual nanotubes. Rayleigh scattering—the ubiquitous process of elastic light scattering from a small, polarizable object—provides spectroscopic information about the system through the scattering resonant enhancement when the photon energy matches that of an electronic transition. Rayleigh scattering occurs whether or not the sample luminesces, and it is intrinsically stronger than inelastic Raman scattering because it does not require the incident light to couple to the vibrations of the system. As such, the approach should be broadly applicable for probing an arbitrary nanoscale object. When implemented with a bright white-light source, the technique offers sufficient versatility and speed to probe spatially localized regions along an individual nanotube, as well as tube-tube interactions in bundles. The method can be easily combined with other types of single-nanotube measurements.

Rayleigh scattering is normally not considered for nanoscale objects because of the expectation that signals will be extremely weak. However, we report that Rayleigh scattering spectra from individual SWNTs can be obtained with high signal-to-noise ratio in less than 1 min with a white-light source of laser brightness. The white-light

¹Department of Chemistry, ²Departments of Physics and Electrical Engineering, ³Department of Applied Physics and Applied Mathematics, ⁴Department of Mechanical Engineering, Columbia University, 3000 Broadway, New York, NY 10027, USA.

*These authors contributed equally to this work.

†To whom correspondence should be addressed.
E-mail: tony.heinz@columbia.edu, leb26@columbia.edu

supercontinuum is generated by passing femtosecond laser pulses from the output of a mode-locked Ti:sapphire laser operating at a wavelength of 800 nm through a microstructured optical fiber. The nonlinear response of the fiber yields radiation covering a spectral range of ~ 450 to 1550 nm with an average power of tens of mW (12).

To minimize background scattering and to produce nanotubes free from the local perturbations of a substrate, we used standard optical lithography and wet etching procedures to prepare slits (width 30 μm , length 1 mm) etched completely through a silicon substrate. SWNTs were prepared using a chemical vapor deposition process in which the flow of the carbon feed gas was arranged to yield directionally controlled growth of SWNTs across the slit (Fig. 1) (13). Various catalysts and feed gases were used (14–16), with the catalyst density chosen so that about 20 nanotubes, typically well separated from one another, were grown along the length of the slit.

The white light is focused with a microscope objective to $\sim 2 \mu\text{m}^2$ at the slit and is directed at normal incidence onto a suspended SWNT. The scattered light is collected at an oblique angle in a confocal arrangement and is analyzed with a spectrograph equipped with a two-dimensional charge-coupled device (CCD) array. The Rayleigh scattering spectra are then obtained after correction for the profile of the supercontinuum light and the detection sensitivity of the system. The incident supercontinuum light is filtered to remove the infrared component and attenuated to an average power of a few mW, comparable to what is typically used in Raman scattering experiments. Under these conditions, possible contributions from nonlinear and thermal effects are ruled out experimentally because the Rayleigh scattering spectra are independent of excitation intensity. Rayleigh scattering data in the spectral range of 450 to 850 nm were recorded with integration times of 10 to 30 s. Complementary resonance Raman spectra in a backscattering geometry (6) were obtained for selected SWNTs; we used a few mW of 1.96-eV laser radiation and holographic notch filters to reject the elastic Rayleigh component. Data collection times for the resonance Raman scattering typically exceeded those for Rayleigh scattering by a factor of 100.

By comparing the results of scanning electron microscopy (SEM, Fig. 1A) to those for Rayleigh scattering (Fig. 1B), we found that we detected scattering from all of the suspended tubes—both metallic and semiconducting isolated tubes as well as small bundles. This result contrasts with the case of fluorescence, for which only isolated single semiconducting tubes are observable.

In the optical image, the bright center spot is the elastic scattering of the focused supercontinuum from an individual suspended SWNT, shown in a color that represents the specific wavelength of the nanotube resonant response. The white lines above and below this region arise from scattering of stray supercontinuum light from the slit edges.

Representative experimental Rayleigh scattering spectra (Fig. 2) comprise well-defined and highly reproducible peaks that reflect the optical transitions of the SWNT under study. The resolution of our experiment is sufficient to distinguish between two peaks separated by as little as 5 meV. The ~ 50 individual SWNTs observed display the basic motifs of Fig. 2A, with two well-

resolved and separated peaks, or of Fig. 2B, with one broad or slightly split peak. The electronic states of the periodic SWNT structure have band-like character, with successive bands indexed by the angular quantization number around the nanotube. Because of their quasi-one-dimensional nature, the density of states exhibits a van Hove singularity at the onset of each energy band, as shown schematically in Fig. 2, A and B. Within a free-carrier picture of the optical excitation, the sharp resonances in the Rayleigh scattering spectrum arise from the singularity in the joint density of states (JDOS) for transitions between two bands. The energy of these transitions varies with the nanotube diameter and helicity in a

Fig. 1. Images of a suspended isolated carbon nanotube. (A) SEM image showing the silicon substrate (upper and lower dark areas) and the isolated carbon nanotube that spans the slit. Small sections of other nanotubes are also visible at the slit edges. (B) Rayleigh scattering imaged on a CCD camera. The suspended nanotube is excited by supercontinuum light in the center of the slit, leading to observable scattered radiation, as shown here in a color corresponding to the electronic resonance. The edges of the slits, represented in white, are visible because of scattering of background light.

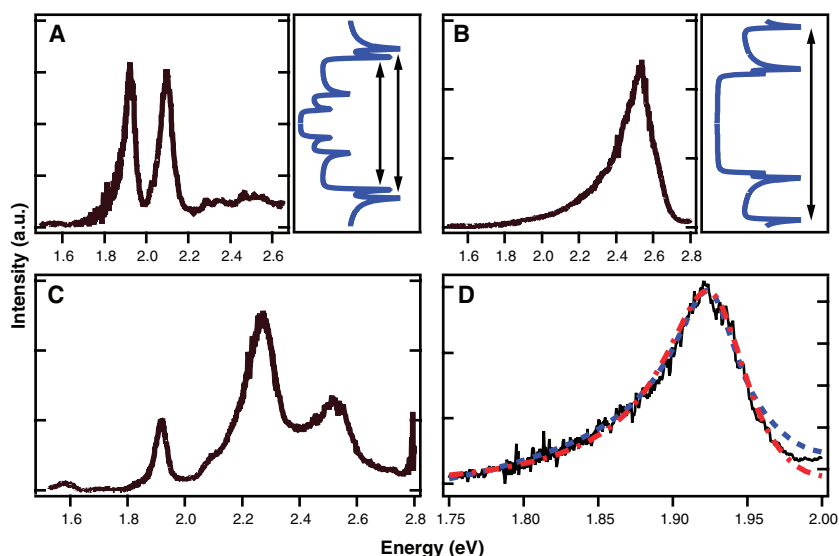
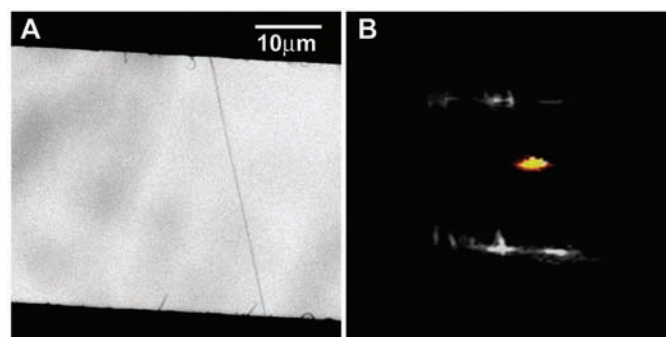


Fig. 2. Rayleigh scattering spectra. (A) Spectrum of an isolated SWNT showing the E_{33} and E_{44} transitions of a semiconducting nanotube. The instrumental resolution is 5 meV. The density of states (with van Hove singularities) of a similar semiconductor nanotube is illustrated at the right; arrows represent assigned transitions. (B) Spectrum from the E_{22} transition of a metallic carbon nanotube. The broader linewidth is attributed to lifetime broadening or unresolved splitting caused by the trigonal warping effect. The density of states is shown at the right; an arrow illustrates the assigned transition for a similar nanotube. (C) Spectrum of a small carbon nanotube bundle. This type of spectrum is easily distinguishable from that of a single isolated tube. (D) Fit of lower energy peak in (A) to the free-carrier (blue dashed line) and excitonic (red dot-dashed line) models discussed in the text.

characteristic fashion (1, 17). We assign the two separated peaks to the E_{33} and E_{44} transitions of an individual semiconducting tube, and the single broadened peak to the E_{22} transition of an individual metallic tube, as expected for SWNTs in the 1.7-nm diameter range that is typically obtained in our synthesis. The much larger apparent width of the metallic transition could be due to lifetime broadening from the shorter-lived excited state. It may also be the result of two closely positioned peaks, which are sometimes resolvable experimentally, associated with the trigonal warping effect (6, 18). In addition to the individual SWNT spectra, we observe Rayleigh scattering with increased strength and spectral complexity that we assign to bundles of SWNTs. A representative example in which the spectrum reflects the presence of two SWNTs (Fig. 2C) illustrates a unique feature of our technique: It can readily distinguish between small bundles and individual nanotubes, while still retaining the capability to reveal distinct spectral features of each species.

We probe the local response in different spatial regions by moving the focus of the white-light supercontinuum along a given SWNT. As an example, Fig. 3A shows Rayleigh scattering spectra taken at the two ends of a particular suspended nanotube. It is expected that because SWNTs are in a robust and stable configuration, they retain their specific chirality for the entire length. There is, however, little direct experimental evidence to support this widely held hypothesis. The excellent match of the Rayleigh scatter-

ing spectra of Fig. 3A shows unambiguously that the SWNT retains precisely the same chirality and diameter over the 30- μm separation, a distance corresponding to more than 1 million carbon atoms in the nanotube.

Resonant Rayleigh scattering provides information about both the energies and lineshapes of the electronic transitions. We model the Rayleigh scattering from an individual SWNT as electromagnetic scattering from an infinite right cylinder. The scattering cross section per unit length is $\sigma(\omega) \propto r^4 \omega^3 |\epsilon(\omega) - 1|^2$ (19), where ω is the frequency of the scattered light, r is the radius of the cylinder, and $\epsilon(\omega)$ is the effective dielectric function of the nanotube. The features of the Rayleigh spectra arise from the frequency-dependent dielectric function, which in turn reflects the wave functions and electronic transitions.

One of the major outstanding issues concerning optically excited states in SWNTs is the importance of the electron-hole interaction. For weak interactions, an optical transition generates free electrons and holes, as would generally be the case for bulk three-dimensional semiconductors at room temperature. In quasi-one-dimensional systems such as SWNTs, however, electron-hole interactions are expected to be enhanced, and theoretical studies suggest the formation of excitons rather than free carriers (20–22). In this context, we compare the experimental lineshapes with the predictions for free-carrier and excitonic transitions. In Fig. 2D we show a detail of the Rayleigh scattering spectrum for the lower energy feature in Fig.

2A, which has a linewidth (full width at half-maximum) of ~ 55 meV. The shape of other measured transitions is quite similar. To analyze the data, we consider the free-carrier response to be dominated by the van Hove singularity in the JDOS (17) and consider the excitonic response to feature a Lorentzian resonance of a width chosen to fit the experimental data. An arbitrary, spectrally flat component is included in the real part of the dielectric function for both models to account for the nonresonant contribution to the scattering from other electronic transitions in the SWNT. Interestingly, we find (Fig. 2D) that both models are compatible with the experimental data. The required phenomenological broadening in the two pictures (20 meV and 35 meV, respectively) is, however, significantly different. Theoretical studies that provide a reliable prediction for the broadening should consequently be able to discriminate between these two pictures, using the experimental lineshapes reported here.

The well-defined experimental geometry also allows us to examine the polarization properties of the Rayleigh scattering process. Shown in Fig. 3B is the Rayleigh scattering amplitude as a function of the scattered light polarization; the same effect is measured when varying the polarization of the incident supercontinuum radiation. The strongest scattering is achieved when the incident light and scattered light are polarized parallel to the tube. The polarization dependence follows closely the $\cos^2 \theta$ form expected for dipole emission along the nanotube axis. As indicated in Fig. 3A, however, weak Rayleigh scattering can be seen for incident light polarized perpendicular to the nanotube axis. The spectra of light scattering when polarized along the nanotube obey the selection rule of $\Delta J = 0$ (i.e., symmetric transitions between the valence and conduction energy bands with the same band index J), such as the above-mentioned E_{22} , E_{33} , and E_{44} transitions. When the electric field is perpendicular to the nanotube axis, the tight-binding model predicts selection rules allowing for $\Delta J = 1$ transitions of comparable strength (23). We observe behavior that reflects the role of the depolarization or “antenna” effect (24), essentially a manifestation of the ability of a SWNT to act like a macroscopic object in perturbing the incident light through strong local-field screening of the perpendicular component of the exciting electric field. Although previous experimental results of Rayleigh scattering on large bundles and Raman scattering (25, 26) provided evidence of this effect, other investigations have suggested that $\Delta J = 1$ transitions play a role in resonance Raman scattering in nanotubes (27). Our measurements on aligned individual nanotubes pro-

Fig. 3. Polarization dependence of the Rayleigh scattering. (A) The black line is the spectrum obtained from one end of the nanotube when the incident light is polarized parallel to the tube axis. The red line shows the identical spectrum obtained from the opposite end of the suspended tube ~ 30 μm away. The blue spectrum (magnification $\times 5$) is obtained for incident light polarized perpendicular to the axis of the nanotube. (B) Rayleigh scattering intensity as a function of the angle between the electric field polarization and the tube axis. The solid line is a $\cos^2 \theta$ fit.

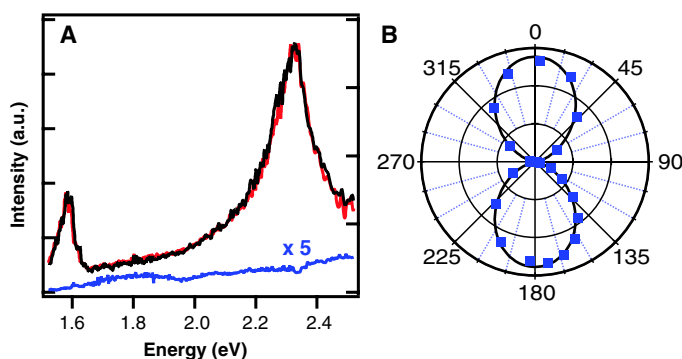
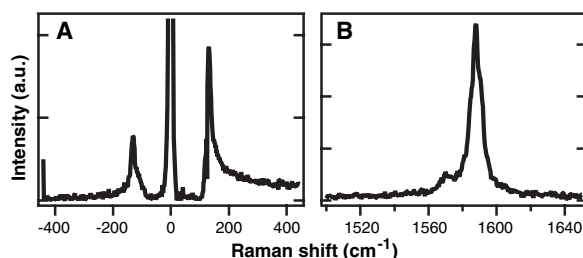


Fig. 4. Resonance Raman scattering spectra for the SWNT of Fig. 2A obtained with excitation at a photon energy of 1.96 eV. (A) Stokes and anti-Stokes Raman spectra of the RBM. The instrumental resolution is less than 3 cm^{-1} . The frequency of this mode implies a diameter of 1.89 nm. (B) Raman spectrum of the G-mode.



vide a direct demonstration of the dominant role of local-field screening.

The Rayleigh spectra provide information that can guide other optical measurements. The Rayleigh data are particularly useful for Raman scattering, which requires an electronic resonance to make measurements from an individual SWNT. Shown in Fig. 4 are resonance Raman spectra for the same SWNT examined in Fig. 2A by Rayleigh scattering. The Rayleigh spectrum was recorded first and found to have resonances at 1.92 and 2.10 eV; we were then able to choose the Raman laser excitation energy (1.96 eV) to match one of the observed transitions. Without such prior knowledge of the resonance energy, experiments must rely on a difficult and time-consuming trial-and-error approach using available laser excitation wavelengths (28). Raman measurements provide additional structural information about SWNTs through the sensitivity of the vibrational modes on the nanotube diameter and chirality (6, 18). We collected both Stokes and anti-Stokes Raman spectra of the radial breathing mode (RBM) (Fig. 4A) as well as the Stokes Raman spectrum of the carbon-carbon stretch G-mode (Fig. 4B). According to the formula relating the Raman shift of the RBM mode frequency (ω_{RBM}) to nanotube diameter (d_t) (7), $\omega_{\text{RBM}} = 248/d_t$, the diameter of this nanotube is 1.89 nm. We then assigned the transitions on the basis of the qualitative pattern of close-lying E_{44} (2.10 eV) and E_{33} (1.92 eV) transitions with a large gap to an unobserved E_{22} transition lying below 1.4 eV, as predicted by tight-binding theory for

semiconducting tubes near 1.89 nm (1, 29). This may be the nanotube with a diameter of 1.85 nm and chiral indices of (21, 4). We calculate that this tube would have Rayleigh peaks at 0.88, 1.87, and 2.10 eV for a γ_0 value (the overlap integral between nearest neighboring atomic sites) of 2.89 eV.

The effectiveness of the characterization of nanoscale objects by Rayleigh scattering with high-brightness white light is apparent from this initial report. We expect that the approach will permit optical probing of a wide variety of other individual nanoscale structures. In the context of carbon nanotubes, a systematic study should yield firm assignments for the entire family of semiconducting and metallic nanotubes. This will permit complementary investigations of transport, mechanical, and chemical properties of nanotubes to be conducted with a convenient spectroscopic identification of the precise structure of the nanotube under study, thus alleviating one of the major limitations of current studies.

References and Notes

1. R. Saito, G. Dresselhaus, M. S. Dresselhaus, *Physical Properties of Carbon Nanotubes* (Imperial College Press, London, 1998).
2. M. M. J. Treacy, T. W. Ebbesen, J. M. Gibson, *Nature* **381**, 678 (1996).
3. S. J. Tans, A. R. M. Verschueren, C. Dekker, *Nature* **393**, 49 (1998).
4. P. Kim, L. Shi, A. Majumdar, P. L. McEuen, *Phys. Rev. Lett.* **87**, 215502 (2001).
5. G. S. Duesberg, I. Loa, M. Burghard, K. Syassen, S. Roth, *Phys. Rev. Lett.* **85**, 5436 (2000).
6. Z. Yu, L. E. Brus, *J. Phys. Chem. B* **105**, 6831 (2001).
7. A. Jorio et al., *Phys. Rev. Lett.* **86**, 1118 (2001).
8. A. Jorio et al., *Phys. Rev. B* **63**, 245416 (2001).
9. M. J. O'Connell et al., *Science* **297**, 593 (2002).

10. A. Hartschuh, H. N. Pedrosa, L. Novotny, T. D. Krauss, *Science* **301**, 1354 (2003).
11. J. Lefebvre, Y. Homma, P. Finnie, *Phys. Rev. Lett.* **90**, 217401 (2003).
12. J. C. Knight, T. A. Birks, P. S. J. Russell, D. M. Atkin, *Opt. Lett.* **21**, 1547 (1996).
13. S. Huang, X. Cai, J. Liu, *J. Am. Chem. Soc.* **125**, 5636 (2003).
14. C. L. Cheung, A. Kurtz, H. Park, C. M. Lieber, *J. Phys. Chem. B* **106**, 2429 (2002).
15. L. An, J. M. Owens, L. E. McNeil, J. Liu, *J. Am. Chem. Soc.* **124**, 13688 (2002).
16. S. Maruyama, R. Kojima, Y. Miyauchi, S. Chiashi, M. Kohno, *Chem. Phys. Lett.* **360**, 229 (2002).
17. M. F. Lin, K. W. K. Shung, *Phys. Rev. B* **50**, 17744 (1994).
18. R. Saito et al., *Phys. Rev. B* **64**, 085312 (2001).
19. C. F. Bohren, D. R. Huffman, *Absorption and Scattering of Light by Small Particles* (Wiley, New York, 1983).
20. T. Ando, *J. Phys. Soc. Jpn.* **66**, 1066 (1997).
21. C. L. Kane, E. J. Mele, *Phys. Rev. Lett.* **90**, 207401 (2003).
22. C. D. Spataru, S. Ismail-Beigi, L. X. Benedict, S. G. Louie, *Phys. Rev. Lett.* **92**, 077402 (2004).
23. M. F. Lin, *Phys. Rev. B* **62**, 13153 (2000).
24. H. Ajiki, T. Ando, *Physica B* **201**, 349 (1994).
25. Z. H. Yu, L. Brus, *J. Phys. Chem. B* **105**, 1123 (2001).
26. A. Jorio et al., *Phys. Rev. B* **65**, 121402 (2002).
27. A. Jorio et al., *Phys. Rev. Lett.* **90**, 107403 (2003).
28. C. Fantini et al., *Phys. Rev. Lett.* **93**, 087401 (2004).
29. R. Saito, G. Dresselhaus, M. S. Dresselhaus, *Phys. Rev. B* **61**, 2981 (2000).
30. We thank M. Hybertsen, X. Cui, G. Dukovic, I. Mandelbaum, and V. Perebeinos for helpful discussions and O. Cherniavskaya for assistance with sample growth and characterization. Supported by the NSF Nanoscale Science and Engineering Initiative (grant CHE-0117752), the New York State Office of Science, Technology, and Academic Research (NYSTAR), and the Office of Basic Energy Sciences, U.S. Department of Energy (grants DE-FG02-98ER 14861 and DE-FG02-03ER 15463).

27 July 2004; accepted 5 October 2004

Published online 28 October 2004;

10.1126/science.1103294

Include this information when citing this paper.

Seismic Anisotropy Beneath Ruapehu Volcano: A Possible Eruption Forecasting Tool

Alexander Gerst^{1,2*}† and Martha K. Savage¹

The orientation of crustal seismic anisotropy changed at least twice by up to 80° because of volcanic eruptions at Ruapehu Volcano, New Zealand. These changes provide the basis for a new monitoring technique and possibly for future midterm eruption forecasting at volcanoes. The fast anisotropic direction was measured during three seismometer deployments in 1994, 1998, and 2002, providing an in situ measurement of the stress in the crust under the volcano. The stress direction changed because of an eruption in 1995–1996. Our 2002 measurements revealed a partial return to the pre-eruption stress state. These changes were probably caused by repeated filling and depressurizing of a magmatic dike system.

About 10% of the world's population live near an active volcano and are therefore threatened by volcanic eruptions (1). More tools are needed to fill in the gap between short-term eruption forecasting (days to weeks) and long-

term forecasting (several years) to provide information about the future onset of an eruption and the current state of the volcano within an eruption cycle (2). The method of shear-wave splitting analysis at volcanoes has

the potential to provide a new tool for midterm eruption forecasts (months to years).

Mount Ruapehu is the largest andesite-dacite volcano in New Zealand. Eruptions have caused the loss of life and property and are likely to recur in the near future. In 1995 and 1996, the largest historical eruption of Ruapehu took place with little warning, ejecting a volume of material of about 0.05 km³, producing a 12-km-high volcanic plume, sending major lahars down the flanks (3, 4), and producing economic damage of about US\$50 million (5). Major eruptions also occurred in 1945, 1969, 1975, 1981, and 1988, many with little or no warning.

Volcanic eruptions are almost always preceded by magma movements in the feeder

¹Institute of Geophysics, School of Earth Sciences, Victoria University of Wellington, New Zealand.
²University of Karlsruhe, Germany.

*Present address: Institute of Geophysics, University of Hamburg, Bundesstrasse 55, 20146 Hamburg, Germany.

†To whom correspondence should be addressed. E-mail: publications@planet3.de

system of the volcano. Such movements involve high pressures and great masses, and are therefore likely to influence the stress state of the crust around the volcano. Stresses in the crust influence the alignment of fluid-filled microcracks and pore space (which we will from now on loosely refer to as “cracks”) and therefore cause seismic anisotropy (6–9). Seismic anisotropy is the analog to optical birefringence and leads to a direction-dependent speed of earthquake waves. This anisotropy influences wave propagation in the crust, leading to the splitting of a near-vertically traveling *S*-wave from a local or distant earthquake into two nearly perpendicular components with different velocities. The polarization direction of the faster *S*-wave at the surface (also called the “fast direction,” or Φ) is commonly observed subparallel to the crack alignment and the direction of maximum principal horizontal stress σ_H (7, 10, 11). Observations of Φ and the delay time (δt) between the fast and slow wavelets provide the direction and relative strength of σ_H in the crust (12, 7). In contrast to other stress-monitoring methods, such as earthquake source mechanism inversions, which deter-

mine stress at earthquake depths, the technique of analyzing anisotropy determines the average stress state in a region around the ray path. Complex fluctuations of the stress field are averaged out, and an in situ measurement of the stress state of the crust is possible, with the probed area mainly controlled by the receiver location. Also, studies that monitor stress changes by the use of source mechanisms often use migrating earthquake swarms, which means they have systematically changing source conditions, making it difficult to distinguish a heterogeneous stress field from a temporal stress change.

Three deployments of seismometers recording local earthquakes were conducted at Ruapehu in 1994, 1998, and 2002. An earlier study (13) examined data from the seismometers deployed in 1994 and 1998 and reported indications for a temporal change in anisotropy between the two deployments. However, doubts remained whether a change really occurred, because the station locations of these two deployments were several (~1 to 10) kilometers apart, which in other studies produced major differences in the measured fast directions without a temporal change in anisot-

ropy (in an extreme case, up to 45° difference at stations as closely spaced as 200 m) (10, 14–16). In addition, frequency and back azimuth effects could not be excluded. Therefore, we deployed instruments in 2002, covering all but one previously occupied station location, to determine whether the measured changes are of a temporal nature rather than a misinterpretation of heterogeneities.

We examined waveforms of local and regional earthquakes [magnitude (*M*) 2 to 5.5] from depths between 5 and 250 km and at distances as far away as 150 km from Ruapehu. These earthquakes mainly have a tectonic origin and were therefore not necessarily caused by the volcanic system, but their waves traveled through it (17). After the splitting measurements were obtained by a semiautomatic algorithm (17), the splitting parameters were divided into those from shallow events (crustal, depth <35 km), and deep events (mantle, depth >55 km), based on similar splitting parameters within the two subsets (18) (Table 1). We reprocessed data from the earlier study (13) with advanced processing techniques, leading to a higher number of measurements (17, 19).

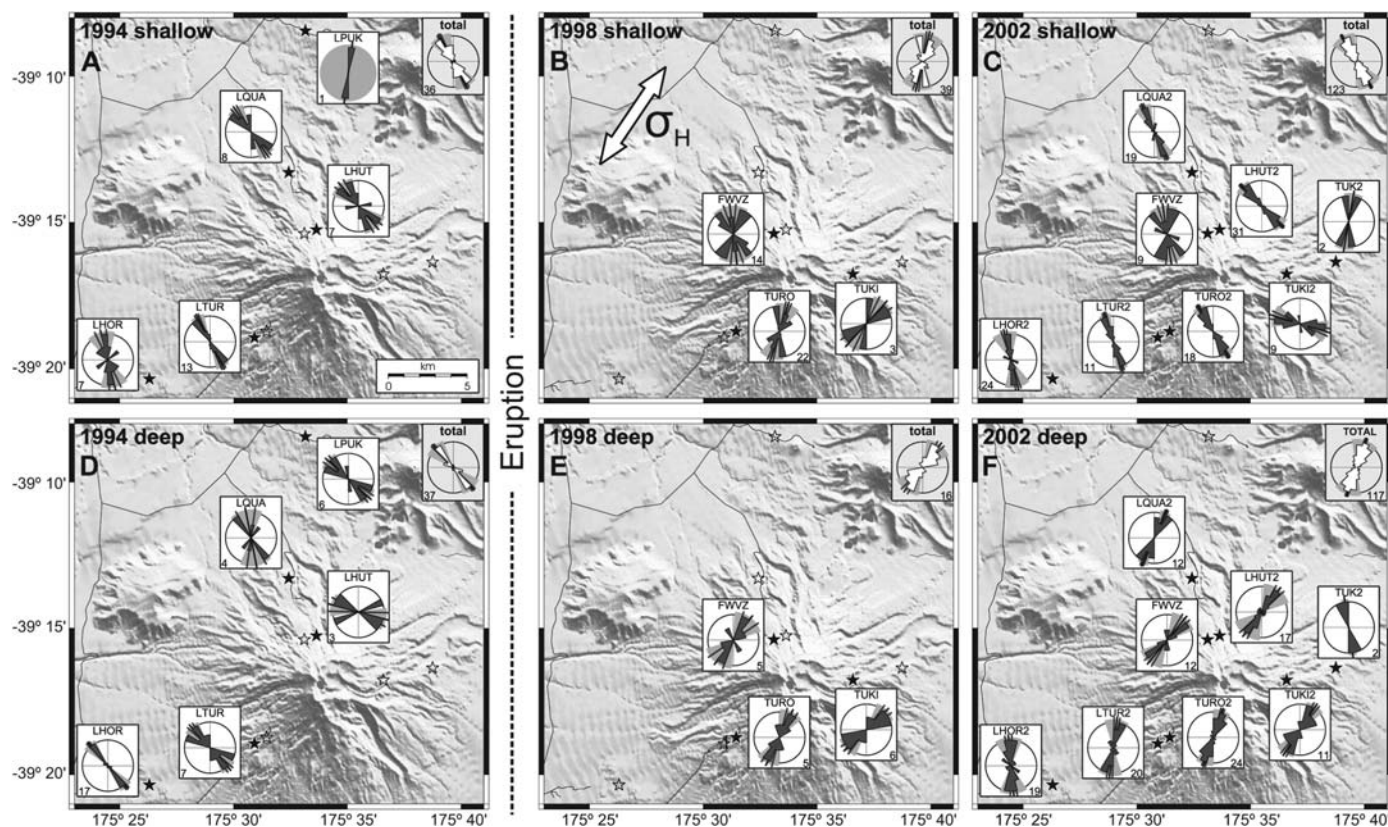


Fig. 1. Station histograms of the fast direction. (A to C) Shallow earthquakes (<35 km); (D to F) deep earthquakes (>55 km) (18). The histograms visualize the number of measurements in every 15° angle segment of the fast direction for each station. In each histogram, the underlying gray area shows the standard deviation of the fast directions, the center bar shows the mean fast direction, the two outer bars show the standard deviation of the mean fast direction (standard error). The numbers in the corner of the histograms show the number of measure-

ments. The histogram in the upper right corner of each subset is a composite for all the stations. Filled stars show the station locations that were occupied at the respective deployments; open stars show stations from other deployments for orientation. In (B), the white arrow shows the direction of σ_H , as deduced from geodetic measurements (20). Note the 80° change of fast directions between the deep events of 1994 (D) and 1998 (E), and the two ~40° changes in the shallow fast directions between 1994 (A), 1998 (B), and 2002 (C).

The combined data show a change in anisotropy between 1994 and 1998, when the mean Φ from deep earthquakes (Φ_{deep}) changed by 80° (Table 1 and Figs. 1 and 2) (17), rotating from a perpendicular to a parallel alignment relative to the regional σ_H [roughly north-northeast to south-southwest (NNE-SSW)] (20). This change was measured after the largest historical eruption in 1995–1996. The mean Φ from shallow earthquakes (Φ_{shallow}) changed by 42° between the 1994 and 1998 measurements (Fig. 2 and Table 1). The 99.9% confidence regions for the average Φ_{deep} are -55° to -31° in 1994, and 13° to 62° in 1998. The hypothesis that

no change occurred must be rejected at the 99.9% confidence level. With a confidence level of at least 95%, the change of Φ_{deep} (1994 to 1998) was between 58° and 102° .

Another major change occurred in the shallow events between 1998 and 2002: The Φ_{shallow} of the 2002 data set is different from the Φ_{shallow} of the 1998 data set by 43° , again with a high statistical significance ($>99.9\%$). This change almost completely reversed the change of Φ_{shallow} that occurred between 1994 and 1998 (Fig. 2). Therefore, the Φ_{shallow} in 2002 is similar to the one in 1994 (before the eruption) and is perpendicular to the regional σ_H . The change is visible at all stations (21). In contrast, the Φ_{deep} remained almost constant between 1998 and 2002 (Figs. 1 and 2).

Both Φ_{shallow} and Φ_{deep} are independent of ray paths, source regions, frequencies, focal mechanisms, and initial polarizations (17). Furthermore, none of these parameters showed relevant variations between the deployments; hence, they cannot be the cause for the measured changes in anisotropy. Thus, the observed changes reflect a temporal change in the anisotropic medium and cannot be accounted for by other effects. In contrast to the changes in Φ , we were not able to distinguish statistically significant changes in the delay times (22).

Now that the occurrence of a temporal change in Φ is established, the question of its cause arises. The alignment of Φ_{deep} on the North Island is controlled by mantle anisotropy above a subduction zone (23). The deep events at Ruapehu acquired their first splitting in the mantle. No known processes could change the fast direction over a large (>300 by 300 km) region of the mantle over the observed time scales (4 years). Thus, we must assume that during the three deployments, the fast direction of anisotropy beneath the crust did not change but was constant and subparallel to the commonly observed NNE-SSW-aligned Φ_{deep} (23). In 1994, when a Φ_{deep} different from NNE-SSW was observed, the fast direction must have been altered while passing through the upper crust. Therefore, at least two independent layers of anisotropy are present: one in the mantle, and a temporally

variable region in the upper crust, which we refer to as the “anomalous region.”

Shallow (<35 km) earthquakes in 2002 have δt between 0.05 and 0.2 s, which do not increase with depth (19). This behavior implies that the anomalous region must be closer to the stations than are the closest earthquakes, with path lengths slightly less than 10 km. Assuming that the whole path lies in the anisotropic medium, and assuming an average S -wave speed of 2.5 km/s and a δt of 0.2 s, we calculate at least 5% anisotropy. As a result of strong velocity gradients (17) that lead to very steep incoming ray paths, and at the typical frequencies in this study (~ 4 Hz), stations separated by more than 300 m will sample different regions of the shallow crust. Because all stations in the network show the changes, these changes must have occurred in a region that is at least as large as the station network (~ 100 km²). Therefore, the anomalous region has a minimum size of about 10 by 10 km.

The only plausible mechanism for rapid temporal changes in anisotropy (i.e., within 4 years) is a stress change in the medium (11). The obvious source for stress changes is volcanic activity at Ruapehu. Under the given stress conditions ($\sigma_V \gg \sigma_H > \sigma_h$; where σ_h and σ_V are the minimum horizontal and the vertical principal stress) of the back-arc spreading zone in which Ruapehu is situated, the expected shape of a magma intrusion in the shallow crust is a hydraulic extension fracture: one or multiple vertical dikes aligned with σ_H (24).

We propose that magma intruded under Ruapehu into a shallow (<10 km) magma chamber, which has the form of a single dike or a swarm of subparallel dikes, aligned perpendicular to the inferred minimum principal stress and therefore parallel to σ_H (\sim NNE-SSW) (Fig. 3). The length of the dike system is unknown, but considering that all stations in the network (~ 10 by 10 km) are showing changes in the crust beneath them, we expect it to extend at least 5 km in either direction from the summit. This model is consistent with a study (25) that reported anomalously high S -wave attenuation under the summit of

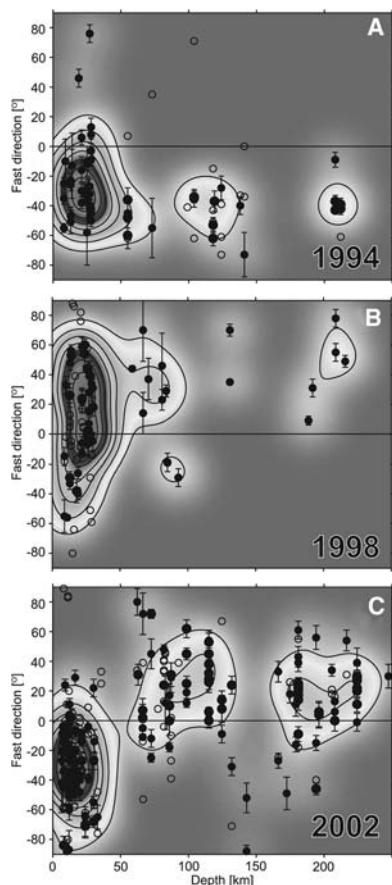


Fig. 2. Fast directions versus depth in a density plot. Filled circles represent high-quality measurements; open circles represent medium-quality measurements. Every measurement of high quality has an error bar and a weight function attached. The weight is 1 at the point of the measurement and decays exponentially when moving away in depth or Φ direction. The underlying map is the sum of all weight functions; its contours indicate the density of the measurements. Note the different fast directions during the three deployments. In 1994 (A) and 1998 (B), the deep events yield approximately the same average fast directions as the shallow events in the respective deployment. In 2002 (C), however, the deep events show a different average fast direction from the shallow ones. [This figure is also provided in color in (17).]

Table 1. Shallow events have a source depth of <35 km; deep events have a source depth of >55 km (18). $\bar{\Phi}$ is the circular mean fast direction; $\pm\bar{\Phi}$ is the circular standard error of the mean fast direction (s_e), whereas $\pm\Phi$ is the circular standard deviation of the fast directions (s_d). $\bar{\delta t}$ and $\pm\delta t$ are the mean delay time and the standard deviation of the delay times. “No.” shows the respective number of measurements. Multiply standard error by 1.96, 2.58, or 3.29 to get 95%, 99%, or 99.9% confidence interval for mean. Delay times, because of their large variance, were not interpreted.

Year/subset	$\bar{\Phi}$ (°)	$\pm\bar{\Phi}$ (°)	$\pm\Phi$ (°)	$\bar{\delta t}$ (s)	$\pm\delta t$ (s)	No.
1994 shallow	-28.3	3.9	23.3	0.108	0.060	36
1994 deep	-42.8	3.6	22.3	0.231	0.129	37
1998 shallow	13.4	5.8	33.0	0.113	0.058	39
1998 deep	37.4	7.5	28.9	0.118	0.063	16
2002 shallow	-30.0	2.4	26.2	0.107	0.053	123
2002 deep	19.2	2.7	28.6	0.272	0.175	117

Ruapehu at depths from 2 to at least 10 km and proposed the presence of three dike-shaped intrusions of partially molten rock aligned with the regional σ_H . On Ruapehu and in the surrounding region, several old exposed dikes are mapped, with lengths up to several kilometers and thicknesses of several meters (26). The majority of them aligned NNE-SSW, parallel to σ_H (27) and subparallel to the alignment of faults and volcanic vents in the region, therefore supporting our model.

A dike in the crust exerts pressure on the surrounding rock, generating a local stress field that is superimposed on the regional stress field. The stresses of such an elongated structure are mainly oriented perpendicular to the strike axis ($\sim\sigma_H$) and are therefore parallel to σ_h (24) (Fig. 3). When the pressure in the dike system is high enough, the generated stress field locally reorients the principal stresses as well as the local “crack” alignment

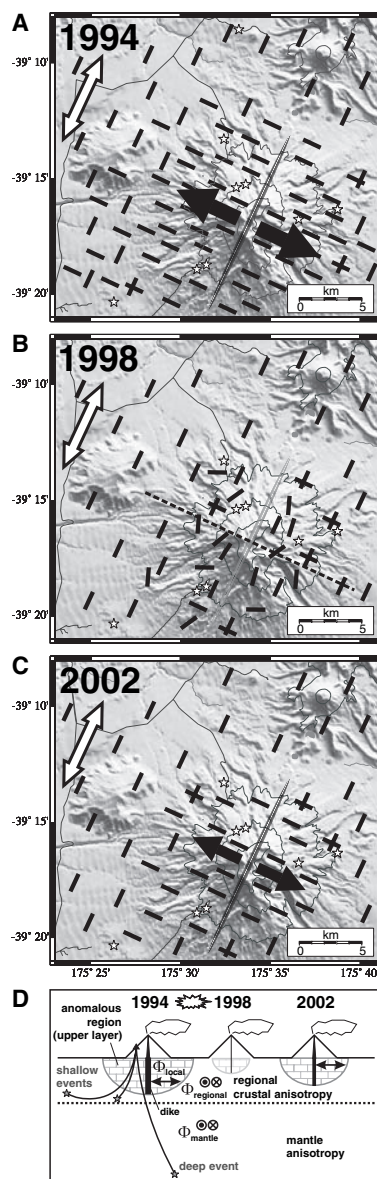
(i.e., fluid-filled microcracks and aligned pore space) (12), effectively swapping σ_H and σ_h in the anomalous region. We suggest that, before the eruption, the dike system was highly pressurized by new magma arriving from a deeper reservoir, rotating σ_H and the crack alignment (and therefore Φ) in the anomalous region (28), and eventually exceeding the strength of the rock and triggering an eruption. In this region, the direction of σ_H and Φ became nearly perpendicular to the dike. The time scale for these changes in anisotropy, as a result of fluid movement between cracks under applied differential stress, is dependent on the rock permeabilities but is on the order of several minutes or less for even low permeabilities of 10^{-9} to 10^{-6} Darcy, assuming a differential stress of 10 MPa (29). We emphasize that the cracks, which are a common phenomenon in Earth’s crust (8), are not directly caused by volcanic processes but act

as an indicator for stresses in the crust, as described by the anisotropic poroelasticity (APE) theory (29).

We suggest that the anomalous region was large (>5% anisotropy distributed over a region at least 10 km wide with a maximum depth of 10 km) in 1994 as a result of a highly pressurized dike system. The eruption in 1995–1996 caused the pressure in the system to drop, consequently leading to a decreased size or a disappearance of the anomalous region in 1998 (Fig. 3). In 2002, the dike system began to repressurize, leading to a reappearance of the anomalous region. The direction of the measured Φ followed the stress changes and therefore showed an almost 90° change between 1994 and 1998 (Figs. 1 and 3). The repressurization of the magma chamber is reflected in the changes of Φ_{shallow} between 1998 and 2002. The observation that the Φ_{deep} in 2002 does not show any changes may be due to insufficient pressure in the dike system leading to weaker anisotropy or a smaller anomalous region than in 1994, which cannot be detected with the longer wavelengths of the deeper waves. Deep events in our study generally have lower frequencies than shallow events, and have already acquired shear-wave splitting with long delay times (>0.2 s) in the mantle (19, 23). They are therefore not as easy to resplit in the upper crust as the shallow events and will only show this behavior when the anisotropy in the upper layer is strong enough. If this is the case, the Φ_{deep} would be expected to realign to a state similar to that in 1994 if the pressures in the dike system also increase to a state similar to that before the eruption. Such a situation might indicate the onset of another eruption. Additional support for such behavior, and for the decoupling of the splitting in the mantle and crust, is provided by synthetic seismograms through models with two anisotropic layers (17) and by the measured initial polarizations (17).

An alternative way for explaining the changes in anisotropy is a mechanism called 90° flip (9, 30), which is a mathematical prediction of the APE theory (29). It suggests that highly overpressured pore fluid could lead to a fast S-wave with a polarization direction perpendicular to σ_H , that is, changing the observed Φ by 90° without a change in the stress direction. However, possible observations of the phenomenon (30–32) cannot clearly be distinguished from conventional explanations such as fault-controlled anisotropy (14, 33). To explain our data with such a mechanism, a pore fluid substantially larger than the hydrostatic pressure is required to be sustained over an area spanning at least the whole station network (>100 km²). Even though high fluid pressures can be common directly in or above

Fig. 3. (A to C) Stress and anisotropy model. In 1994, a pressurized dike (here representative of a dike system) created a local stress field with σ_h (black arrow) oriented perpendicular to the regional σ_H (white arrow). Within the reach of this local stress field, fluid-filled microcracks and pore space effectively realigned (as indicated by bars), following the local σ_H . In 1998, after the eruption, when the dike system was depressurized, σ_H (and with it the crack alignment) partially returned to the regional trend. In 2002, the dike system is refilling, and the stress field in the anomalous region is dominated by the dike again. The alignment of cracks is not yet as strong as in 1994, so the anisotropy in the anomalous region is not strong enough to affect fast directions from deep events. (D) Schematic cross section along the dashed line in (B). Φ_{mantle} , Φ_{regional} (crustal), and the dike alignment are perpendicular to the plane of the paper, whereas Φ_{local} (anomalous region) is within the plane. The thickness of the anomalous region (<10 km) is exaggerated with respect to the depth of the deepest earthquakes (\sim 250 km). Before entering the anomalous region, waves have acquired the splitting parameters from either Φ_{mantle} or Φ_{regional} .



volcanic systems, it is unlikely that such a pressure is sustained over such a large area inside the brittle volcanic deposits surrounding Ruapehu. However, because our data cannot rule out this possibility, we consider it a potential explanation. Both explanations involve the magma system of Ruapehu in connection with an eruption as a source for the changes in anisotropy, and the deduced assumptions about eruption forecasting are similar for both mechanisms.

We conducted a three-dimensional numerical stress calculation (17) to check quantitatively whether our proposed dike model can explain the required stress changes. Results show that stress changes inflicted by the proposed dike system can be strong enough to influence anisotropy. Other studies also find temporal and spatial variations in stress around active volcanoes, which suggests that favorable stress conditions may be common at other volcanoes. At Spurr Volcano, the direction of σ_H as determined by focal mechanism analysis, changed by 90° (34) as a result of an inflating magma dike before the eruption. At Unzen Volcano (35), σ_H is spatially rotated by 90°, which indicates a local stress field with dimensions similar to those in our study, produced by pressurized volcanic gas or magma. At Vesuvius volcano, splitting parameters determined from a local earthquake swarm (36) show a slight increase in δt and minor variations of Φ before the time of the largest earthquake (M3.6) of the swarm, interpreted as a stress-change caused by the earthquake. All these findings and their interpretations are consistent with our proposed model. Because the observations from Mt. Spurr show a 90° rotation of the stress direction, they do not provide evidence for the 90°-flip model (30), which involves a rotation of Φ but not of the stress direction.

If the anisotropy changes recur before and after eruptions, they could be used for midterm forecasting of eruptions. Once the time intervals between changes and eruption, or the existence of a certain “stress threshold” before an eruption, have been established by further monitoring, predictions can be made for the onset of new eruptions. Achievable warning times could be months to a few years in advance, therefore possibly filling a gap in the available forecasting methods. Additionally, the changes between 1998 and 2002 suggest that the technique can be used to monitor real-time stress changes in and around magma chambers that are more subtle than those caused by a large eruption. For other areas in geophysics, the evidence presented in this paper suggests that renewed attempts at using anisotropy for stress monitoring associated with other activities, such as reservoir loading, mining, or even natural changes associated with earthquake activity, could be fruitful.

References and Notes

- D. W. Peterson, *Studies in Geophysics: Active Tectonics* (National Academy Press, Washington, DC, 1986), pp. 2311–2346.
- D. Dzurisin, *Rev. Geophys.* **41**, 1 (2003).
- C. Bryan, S. Sherburn, *J. Volcanol. Geotherm. Res.* **90**, 1 (1999).
- M. Nakagawa, K. Wada, T. Thordarson, C. P. Wood, J. A. Gamble, *Bull. Volcanol.* **61**, 15 (1999).
- D. Johnston, D. Paton, B. Houghton, V. Neall, K. Ronan, *Bull. Geol. Soc. Am.* **112**, 720 (2000).
- A. Nur, G. Simmons, *J. Geophys. Res.* **74**, 6667 (1969).
- S. Crampin, D. C. Booth, *Geophys. J. R. Astron. Soc.* **87**, 75 (1985).
- V. Babuska, M. Cara, *Seismic Anisotropy in the Earth* (Kluwer Acad., Norwell, Mass., 1991).
- S. Crampin, S. Chastin, *Geophys. J. Int.* **155**, 221 (2003).
- M. K. Savage, X. Shih, R. Meyer, R. Aster, *Tectonophysics* **165**, 279 (1989).
- M. K. Savage, *Rev. Geophys.* **37**, 65 (1999).
- Below a depth of a few hundred meters, the minimum stress is typically horizontal and therefore causes cracks with a vertical crack plane (37). This system yields a hexagonal or orthorhombic symmetry system with a horizontal symmetry axis. The fast direction is commonly observed parallel to σ_H .
- V. Miller, M. Savage, *Science* **293**, 2231 (2001).
- K. Gledhill, *J. Geophys. Res.* **96**, 21,503 (1991).
- C. Munson, C. Thurber, Y. Li, P. Okubo, *J. Geophys. Res.* **100**, 20,367 (1995).
- T.-C. Chen, *Geophys. J. R. Astron. Soc.* **91**, 287 (1987).
- Materials and methods are available as supporting material on Science Online.
- There are few earthquakes between 35 km and 55 km in depth in the region, leading to only two measurements. A complete list of all individual measurements of all deployments is available (19).
- A. Gerst, thesis, Victoria University of Wellington, New Zealand (2003).
- D. Darby, C. Meertens, *J. Geophys. Res.* **100**, 8221 (1995).
- At the Far West T-Bar station (FWYZ), which usually shows strong scatter, this trend is visible when events at frequencies higher than 3.5 Hz are excluded (19).
- Throughout this study, scatter of the delay times was more than 10 times higher than scatter of the fast directions. Further, the average delay times depend on the observed frequencies and depths, and thus on processing techniques (e.g., frequency filters) and earthquake magnitudes.
- E. Audoin, M. Savage, K. Gledhill, *J. Geophys. Res.*, in press.
- T. Parsons, G. A. Thompson, *Science* **253**, 1399 (1991).
- J. H. Latter, *J. Volcanol. Geotherm. Res.* **10**, 125 (1981).
- W. R. Hackett, thesis, Victoria University of Wellington, New Zealand (1985).
- I. A. Nairn, T. Kobayashi, M. Nakagawa, *J. Volcanol. Geotherm. Res.* **86**, 19 (1998).
- Cracks that are aligned perpendicular to the new σ_H were forced to close, with their pore fluid migrating into cracks that are aligned parallel to the new σ_H (which were previously closed). Effectively, the alignment of the cracks adjusted to the new stress field and became parallel to the new σ_H .
- S. V. Zatsepin, S. Crampin, *Geophys. J. Int.* **129**, 477 (1997).
- S. Crampin, T. Volti, S. Chastin, A. Gudmundsson, R. Stefansson, *Geophys. J. Int.* **151**, F1 (2002).
- Y. Liu, S. Crampin, I. Main, *Geophys. J. Int.* **130**, 771 (1997).
- E. Angerer, S. Crampin, X. Y. Li, T. L. Davis, *Geophys. J. Int.* **149**, 267 (2001).
- J. C. Zinke, M. D. Zoback, *Bull. Seismol. Soc. Am.* **90**, 1305 (2000).
- D. Roman, S. Moran, J. Power, K. Cashman, *Bull. Seismol. Soc. Am.* (2004).
- K. Umakoshi, H. Shimizu, N. Matsuwo, *J. Volcanol. Geotherm. Res.* **112**, 117 (2001).
- E. D. Pezzo, F. Bianco, S. Petrosino, G. Saccorrotti, *Bull. Seismol. Soc. Am.* **94**, 439 (2004).
- S. Crampin, *Geophys. J. Int.* **118**, 428 (1994).
- We thank Earthquake Commission, Marsden, Foundation for Research Science and Technology, Deutsches Akademisches Austausch Dienst (German Academic Exchange Service), and Planet Earth fund for funding this study. Thanks to J. Neuberger and G. Stuart from Leeds University for data and to Institute of Geological and Nuclear Sciences for providing instruments and resources. We also thank S. Hofmann, K. Gledhill, T. Hurst, M. Hagerty, J. Gamble, J. Townend, E. Smith, T. Stern, V. Miller, and F. Wenzel for invaluable help. Thanks to S. Toda and J. Park for help with their software. Maps were generated with Generic Mapping Tools by Wessel and Smith. Thanks to H. Keys and Department of Conservation for field support.

Supporting Online Material

www.sciencemag.org/cgi/content/full/306/5701/1543/DC1

Materials and Methods
Figs. S1 to S7

Tables S1 and S2
References

30 July 2004; accepted 14 October 2004

Evidence for Positive Epistasis in HIV-1

Sebastian Bonhoeffer,^{1*} Colombe Chappey,² Neil T. Parkin,² Jeanette M. Whitcomb,² Christos J. Petropoulos²

Reproductive strategies such as sexual reproduction and recombination that involve the shuffling of parental genomes for the production of offspring are ubiquitous in nature. However, their evolutionary benefit remains unclear. Many theories have identified potential benefits, but progress is hampered by the scarcity of relevant data. One class of theories is based on the assumption that mutations affecting fitness exhibit negative epistasis. Retroviruses recombine frequently and thus provide a unique opportunity to test these theories. Using amino acid sequence data and fitness values from 9466 human immunodeficiency virus 1 (HIV-1) isolates, we find in contrast to these theories strong statistical evidence for a predominance of positive epistasis in HIV-1.

One of the most fundamental questions in biology is why sexual reproduction and recombination are so widespread. Meiotic recombination and sexual reproduction both induce the shuffling of parental genomes for the produc-

tion of offspring. Intuitively, shuffling might appear to be beneficial, because it promotes genetic diversity among the offspring and thus allows for a faster rate of adaptation. However, this explanation has several shortcomings.

First, sexual reproduction and recombination do not always increase genetic variation. Second, even when they do, it is not clear why greater genetic variation should generally be adaptive. Third, recombination may not only create but also destroy favorable combinations of mutations. Therefore, what is the evolutionary benefit of shuffling two genotypes that are proven viable in their current environment?

Many theories have been proposed to account for the possible advantages of recombination [see reviews in (1–4)]. Currently favored are population genetic theories that are based on interactions between selection and genetic variation. These theories can be grouped into two classes: (i) those based on the effect of genetic drift in populations that are limited in size and (ii) those based on the effects of fitness interactions between alternative alleles at different loci (epistasis). Although there is growing belief that an explanation for the evolution of recombination could emerge from one or a combination of the existing theories, the key problem that has hampered progress is the limited amount of data that allows the testing of these theories.

The population genetic theories based on epistasis require a particular form of interaction for recombination to be advantageous. Beneficial mutations need to interact antagonistically (that is, they need to increase fitness less than multiplicatively with increasing number of mutations) and detrimental mutations need to act synergistically (they need to decrease fitness more than multiplicatively with increasing number of mutations) (5–7). In both cases, the interaction is characterized by negative epistasis, which is a measure of the deviation from multiplicativity of the fitness effect caused by the individual mutations. In a two-locus–two-allele model, epistasis can be defined as $E = w_{ab} + w_{AB} - w_{aB} - w_{Ab}$, where a/A and b/B are the alternative alleles at the two loci and w_{**} is the log fitness of the corresponding genotype.

The appeal of theories about the evolution of recombination based on negative epistasis (in particular between deleterious mutations) is that recombination can efficiently eliminate deleterious mutations under these circumstances. Provided that the deleterious mutation rate is sufficiently high, this could be a strong selective advantage for all living organisms, and hence these theories could account for the ubiquity of recombination and sexual reproduction in nature (6, 8). Many studies have tested for epistasis [reviewed in (9)]. However, no clear evidence

has yet been found for an overall predominance of positive or negative epistasis (10–16), probably because of limited statistical power. Moreover, few of these studies have been carried out in organisms with high rates of sexual recombination, and often epistasis was measured with regard to fitness-related properties rather than total fitness (15, 17). Only one recent study of RNA bacteriophages inferred positive epistasis by accumulation of mutations in lineages with different fitness (18).

Retroviruses such as human immunodeficiency virus 1 (HIV-1) provide a unique opportunity to test theories about the evolution of recombination, because their replication cycle can be viewed as a primitive form of sexual replication (19). Retroviruses package two full-length copies of the RNA genome. After infection of a cell, the viral polymerase [reverse transcriptase (RT)] engages one copy of the genomic RNA and converts the sequence into proviral DNA. During this process, the RT carrying the nascent DNA provirus may disengage from the first RNA template and reengage the second. If the infecting virion is heterozygous (that is, if it carries two distinct genomic RNA strands), this process of template switching may lead to the production of a recombinant provirus. Heterozygous virions are produced when cells are simultaneously infected by two or more distinct proviruses, which occurs frequently in HIV-1 infection (20). Recent estimates suggest that in HIV-1, the RT switches RNA templates approximately 10 times per replication cycle (21), yielding an average of about one recombination event per 1000 base pairs.

To test whether negative epistasis predominates in HIV-1, we analyzed 9466 virus samples derived from HIV-1–infected patients for routine drug-resistance testing. Viral fitness was assayed based on the construction of HIV-derived test vectors (22). In essence, patient virus–derived amplicons representing all of protease (PR) and most of RT are inserted into the backbone of a resistance test vector. This vector is based on the NL4-3 molecular HIV clone and has been modified so that it can undergo only a single round of replication. The fitness assay then quantifies the total production of infectious progeny virus after a single round of infection of the patient-derived virus relative to that of an NL4-3–based control virus. The fitness of the NL4-3–based control virus thus equals 1. Note that although most mutations in our data set evolved in patients in the context of drug therapy, fitness is measured *in vitro* in the absence of drugs. In addition to the fitness measurement, all of PR and amino acids 1 to 305 of RT were sequenced by population sequencing.

The distribution of log fitness values ranges over three orders of magnitude and has a long tail extending to low fitness values (Fig. 1A), which likely reflects the fact that mutations acquired during drug therapy are often detrimental in the absence of drugs. One commonly used method to test for epistasis is to plot the logarithm of fitness as a function of the number of mutations relative to a reference strain (10, 11). If there is no epistasis, the fitness effects of the individual mutations contribute multiplicatively to fitness, and thus log fitness decreases lin-

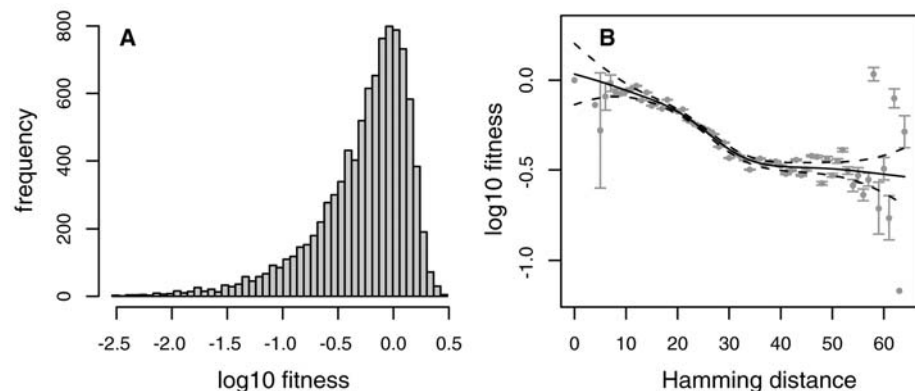


Fig. 1. (A) Distribution of relative fitness values of all 9466 sequences included in the data set. (We use \log_{10} -transformed data throughout.) The fitness is based on a recombinant virus assay (22), which measures the total production of infectious progeny virus after one complete round of replication relative to a reference control virus. (B) Mean and standard error (gray dots and bars) of log fitness as a function of the number of amino acids differing from the reference virus (Hamming distance) for all sequences in the data set. The lines represent fitted values (solid lines) and 95% confidence intervals (dashed lines) of a nonparametric regression based on cubic splines (using the implementation of generalized additive models in the R statistical software package) (28). For small (<10) and large (>50) Hamming distances, the large standard errors are due to the small number of sequences in each Hamming distance class. Missing error bars indicate that there is only one sequence in this Hamming distance class. In the intermediate range of Hamming distances (10 to 50), standard errors are low because all classes are represented by between 36 and 498 sequences.

¹Ecology and Evolution, ETH Zurich, ETH Zentrum NW, CH-8092 Zurich, Switzerland. ²ViroLogic, 345 Oyster Point Boulevard, South San Francisco, CA 94080–1913, USA.

*To whom correspondence should be addressed. E-mail: seb@env.ethz.ch

early with increasing number of mutations. A less than linear decrease suggests the predominance of positive epistasis and a more than linear decrease suggests negative epistasis. Figure 1B shows the mean and standard error of log fitness as a function of the number of amino acid differences compared to the NL4-3 reference virus (the Hamming distance). Because there are limited numbers of sequences in the data set with Hamming distances smaller than 10 or larger than 50, the fluctuations in mean and standard error are large in these Hamming ranges. In the intermediate range, however, the standard errors are small because of the large number of sequences in each Hamming distance class. The 95% confidence interval of a nonparametric fit shows that there is a highly significant deviation from linearity for large Hamming distances, which is suggestive of positive epistasis.

Alternatively, the less than linear decrease could be explained by a bias in the data set against sequences with very low fitness. Such a general bias is unlikely in our data set, because these viral sequences are generally derived from patients receiving drug therapy, whereas fitness is measured in the absence of drugs. Mutations that confer high fitness in the presence of drugs therefore have an increased probability of existing in our data set. However, these mutations are included in the data set irrespective of their effect on fitness in the absence of drugs, and it is therefore unlikely that they are biased against low fitness in our assay. Nevertheless, for very large Hamming distance it is possible that the less than linear decrease of log fitness is a result of the exhaustion of those mutants that have high fitness in the presence but low fitness in the absence of drugs, and an underrepresentation of sequences with low fitness in both environments.

A more direct test for epistasis is to measure fitness interactions between pairs of alternative amino acids at different positions in the aligned sequence set. Assume we have two alternative amino acids *a* and *A* at position *i* and *b* and *B* at position *j*. Provided that there are sequences in the data set for all

four possible combinations of the two amino acids at both positions, we estimate epistasis as $E = \bar{w}_{ab} + \bar{w}_{AB} - \bar{w}_{aB} - \bar{w}_{Ab}$, where \bar{w}_{ab} denotes the mean log fitness of all sequences that have amino acid *a* at position *i* and amino acid *b* at position *j* in the aligned sequence set. The definition of epistasis requires the selection of a reference genotype. That is, it is necessary to define which of the four genotypes represents *ab*, because otherwise the sign of *E* is arbitrary. Commonly, *ab* is defined as the fittest genotype. However, if there is measurement error in fitness, it can be shown that defining *ab* as the fittest genotype results in a bias toward positive epistasis. Similarly, defining *AB* as the least fit genotype results in a bias toward negative epistasis. Measuring epistasis with regard to a predefined genotype does not result in a bias. Therefore we choose as the reference genotype the amino acid combination found in the NL4-3 strain, because fitness is measured relative to this strain. (Repeating the analyses below with the consensus sequence as the reference sequence had negligible effects, because the NL4-3 strain and the consensus sequence differ in only six amino acid positions.)

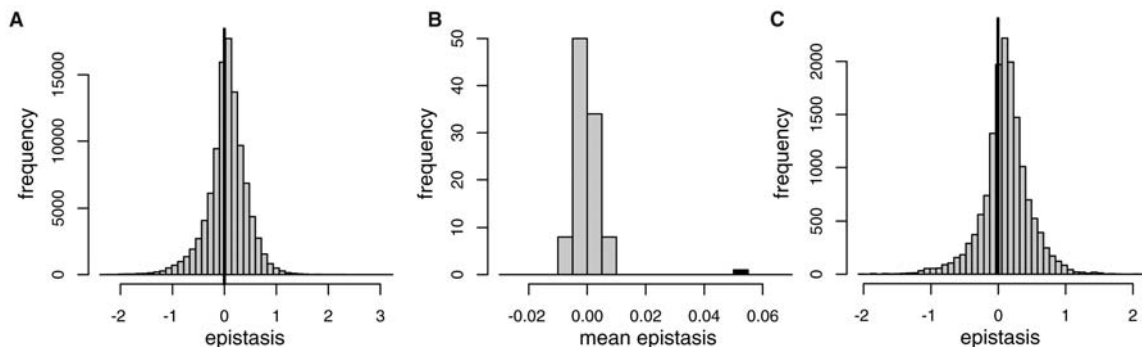
A computer program identified 103,286 pairs of alternative amino acids in the data set, where one genotype represented the amino acid combination found in the NL4-3 strain. The distribution of epistasis values between these pairs extends to both positive and negative values of epistasis (Fig. 2A). The mean of the distribution is 0.052, and 60% of all pairs have positive epistasis. Clearly, the measurements of epistasis are not all independent, because pairs of mutations may be linked to each other. To test whether the observed mean epistasis is significantly different from zero, we randomized the association between sequence and corresponding fitness value and repeated the analysis 100 times. This randomization procedure revealed that the difference in mean epistasis between the real and randomized data is highly significant (Fig. 2B). The observation that the mean epistasis for the randomized data set did not differ sig-

nificantly from 0 (*t* test, $P = 0.5$) shows that measuring epistasis with regard to a predefined genotype does not introduce a bias toward nonzero epistasis.

To test whether the observed positive mean epistasis resulted from random measurement errors, we restricted the analysis only to those positions at which we were able to detect amino acid variants that significantly affect fitness (22). A comparison of the 59 identified positions with data downloaded from the Stanford HIV Drug Resistance Database (<http://hivdb.stanford.edu/>) showed that all identified sites exhibit known drug treatment-associated polymorphisms (22). Repeating the epistasis analysis restricted to the selected 59 positions, we obtained a mean epistasis of 0.109 (Fig. 2C). Restricting the analysis to positions with significant fitness effects thus shifted the mean epistasis to a more positive value.

These analyses provide strong statistical evidence for the predominance of positive epistasis in the genome of an organism undergoing frequent recombination and thus challenge hypotheses about the evolution of recombination based on negative epistasis. Our findings relate to the larger context of the evolution of recombination as follows. First, as in most other studies, fitness is not measured in the natural environment. However, we see no reason why the in vitro estimates of epistasis should be shifted toward positive values in comparison to the natural environment. Both PR and RT activity are essential for viral replication, and mutations affecting these viral enzymes probably have similar effects in vivo and in vitro. Second, our analysis is restricted to mutations in PR and RT. The genomic region surveyed constitutes around 15% of the coding HIV-1 genome. Because the prevailing form of epistasis may depend on the biological process that is affected (23), it is conceivable that positive epistasis prevails only among mutations in PR and RT. Whether it also prevails in other regions of the HIV genome will require additional investigation. The predominance of positive epistasis among drug resistance mu-

Fig. 2. (A) Distribution of epistasis values between all possible pairs of alternative amino acids across the aligned sequence set ($n = 103,286$). The solid vertical line indicates zero epistasis. To test whether the mean of this distribution (0.052) is significantly different from zero, we repeated the analysis 100 times based on randomized data sets. (B) The mean epistasis observed for the real data (black bar) is highly significantly different from the mean epistasis for the 100 randomized data sets (gray bars). (C) Distribution of epistasis



values when the analysis is restricted to positions that have a highly significant effect on fitness (22). Restricting the analysis to these 59 positions shifts the distribution toward more positive values (mean = 0.109).

tations may have implications for drug therapy, because computer simulations suggest that under these conditions, recombination impairs rather than facilitates the evolution of drug resistance in HIV (24). Third, it is unclear whether the beneficial effects of recombination for negative epistasis are negated by detrimental effects reflecting an equal degree of positive epistasis. However, approximate calculations assuming weak linkage between the locus coding for recombination rate and the loci under selection suggest that variation in the epistatic interactions weakens the selection for recombination and that recombination is selected against for positive mean epistasis (25). Finally, it remains to be shown whether the pattern of epistasis found in HIV-1 is representative of that in other organisms (in particular of that in eukaryotes). However, in contrast to studies measuring epistasis in *Escherichia coli*, yeast, or *Caenorhabditis elegans* (10, 13, 15), we have measured epistasis in an organism in which recombination occurs frequently. Therefore, it may in fact be more appropriate to extrapolate from retroviruses than from organisms that are effectively asexual.

The predominance of interactions with positive epistasis in HIV-1 raises the question of why retroviruses have evolved the capacity to recombine (24). Whether drift-based explanations for the benefits of recombination are applicable to HIV-1 remains to be investigated. Recent studies suggest that drift can favor the evolution of recombination even for very large populations, as long as there are a sufficient number of loci under selection (26). An alternative explanation is the repair of single-strand breaks (27). Retroviruses have single-stranded RNA genomes that are susceptible to ribonucleases and other agents during the viral life cycle. Template switching by RT in retroviruses could extend transcription beyond breakage points and could thus explain why retroviruses evolved to carry two complete genomes. According to this hypothesis, however, recombination in retroviruses would be the consequence but not the cause of the evolution of template switching.

Note added in proof: After this paper had been accepted, a related paper on epistasis in the vesicular stomatitis virus by Sanjuán *et al.* appeared (29).

References and Notes

1. J. Maynard Smith, Ed., *The Evolution of Sex* (Cambridge Univ. Press, Cambridge, 1976).
2. R. E. Michod, B. R. Levin, Eds., *The Evolution of Sex* (Sinauer Press, Sunderland, MA, 1988).
3. N. H. Barton, B. Charlesworth, *Science* **281**, 1986 (1998).
4. S. P. Otto, T. Lenormand, *Nature Rev. Genet.* **3**, 252 (2002).
5. M. W. Feldman, F. B. Christiansen, L. D. Brooks, *Proc. Natl. Acad. Sci. U.S.A.* **77**, 4838 (1980).
6. A. S. Kondrashov, *Nature* **336**, 435 (1988).
7. N. H. Barton, *Genet. Res.* **65**, 123 (1995).
8. A. S. Kondrashov, *J. Hered.* **84**, 372 (1993).
9. W. R. Rice, *Nature Rev. Genet.* **3**, 241 (2002).

10. S. F. Elena, R. E. Lenski, *Nature* **390**, 395 (1997).
11. S. F. Elena, *J. Mol. Evol.* **49**, 703 (1999).
12. M. de la Pena, S. F. Elena, A. Moya, *Evolution* **54**, 686 (2000).
13. A. D. Peters, P. D. Keightley, *Genetics* **156**, 1635 (2000).
14. M. C. Whitlock, D. Bourguet, *Evolution* **54**, 1654 (2000).
15. D. M. Wloch, K. Szafraniec, R. H. Borts, R. Korona, *Genetics* **159**, 441 (2001).
16. C. L. Burch, P. E. Turner, K. A. Hanley, *J. Evol. Biol.* **16**, 1223 (2003).
17. A. Rivero, F. Balloux, S. A. West, *Evolution* **57**, 1698 (2003).
18. C. L. Burch, L. Chao, *Genetics* **167**, 559 (2004).
19. H. M. Temin, *Trends Genet.* **7**, 71 (1991).
20. A. Jung *et al.*, *Nature* **418**, 144 (2002).
21. D. N. Levy, G. M. Aldrovandi, O. Kutsch, G. M. Shaw, *Proc. Natl. Acad. Sci. U.S.A.* **101**, 4204 (2004).
22. Materials and methods are available as supporting material on Science Online.
23. E. Szathmary, *Genetics* **133**, 127 (1993).
24. M. T. Bretscher, C. L. Althaus, V. Müller, S. Bonhoeffer, *BioEssays* **26**, 180 (2004).
25. S. P. Otto, M. W. Feldman, *Theor. Popul. Biol.* **51**, 134 (1997).
26. M. M. Iles, K. Walters, C. Cannings, *Genetics* **165**, 2249 (2003).
27. J. M. Coffin, *J. Gen. Virol.* **42**, 1 (1979).
28. The R Project for Statistical Computing (www.r-project.org).
29. R. Sanjuán, A. Moya, S. F. Elena, *Proc. Natl. Acad. Sci. U.S.A.* **101**, 15376 (2004).
30. We acknowledge the ViroLogic Clinical Reference Laboratory for their efforts in generating the replication capacity and PR/RT sequence data and C. Althaus, V. Müller, S. Otto, T. Pfeiffer, and M. Salathé for valuable comments. S.B. acknowledges the Swiss National Science Foundation for financial support. The development of the drug resistance database and replication capacity assay used in this study was funded in part by Small Business Innovative Research-Advanced Technology Grants from the National Institute of Allergy and Infectious Diseases, NIH (R43 AI057068 and R43 AI050321). S.B. is an equity holder in ViroLogic, Inc.

Supporting Online Material

www.sciencemag.org/cgi/content/full/306/5701/1547/DC1

Materials and Methods
References

22 June 2004; accepted 14 October 2004

Femtomolar Sensitivity of a NO Sensor from *Clostridium botulinum*

Pierre Nioche,¹ Vladimir Berka,² Julia Vipond,³ Nigel Minton,⁴ Ah-Lim Tsai,² C. S. Raman^{1*}

Nitric oxide (NO) is extremely toxic to *Clostridium botulinum*, but its molecular targets are unknown. Here, we identify a heme protein sensor (SONO) that displays femtomolar affinity for NO. The crystal structure of the SONO heme domain reveals a previously undescribed fold and a strategically placed tyrosine residue that modulates heme-nitrosyl coordination. Furthermore, the domain architecture of a SONO ortholog cloned from *Chlamydomonas reinhardtii* indicates that NO signaling through cyclic guanosine monophosphate arose before the origin of multicellular eukaryotes. Our findings have broad implications for understanding bacterial responses to NO, as well as for the activation of mammalian NO-sensitive guanylyl cyclase.

Nitric oxide (NO) is a small, short-lived, and highly reactive gaseous molecule. In mammals, NO is biosynthesized from L-arginine by nitric oxide synthases, and it plays a key role in many and disparate cellular responses including host defense against microbial pathogens (1). Denitrifying bacteria generate NO (1 to 70 nM) by a unique mode of respiration in which nitrogen oxides (NO₃⁻, NO₂⁻, NO, and N₂O) are reduced to N₂ (2). Nondenitrifiers, like *Escherichia coli*, can produce NO during anaerobic nitrate respiration (NO₃⁻ → NO₂⁻ → NH₄⁺), although at much reduced

levels (3). *Clostridium botulinum*, a strict anaerobe, is neither a denitrifier nor capable of making NO via other mechanisms. It is the etiological agent of botulism and produces the most toxic substance known to humans [median lethal dose (LD₅₀) ≈ 0.2 ng per kilogram of body weight]. Since the late 1920s sodium nitrite, with NO as the antimicrobial principle, has been used to inhibit the growth of heat-resistant *C. botulinum* spores and toxin production in cured meats (4–6). However, the molecular strategies used by this bacterium to recognize and avoid NO in its native and host environments have remained elusive.

To identify candidate NO sensors in *C. botulinum*, we investigated the hypothesis (7, 8) that a prokaryotic counterpart to the mammalian NO receptor, soluble guanylyl cyclase (sGC) (9, 10), exists and that a bacterial NO sensor may communicate with the chemotaxis machinery. Thus, we screened the genome of *C. botulinum* (www.sanger.ac.uk/Projects/C_botulinum/) for an ortholog

¹Structural Biology Research Center and Department of Biochemistry and Molecular Biology, ²Division of Hematology, Internal Medicine, University of Texas Medical School, Houston, TX 77030, USA. ³Health Protection Agency, Porton Down, Salisbury, Wiltshire SP4 0JG, UK. ⁴Center of Biomolecular Sciences and Institute of Infection, Immunity and Inflammation, University of Nottingham, Nottingham NG7 2RD, UK.

*To whom correspondence should be addressed: E-mail: c.s.raman@uth.tmc.edu

of the NO-binding heme domain (11) of human sGC- β_1 . We found a gene that encodes a two-domain protein (598 amino acids in length) in which the N-terminal domain shares 15% sequence identity with the first 186 amino acids of sGC- β_1 and the C-terminal domain is similar to that of a methyl-accepting chemotaxis protein (MCP). Because the N-terminal region of mammalian sGC is indispensable for NO binding, we named the *C. botulinum* protein SONO (sensor of NO). Reverse transcription–polymerase chain reaction analysis (fig. S1) (12) showed a transcript of the predicted size and confirmed that SONO was expressed in actively growing vegetative *C. botulinum* cells.

We overproduced SONO N-terminal heme domain (residues 1 to 186, CB-SONO_{HD}) in *E. coli*. Purified CB-SONO_{HD} is red in color, and electronic spectroscopy revealed the presence of a b-type heme (12). Mass spectrometry confirmed the identity of the heme prosthetic group (iron protoporphyrin IX) (13). A heme protein has not been previously identified in *clostridia*. To assess the coordination structure of the heme in CB-SONO_{HD}, we recorded its electron paramagnetic resonance (EPR) spectra (12). The protein yielded a classic three-line spectrum (14) (Fig. 1A) diagnostic of a five-coordinate (5c) low-spin heme-nitrosyl, Fe(II)(NO), complex that is unaffected by exposure to air. The main spectral feature is the three-line hyperfine splitting centered at $g_z = 2.007$ with a separation of 1.7 mT. The splitting arises from the strong coupling between the unpaired electron spin and the nuclear spin ($I = 1$) of the ^{14}N atom of NO. It further indicates that the proximal Fe–histidine bond in the protein is readily broken. Such an air-stable heme-nitrosyl is unprecedented (15–17) [supporting online material (SOM) note 1]. We followed the aerobic decay of the three-line EPR signal of CB-SONO_{HD} as a function of time. A half-life ($t_{1/2}$) of 70 ± 16 hours ($n = 3$) was obtained (fig. S2) and is equivalent to a dissociation rate constant (k_{off}) of $\approx 3 \times 10^{-6} \text{ s}^{-1}$. NO binding to SONO_{HD} is diffusion limited [$k_{\text{on}} \approx 10^8 \text{ M}^{-1} \text{ s}^{-1}$ (18)], and we obtain an equilibrium dissociation con-

stant ($K_D = k_{\text{off}}/k_{\text{on}}$) of $\approx 30 \times 10^{-15} \text{ M}$. This value approaches that suggested for NO binding to four-coordinate model heme compounds (15), but has not been previously reported for Fe(II)-heme proteins (SOM note 2). The presence of an air-stable Fe(II)(NO) species indicates that molecular oxygen cannot react with this complex.

We used CB-SONO_{HD} to quantify the amount of NO generated during aerobic growth of *E. coli*. *E. coli* are thought to generate NO only during anaerobic nitrate respiration (3) because NO production is undetectable during aerobic growth [as we confirmed with chemiluminescence-based NO analyzer (Eco Physics CLD88sp) with a sensitivity of <1 part per billion]. However, the EPR spectra of intact *E. coli* cells aerobically expressing CB-SONO_{HD} (Fig. 1B) resembled those of purified CB-SONO_{HD}, suggesting that the bound NO originated in the *E. coli* cytosol (SOM note 3). Cells that did not express CB-SONO_{HD} are devoid of this signal. Quantitative EPR measurements (12) indicated that the *E. coli* cells produced (assuming a linear rate of formation) approximately one molecule of NO cell⁻¹ min⁻¹ (SOM note 4). The number of NO molecules bound to highly purified CB-SONO_{HD} was in the same range as that measured from intact cells. Note, however, that one free molecule of NO per *E. coli*, with a cell volume of 10^{-15} liter (19), translates to a concentration of $\sim 10^{-9} \text{ M}$. It is conceivable that one or more NO molecules may persist within the cytoplasm of a denitrifying cell, but this would not be true for *E. coli*, which lacks the denitrification machinery (SOM note 5). Therefore, our ability to detect NO production in aerobically grown *E. coli* (12) is a direct consequence of CB-SONO_{HD} functioning as a high-affinity sensor of NO.

We determined the crystal structure of a SONO ortholog (table S1) from the extremely thermophilic organism *Thermoanaerobacter tengcongensis*, strain MB4^T (20) (SOM note 6) [TT-SONO; 39% sequence identity with CB-SONO (fig. S3)] due to difficulties in growing crystals of CB-SONO_{HD}. The tertiary topology of TT-SONO heme domain (TT-SONO_{HD}) is characterized by a proxi-

mal domain with an $\alpha\beta\alpha\beta\beta$ motif and an α -helical distal domain (fig. S4). This fold has not been described previously. The heme is sandwiched between the two domains (Fig. 2), and its iron atom is coordinated by His¹⁰². Heme recognition is mediated by hydrogen bonds between the propionates and the strictly conserved side chains of Tyr¹³¹, Ser¹³³, and Arg¹³⁵ (figs. S3 and S5; SOM note 7). Numerous nonbonded contacts exist between the tetrapyrrole and the residues that form the binding pocket. With the exception of Tyr¹⁴⁰, the distal heme pocket is apolar and there are no polar atoms within 7 Å of the heme iron. During structure refinement, it became clear that a distal ligand was bound to the heme iron. The protein has a Soret maximum at 416 nm, which suggests the presence of a hexacoordinate Fe(II)(O₂) complex (SOM note 8). As a consequence, we modeled dioxygen into the density (Fig. 3). The chemical makeup of the TT-SONO_{HD} distal heme pocket resembles that of the Thr-E11→Val variant (21) of *Cerebratulus lacteus* minihemoglobin (fig. S6). This protein also purifies as a high-affinity Fe(II)(O₂) complex and, like TT-SONO_{HD}, has a Tyr residue within hydrogen-bonding distance to the terminal oxygen (SOM note 9).

Although both TT-SONO_{HD} and CB-SONO_{HD} have a similar constellation of side chains in the distal heme pocket (fig. S6), we have been unable to generate a stable Fe(II)(O₂) complex with CB-SONO_{HD}. NO-stripped CB-SONO_{HD} also readily oxidizes to its Fe(III) state. Like *C. botulinum*, *T. tengcongensis* is a strict anaerobe; however, it has an optimal growth temperature of 75°C (20). At 70°C, TT-SONO_{HD} did not form a stable Fe(II)(O₂) complex, but instead readily oxidized to the Fe(III) state. Upon addition of exogenous NO, TT-SONO_{HD} also

Fig. 1. EPR spectra of SONO heme domain (SONO_{HD}). (A) CB-SONO_{HD} purifies as a heme-nitrosyl complex. (B) *E. coli* cells overproducing CB-SONO_{HD}. (C) Purified NP-SONO. (Sidebar) Coomassie-stained SDS-polyacrylamide gel. The relative molecular sizes of NP- and CB-SONO_{HD} are 22,482 and 22,630, respectively.

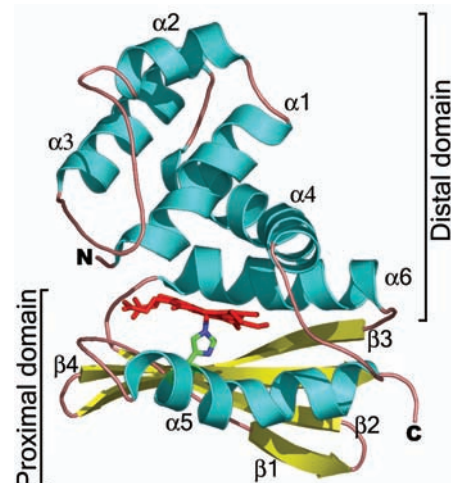
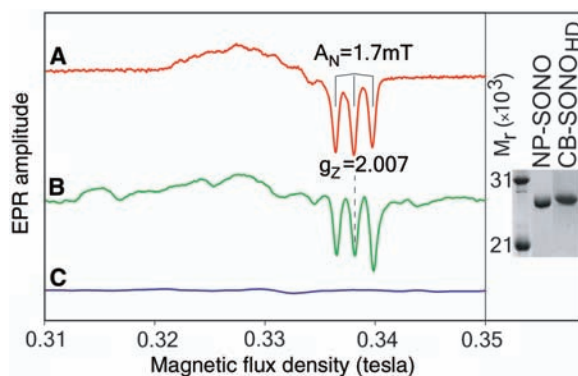


Fig. 2. Three-dimensional structure of TT-SONO_{HD}. Ribbon diagram depicts residues 1 to 181 of the protein. The heme prosthetic group (red) and the histidine coordinating its iron are also shown.

generated a five-coordinate Fe(II)(NO) complex at 70°C. In contrast, a six-coordinate (6c) Fe(II)(NO) complex was formed at 25°C, and we found no evidence for a heme-nitrosyl complex in purified TT-SONO_{HD}.

To assess the role of electrostatic interactions (22, 23) in stabilizing the bound ligand, we replaced the distal Tyr¹³⁹ with a Phe in CB-SONO_{HD} (fig. S6). This substitution resulted in a protein that was unable to generate a 5c-heme-nitrosyl, but instead produced a stable 6c-Fe(II)(NO) complex (fig. S7). The ability of an amino acid side chain in the distal pocket to modulate the bond strength of the proximal Fe-His linkage is unparalleled in heme protein research. Altogether, these results identify that NO binds on the distal side in CB-SONO_{HD} and suggest that electrostatic interaction with Tyr¹³⁹ is necessary for generating a neat 5c-Fe(II)(NO) complex and subsequently breaking the Fe-His bond (SOM note 10).

There appears to be a strong evolutionary pressure to modulate the NO sensitivity and specificity for SONO. For example, the rate of NO dissociation from CB-SONO_{HD} is at least two orders of magnitude slower than that of sGC (24). To evaluate the structural basis for such variation, we used TT-SONO_{HD} as a template to generate homology models of SONO_{HD} from human sGC-β₁ and *Nostoc punctiforme* (filamentous cyanobacterium) [(NP-SONO; the full-length protein, comprising amino acids 1 to 183, represents the heme domain and shares 40% sequence identity with human sGC-β₁ (fig. S3)]. Unlike CB-SONO_{HD} and TT-SONO_{HD}, neither human sGC-β₁ nor NP-SONO incorporates a Tyr side chain for interacting with the bound

ligand (fig. S6). Furthermore, the distal heme pocket lacks a polar atom within 7 Å of the heme iron. Consistent with this, purified NP-SONO is characterized by a Soret maximum at 431 nm and shows no apparent EPR signal (Fig. 1C) because it contains a Fe(II) five-coordinate high-spin heme (SOM note 11). Most heme proteins, except sGC (25, 26), can maintain this state only under anaerobic conditions, because oxygen will readily bind to the sixth coordination position. However, the Fe(II)-heme of NP-SONO remains five-coordinate even after several weeks of aerobic storage at 4°C. Because fossil data show that the *Nostoc* branch of the cyanobacterial tree diverged by 2.1 billion years ago (27), total exclusion of oxygen from the coordination sphere of SONO, concomitant with a diminution of NO sensitivity, may have occurred before the origin of unicellular eukaryotes.

To better delimit when during evolution the functional transition from SONO to sGC may have taken place, we examined the genome of *Chlamydomonas reinhardtii*—the eukaryotic unicellular green alga whose chloroplasts are derived from cyanobacteria (28). We found a *Chlamydomonas* expressed sequence tag whose product shares similarity with NP-SONO. We cloned the gene, and its product represents a full-length sGC-β with close resemblance to human sGC-β₁ (fig. S8; SOM note 12). A sGC ortholog has not been previously reported in a chloroplast-containing organism. The two proteins share similar nonpolar distal heme pockets, and both contain a Phe side chain in close proximity to the heme iron. Thus, eukaryotic sGC-β₁ may have evolved by the fusion of bacterial SONO_{HD} and a cyclase, thereby coupling NO binding to cyclic guanosine monophosphate production before the origin of animals.

In summary, we have uncovered a heme protein sensor that may be used by *C. botulinum* to recognize the presence of NO and mediate a phobic response as a protective mechanism (SOM note 13). Although *C. botulinum* is a motile organism, we have no direct evidence that it moves away from a source of noxious NO. However, two independent observations suggest that CB-SONO can sense and transduce signals to the chemotaxis machinery. First, the two-domain architecture of CB-SONO is reminiscent of the soluble aerotransducer HemAT (29) in which a myoglobin-like heme domain is used to sense O₂ and the methyl-accepting chemotaxis protein domain helps with initiating bacterial aerotaxis. Second, the gene encoding SONO in *Vibrio cholerae* is repressed by about eightfold alongside other chemotaxis genes in vibrios shed by cholera-infected individuals (30, 31). Furthermore, we draw a parallel between the suggested taxis role for SONO in bacteria and the ability of sGC to confer chemoattractive responses to dendrites

and axons (32). Our structural findings also provide mechanistic insights into how NO activates sGC in mammalian systems (figs. S9 and S10; SOM note 14). Taken together, our studies indicate that SONO_{HD}, with alterations to its NO sensitivity, may have been coopted to serve as a NO-activated molecular switch for regulating distinct cellular processes.

Note added in proof: During revision of this manuscript, structural characterization (33, 34) of a similar protein was reported.

References and Notes

1. L. J. Ignarro, in *Nitric Oxide: Biology and Pathobiology*, L. Ignarro, Ed. (Academic Press, San Diego, CA, 2000), pp. 3–19.
2. W. G. Zumft, *J. Mol. Microbiol. Biotechnol.* **4**, 277 (2002).
3. H. Corker, R. K. Poole, *J. Biol. Chem.* **278**, 31584 (2003).
4. D. Reddy, J. R. Lancaster Jr., D. P. Cornforth, *Science* **221**, 769 (1983).
5. R. Cammack et al., *Biochim. Biophys. Acta* **1411**, 475 (1999).
6. P. M. Davidson, in *Food Microbiology: Fundamentals and Frontiers*, M. P. Doyle, L. R. Beuchat, T. J. Montville, Eds. (American Society for Microbiology, Washington, DC, 2001), pp. 593–627.
7. R. J. P. Williams, *Biochim. Biophys. Acta* **1058**, 71 (1991).
8. S. J. Ferguson, *Biochim. Biophys. Acta* **1058**, 17 (1991).
9. F. Murad, *Angew. Chem. Int. Ed. Engl.* **38**, 1856 (1999).
10. D. Koelsing, M. Russwurm, E. Mergia, F. Mullershausen, A. Friebe, *Neurochem. Int.* **45**, 813 (2004).
11. B. Wedel et al., *Proc. Natl. Acad. Sci. U.S.A.* **91**, 2592 (1994).
12. Materials and methods are available as supporting material on Science Online.
13. R. Timkovich, personal communication.
14. T. Yonetani, A. Tsuneshige, Y. Zhou, X. Chen, *J. Biol. Chem.* **273**, 20323 (1998).
15. T. G. Traylor, V. S. Sharma, *Biochemistry* **31**, 2847 (1992).
16. P. C. Ford, I. M. Lorkovic, *Chem. Rev.* **102**, 993 (2002).
17. G. R. Wyllie, W. R. Scheidt, *Chem. Rev.* **102**, 1067 (2002).
18. J. S. Olson, personal communication.
19. C. E. Outten, T. V. O'Halloran, *Science* **292**, 2488 (2001).
20. Y. Xue, Y. Xu, Y. Liu, Y. Ma, P. Zhou, *Int. J. Syst. Evol. Microbiol.* **51**, 1335 (2001).
21. A. Pesce et al., *J. Biol. Chem.* **279**, 33662 (2004).
22. G. N. Phillips Jr., M. L. Teodoro, T. Li, B. Smith, J. S. Olson, *J. Phys. Chem.* **103**, 8817 (1999).
23. M. R. Thomas, D. Brown, S. Franzen, S. G. Boxer, *Biochemistry* **40**, 15047 (2001).
24. V. G. Kharitonov, V. S. Sharma, D. Magde, D. Koelsing, *Biochemistry* **36**, 6814 (1997).
25. R. Gerzer, E. Böhme, F. Hofmann, G. Schultz, *FEBS Lett.* **132**, 71 (1981).
26. J. R. Stone, M. A. Marletta, *Biochemistry* **33**, 5636 (1994).
27. A. H. Knoll, *Science* **285**, 1025 (1999).
28. W. Martin et al., *Nature* **393**, 162 (1998).
29. S. Hou et al., *Nature* **403**, 540 (2000).
30. D. S. Merrell et al., *Nature* **417**, 642 (2002).
31. A. Camilli, personal communication.
32. F. Polleux, T. Morrow, A. Ghosh, *Nature* **404**, 567 (2000).
33. P. Pellicena et al., *Proc. Natl. Acad. Sci. U.S.A.* **101**, 12854 (2004).
34. D. S. Karow et al., *Biochemistry* **43**, 10203 (2004).
35. C.S.R. dedicates this paper to M. Perutz and T. Traylor. C.S.R. is grateful to F. Rudolph and Rice University for providing laboratory space during the 2001 Houston flood; S. Boxer, J. Eraso, P. Ford, A. Grossman, J. Groves, M. Ikeda-Saito, J. Linder, W. Martin, J. Meeks, J. Olson, T. Poulos, F. Robb, J. Schragger, J. Schultz, J. Shapleigh, T. Spiro, S. Veeraraghavan, F.A. Walker, and W. Zumft for stimulating discussions; A. Camilli, J. Kaper, J. Olson, N. Stokes, R. Timkovich, T. Tomita, and B. Weiss for communicating unpublished results; C. Churcher, E. Harris, J. Kropat, T. McKerns, J. Meeks, S. Merchant, F. Murad, J. Parkhill, I. Scott, Eco Physics, Japanese Collection of Microorganisms, and Kazusa DNA Research Institute for access to strains, genomic DNA, RNA, protocols, and instrumentation; G. Bricogne for providing BUSTER and C. Vornrhein for assistance with using the program; and the Advanced Light Source (beamline 8.3.1, J. Holton, J. Tanamachi), Stanford

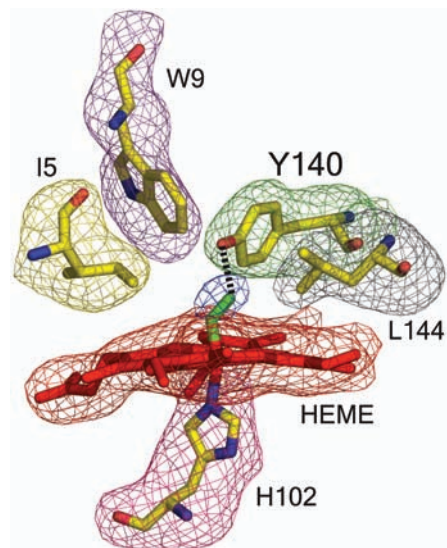


Fig. 3. Omit difference electron density map ($F_{obs} - F_{calc}$) of the heme pocket. Maps are shown at 3σ level. Oxygen ligand density is in blue. Dotted line indicates that the phenolic -OH of Tyr¹⁴⁰ is within hydrogen-bonding distance of the oxygen ligand.

Synchrotron Radiation Laboratories (beamline 9.2, M. Soltis), and European Synchrotron Radiation Facility (beamline ID29, W. Shepard) for beam time and help with data collection. This work is supported by the Pew Charitable Trusts through a Pew Scholar Award (C.S.R.), The Robert A. Welch Foundation grant AU-1524 (C.S.R.), NIH grant R01 AI054444 (C.S.R.), and Association pour la Recherche sur le Cancer (P.N.).

The GenBank accession number for *C. reinhardtii* sGC- β cloned in this work is AY343540. Coordinates and structure factors are available from the RCSB Protein Data Bank under accession code 1XBN.

Supporting Online Material
www.sciencemag.org/cgi/content/full/1103596/DC1
Materials and Methods

Figs S1 to S10
Table S1
References and Notes

3 August 2004; accepted 27 September 2004
Published online 7 October 2004;
10.1126/science.1103596
Include this information when citing this paper.

Compensated Deleterious Mutations in Insect Genomes

Rob J. Kulathinal,¹ Brian R. Bettencourt,² Daniel L. Hartl^{1*}

Relatively little is known about the importance of amino acid interactions in protein and phenotypic evolution. Here we examine whether mutations that are pathogenic in *Drosophila melanogaster* become fixed via epistasis in other Dipteran genomes. Overall divergence at pathogenic amino acid sites is reduced. However, ~10% of the substitutions at these sites carry the exact same pathogenic amino acid found in *D. melanogaster* mutants. Hence compensatory mutation(s) must have evolved. Surprisingly, the fraction 10% is not affected by phylogenetic distance. These results support a selection-driven process that allows compensated amino acid substitutions to become rapidly fixed in taxa with large populations.

By mapping sequence space onto a fitness surface, the “fitness landscape” provides a powerful metaphor to understand how proteins evolve in populations. Sequence evolution may be visualized to traverse fitness peaks and valleys as certain sequence combinations are deleterious, advantageous, or neutral to an organism’s overall reproductive success. Using this landscape, Sewall Wright (1) championed the view that evolution occurs via epistatic or “coadapted” genetic interactions (2). In contrast, R.A. Fisher envisioned selection primarily acting on additive effects of individual loci (3). Whether epistatic interactions play an important role in the evolutionary trajectory of proteins—particularly in species with large effective population sizes—remains an open question.

The recently completed genomic sequence of *D. pseudoobscura* (4) offers a unique opportunity to approach this question by integrating the extensive mutant phenotypic information from *D. melanogaster* with a full set of orthologous gene sequences. These two fly species diverged between 40 and 50 million years ago (mya) and contain ample divergence information for comparative analyses. For nearly a century, *D. melanogaster* has been the target of extensive mutagenic screens, and a curated database of characterized mutant phenotypes and their corresponding molecular etiologies is freely accessible in the public domain (5).

We analyzed single amino acid residues that, when mutated in *D. melanogaster*, cause a

drastic fitness loss yet appear as the wild-type amino acid at its homologous site (termed “index site”) in the *D. pseudoobscura* protein. For such pathogenic substitutions to become fixed in another species, second-site or compensatory mutations must have coevolved (6). The number of compensated pathogenic deviations—or CPDs, using the parlance of Kondrashov *et al.* (6)—was compared to the number of index-site substitutions in *D. pseudoobscura* that contain an amino acid other than the one known to be pathogenic in *D. melanogaster* (Fig. 1). “%CPD” refers to the fraction of CPDs among substituted index sites. We sorted through all phenotypic mutants available from FlyBase (version 3.1) with the assumption that none of these mutants could persist in a natural population. From 35,311 “Gene” entries in FlyBase, we found 2245 single-site amino acid mutations that lead to a defined mutant phenotype, representing 525 unique genes. Most genes have between one and three different mutations; thus, our sample is not biased toward particular loci.

Of these genes, 475 had unambiguously aligned orthologs in *D. pseudoobscura* (4) representing 328,060 aligned amino acid sites. Overall, 77.8% of all amino acid sites were conserved between the two species. All instances in which a pathogenic amino acid site in *D. melanogaster* was present in the wild-type *D. pseudoobscura* protein were tabulated. To ensure site-specific orthology, we counted the number of conserved sites among 10 flanking amino acids on each side of the index site. Single-site insertion/deletion mutations were counted as one amino acid change. When a 50% identity criterion among flanking sites

was used, we found that among 1527 amino acid sites causing a phenotypic mutation in *D. melanogaster*, only 64 had substitutions in the *D. pseudoobscura* ortholog. Thus, substitutions among index sites were significantly less frequent than were random substitutions (95.8% versus 77.8%, $P < 0.0001$), an observation also reported in humans and mice (7), which suggests that selective constraints are maintained over time. Surprisingly, six of these index sites, or 1 in 10 substitutions at pathogenic sites, contained exactly the same amino acid that causes a deleterious phenotypic change in *D. melanogaster* [%CPD ~ 10% (Table 1)]. Similarly, using a 75% identity criterion (close to the average protein divergence estimated between these species), we found four CPDs among 31 index sites.

The same analysis was then applied to the more distantly related *Anopheles gambiae* genome (divergence ~250 mya). We aligned 210,778 orthologous amino acid sites (insertions and deletions ignored) from 317 proteins, with an overall 52.4% identity. When a 50% flanking region cutoff was used (corresponding approximately to the average amino acid divergence between these species), there were 77 substitutions among 784

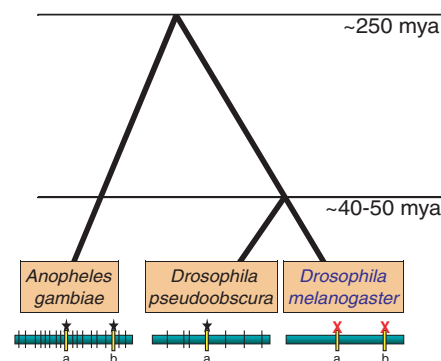


Fig. 1. Phylogenetic relationship of *D. melanogaster*, *D. pseudoobscura*, and *A. gambiae* and identification of compensated deleterious mutations. *D. melanogaster* is the reference species with site-specific mutational data on phenotypic mutants. Sites possessing amino acid residues that cause phenotypic deviations in *D. melanogaster* are called index sites (yellow bars). Other substituted sites are not informative (black vertical bars). We concentrate on index sites that contain substitutions (indicated as a and b) in at least one of the other species (denoted by a star). Index-site substitutions are of two types: the exact same pathogenic amino acid (CPDs) or other, non-exact amino acid substitutions.

¹Department of Organismic and Evolutionary Biology, ²Department of Molecular and Cellular Biology, Harvard University, Cambridge, MA 02138, USA.

*To whom correspondence should be addressed. E-mail: dhartl@oeb.harvard.edu

Table 1. Compensated amino acid substitutions from *D. melanogaster* versus *D. pseudoobscura* and *D. melanogaster* versus *A. gambiae*.

<i>D. melanogaster</i> versus	Number of orthologs*	Protein identity	Index sites	Substituted amino acids	Exact amino acids substituted
<i>D. pseudoobscura</i>	475	77.8%	1527	64 (4.2%)	6 (9.4%)
<i>A. gambiae</i>	317	52.4%	784	77 (9.8%)	7 (9.1%)

*Phenotypic mutants with known single-amino acid mutations and identified orthologous sites. A 50% identity criterion among flanking sites was used in both comparisons.

index sites; 7 of these sites were CPDs. Although we again observed a significantly higher degree of conservation at index sites as compared to random sites in the *D. melanogaster*–*Anopheles gambiae* (*mel-Anoph*) comparison, index sites appear relatively less conserved over larger phylogenetic distance [*D. melanogaster*–*D. pseudoobscura* (*mel-pse*) 95.8% divergence versus *mel-Anoph* 90.2% divergence]. In contrast, among substituted index sites, the proportion with pathogenic amino acid changes remained remarkably constant over phylogenetic distance (%CPD ~ 10%; Table 1).

Using a somewhat different methodological approach on a set of 32 mammalian proteins, Kondrashov *et al.* (6) estimated that about 10% of all amino acid sites producing a pathogenic deviation in humans are present as the wild-type amino acid in at least one nonhuman mammal, independent of phylogenetic distance. Whereas we calculated %CPD from all possible and informative orthologs of three reference genomes, Kondrashov and colleagues used a large number of missense and nonsense mutations from a small but well-characterized subset of proteins to estimate %CPD among a variable set of organisms. We note that the quality of available mutational information is very different between the mammalian OMIM (Online Mendelian Inheritance in Man) and FlyBase databases, and the number of *Drosophila* genes with both missense and nonsense molecular information is insufficient to provide a comparable estimate of %CPDs using the same statistical methods as in Kondrashov *et al.* (6). From their results, the authors argue that, in mammals, nearby second-site compensatory mutation(s) must have rapidly coevolved with the index-site mutation to quickly traverse fitness valleys. Such valleys, as Wright (1) surmised, are important routes of evolutionary change in small isolated populations involving genotypic combinations that are deleterious in the presence of more fit neighboring genotypes. Their results effectively refute the hypothesis of the gradual and independent fixation of single compensatory mutations, because the accumulation of such modifiers would increase the fixation probability of the compensated deviations themselves, causing the fraction of CPDs among index sites to increase over phylogenetic distance.

Our results from three complete Dipteran genomes also reveal a high degree of compensatory mutational events. Epistatic interactions are evolving in insects, as the deleterious consequences of less-fit index site substitutions have become masked (or compensated) by at least one other mutation. By itself, the compensatory mutation(s) may have been neutral, beneficial, or even deleterious, and the series of mutational events could have occurred in either the *D. melanogaster* lineage or its sister lineages. Although the overall proportion of substituted index sites increases over phylogenetic distance, the %CPD remains constant and higher than expected. Therefore, compensated mutations must evolve frequently and regularly. We also found that most CPDs detected in this study were biochemically conservative amino acid changes appearing at a higher than expected frequency than other substitutions. Such conservative changes were observed at a significantly higher frequency among CPDs in the *mel-Anoph* lineage [$P = 0.029$ for *mel-Anoph*, $P = 0.071$ for *mel-pse* (Table 2)]. The conservative nature of substitutional change also suggests that compensatory mechanisms need not involve dramatic changes in fitness.

Using *A. gambiae* as an outgroup, we can also infer where in each gene tree specific mutational and compensatory events have arisen. Two protein-encoding genes, *carnation* and *Amylase proximal*, contain identified CPDs that are common to both the *D. pseudoobscura* and *Anopheles* data sets, indicating that molecular compensation must have evolved in the *melanogaster* branch (Fig. 1 and table S1). In these two cases, the ancestral amino acid at the index site causes a mutant phenotype in *D. melanogaster*, providing evidence for a deleterious mutational step in the compensatory process. One of these proteins, *Amylase proximal*, contains two CPD sites (T398A and D278N), each evolving in separate lineages. Four and five identified compensated sites appear to have evolved in the *D. pseudoobscura* and *Anopheles* lineages, respectively (table S1).

Even though Dipterans possess much larger effective population sizes than mammals (8), resulting in deleterious alleles persisting for shorter times due to efficient selection against them, we obtained a similar fraction of

Table 2. Composition of total substitutions versus compensated amino acid substitutions.

<i>D. melanogaster</i> versus	Number of substitutions	Conservative
<i>D. pseudoobscura</i>	Total*	583,423 45.3%
	CPD	6 66.7%
<i>A. gambiae</i>	Total	1,069,768 43.2%
	CPD	7 71.4%

*All available reciprocally best-hit protein orthologs.

compensated mutations as were found in mammals (6). These observations strongly support the contention that compensatory mutational evolution is independent of population size. When conditioned on other genetic backgrounds, the pool of mutations presently lethal in a *D. melanogaster* genetic background may become neutral (9, 10)—or possibly even advantageous—and rapidly become fixed by selection for favorable epistatic interactions. Such rapid fixation of compensatory events has been demonstrated in RNA secondary structure (11), and these results suggest an analogous process acting on protein structure. Recent analyses of selection at the molecular level also support the presence of considerable positive selection in *Drosophila* (12–14). In the future, it should be possible to combine mutational screens and fitness assays so as to finely dissect elements of compensation at the molecular level.

References and Notes

1. S. Wright, *Proc. Int. Congr. Genet.* 6th (1932), vol. 1, pp. 356–366.
2. T. Dobzhansky, *Genetics of the Evolutionary Process* (Columbia Univ. Press, NY, 1970).
3. R. A. Fisher, *The Genetical Theory of Natural Selection* (Clarendon, Oxford, 1930).
4. S. Richards *et al.*, *Genome Res.*, in press.
5. FlyBase Consortium, *Nucleic Acids Res.* 31, 172 (2003).
6. A. S. Kondrashov, S. Sunyaev, F. A. Kondrashov, *Proc. Natl. Acad. Sci. U.S.A.* 99, 14878 (2002).
7. R. H. Waterston *et al.*, *Nature* 420, 520 (2002).
8. R. K. Kliman *et al.*, *Genetics* 156, 1913 (2000).
9. M. Kimura, *J. Genet.* 64, 7 (1985).
10. W. Stephan, *Genetics* 144, 419 (1996).
11. C. O. Wilke, R. E. Lenski, C. Adami, *BMC Evol. Biol.* 3, 3 (2003).
12. J. C. Fay, G. J. Wyckoff, C. I. Wu, *Nature* 415, 1024 (2002).
13. N. G. C. Smith, A. Eyre-Walker, *Nature* 415, 1022 (2002).
14. S. A. Sawyer, R. J. Kulathinal, C. D. Bustamante, D. L. Hartl, *J. Mol. Evol.* 57, S154 (2004).
15. We thank members of the Hartl lab, especially D. Weinreich, for helpful discussions and the Computational Biology Group at the Bauer Center for Genomics Research for the use of their cluster. This work was supported by a Natural Sciences and Engineering Research Council of Canada (NSERC) Postdoctoral Fellowship (R.J.K.), a National Human Genome Research Institute (NHGRI) grant (P41-HG00739) to FlyBase (B.R.B.), and an NIH grant (GM068465) (D.L.H.).

Supporting Online Material

www.sciencemag.org/cgi/content/full/1100522/DC1 Table S1

20 May 2004; accepted 22 September 2004
 Published online 21 October 2004;
 10.1126/science.1100522
 Include this information when citing this paper

A Probabilistic Functional Network of Yeast Genes

Insuk Lee,¹ Shailesh V. Date,^{1*} Alex T. Adai,^{1†}
Edward M. Marcotte^{1,2‡}

A conceptual framework for integrating diverse functional genomics data was developed by reinterpreting experiments to provide numerical likelihoods that genes are functionally linked. This allows direct comparison and integration of different classes of data. The resulting probabilistic gene network estimates the functional coupling between genes. Within this framework, we reconstructed an extensive, high-quality functional gene network for *Saccharomyces cerevisiae*, consisting of 4681 (~81%) of the known yeast genes linked by ~34,000 probabilistic linkages comparable in accuracy to small-scale interaction assays. The integrated linkages distinguish true from false-positive interactions in earlier data sets; new interactions emerge from genes' network contexts, as shown for genes in chromatin modification and ribosome biogenesis.

Knowledge of the correct overall structures of gene networks will be invaluable for characterizing the complex roles of individual genes and the interplay between the many systems in a cell. Deriving gene networks from heterogeneous functional genomics data, however, is often difficult, because experiments such as microarray analyses of gene expression (1) or systematic protein interaction mapping measure different aspects of gene or protein associations. Affinity purification of proteins analyzed by mass spectrometry (2, 3), for instance, measures the tendency for proteins to be components of the same physical complex, although not necessarily to contact each other directly. By contrast, yeast two-hybrid assays may often indicate direct physical interactions (stable or transient) between proteins (4–6), whereas synthetic lethal screens (7) measure the tendency for genes to compensate for the loss of other genes. Further, these analyses range considerably in accuracy (8), and it is not clear a priori which measurements are correct. In spite of these differences, these data sets can, in principle, be computationally integrated, primarily by the reconstruction of network models of the relations between genes (9–12). Such network reconstructions have largely focused on physical protein interactions and

so represent only a subset of biologically important relations.

We sought to construct a more accurate and extensive gene network by considering functional, rather than physical, associations, realizing that each experiment, whether genetic, biochemical, or computational, adds evidence linking pairs of genes, with associated error rates and degree of coverage. In this framework, gene-gene linkages are probabilistic summaries representing functional coupling between genes. Only some of the links represent direct protein-protein interactions; the rest are associations not mediated by physical contact, such as regulatory, genetic, or metabolic coupling, that, nonetheless, represent functional constraints satisfied by the cell during the course of the experi-

ments. Working with probabilistic functional linkages allows many diverse classes of experiments to be integrated into a single, coherent network (Fig. 1), which enables the linkages themselves to be more reliably established.

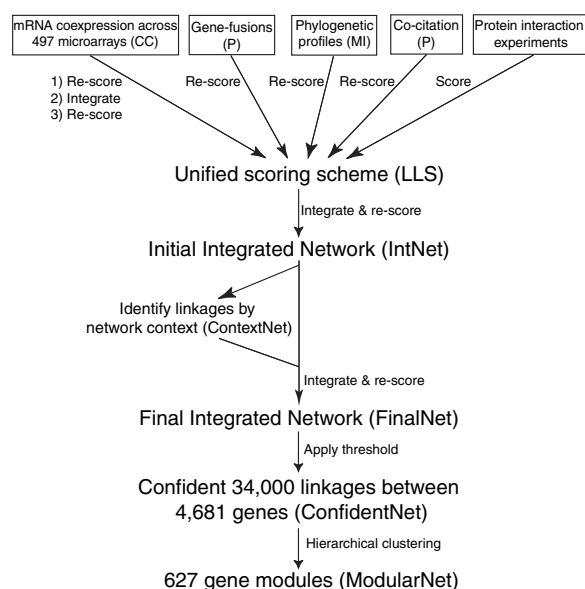
We first developed a unified scoring scheme for linkages, based on a Bayesian statistics approach. Each experiment is evaluated for its ability to reconstruct known gene pathways and systems by measuring the likelihood that pairs of genes are functionally linked conditioned on the evidence, calculated as a log likelihood score:

$$LLS = \ln \left(\frac{P(L|E)/\sim P(L|E)}{P(L)/\sim P(L)} \right)$$

where $P(L|E)$ and $\sim P(L|E)$ are the frequencies of linkages (L) observed in the given experiment (E) between annotated genes operating in the same pathway and in different pathways, respectively, whereas $P(L)$ and $\sim P(L)$ represent the prior expectations (i.e., the total frequency of linkages between all annotated yeast genes operating in the same pathway and operating in different pathways, respectively). Scores greater than zero indicate that the experiment tends to link genes in the same pathway, with higher scores indicating more confident linkages.

The log likelihood score can be interpreted as being proportional to the accuracy of the experiments and their ability to inform us about cellular pathways. Because each experiment is measured on a common benchmark, different experiments' scores are directly comparable, even when the natures of experiments are distinct (e.g., comparing genetic relations to physical interactions),

Fig. 1. The method for integrating functional genomics data. Functional genomics data sets are first benchmarked for their relative accuracies; these are used as weights in a probabilistic integration of the data. Several raw data sets already have intrinsic scoring schemes, indicated in parentheses (e.g., CC, correlation coefficients; P, probabilities, and MI, mutual information scores). These data are rescored with LLS, then integrated into an initial network (IntNet). Additional linkages from the genes' network contexts (ContextNet) are then integrated to create the final network (FinalNet), with ~34,000 linkages between 4681 genes (ConfidentNet) scoring higher than the gold standard (small-scale assays of protein interactions). Hierarchical clustering of ConfidentNet defined 627 modules of functionally linked genes spanning 3285 genes ("ModularNet"), approximating the set of cellular systems in yeast.



¹Center for Systems and Synthetic Biology, and
²Department of Chemistry and Biochemistry, Institute for Molecular Biology, University of Texas at Austin, Austin, TX 78712–1064, USA.

*Present address: Center for Bioinformatics, 423 Guardian Drive, University of Pennsylvania, Philadelphia, PA 19104, USA.

†Present address: Mission Bay Genentech Hall, 600 16th Street, Suite N472D, University of California at San Francisco, San Francisco, CA 94143–2240, USA.

‡To whom correspondence should be addressed. E-mail: marcotte@icmb.utexas.edu

and can be added to indicate confidence of combined evidence.

As scoring “benchmarks,” we tested the method against two primary annotation references: the Kyoto-based KEGG pathway database (13) and the experimentally observed yeast protein subcellular locations determined by genomewide green fluorescent protein (GFP)-tagging and microscopy (14). KEGG scores were used for integrating linkages, with the other benchmark withheld as an independent test of linkage accuracy. Cross-validated benchmarks and benchmarks based on the Gene Ontology (GO) (15) and KOG gene annotations (16) provided comparable results (17).

Seven large-scale yeast protein interaction experiments, including small-scale protein interaction assays collected from the Database of Interacting Proteins (DIP) (18), high-throughput mass spectrometry (2, 3), yeast two-hybrid (4–6), and synthetic lethal assays (7), showed similar rankings of accuracy across the four benchmark tests (Fig. 2; fig. S8, A and B). These tests indicate that small-scale experiments (our “gold standard” for high accuracy linkages) have been the most accurate of all, whereas the large-scale experiments vary considerably in quality. Even the least accurate experiments score better than random linkages (for which LLS = 0), highlighting the merit of this method: weak evidence from multiple sources can be combined to provide strong overall evidence for a linkage.

Functional linkages were first inferred on the basis of genes’ mRNA coexpression across each of 12 sets of DNA microarray

experiments (497 microarray experiments in total), then integrated via a rank-weighted sum of log likelihood scores (17) to create the combined set of coexpression-derived linkages. To construct the initial integrated network (“IntNet,” Fig. 1), we combined eight categories of data, including the physical and genetic interaction data sets, mRNA coexpression linkages, functional linkages from literature mining (17), and computational linkages from two comparative genomics methods, Rosetta stone (gene-fusion) linkages (19, 20) and phylogenetic profiles (21). Integrating functional genomics data also allowed discovery of additional relations between genes linked, in turn, to a common set of genes [“ContextNet” (17, 22–25)]; these linkages were scored and integrated as above to construct the final gene network (“FinalNet,” Fig. 3A). The final network has ~34,000 linkages at an accuracy comparable to the gold standard small-scale interaction assays (Fig. 2), which provides linkages (“ConfidentNet”) for more than 4681 yeast genes (~81% of the yeast proteome). The network is reasonably distinct from networks of physical interacting proteins [e.g., sharing only ~16% of linkages with (11); see (17)].

Adding context-inferred linkages increased clustering of genes (fig. S7, C and D), which produced a highly modular gene network with well-defined subnetworks. We expected these gene clusters to reflect gene systems and modules (26–30). We could therefore generate a simplified view of the major trends in the network (Fig. 3B) by clustering genes of ConfidentNet according to their connectivities (17). Of the 4681

genes, 3285 (~70.2%) were grouped into 627 clusters, reflecting the high degree of modularity. Genes’ functions within each cluster are highly coherent (fig. S12), and with 2 to 154 genes per cluster (~5 genes per cluster on average), the clusters effectively capture typical gene pathways and/or systems. A region of the modular network centered on the DNA damage response and repair systems is shown in Fig. 3C. The network is clearly hierarchical: Individual clusters represent distinct systems related to DNA damage response and/or repair; these clusters are in turn connected to modules of cell cycle regulatory genes and chromatin silencing (fig. S13), functionally linked to the DNA damage response and/or repair system. [For cluster descriptions and interactive three-dimensional visualizations, see (17).]

One can infer individual genes’ functions on the basis of linked neighbors. For example, seven uncharacterized genes are implicated in chromatin remodeling (Fig. 3D). All but 1 of the 18 linkages made by these genes arise from the comparative genomics analysis or from the network context methods, which represent examples of the insights that arise only after data integration. Three of the uncharacterized proteins are predicted by sequence homology to have helicase activity, which is reasonable for a relation to chromatin remodeling; four of these proteins localize to the nucleus, further supporting their association. After this network’s construction, one gene, VID21, was implicated in chromatin modification as a component of the NuA4 histone acetyl transferase.

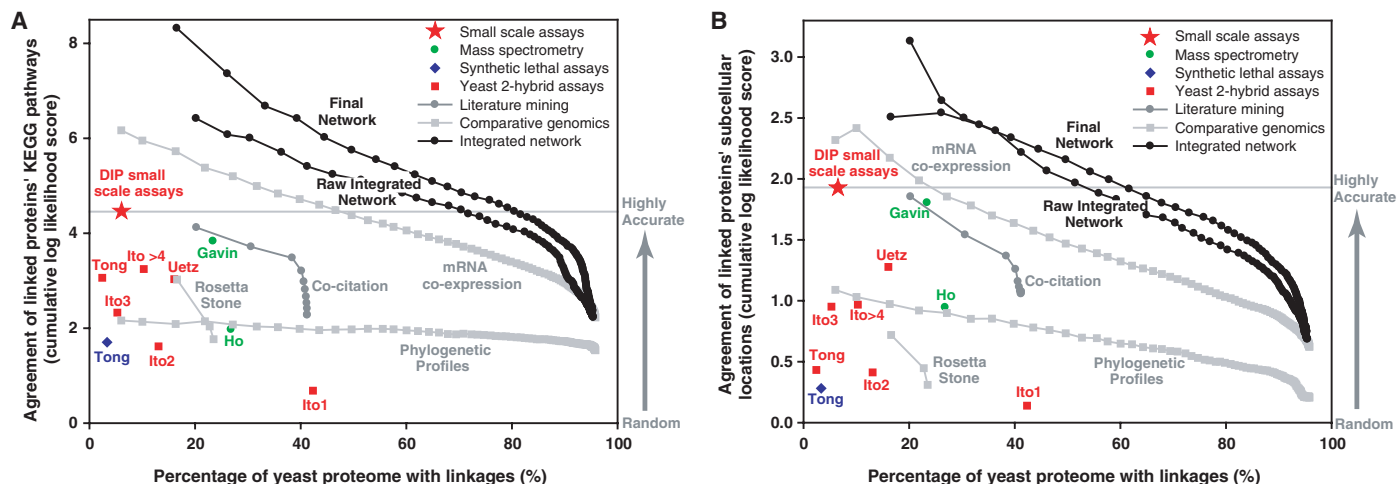


Fig. 2. Benchmarked accuracy and extent of functional genomics data sets and the integrated networks. A critical point is the comparable performance of the networks on distinct benchmarks, which assess the tendencies for linked genes to share (A) KEGG pathway annotations (13) or (B) protein subcellular locations (14). Each x axis indicates the percentage of protein-encoding yeast genes provided with linkages by the plotted data; each y axis indicates relative accuracy, measured as the agreement of the linked genes’ annotations on that benchmark. The gold

standards of accuracy (red star) for calibrating the benchmarks are small-scale protein-protein interaction data from DIP (18). Colored markers indicate experimental linkages; gray markers, computational. The initial integrated network (lower black line), trained using only the KEGG benchmark, has measurably higher accuracy than any individual data set on the subcellular localization benchmark; adding context-inferred linkages in the final network (upper black line) further improves the size and accuracy of the network [see (17) for additional benchmarks].

The function of the RNA helicase PRP43, previously thought to be involved only in pre-mRNA splicing and implicated in lariatintron release from the spliceosome (31), is also clarified in the network. PRP43 is linked most strongly to genes of ribosome biogenesis and rRNA processing. The tightest links are to ERB1, RRB1, NUG1, LHP1, and PWP1, the first three of which are confirmed

ribosome biogenesis factors. These links derive only from the coexpression and context methods [with a single exception from (3)]; data integration is therefore critical. The association of PRP43 with ribosome biogenesis has now been experimentally validated (32): the growth defect conferred by a PRP43 conditional lethal mutation corresponds to a rapid and major defect in rRNA processing.

These data indicate that rRNA processing is the essential function of PRP43, and it joins a growing group of RNA helicases with two or more distinct functions.

The probabilistic gene network we describe integrates evidence from diverse sources to reconstruct an accurate network, by estimating the functional coupling among yeast genes, and provides a view of the relations between

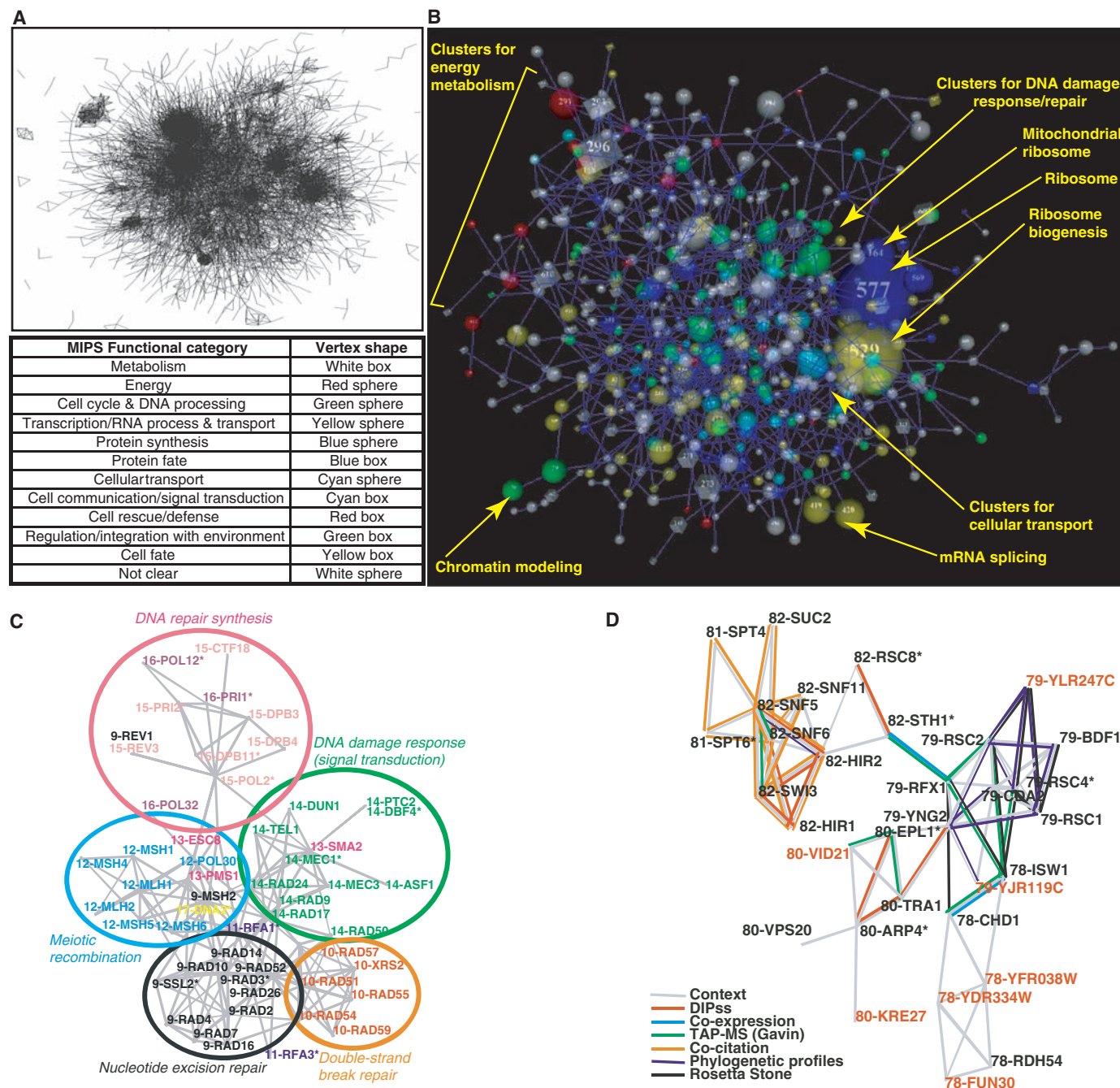


Fig. 3. Features of integrated networks. The final network shows extensive clustering of genes into modules, evident in the “clumping” (A). At an intermediate degree of clustering that maximizes cluster size and functional coherence (B), 564 (of 627) modules are shown connected by the 950 strongest intermodule linkages. Module colors and shapes indicate associated functions, as defined by Munich Information Center for Protein Sequencing (MIPS) (34), with sizes proportional to the

number of genes, and connections inversely proportional to the fraction of genes linking the clusters. Portions of the final, confident gene network are shown for (C) DNA damage response and/or repair, where modularity gives rise to gene clusters, indicated by similar colors (see also fig. S13), and (D) chromatin remodeling, with several uncharacterized genes (red labels). Networks are visualized with Large Graph Layout (LGL) (35).

yeast proteins distinct from their physical interactions. The application of this strategy to other organisms, such as to the human genome, is conceptually straightforward: (i) assemble benchmarks for measuring the accuracy of linkages between human genes based on properties shared among genes in the same systems, (ii) assemble gold standard sets of highly accurate interactions for calibrating the benchmarks, and (iii) benchmark functional genomics data for their ability to correctly link human genes, then integrate the data as described. New data can be incorporated in a simple manner [e.g., see (33)], serving to reinforce the correct linkages. Thus, the gene network will ultimately converge by successive approximation to the correct structure simply by continued addition of functional genomics data in this framework.

References and Notes

1. J. Gollub *et al.*, *Nucleic Acids Res.* **31**, 94 (2003).
2. A. C. Gavin *et al.*, *Nature* **415**, 141 (2002).
3. Y. Ho *et al.*, *Nature* **415**, 180 (2002).
4. P. Uetz *et al.*, *Nature* **403**, 623 (2000).
5. T. Ito *et al.*, *Proc. Natl. Acad. Sci. U.S.A.* **98**, 4569 (2001).
6. A. H. Tong *et al.*, *Science* **295**, 321 (2002).

7. A. H. Tong *et al.*, *Science* **294**, 2364 (2001).
8. C. von Mering *et al.*, *Nature* **417**, 399 (2002).
9. E. M. Marcotte, M. Pellegrini, M. J. Thompson, T. O. Yeates, D. Eisenberg, *Nature* **402**, 83 (1999).
10. T. Ideker *et al.*, *Science* **292**, 929 (2001).
11. R. Jansen *et al.*, *Science* **302**, 449 (2003).
12. C. von Mering *et al.*, *Nucleic Acids Res.* **31**, 258 (2003).
13. M. Kanehisa, S. Goto, S. Kawashima, A. Nakaya, *Nucleic Acids Res.* **30**, 42 (2002).
14. W. K. Huh *et al.*, *Nature* **425**, 686 (2003).
15. S. S. Dwyer *et al.*, *Nucleic Acids Res.* **30**, 69 (2002).
16. R. L. Tatusov *et al.*, *BMC Bioinformatics* **4**, 41 (2003).
17. Materials and methods, supporting text, figures, tables, and data are available on Science Online.
18. I. Xenarios *et al.*, *Nucleic Acids Res.* **30**, 303 (2002).
19. E. M. Marcotte *et al.*, *Science* **285**, 751 (1999).
20. A. J. Enright, I. Iliopoulos, N. C. Kyrpides, C. A. Ouzounis, *Nature* **402**, 86 (1999).
21. M. Pellegrini, E. M. Marcotte, M. J. Thompson, D. Eisenberg, T. O. Yeates, *Proc. Natl. Acad. Sci. U.S.A.* **96**, 4285 (1999).
22. M. Thompson, E. Marcotte, M. Pellegrini, T. Yeates, D. Eisenberg, in *Currents in Computational Molecular Biology*, S. Miyano, R. Shamir, T. Takagi, Eds. (Universal Academy Press, Tokyo, 2000).
23. D. S. Goldberg, F. P. Roth, *Proc. Natl. Acad. Sci. U.S.A.* **100**, 4372 (2003).
24. M. P. Samanta, S. Liang, *Proc. Natl. Acad. Sci. U.S.A.* **100**, 12579 (2003).
25. T. Schlitt *et al.*, *Genome Res.* **13**, 2568 (2003).
26. L. H. Hartwell, J. J. Hopfield, S. Leibler, A. W. Murray, *Nature* **402**, C47 (1999).

27. J. B. Pereira-Leal, A. J. Enright, C. A. Ouzounis, *Proteins* **54**, 49 (2004).
28. V. Spirin, L. A. Mirny, *Proc. Natl. Acad. Sci. U.S.A.* **100**, 12123 (2003).
29. A. W. Rives, T. Galitski, *Proc. Natl. Acad. Sci. U.S.A.* **100**, 1128 (2003).
30. C. von Mering *et al.*, *Proc. Natl. Acad. Sci. U.S.A.* **100**, 15428 (2003).
31. A. Martin, S. Schneider, B. Schwer, *J. Biol. Chem.* **277**, 17743 (2002).
32. Scott Stevens, personal communication.
33. A. G. Fraser, E. M. Marcotte, *Nat. Genet.* **36**, 559 (2004).
34. H. W. Mewes *et al.*, *Nucleic Acids Res.* **30**, 31 (2002).
35. A. T. Adai, S. V. Date, S. Wieland, E. M. Marcotte, *J. Mol. Biol.* **340**, 179 (2004).
36. We thank S. Stevens for sharing prepublication PRP43 results and A. Fraser, A. Ramani, Z. Simpson, and A. Johnson for critical comments and discussion. This work is supported by the Welch (F-1515) and Dreyfus Foundations, NSF, a Packard Fellowship (E.M.M.), and NIH (GM067779-01).

Supporting Online Material

www.sciencemag.org/cgi/content/full/306/5701/1555/DC1
 Materials and Methods
 SOM Text
 Figs. S1 to 14
 Tables S1 to S4
 Supporting Data S1 to S5

22 April 2004; accepted 8 October 2004

Requirement of JNK2 for Scavenger Receptor A–Mediated Foam Cell Formation in Atherogenesis

Romeo Ricci,^{1,2*} Grzegorz Sumara,^{1,2†} Izabela Sumara,³ Izabela Rozenberg,¹ Michael Kurrer,⁴ Alexander Akhmedov,¹ Martin Hersberger,⁵ Urs Eriksson,⁷ Franz R. Eberli,¹ Burkhard Becher,⁶ Jan Borén,⁸ Mian Chen,⁹ Myron I. Cybulsky,⁹ Kathryn J. Moore,¹⁰ Mason W. Freeman,¹⁰ Erwin F. Wagner,¹¹ Christian M. Matter,^{1‡} Thomas F. Lüscher^{1‡}

In vitro studies suggest a role for c-Jun N-terminal kinases (JNKs) in pro-atherogenic cellular processes. We show that atherosclerosis-prone *ApoE*^{-/-} mice simultaneously lacking JNK2 (*ApoE*^{-/-} *JNK2*^{-/-} mice), but not *ApoE*^{-/-} *JNK1*^{-/-} mice, developed less atherosclerosis than do *ApoE*^{-/-} mice. Pharmacological inhibition of JNK activity efficiently reduced plaque formation. Macrophages lacking JNK2 displayed suppressed foam cell formation caused by defective uptake and degradation of modified lipoproteins and showed increased amounts of the modified lipoprotein-binding and -internalizing scavenger receptor A (SR-A), whose phosphorylation was markedly decreased. Macrophage-restricted deletion of JNK2 was sufficient to decrease atherogenesis. Thus, JNK2-dependent phosphorylation of SR-A promotes uptake of lipids in macrophages, thereby regulating foam cell formation, a critical step in atherogenesis.

Atherosclerosis is the result of complex interactions between modified lipoproteins, monocyte-derived macrophages that become foam cells, T lymphocytes, and cells from the vessel wall (1, 2). The c-Jun N-terminal kinases (JNKs) belong to the mitogen-activated protein kinase (MAPK) family. Ten JNK

isoforms have been identified in the human brain, corresponding to alternative spliced isoforms derived from the JNK1, JNK2, and JNK3 genes (3). JNK1 and JNK2 are widely expressed. In contrast, JNK3 has a more limited pattern of expression that is largely restricted to brain, heart, and testis. Al-

though mice lacking JNK1 or JNK2 appear morphologically normal, they are immunocompromised because of T-cell defects (4). Recent studies in murine disease models defined specific functions for JNK1 and JNK2. JNK1 regulates insulin resistance and obesity (5). JNK2 is required for collagen-induced arthritis (6). In vitro studies have revealed that JNK proteins act in a variety of pro-atherogenic cellular processes involving endothelial cell activation, T-effector cell differentiation and proliferation, and migration of vascular smooth muscle cells (VSMCs) (7).

To investigate the role of JNK in atherosclerotic plaque formation in vivo, we used atherosclerosis-prone apolipoprotein E

¹Cardiovascular Research, Institute of Physiology, and Division of Cardiology, University Hospital Zurich, CH-8057 Zurich, Switzerland. ²Institute of Cell Biology, ³Institute of Biochemistry, Eidgenössische Technische Hochschule, Höggerberg, CH-8093 Zurich, Switzerland. ⁴Department of Pathology, ⁵Institute of Clinical Chemistry, ⁶Department of Neurology/Neuroimmunology Unit, University Hospital Zurich, CH-8091 Zurich, Switzerland. ⁷Experimental Critical Care Medicine, Department of Research and Medicine A, Basel University Hospital, CH-4031 Basel, Switzerland. ⁸Wallenberg Laboratory for Cardiovascular Research, Goteborg University, Goteborg S-4345, Sweden. ⁹Toronto General Research Institute and Department of Laboratory Medicine and Pathobiology, University of Toronto, Toronto, ON, Canada. ¹⁰Lipid Metabolism Unit, Massachusetts General Hospital, Harvard Medical School, Boston, MA 02114, USA. ¹¹Institute of Molecular Pathology, A-1030 Vienna, Austria.

*To whom correspondence should be addressed. E-mail: romeo.ricci@cell.biol.ethz.ch

†These authors contributed equally to this work.

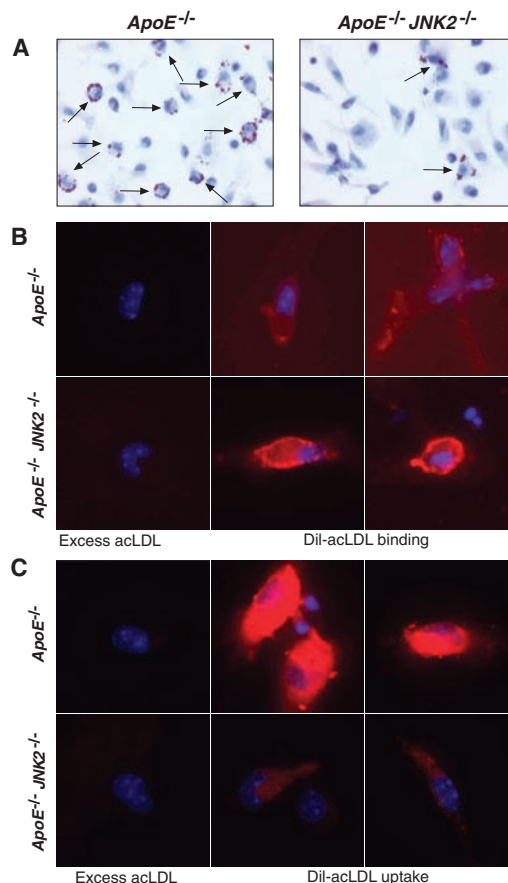
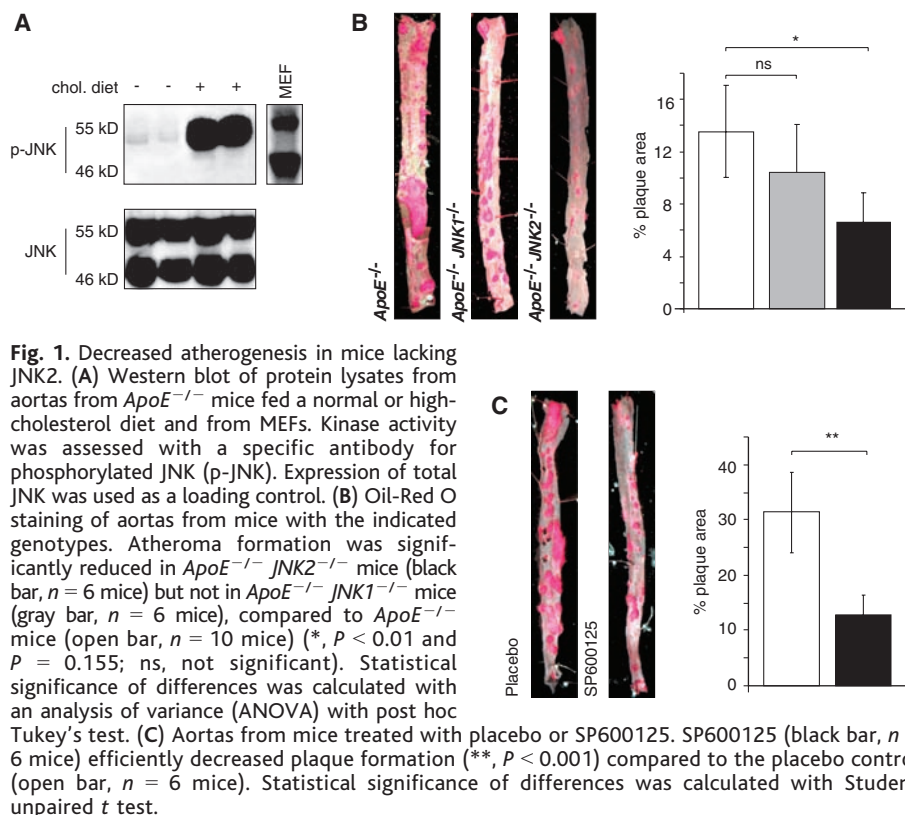
‡These authors contributed equally to this work.

(ApoE) knockout mice (*ApoE*^{-/-} mice) (8) (fig. S1). We compared JNK activation in *ApoE*^{-/-} mice that were fed either a normal chow or a high-cholesterol diet for 14 weeks. Western blotting of lysates from the whole aorta with a phosphospecific antibody showed increased activation of JNK after 14 weeks of a high-cholesterol diet correlating with the presence of clearly established plaques, which were hardly visible in chow-fed *ApoE*^{-/-} mice at the same time point. Only the larger JNK isoforms (55 kD) were phosphorylated in aortic vessels. In contrast, both isoforms were activated in serum-stimulated mouse embryonic fibroblasts (MEFs) (Fig. 1A).

To assess the function of JNK1 and JNK2 in atheroma formation, double knockout *ApoE*^{-/-} *JNK1*^{-/-} and *ApoE*^{-/-} *JNK2*^{-/-} mice and corresponding *ApoE*^{-/-} control mice were subjected to a high-cholesterol diet for 14 weeks. The mouse aortas were opened longitudinally and stained with Oil-Red O to visualize atherosclerotic plaques. We found smaller plaques in *ApoE*^{-/-} *JNK2*^{-/-} mice than in *ApoE*^{-/-} control mice. Absence of JNK1 had little or no effect. Plaque areas expressed as a percentage of the total vessel wall area were reduced about 50% in *ApoE*^{-/-} *JNK2*^{-/-} (*P* < 0.01) but not in *ApoE*^{-/-} *JNK1*^{-/-} (*P* = 0.155) mice (Fig. 1B). We treated *ApoE*^{-/-} mice with either SP600125, a pharmacological inhibitor of JNK (9), or a placebo for the last 4 weeks of a total of 14 weeks of a high-cholesterol diet. SP600125 caused an ~50% reduction of plaque formation in *ApoE*^{-/-} mice (*P* < 0.001) (Fig. 1C). Plasma triglycerides and cholesterol levels were equally increased (fig. S2, A and B), and lipoprotein fractionation (fig. S2, C and D) looked equivalent in *ApoE*^{-/-} and *ApoE*^{-/-} *JNK2*^{-/-} mice, implicating that the reduction of atheroma formation occurred independently of the lipid profile in double mutant mice.

Activation of endothelial cells by proinflammatory stimuli occurs through expression of various leukocyte adhesion molecules such as vascular cell adhesion molecule 1 (VCAM-1), intercellular adhesion molecule 1 (ICAM-1), and E-selectin, which is an important event in the initiation of atherosclerosis (10, 11). However, immunohistochemical stainings of cross sections of aortic atherosclerotic plaques from *ApoE*^{-/-} *JNK2*^{-/-} and *ApoE*^{-/-} mice revealed no difference in expression of VCAM-1 and ICAM-1 in endothelial cells after 8 weeks of a high-fat diet (fig. S3A). Consistently, real-time reverse transcription polymerase chain reaction (RT-PCR) for VCAM-1 and E-selectin showed no significant differences (fig. S3, B and C).

The role of adaptive immunity during atherogenesis has been broadly investigated.



Specifically, pro-inflammatory T_H1-effector cells are thought to be important in the development of atherosclerosis (12). JNK2 is specifically required for differentiation of CD4-expressing T-cells into effector cells (13). Similar amounts of CD3-, CD4-, and CD8-expressing T-cells were quantified (fig. S4, A to C). Total lymphocyte deficiency in *ApoE*^{-/-} mice has no effect on the extent of atherosclerosis when lesion development is accelerated in mice fed a high-fat Western-type diet (14, 15). JNK1 and JNK2 have similar functions in T-effector cell differentiation (16), but JNK1 had little or no effect on plaque development in our experiments. Thus, plaque development appeared to occur independently of T-cells. Similarly sized areas containing macrophages expressing F4/80, a 160-kD glycoprotein expressed by most murine macrophages, were detected in *ApoE*^{-/-} *JNK2*^{-/-} and *ApoE*^{-/-} controls (fig. S4D). Collagen staining revealed the same pattern of fibrosis in plaques of both groups (fig. S4E). Altogether, JNK2 deficiency did not affect plaque composition and cellularity.

Enhanced proliferation and migration of VSMCs contribute to the pathogenesis of atherosclerosis (17). A JNK-mediated pathway is involved in platelet-derived growth factor (PDGF)-induced proliferation and migration of VSMCs (18). However, primary aortic

VSMCs isolated from *JNK2*^{-/-} and wild-type mice showed similar proliferation and migration rates upon PDGF stimulation (fig. S4, F and G).

Foam cell formation is a crucial step in atherogenesis. Circulating monocytes adhere to activated endothelial cells and transigrate into the subintima to become tissue macrophages. Upon exposure to modified lipoproteins such as the oxidized and acetylated forms of low-density lipoproteins (oxLDL and acLDL), these macrophages become foam cells (19). We subjected peritoneal macrophages isolated from *ApoE*^{-/-} *JNK2*^{-/-} and *ApoE*^{-/-} control mice to oxLDL in vitro. *JNK2*^{-/-} macrophages formed only half as many foam cells as did control cells (*P* < 0.02) (Fig. 2A and fig. S5A). However, foam cell formation in *ApoE*^{-/-} *JNK1*^{-/-} macrophages was not significantly altered (fig. S5A) (*P* = 0.998).

We investigated whether decreased binding or defective uptake of modified lipoproteins could account for impaired foam cell formation in the absence of JNK2. We assessed receptor-mediated binding and uptake of fluorescently labeled acLDL (Dil-labeled acLDL). Immunofluorescence revealed a two-fold increase in binding of Dil-labeled acLDL in the absence of JNK2 (*P* < 0.01) (Fig. 2B

and fig. S5B). In contrast, uptake and degradation of [¹²⁵I]-acLDL was about one third of that in control cells (*P* < 0.01) (Fig. 2C and fig. S5, C and D). We also observed that cellular cholesterol efflux to apolipoprotein AI (apoAI) was increased in *JNK2*^{-/-} macrophages, suggesting that enhanced cholesterol efflux might also contribute to reduced foam cell formation in the absence of JNK2 (fig. S5E).

To test whether a JNK2-dependent mechanism in macrophages accounts for the reduction of atherosclerosis in vivo, we performed bone marrow transplantation experiments. Bone-marrow from *ApoE*^{-/-} or *ApoE*^{-/-} *JNK2*^{-/-} mice was transplanted into 6-week-old, lethally irradiated *ApoE*^{-/-} or *ApoE*^{-/-} *JNK2*^{-/-} mice. After 4 weeks of recovery, the mice were fed a high-fat diet for 14 weeks. Chimerism was determined in bone-marrow cells by PCR (fig. S6). Chimeric *ApoE*^{-/-} mice with *ApoE*^{-/-} *JNK2*^{-/-} macrophages showed a reduction of atherosclerotic lesions compared to *ApoE*^{-/-} *JNK2*^{-/-} mice transplanted with *ApoE*^{-/-} bone-marrow (*P* < 0.01). *ApoE*^{-/-} *JNK2*^{-/-} mice transplanted with *ApoE*^{-/-} *JNK2*^{-/-} bone-marrow also had reduced plaque formation compared to *ApoE*^{-/-} mice transplanted with *ApoE*^{-/-} bone-marrow (*P* < 0.01) (Fig.

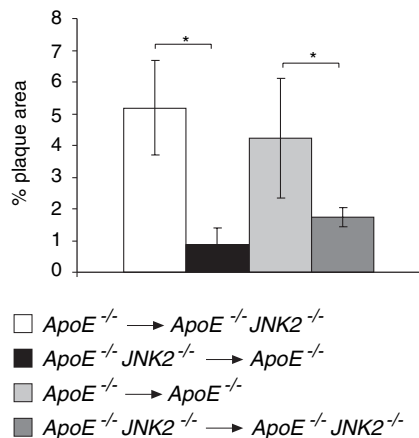


Fig. 3. Macrophage-restricted deletion of JNK2 was sufficient to decrease atherosclerosis. Transplantation of *ApoE*^{-/-} *JNK2*^{-/-} bone marrow into *ApoE*^{-/-} mice (*ApoE*^{-/-} *JNK2*^{-/-} → *ApoE*^{-/-}, black bar, *n* = 5 mice) revealed reduced atherosclerosis similar to that in *ApoE*^{-/-} *JNK2*^{-/-} animals transplanted with *ApoE*^{-/-} *JNK2*^{-/-} bone marrow (*ApoE*^{-/-} *JNK2*^{-/-} → *ApoE*^{-/-} *JNK2*^{-/-}, dark gray bar, *n* = 5 mice). Transplantation of *ApoE*^{-/-} bone marrow into *ApoE*^{-/-} *JNK2*^{-/-} mice (*ApoE*^{-/-} → *ApoE*^{-/-} *JNK2*^{-/-}, white bar, *n* = 5 mice) revealed a similar amount of atherosclerosis as in *ApoE*^{-/-} mice transplanted with *ApoE*^{-/-} deficient bone marrow (*ApoE*^{-/-} → *ApoE*^{-/-}, light gray bar, *n* = 5 mice) (**P* < 0.01). Statistical significance of differences was calculated with an ANOVA variance with post hoc Tukey's test.

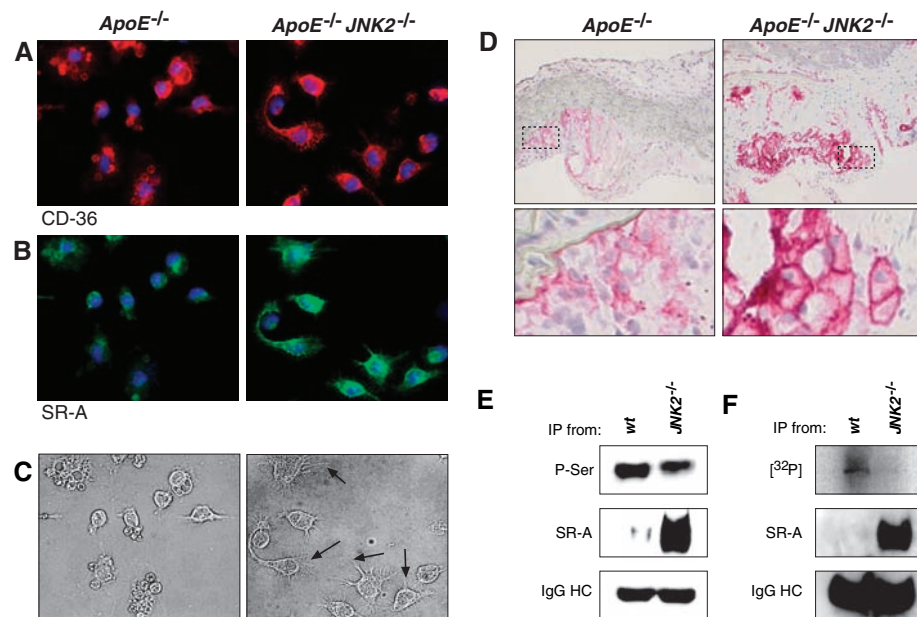


Fig. 4. *JNK2*^{-/-} macrophages display increased expression but decreased phosphorylation of SR-A. (A) CD36 immunofluorescence on peritoneal macrophages. No difference in fluorescence intensity was observed. For quantification, see fig. S7A. (B) SR-A immunofluorescence revealed a twofold increased staining in *ApoE*^{-/-} *JNK2*^{-/-} macrophages compared to *ApoE*^{-/-} cells. Quantification is shown in fig. S7. (C) Phase-contrast microscopy revealed filopodia formation in *ApoE*^{-/-} *JNK2*^{-/-} macrophages (arrows). (D) SR-A immunohistochemistry on plaques from aortic sinus, with higher magnifications of selected areas, showed increased expression of SR-A in *ApoE*^{-/-} *JNK2*^{-/-} macrophages. (E) Western blotting of immunoprecipitated SR-A with antibodies against SR-A and phosphoserine (P-Ser). A reduction of serine phosphorylation was detected in *JNK2*^{-/-} extracts. IgG HC, immunoglobulin G heavy chain; IP, immunoprecipitation; wt, wild-type. (F) Western blotting of immunoprecipitated SR-A with antibody against SR-A and phosphorylation in intact cells. Autoradiography revealed markedly decreased phosphorylation of SR-A ([³²P]) in *JNK2*^{-/-} cells (28).

3). Thus, deletion of JNK2 in macrophages was sufficient to decrease atherogenesis.

Two receptors appear to be essential in foam cell formation and receptor-mediated binding and uptake of modified lipoproteins: CD36 and scavenger receptor A (SR-A) (20). Immunofluorescence analyses revealed that expression of CD36 was unchanged in acLDL-stimulated peritoneal *ApoE*^{-/-} *JNK2*^{-/-} macrophages (Fig. 4A and fig. S7A). However, analyses with antibodies to SR-A showed increased abundance of this receptor (Fig. 4B and fig. S7B) ($P < 0.01$). Protein immunoblotting confirmed increased abundance of SR-A in protein extracts prepared from macrophages stimulated with acLDL. Amounts of SR-A were not altered in response to acLDL in double knockout or control animals (fig. S7C). *ApoE*^{-/-} *JNK2*^{-/-} macrophages formed filopodia-like projections, which were not observed in controls (Fig. 4C). This cellular phenotype is associated with increased adhesion and has been described in macrophages overexpressing SR-A (21). To examine whether increased abundance of SR-A in cultured macrophages also occurred in vivo, we used immunohistochemistry to detect SR-A on plaques from *ApoE*^{-/-} *JNK2*^{-/-} mice and *ApoE*^{-/-} control mice. Increased amounts of SR-A were detected in macrophages in plaques of *ApoE*^{-/-} *JNK2*^{-/-} mice compared to those of control mice (Fig. 4D).

Alternative splicing results in three types of SR-A transcripts in humans. Occurrence of the Type III SR-A blocks modified LDL uptake (22). Therefore, we analyzed the expression of all three splicing variants in macrophages by semiquantitative RT-PCR using specific primers. We could not detect Type III mRNA in macrophages of either genotype. Type I and Type II mRNA was not increased in the absence of JNK2 (fig. S7D). Expression of CD36 or peroxisome proliferator-activated receptor (PPAR γ) (23), was also not affected. Activation of the well-known JNK target c-jun in aortas from *ApoE*^{-/-} and *ApoE*^{-/-} *JNK2*^{-/-} mice fed either a normal or high-cholesterol diet was not affected, suggesting that c-jun-dependent gene expression was not impaired (fig. S7E). Phosphorylation of SR-A on specific serines is essential for SR-A-dependent processing of modified LDL and for surface expression of SR-A (24–26). We immunoprecipitated SR-A from total protein extracts of *JNK2*^{-/-} macrophages and corresponding wild-type cells. Western blotting of immunoprecipitated SR-A revealed an increased amount of SR-A in *JNK2*^{-/-} cells compared to wild-type cells (Fig. 4, E and F). Blotting with phosphoserine-specific antibody indicated that the amount of serine-phosphorylated SR-A was lower in *JNK2*^{-/-} extracts even though more SR-A protein was present (Fig. 4E). We confirmed decreased phosphorylation of SR-A

after labeling of *JNK2*^{-/-} macrophages with [³²P] orthophosphoric acid (Fig. 4F).

In this study, we provide in vivo evidence that JNK2 is required in a mouse model of atherogenesis. At the molecular level, we propose that JNK2-dependent decrease of SR-A phosphorylation and increase in SR-A abundance may lead to decreased internalization and degradation of receptor-bound modified LDL and as a consequence to reduced foam cell formation. Indeed, macrophage-specific overexpression of SR-A has been shown to be sufficient to reduce atherosclerosis in ApoE-deficient mice (27). In conclusion, specific inhibition of JNK2 activity may provide a therapeutic approach to decrease atheroma formation in patients.

References and Notes

1. P. Libby, *Nature* **420**, 868 (2002).
2. C. K. Glass, J. L. Witztum, *Cell* **104**, 503 (2001).
3. S. Gupta et al., *EMBO J.* **15**, 2760 (1996).
4. C. Dong et al., *Nature* **405**, 91 (2000).
5. J. Hirosumi et al., *Nature* **420**, 333 (2002).
6. Z. Han, L. Chang, Y. Yamanishi, M. Karin, G. S. Firestein, *Arthritis Rheum.* **46**, 818 (2002).
7. A. M. Manning, R. J. Davis, *Nature Rev. Drug Discov.* **2**, 554 (2003).
8. A. S. Plump et al., *Cell* **71**, 343 (1992).
9. Y. S. Heo et al., *EMBO J.* **23**, 2185 (2004).
10. M. I. Cybulsky et al., *J. Clin. Invest.* **107**, 1255 (2001).
11. Z. M. Dong, A. A. Brown, D. D. Wagner, *Circulation* **101**, 2290 (2000).
12. G. K. Hansson, P. Libby, U. Schonbeck, Z. Q. Yan, *Circ. Res.* **91**, 281 (2002).
13. D. D. Yang et al., *Immunity* **9**, 575 (1998).
14. H. M. Dansky, S. A. Charlton, M. M. Harper, J. D. Smith, *Proc. Natl. Acad. Sci. U.S.A.* **94**, 4642 (1997).
15. A. Daugherty et al., *J. Clin. Invest.* **100**, 1575 (1997).
16. C. Dong et al., *Science* **282**, 2092 (1998).
17. V. J. Dzau, R. C. Braun-Dullaeus, D. G. Sedding, *Nature Med.* **8**, 1249 (2002).
18. Y. Zhan et al., *Arterioscler. Thromb. Vasc. Biol.* **23**, 795 (2003).
19. A. C. Li, C. K. Glass, *Nature Med.* **8**, 1235 (2002).
20. V. V. Kunjathoor et al., *J. Biol. Chem.* **277**, 49982 (2002).
21. S. R. Post et al., *J. Lipid Res.* **43**, 1829 (2002).
22. P. J. Gough, D. R. Greaves, S. Gordon, *J. Lipid Res.* **39**, 531 (1998).
23. P. Tontonoz, L. Nagy, J. G. Alvarez, V. A. Thomazy, R. M. Evans, *Cell* **93**, 241 (1998).
24. H. Heider, E. S. Wintergerst, *FEBS Lett.* **505**, 185 (2001).
25. L. G. Fong, D. Le, *J. Biol. Chem.* **274**, 36808 (1999).
26. N. Kosswig, S. Rice, A. Daugherty, S. R. Post, *J. Biol. Chem.* **278**, 34219 (2003).
27. S. C. Whitman, D. L. Rateri, S. J. Szilvassy, J. A. Cornicelli, A. Daugherty, *J. Lipid Res.* **43**, 1201 (2002).
28. Macrophages were pulse-labeled with [³²P]orthophosphoric acid in sodium-phosphate-deficient culture medium 12 hours before harvesting.
29. We thank P. Lerch who provided us with oxLDL; D. Zhang and P. Meier, who helped us with isolation of aortas; H. Joch and A. Jaschko, who helped us with smooth muscle cell isolation; P. Bargsten, who helped us with bone marrow transplantation experiments; W. Krek and P. J. Gough, with whom we had very fruitful scientific discussions; and R. Eferl, for critical reading. Supported by the Swiss National Science Foundation (grant no. 3100-068118), the European Union (grant no. G5RD-CT-2001-00532), the Bundesamt für Bildung und Wissenschaft, and the Swiss Heart Foundation, and the "Forschungskredit 2003" of the University of Zurich.

Supporting Online Material

www.sciencemag.org/cgi/content/full/306/5701/1558/DC1

Materials and Methods

Figs. S1 to S7

References and Notes

23 June 2004; accepted 13 October 2004

Rise and Fall of the Beringian Steppe Bison

Beth Shapiro,^{1,2} Alexei J. Drummond,² Andrew Rambaut,² Michael C. Wilson,³ Paul E. Matheus,⁴ Andrei V. Sher,⁵ Oliver G. Pybus,² M. Thomas P. Gilbert,^{1,2} Ian Barnes,⁶ Jonas Binladen,⁷ Eske Willerslev,^{1,7} Anders J. Hansen,⁷ Gennady F. Baryshnikov,⁸ James A. Burns,⁹ Sergei Davydov,¹⁰ Jonathan C. Driver,¹¹ Duane G. Froese,¹² C. Richard Harington,¹³ Grant Keddie,¹⁴ Pavel Kosintsev,¹⁵ Michael L. Kunz,¹⁶ Larry D. Martin,¹⁷ Robert O. Stephenson,¹⁸ John Storer,¹⁹ Richard Tedford,²⁰ Sergei Zimov,¹⁰ Alan Cooper^{1,2*}

The widespread extinctions of large mammals at the end of the Pleistocene epoch have often been attributed to the depredations of humans; here we present genetic evidence that questions this assumption. We used ancient DNA and Bayesian techniques to reconstruct a detailed genetic history of bison throughout the late Pleistocene and Holocene epochs. Our analyses depict a large diverse population living throughout Beringia until around 37,000 years before the present, when the population's genetic diversity began to decline dramatically. The timing of this decline correlates with environmental changes associated with the onset of the last glacial cycle, whereas archaeological evidence does not support the presence of large populations of humans in Eastern Beringia until more than 15,000 years later.

Climatic and environmental changes during the Pleistocene epoch [from 2 million years ago (Ma) to 10,000 years before the present

(ky B.P.)] played an important role in the distribution and diversity of modern plants and animals (1, 2). In Beringia, local climate

and geology created an ice-free refugium stretching from eastern Siberia to Canada's Northwest Territories (3). Periodic exposure of the Bering Land Bridge facilitated the exchange of a diverse megafauna (such as bison, mammoth, and musk ox) supported by tundra-steppe grasses and shrubs (3, 4). Humans are believed to have colonized North America via this route, and the first well-accepted evidence of human settlement in Alaska dates to around 12 ky B.P. (5). The latest Pleistocene saw the extinction of most Beringian megafauna including mammoths, short-faced bears, and North American lions. The reasons for these extinctions remain unclear but are attributed most often to human impact (6, 7) and climate change associated with the last glacial cycle (8).

Pleistocene bison fossils are abundant across Beringia and they provide an ideal marker of environmental change. Bison are believed to have first entered eastern Beringia from Asia during the middle Pleistocene [marine oxygen isotope stages (MISs) 8 to 6, circa (ca.) 300 to 130 ky B.P.] and then moved southward into central North America

during the MIS 5 interglacial period (130 to 75 ky B.P.), where they were distributed across the continental United States (9). During this time, Beringian and central North American bison populations may have been periodically separated by glacial ice that formed over most of Canada (10, 11). The timing and extent of genetic exchange between these areas remain unclear (2).

The abundance and diversity of bison fossils have prompted considerable paleontological and archaeological research into their use as stratigraphic markers. Extensive morphological diversity, however, has complicated discrimination between even the most accepted forms of fossil bison, and the lack of stratigraphy in Beringian sites has prevented the development of a chronological context. These complications create a complex literature of conflicting hypotheses about bison taxonomy and evolution (9, 12). After a severe population bottleneck, which occurred only 200 years ago (13), two subspecies survive in North America: *Bison bison bison*, the plains bison, and *B. b. athabascae*, the wood bison (9, 13).

To investigate the evolution and demographic history of Pleistocene bison, we col-

lected 442 bison fossils from Alaska, Canada, Siberia, China, and the lower 48 United States (14). We used ancient DNA techniques to sequence a 685-base pair (bp) fragment of the mitochondrial control region (14). Accelerator mass spectrometry radiocarbon dates were obtained for 220 samples, which spanned a period of >60 ky (14).

The association of radiocarbon dates with DNA sequences enables the calibration of evolutionary rates within individual species (15). Bayesian phylogenetic analyses produced an evolutionary rate estimate for the bison mitochondrial control region of 32% per million years (My) [95% highest posterior density (HPD): 23 to 41% per My] (14). This estimate is independent of paleontological calibrations but agrees with fossil-calibrated rates for cattle of 30.1% per My (16) and 38% per My (17). This rate was used to calculate the ages of key nodes in the bison genealogy (14). The most recent common ancestor (MRCA) of all bison included in this analysis lived around 136 ky B.P. (95% HPD: 164 to 111 ky B.P.). In the majority (66%) of estimated trees, Eurasian bison cluster into a single clade, with a MRCA between 141 and 89 ky B.P. Although

¹Henry Wellcome Ancient Biomolecules Centre, ²Department of Zoology, Oxford University, South Parks Road, Oxford OX13PS, UK. ³Department of Geology and Department of Anthropology, Douglas College, Post Office Box 2503, New Westminster, British Columbia V3L 5B2, Canada. ⁴Alaska Quaternary Center and Institute of Arctic Biology, University of Alaska Fairbanks, 900 Yukon Drive, Fairbanks, AK 99775-5940, USA. ⁵Severtsov Institute of Ecology and Evolution, Russian Academy of Sciences, 33 Leninsky Prospect, 119071 Moscow, Russia. ⁶The Centre for Genetic Anthropology, Department of Biology, Darwin Building, University College London, Gower Street, London WC1E 6BT, UK. ⁷Department of Evolutionary Biology, Zoological Institute, University of Copenhagen, Universitetsparken 15-2100 Copenhagen, Denmark. ⁸Zoological Institute, Russian Academy of Sciences, 199034 St. Petersburg, Russia. ⁹Quaternary Paleontology, Provincial Museum of Alberta, Edmonton, Alberta T5N 0M6, Canada. ¹⁰North-East Scientific Station of Russian Academy of Science, Post Office Box 18, Cherskii, Republic Sakha-Yakutia, Russia. ¹¹Department of Archaeology, Simon Fraser University, Burnaby, British Columbia V5A 1S6, Canada. ¹²Department of Earth and Atmospheric Sciences, University of Alberta, Edmonton, Alberta T6G 2E3, Canada. ¹³Canadian Museum of Nature (Paleobiology), Ottawa, Ontario K1P 6P4, Canada. ¹⁴Department of Archaeology, Royal British Columbia Museum, 675 Belleville Street, Victoria, British Columbia V8V 1X4, Canada. ¹⁵Institute of Plant and Animal Ecology, Russian Academy of Sciences, 202 8 Martas Street, Ekaterinburg 620144, Russia. ¹⁶Bureau of Land Management, 1150 University Avenue, Fairbanks, AK 99708 USA. ¹⁷Department of Ecology and Evolutionary Biology, University of Kansas, Lawrence, KS 66045, USA. ¹⁸Alaska Department of Fish and Game, 1300 College Road, Fairbanks, AK 99701, USA. ¹⁹Yukon Paleontologist, Heritage Resources, Yukon Department of Tourism and Culture, Box 2703, Whitehorse, Yukon Territory YTY1A 2C6, Canada. ²⁰Department of Paleontology, American Museum of Natural History, Central Park West at 79th Street, New York, NY 10024, USA.

*To whom correspondence should be addressed. E-mail: alan.cooper@zoo.ox.ac.uk

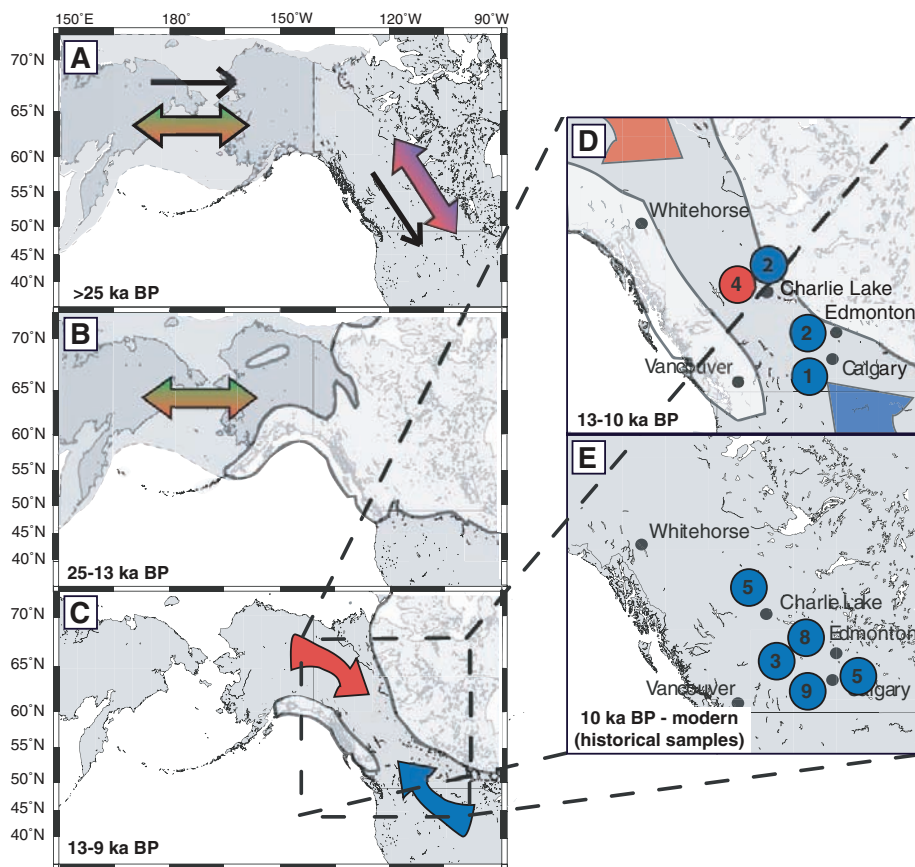


Fig. 1. Distribution of bison in Beringia and central North America through time. (A to C) Double-headed arrows show gene flow between regions. Black arrows indicate colonization events. Circles in maps (D) and (E) designate either northern (red) or southern (blue) ancestry and the number of samples from that location.

these two estimates overlap, the age of the MRCA of Eurasian bison was the same as that of the root in 4.8% of 135,000 posterior genealogies (with a Bayes factor of 20.83 that the Eurasian MRCA is not also the MRCA of all clades), suggesting that the Eurasian clade is not the oldest in the tree. This suggests that late Pleistocene bison from the Ural Mountains to northern China are descendants of one or more dispersals from North America. Several North American lineages fall within the Eurasian clade, indicating subsequent asymmetric genetic exchange, predominantly from Asia to North America.

Figure 1A depicts inferred gene flow between bison populations in Beringia and central North America during MIS 3 (~60 to 25 ky B.P.), which is the interstadial period before the Last Glacial Maximum (LGM, ca. 22 to 18 ky B.P.). Bison were continuously distributed from eastern Beringia southward into central North America during this period, before the formation of the Laurentide (eastern) and Cordilleran (western) ice sheets created a barrier to north-south faunal exchange. Although any coalescence between these ice masses was brief (11), the absence of faunal remains aged 22 to 12 ky B.P. (Fig. 1B) (18) indicates that the area was uninhabitable by large mammals during this time. Bison fossils in central North America during the LGM are sparsely distributed across the continent (9). DNA could be retrieved only from two specimens from this period, both from Natural Trap Cave, Wyoming (20,020 ± 150 and 20,380 ± 90 ky B.P.). These specimens are not closely related (14), indicating that populations south of the ice retained some genetic diversity until the LGM.

The ice sheets began to retreat around 14 ky B.P., forming an ice-free corridor (IFC) through which dispersal between Beringia and North America could occur. The first observed bison haplotypes in the IFC are southern in origin (Fig. 1, C and D), with the oldest specimen being in southern Alberta by 11.3 ky B.P., and others near Athabasca, northern Alberta, by 10.4 ky B.P. This finding is consistent with evidence that the first faunal assemblages and archaeological presence in the IFC were southern in origin (18–20). The opening of the northern end of the IFC saw a limited southward dispersal of Beringian bison, with a subset of the northern diversity found near the Peace River (northwestern British Columbia) by 11.2 to 10.2 ky B.P. (Fig. 1C) (14). Southern bison are also found in this area around 10.5 ky B.P., making it the only location where post-LGM northern and southern clades occurred at the same time. Subsequent genetic exchange between Beringia and central North America was limited by the rapid establishment of spruce forest across Alberta around 10 ky B.P. (21) and by the widespread development of peatland across western and northwestern Canada (22). North of these ecological barriers, grasslands were reduced by invading trees and shrubs, yet despite the decrease in quality and quantity of habitat (3), bison persisted in eastern Beringia until a few hundred years ago (14, 23).

It has been hypothesized that modern bison descended from Beringian bison that moved south through the IFC after the LGM (9, 19) and have since undergone a decline in diversity due to over-hunting and habitat loss (13). In contrast, our data show that modern bison are descended from populations that were south of the ice before the LGM and

that diversity has been restricted to at least 12 ky B.P., around the time of the megafaunal extinctions. All modern bison belong to a clade distinct from Beringian bison. This clade has a MRCA between 22 and 15 ky B.P., which is coincident with the separation of northern and southern populations by the western Canadian ice barrier. This clade diverged from Beringian bison by 83 to 64 ky B.P. and was presumably part of an early dispersal from Beringia, as indicated by the long branch separating it from Beringian bison (14). If other remnants of these early dispersals survived the LGM, they contributed no mitochondrial haplotypes to modern populations.

Coalescent theory is used to evaluate the likelihood of a demographic history, given plausible genealogies (24). Under a coalescent model, the timing of divergence dates provides information about effective population sizes through time. To visualize this for bison, a technique called the skyline plot was used (14, 25). The results showed two distinct demographic trends since the MRCA, suggesting that a simple demographic model, such as constant population size or exponential growth, was insufficient to explain the evolutionary history of Beringian bison. We therefore extended the Bayesian coalescent method (26) to a two-epoch demographic model with exponential population growth at rate r_{early} , until a transition time, t_{trans} , after which a new exponential rate, r_{late} , applies until the present effective population size, N_0 , is reached (Fig. 2A). In this model, both the early and late epochs can have positive or negative growth rates, with both the rates and the time of transition estimated directly from the data.

The analysis strongly supported a boom-bust demographic model (Table 1), in which

Fig. 2. (A) The two-epoch demographic model with four demographic parameters: N_0 , r_{early} , r_{late} , and t_{trans} . The effective population size is a compound variable considered linearly proportional to census population size. **(B)** Log-linear plot describing the results of the full Bayesian analyses. Smoothed curves provide mean and 95% HPD (blue-shaded region) values for effective population size through time. Dashed vertical lines and gray-shaded regions describe mean and 95% HPD for the estimated time of the MRCA (111 to 164 ky B.P.), transition time (32 to 43 ky B.P.), and the earliest unequivocal reported human presence in eastern Beringia (~12 ky B.P.) (5). The stepped line is the generalized skyline plot derived from the maximum a posteriori tree of the exponential growth analysis. The bar graph shows the number of radiocarbon-dated samples in bins of 1000 radiocarbon years. No relation is apparent between the absolute number of samples and the estimated effective population size or transition time.

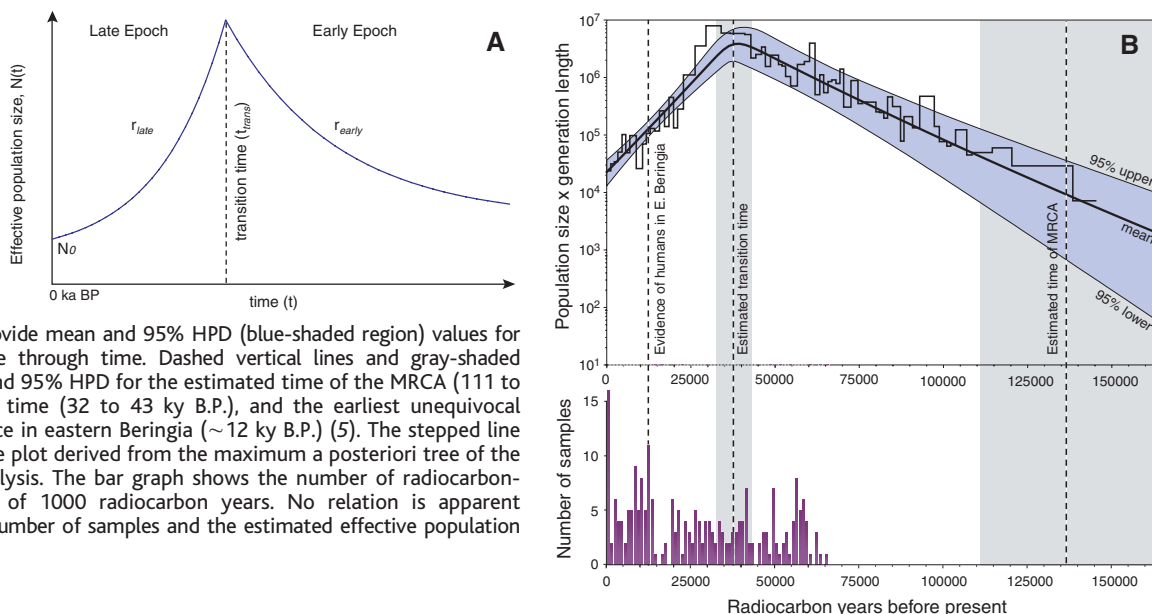


Table 1. Results of Bayesian analyses assuming constant population size, exponential growth, and a two-epoch model for the full analysis of 191 bison associated with finite radiocarbon dates (14). Model parameters are as defined in (26). The large difference between the mean goodness-of-

fit statistics [ln(posterior)] indicates that under either the Akaike information criterion or Bayesian information criterion tests, the two-epoch model is a significantly better fit to the data than the simpler models.

	Constant size			Exponential growth			Two epoch		
	Lower	Mean	Upper	Lower	Mean	Upper	Lower	Mean	Upper
Age estimates (yr B.P.)									
Root height	117,000	152,000	189,000	113,000	146,000	181,000	111,000	136,000	164,000
Modern/southern clade	20,200	28,000	36,600	18,600	26,400	35,000	15,400	23,200	32,200
Eurasian clade	85,000	116,000	151,000	83,000	112,000	144,000	89,000	114,000	141,000
Model parameters									
Mean ln(posterior)		-6530.795			-6517.35			-6394.568	
Mutation rate (substitutions/site/year)	2.79×10^{-7}	3.78×10^{-7}	4.85×10^{-7}	2.30×10^{-7}	3.20×10^{-7}	4.13×10^{-7}	2.30×10^{-7}	3.20×10^{-7}	4.13×10^{-7}
Kappa	19	27	37	19	27.4	37	19	27	37
Shape parameter	0.22	0.35	0.49	0.22	0.35	0.49	0.22	0.35	0.5
Proportion of invariant sites	0.33	0.45	0.56	0.33	0.45	0.56	0.34	0.45	0.56

an exponential expansion of the bison population was followed by a rapid decline, with a transition around 37 ky B.P. (Fig. 2B). At the height of the boom, the population size was around 230 times (95% HPD: 71 to 454 times) that of the modern population. When this model is applied to the modern clade alone, a growth period peaks around 1000 years ago (95% HPD: 63 to 2300 yr B.P.) and is followed by a rapid decline (14), which is consistent with historical records of a population bottleneck in the late 1800s (13). These results illustrate the power of this method to recover past demographic signals.

The effects of population subdivision and patch extinction and recolonization on coalescence patterns have not been fully characterized, yet they can influence demographic estimates such as skyline plots (27). To test for the effect of population subdivision on our models, the two-epoch analysis was repeated first without the Eurasian bison and then without both Eurasian and central North American bison. The results of these analyses were consistent with those for the entire data set (14), suggesting that the assumption of panmixia does not affect the analysis. These results suggest that the major signal for the boom-bust scenario came from the well-represented eastern Beringian population.

The timing of the decline in Beringian bison populations (Fig. 2B) predates the climatic events of the LGM and events at the Pleistocene-Holocene boundary. The bison population was growing rapidly throughout MIS 4 and 3 (~75 to 25 ky B.P.), approximately doubling every 10,200 (95% HPD: 7500 to 15,500) years. The reversal of this doubling trend at 42 to 32 ky B.P. and the subsequent dramatic decrease in population size are coincident with the warmest part of MIS 3, which is marked by a reduction in steppe-tundra due to treecover reaching its late Pleistocene maximum (28). Modern bo-

real forests serve as a barrier to bison dispersal because they are difficult to traverse and provide few food sources (3). After the interstadial, cold and arid conditions increasingly dominated, and some component of these ecological changes may have been sufficient to stress bison populations across Beringia. Previous reports of local extinction of brown bears (29) and hemionid horses (8) in Alaska around 32 to 35 ky B.P. support the possibility of a larger scale environmental change affecting populations of large mammals.

These results have considerable implications for understanding the end-Pleistocene mass extinctions, because they offer the first evidence of the initial decline of a population, rather than simply the resulting extinction event. These events predate archaeological evidence of significant human presence in eastern Beringia (5), arguing that environmental changes leading up to the LGM were the major cause of the observed changes in genetic diversity. If other species were similarly affected, differences in how these species responded to environmental stress may help to explain the staggered nature of the megafaunal extinctions (7, 30). However, it is possible that human populations were present in eastern Beringia by 30 ky B.P., with reports of human-modified artifacts as old as 42 to 25 ky B.P. from the Old Crow basin in Canada's Yukon Territory (31). Although the archaeological significance of these specimens is disputed and the number of individuals would be low, the specimens are consistent with the timing of the population crash in bison. This emphasizes that future studies of the end-Pleistocene mass extinctions in North America should include events before the LGM.

Ancient DNA is a powerful tool for studying evolutionary processes such as the response of organisms to environmental

change. It should be possible to construct a detailed paleoecological history for late Pleistocene Beringia using similar methods for other taxa. Almost none of the genetic diversity present in Pleistocene bison survived into Holocene populations, erasing signals of the complex population dynamics that took place as recently as 10,000 years ago.

References and Notes

- G. Hewitt, *Nature* **405**, 907 (2000).
- R. W. Graham et al., *Science* **272**, 1601 (1996).
- R. D. Guthrie, *Frozen Fauna of the Mammoth Steppe* (Univ. of Chicago Press, Chicago, 1990).
- G. D. Zazula et al., *Nature* **423**, 603 (2003).
- D. R. Yesner, *Quat. Sci. Rev.* **20**, 315 (2001).
- B. W. Brook, D. Bowman, *J. Biogeogr.* **31**, 517 (2004).
- J. Alroy, *Science* **292**, 1893 (2001).
- R. D. Guthrie, *Nature* **426**, 169 (2003).
- J. N. McDonald, *North American Bison: Their Classification and Evolution* (Univ. of California Press, Berkeley, CA, 1981).
- C. A. S. Mandyk, H. Josenhans, D. W. Fedje, R. W. Mathewes, *Quat. Sci. Rev.* **20**, 301 (2001).
- A. S. Dyke et al., *Quat. Sci. Rev.* **21**, 9 (2002).
- M. F. Skinner, O. C. Kaise, *Bull. Am. Mus. Nat. Hist.* **89**, 126 (1947).
- F. G. Roe, *The North American Buffalo*, (Univ. of Toronto Press, Toronto, ON, ed. 2, 1970).
- Materials and methods are available as supporting material on Science Online.
- D. M. Lambert et al., *Science* **295**, 2270 (2002).
- D. G. Bradley, D. E. MacHugh, P. Cunningham, R. T. Loftus, *Proc. Natl. Acad. Sci. U.S.A.* **93**, 5131 (1996).
- C. S. Troy et al., *Nature* **410**, 1088 (2001).
- J. A. Burns, *Quat. Int.* **32**, 107 (1996).
- M. C. Wilson, *Quat. Int.* **32**, 97 (1996).
- J. C. Driver, in *People and Wildlife in Northern North America*, S. C. Gerlach, M. S. Murray, Eds. (British Archaeological Reports, International Series 944, Archaeopress, Oxford, 2001), pp. 13–22.
- N. Catto, D. G. E. Liverman, P. T. Bobrowsky, N. Rutter, *Quat. Int.* **32**, 21 (1996).
- L. A. Halsey, D. H. Vitt, I. E. Bauer, *Clim. Change* **40**, 315 (1998).
- R. O. Stephenson et al., in *People and Wildlife in Northern North America*, S. C. Gerlach, M. S. Murray, Eds. (British Archaeological Reports, International Series 944, Archaeopress, Oxford, 2001), pp. 125–148.
- R. C. Griffiths, S. Tavare, *Philos. Trans. R. Soc. London Ser. B* **344**, 403 (1994).

25. K. Strimmer, O. G. Pybus, *Mol. Biol. Evol.* **18**, 2298 (2001).
 26. A. J. Drummond, G. K. Nicholls, A. G. Rodrigo, W. Solomon, *Genetics* **161**, 1307 (2002).
 27. J. R. Pannell, *Evolution* **57**, 949 (2003).
 28. P. M. Anderson, A. V. Lozhkin, *Quat. Sci. Rev.* **20**, 93 (2001).
 29. I. Barnes, P. E. Matheus, B. Shapiro, D. Jensen, A. Cooper, *Science* **295**, 2267 (2002).
 30. D. K. Grayson, D. J. Meltzer, *J. Archaeol. Sci.* **30**, 585 (2003).
 31. R. E. Morlan, *Quat. Res.* **60**, 123 (2003).
 32. We thank the museums and collections that donated

material and T. Higham, A. Beaudoin, K. Shepherd, R. D. Guthrie, B. Potter, C. Adkins, D. Gilchinsky, R. Gangloff, S. C. Gerlach, C. Li, N. K. Vereshchagin, T. Kuznetsova, G. Boeskorov, the Alaska Bureau of Land Management, and the Yukon Heritage Branch for samples, logistical support, and assistance with analyses. We thank D. Rubenstein, R. Fortey, and P. Harvey for comments on the manuscript; Balliol College; the Royal Society; the Natural Environment Research Council; the Biotechnology and Biological Sciences Research Council; Rhodes Trust; Wellcome and Leverhulme Trusts for financial support; and Oxford

Radiocarbon Dating Service and Lawrence Livermore National Laboratory for carbon dating.

Supporting Online Material

www.sciencemag.org/cgi/content/full/306/5701/1561/DC1
 Materials and Methods
 SOM Text
 Figs. S1 to S5
 Tables S1 to S4
 References

4 June 2004; accepted 4 October 2004

Periodical Cicadas as Resource Pulses in North American Forests

Louie H. Yang

Resource pulses are occasional events of ephemeral resource superabundance that occur in many ecosystems. Aboveground consumers in diverse communities often respond strongly to resource pulses, but few studies have investigated the belowground consequences of resource pulses in natural ecosystems. This study shows that resource pulses of 17-year periodical cicadas (*Magicicada* spp.) directly increase microbial biomass and nitrogen availability in forest soils, with indirect effects on growth and reproduction in forest plants. These findings suggest that pulses of periodical cicadas create "bottom-up cascades," resulting in strong and reciprocal links between the aboveground and belowground components of a North American forest ecosystem.

Ecologists are increasingly investigating the effects of resource pulses in natural systems (1). Examples of resource pulses include mast years of unusually heavy seed production (2–4), eruptive plant growth after El Niño rainfalls (5–8), postspawning salmon mortality in riparian communities (9, 10), and large-scale insect outbreaks (3, 11–13). Despite great variation in the specific characteristics of these resource pulses, each represents a brief, infrequent event of high resource availability. Resource pulses are of broad interest because they provide extreme examples of the spatiotemporal variability inherent in all ecosystems. Recent theoretical efforts have suggested that many communities may be strongly influenced by transient dynamics after ecological perturbations (14, 15), and empirical studies in diverse systems have demonstrated that resource pulses are often substantial perturbations with strong effects on consumer populations, especially among opportunistic generalist species (1).

Resource pulses have well-documented effects on aboveground consumers, and they may also provide important inputs to belowground systems (1, 16). In many pulsed systems, only a small proportion of resource biomass is consumed aboveground (17–19), and aboveground predator satiation during re-

source pulses could allow large belowground inputs. Many belowground organisms are well-adapted to take advantage of resource pulses because of their high intrinsic rates of growth and rapid foraging responses (20, 21). Studies in natural systems support the idea that aboveground resource pulses may contribute to belowground systems. For example, mast events in boreal forests produce large inputs of rapidly decomposed spruce seeds that increase soil nitrogen availability (22), and large-scale gypsy moth outbreaks in temperate forests influence nutrient cycling through defoliation and frass deposition (11).

The role of arthropods in regulating plant inputs and facilitating decomposition is widely acknowledged (21), although most ecologists have assumed that arthropod bodies are an unimportant ecosystem biomass component (23). However, the unusual life history of periodical cicadas suggests that they may be a substantial, temporally stored resource pulse. Periodical cicadas are the most abundant herbivores in North American deciduous forests in both number and biomass (24), but their role in forest ecosystems is largely unrecognized because of their long belowground life history. Adult periodical cicadas emerge synchronously across large geographic areas, or "broods," often on a scale of 10^5 km². The spatial distribution of cicadas is highly variable and dynamic on small scales (<1 km) and is influenced by fragmentation in forest habitats (17, 23–26). Yet, cicadas are broadly

distributed across a large and diverse area, with a cumulative range encompassing much of the eastern United States (fig. S1). Adult cicadas are aboveground for less than 6 weeks (26). Cicada emergence densities ranging from 3 to 350 cicadas m⁻² are well documented (26), and most cicadas escape predation at high densities (17, 18). Direct measures of cicada densities in 2002 and 2004 support previously reported density estimates (27). In dense populations, the cumulative biomass of periodical cicadas is among the greatest of any terrestrial animal (24) and represents a substantial flux of high-quality biomass (23, 28, 29). Little is known about the belowground effects of this resource pulse.

Here, I investigate the direct belowground and indirect aboveground effects of cicada litter inputs resulting from cicada resource pulses. I conducted field experiments during three con-

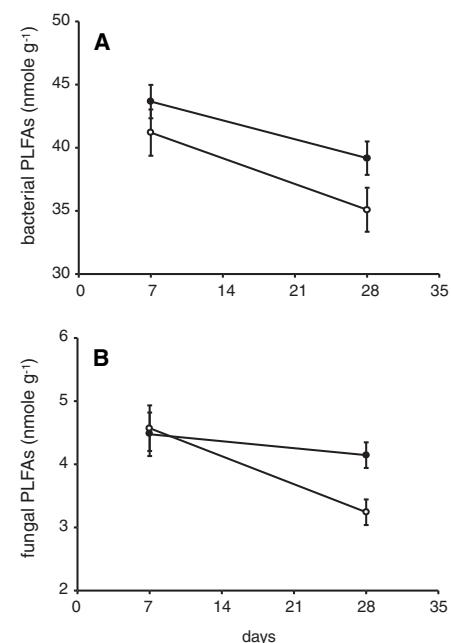
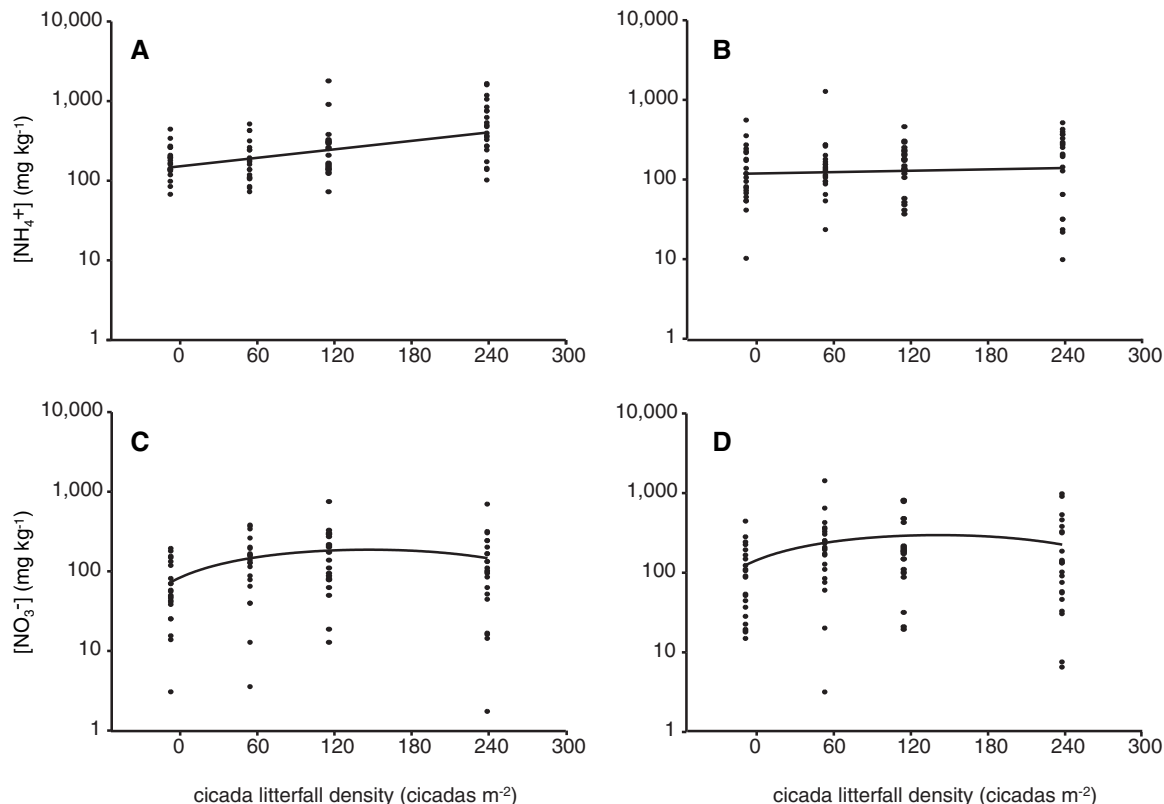


Fig. 1. Cicada litterfall increases soil bacterial and fungal PLFAs relative to those of controls, indicating increased microbial biomass. (A) Bacterial PLFAs in cicada-supplemented and control plots 7 and 28 days after experimental cicada pulse. (B) Fungal PLFAs in cicada-supplemented and control plots 7 and 28 days after experimental cicada pulse. Open circles represent control plots, and filled circles represent plots receiving 120 cicadas m⁻². Error bars show mean \pm SE.

Center for Population Biology, Section of Evolution and Ecology, University of California, One Shields Avenue, Davis, CA 95616, USA. E-mail: lhyang@ucdavis.edu

Fig. 2. Cicada litterfall increases indices of soil nitrate and ammonium availability in forest soils. (A) Soil ammonium availability under experimentally controlled cicada litterfall densities in the first 30 days and (B) in days 31 to 100. (C) Soil nitrate availability under experimentally controlled cicada litterfall densities in the first 30 days and (D) in days 31 to 100. Fitted lines represent least-squares polynomial regressions.



secutive emergence years to examine the effects of cicada carcass deposition on soil microbial biomass, nitrogen availability, and the growth and reproduction of forest plants (27).

The role of soil microbes in mobilizing organic detritus in plant-available forms is well established (30), and many soil communities respond to detrital carbon inputs with rapid increases of bacterial and fungal biomass. To assess the phenology and magnitude of belowground cicada litterfall effects on microbial biomass, I conducted field experiments in which dead cicada carcasses were applied to replicate forest plots to simulate natural cicada litterfall densities. Differences in the abundance of microbial phospholipid fatty acids (PLFAs) between control (0 cicadas m⁻²) and treatment (120 cicadas m⁻²) plots were undetectable 7 days after the pulsed input (Fig. 1). However, 28 days after the cicada resource pulse, the abundance of bacterial PLFAs was 12% greater in cicada litterfall plots relative to control plots (Fig. 1A, $P = 0.0383$), suggesting an increase in bacterial biomass. The abundance of fungal PLFAs in treatment plots increased by 28% (Fig. 1B, $P = 0.0036$), indicating an increase in fungal biomass. There was little change in the microbial community composition: The fungal-to-bacterial ratio increased insignificantly in cicada-supplemented plots compared with that in control plots ($P = 0.0918$) after 28 days. In contrast, the total abundance of microbial PLFAs was

12% greater in cicada-supplemented plots ($P = 0.0280$). These results are consistent with expectations of broad, rapid microbial growth after a short lag in response to cicada litterfall.

Across the distribution of periodical cicadas, primary productivity is generally believed to be nitrogen limited (31), and mineralized soil nitrogen is the primary nitrogen pool for plant uptake in temperate forest systems (30). Pulsed inputs of nitrogen-rich detritus could be expected to cause an ephemeral acceleration of nitrogen mineralization (16), and cicada carcasses are relatively high-nitrogen inputs [N content = 10.4% (27)]. To assess the effect of cicada litterfall on plant-available soil nitrogen, I conducted field experiments in which cicada carcasses were applied at a range of naturally occurring densities to replicate forest plots during two consecutive cicada emergence years in distant locations. In 2002, cicada supplementation was positively correlated with indices of cumulative soil ammonium [adjusted R^2 (R^2_{adj}) = 0.21, $P = 0.006$] and nitrate ($R^2_{adj} = 0.11$, $P = 0.037$) availability during the 100-day experiment (fig. S2). Mean indices of soil ammonium availability were 412% greater in maximally supplemented cicada plots (300 cicada m⁻²) compared with those of controls, and indices of soil nitrate were 199% greater in the same comparison. In 2003, I conducted a second, larger experiment to assess the relationship between cicada litterfall and mineralized soil

nitrogen, the phenology of this relationship, and the generality of previous results. The density of cicada supplementation was again positively correlated with indices of mineralized ammonium (Fig. 2A, $R^2_{adj} = 0.25$, $P < 0.0001$) and nitrate (Fig. 2C, $R^2_{adj} = 0.06$, $P = 0.027$) availability throughout the first 30 days of the experiment. Mean soil ammonium availability increased 306% in maximally supplemented plots (240 cicadas m⁻²) relative to that of controls (Fig. 2A), and mean nitrate availability increased by 249% relative to that of controls (Fig. 2C). A significant interaction effect of cicada litterfall density and sampling period on ammonium availability ($P = 0.007$) suggests that this response was strongly pulsed in time, with larger effects during the first 30 days and no residual effect during the subsequent 70 days of this experiment (Fig. 2B, $P = 0.522$). Conversely, the effect of cicada litterfall on soil nitrate availability was more persistent, showing a positive correlation with cicada litterfall density during the first 30 days, which continued during days 31 to 100 (Fig. 2D, $R^2_{adj} = 0.06$, $P = 0.029$). These results are consistent with expectations of net mineralization from the decomposition of a nitrogen-rich detritus pulse. Although immobilization, plant uptake, and other losses may reduce nitrogen availability over time, these findings suggest that some effects may be long-lasting.

A third field experiment investigated the effects of belowground enrichment from cica-

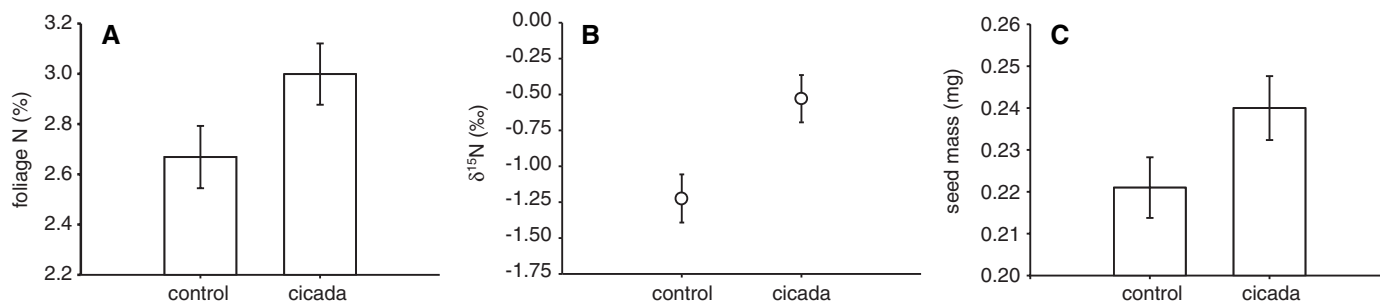


Fig. 3. Cicada litterfall increases (A) foliage nitrogen content, (B) foliage $\delta^{15}\text{N}$, and (C) seed size in cicada-supplemented American bellflowers relative to controls. Error bars show mean \pm SE.

da litterfall on growth and reproduction in a forest plant, the American bellflower (*Campulaurum americanum*). This herbaceous annual/biennial forest understory species is native throughout much of the geographic range of periodical cicadas, and previous studies with this species have suggested that the maternal nutrient environment can contribute to larger seed size (32), which influences germination (33) and seedling performance (34). Pulses of cicada litterfall provide a natural context to interpret plant responses to temporally variable nutrient conditions. This experiment tested the prediction that cicada litterfall increases foliage nitrogen content and seed size in American bellflowers.

In this experiment, cicada-supplemented bellflowers (140 cicadas m^{-2}) from a natural field population produced foliage with 12% greater nitrogen content relative to controls (Fig. 3A, $P = 0.031$), and an 11% decrease in the carbon-to-nitrogen ratio ($P = 0.025$). Stable isotope analysis of bellflower foliage indicated higher $\delta^{15}\text{N}$ in cicada-supplemented plants compared with that in controls [mean $\delta^{15}\text{N}_{\text{treatment}} - \text{mean } \delta^{15}\text{N}_{\text{control}} = 0.695$ per mil (‰), $P = 0.004$, Fig. 3B]. Cicadas show enriched $\delta^{15}\text{N}$ relative to their plant diet ($\delta^{15}\text{N}_{\text{cicada}} = 1.56\text{‰}$), resulting from preferential retention of the heavier isotope in trophic consumers (27). The increased $\delta^{15}\text{N}$ in cicada-supplemented plants suggests a mechanistic link between a cicada-derived nitrogen source and increased plant nitrogen assimilation. These experimental plants also produced seeds that were 9% larger than those of controls (Fig. 3C, $P = 0.028$). These results suggest that the belowground effects of cicada pulses can be rapidly used in plant growth and reproduction during the emergence year and may influence aboveground plant processes. These plant responses indicate reciprocal links between aboveground and belowground communities: indirect aboveground enrichment from the belowground decomposition of an aboveground resource pulse that resulted from the life history of a belowground root-feeding herbivore.

Taken together, these results show that cicada litterfall during emergence years can

cause substantial pulsed enrichment of North American forest soils, with direct effects on belowground systems and indirect effects aboveground. These observations suggest that cicada resource pulses could influence forest dynamics over a landscape scale, and the patchiness of cicada distributions may contribute to spatial and temporal heterogeneity in these resource pulse effects. The costs of cicada herbivory and oviposition in plants are well documented, but these findings also suggest the potential for positive and partially compensatory effects on primary productivity due to pulsed fertilization. Indeed, the heretofore puzzling observation of greater wood accumulation in years following cicada emergence (35) may be related to this belowground resource pulse.

Although these belowground and aboveground consequences result from the unusual life history of a single insect genus, these findings may also illustrate a more general consequence of resource pulses for belowground systems. This study suggests a mechanism by which resource pulses may link aboveground and belowground components of other ecosystems. These findings contribute to an emerging body of theory and observations suggesting that rare perturbations may have large and lasting effects in diverse ecological systems.

References and Notes

1. R. S. Ostfeld, F. Keesing, *Trends Ecol. Evol.* **15**, 232 (2000).
2. W. J. McShea, *Ecology* **81**, 228 (2000).
3. C. G. Jones, R. S. Ostfeld, M. P. Richard, E. M. Schaubert, J. O. Wolff, *Science* **279**, 1023 (1998).
4. J. O. Wolff, *J. Mamm.* **77**, 850 (1996).
5. P. Stapp, G. A. Polis, *Oikos* **102**, 111 (2003).
6. M. Lima, P. A. Marquet, F. M. Jaksic, *Ecography* **22**, 213 (1999).
7. S. J. Wright, C. Carrasco, O. Calderon, S. Paton, *Ecology* **80**, 1632 (1999).
8. M. Holmgren, M. Scheffer, E. Ezcurra, J. R. Gutierrez, G. M. J. Mohren, *Trends Ecol. Evol.* **16**, 89 (2001).
9. M. Ben-David, T. A. Hanley, D. M. Schell, *Oikos* **83**, 47 (1998).
10. J. M. Helfield, R. J. Naiman, *Ecology* **82**, 2403 (2001).
11. G. M. Lovett et al., *Bioscience* **52**, 335 (2002).
12. J. Elkinton et al., *Ecology* **77**, 2332 (1996).
13. S. C. Hahus, K. G. Smith, *J. Mamm.* **71**, 249 (1990).
14. A. Hastings, *Ecol. Lett.* **4**, 215 (2001).
15. X. Chen, J. E. Cohen, *Proc. R. Soc. London Ser. B.* **268**, 869 (2001).
16. D. A. Wardle, *Communities and Ecosystems: Linking*

17. K. S. Williams, K. G. Smith, F. M. Stephen, *Ecology* **74**, 1143 (1993).
18. R. Karban, *Ecology* **63**, 321 (1982).
19. B. W. Sweeney, R. L. Vannote, *Evolution* **36**, 810 (1982).
20. D. C. Coleman, in *Food Webs: Integration of Patterns and Dynamics*, G. Polis, K. Winemiller, Eds. (Chapman and Hall, London, 1996), chap. 3.
21. J. C. Moore, D. E. Walter, H. W. Hunt, *Annu. Rev. Entomol.* **33**, 419 (1988).
22. O. Zackrisson, M. C. Nilsson, A. Jaderlund, D. A. Wardle, *Oikos* **84**, 17 (1999).
23. M. R. Whiles, M. A. Callahan, C. K. Meyer, B. L. Brock, R. E. Charlton, *Am. Midl. Nat.* **145**, 176 (2001).
24. H. S. Dybas, D. D. Davis, *Ecology* **43**, 432 (1962).
25. N. L. Rodenhouse, P. J. Bohlen, G. W. Barrett, *Am. Midl. Nat.* **137**, 124 (1997).
26. K. S. Williams, C. Simon, *Annu. Rev. Entomol.* **40**, 269 (1995).
27. Materials and methods are available as supporting material on Science Online.
28. J. J. Brown, G. M. Chippendale, *J. Insect Physiol.* **19**, 607 (1973).
29. G. L. Wheeler, K. S. Williams, K. G. Smith, *For. Ecol. Manage.* **51**, 339 (1992).
30. J. P. Schimel, J. Bennett, *Ecology* **85**, 591 (2004).
31. C. A. Black, *Soil-Plant Relationships* (Wiley, New York, ed. 2, 1968).
32. L. F. Galloway, *Am. J. Bot.* **88**, 832 (2001).
33. L. F. Galloway, *Ecology* **82**, 2781 (2001).
34. T. E. Richardson, A. G. Stephenson, *Evolution* **46**, 1731 (1992).
35. W. D. Koenig, A. M. Liebhold, *Can. J. For. Res.* **33**, 1084 (2003).
36. I thank R. Karban, J. Stamps, J. Rosenheim, T. Schoener, L. Galloway, K. Scow, R. Drenovsky, T. Bruce, T. Payne, G. Stauffer, J. Busch, M. Watnik, N. Willits, S. Strauss, K. Spence, J. Fordyce, A. Agrawal, M. Stanton, P. Lee, D. Spiller, A. McCall, V. Rudolf, and three anonymous reviewers for advice and assistance; the Division of Agriculture and Natural Resources Analytical Lab, the Scow Lab, and the University of California at Davis (UCD) Stable Isotope Facility for assistance with laboratory analyses; the University of Virginia's Mountain Lake Biological Station and Blandly Farm, the Stonebridge Farm, the Maryland Department of Forestry, the Wilderness Conservancy of Mountain Lake, the Powdermill Nature Reserve, and Concord College for field assistance. This research was supported by an NSF Graduate Research Fellowship grant, an NSF grant DEB-0121050 to R. Karban, the Mountain Lake Biological Station, Sigma Xi, and the Center for Population Biology, the Population Biology Graduate Group, the John Muir Institute of the Environment, the Department of Entomology, and the Section of Evolution and Ecology at UCD.

Supporting Online Material
www.sciencemag.org/cgi/content/full/306/5701/1565/DC1
 Materials and Methods
 Figs. S1 to S3
 References

22 July 2004; accepted 4 October 2004

Gastric Cancer Originating from Bone Marrow–Derived Cells

JeanMarie Houghton,^{1*} Calin Stoicov,¹ Sachiyo Nomura,^{2,3}
 Arlin B. Rogers,⁴ Jane Carlson,¹ Hanchen Li,¹ Xun Cai,¹
 James G. Fox,⁴ James R. Goldenring,^{2,5} Timothy C. Wang^{1*†}

Epithelial cancers are believed to originate from transformation of tissue stem cells. However, bone marrow–derived cells (BMDCs), which are frequently recruited to sites of tissue injury and inflammation, might also represent a potential source of malignancy. We show that although acute injury, acute inflammation, or transient parietal cell loss within the stomach do not lead to BMDC recruitment, chronic infection of C57BL/6 mice with *Helicobacter*, a known carcinogen, induces repopulation of the stomach with BMDCs. Subsequently, these cells progress through metaplasia and dysplasia to intra-epithelial cancer. These findings suggest that epithelial cancers can originate from marrow-derived sources and thus have broad implications for the multistep model of cancer progression.

The link between infection, chronic inflammation, and cancer has long been recognized (1), a prime example being infection with *Helicobacter pylori* and gastric cancer (2). Chronic gastric inflammation, which develops as a consequence of *H. pylori*, leads over time to repetitive injury and repair resulting in

hyperproliferation, an increased rate of mitotic error, and progression to adenocarcinoma. The same inflammatory environment that favors the development of cancer has also been linked to homing and engraftment in peripheral tissue by BMDCs. Recent studies have suggested that BMDCs may possess an unexpected degree of plasticity and often home to sites of chronic injury or inflammation (3, 4). In particular, this may occur where tissue injury induces excessive apoptosis that overwhelms or compromises the supply of endogenous tissue stem cells (5). Although the mechanism and extent of subsequent BMDC differentiation is not established (6), it is clear that engrafting cells rely on external environmental cues for the orderly inactivation of growth programs and progression of appropriate differentiation (3, 4, 7). There is little information on the long-term consequences of recruiting pluripotent cells to areas of chronic inflammation where signals for cell growth and differentiation may be altered.

To investigate the possible role of BMDCs in the metaplasia/dysplasia/carcinoma progression associated with chronic *Helicobacter* infection, we employed the established *H. felis*/C57BL/6 mouse model of gastric cancer (8). After undergoing lethal irradiation, mice were transplanted with bone marrow from C57BL/6.JGtrosa26 (ROSA26) transgenic mice expressing a nonmammalian beta-galactosidase enzyme or from control wild-type littermates (9). Engraftment of ROSA26 marrow-derived cells was tracked with X-galactosidase (X-gal) staining. X-gal staining (blue) was not detected in wild-type mice (Fig. 1A) or wild-type infected mice (Fig. 1C). Uninfected ROSA26 transplanted mice did not demonstrate BMDC engraftment into gastric glands (Fig. 1B). Although acute (3 week) *H. felis* infection was associated with intense bone marrow–derived inflammation, it did not produce major architectural destruction and was not sufficient stimulus for stomach repopulation with BMDCs (table S1). In this model, gastric mucosal apoptosis increases at 6 to 8 weeks after inoculation (2) and, consistent with this, beta-galactosidase–positive (blue-staining) glands appeared after this peak of apoptosis. These cells were initially detectable at 20 weeks of infection, but their numbers increased dramatically with the length of time of infection, such that 90% of the gastric mucosa at the squamocolumnar junction was replaced with cells derived from donor marrow at 52 weeks after infection (Fig. 1D and table S1).

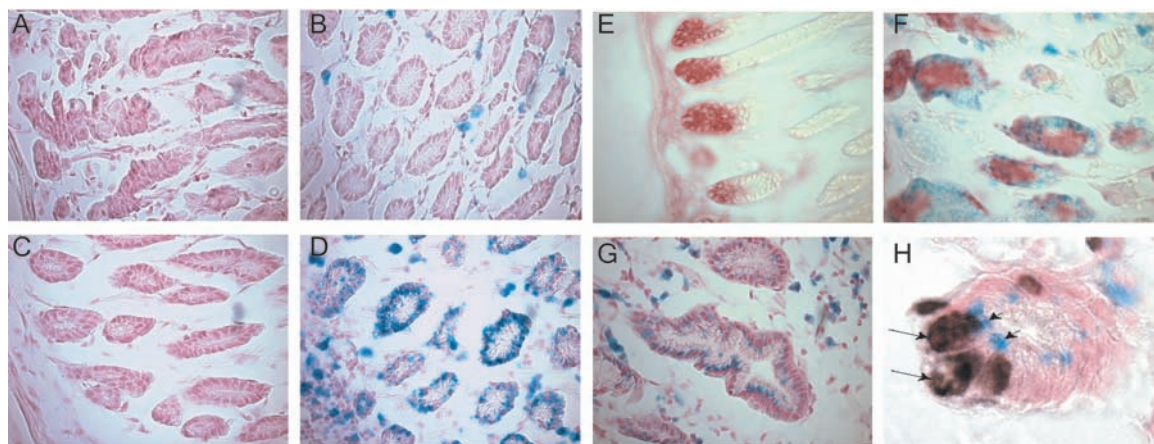
With chronic *Helicobacter* infection, a second proliferative zone forms deeper within the gastric mucosa, giving rise to metaplasia (2), designated SPEM (spasmolytic expressing metaplasia) because of positive staining for trefoil factor 2 (TFF2), also known as spasmolytic polypeptide (10, 11). In chronically infected wild-type mice, TFF2 (red staining) is prominent in deep antral and

¹Department of Medicine and Cancer Biology, University of Massachusetts Medical School, Worcester, MA 01605, USA. ²Epithelial Biology Program, Department of Surgery and Vanderbilt-Ingram Cancer Center, Vanderbilt University School of Medicine, Nashville, TN 37232, USA. ³Department of Gastrointestinal Surgery, Graduate School of Medicine, University of Tokyo, Bunkyo-ku, Tokyo, 113-8655, Japan. ⁴Division of Comparative Medicine, Massachusetts Institute of Technology, Cambridge, MA 02139, USA. ⁵The Veterans Administration Medical Center, Nashville, TN 37232, USA.

*To whom correspondence should be addressed. E-mail: tcw21@columbia.edu (T.C.W.); jeanmarie.houghton@umassmed.edu (J.H.)

†Present address: Department of Medicine and Cancer Center, Columbia College of Physicians and Surgeons, New York, NY 10032, USA.

Fig. 1. (A and C) X-gal staining (blue) of C57BL/6 mouse transplanted with wild-type marrow and (A) mock infected or (C) infected with *H. felis* for 30 weeks. (B and D) C57BL/6 mouse transplanted with ROSA26 marrow and (B) mock infected or (D) infected with *H. felis* for 30 weeks. (E) Wild-type mouse with chronic *H. felis* infection shows TFF2 (red) staining and is X-gal negative (blue). (F) In the infected



ROSA26-transplanted mouse, BMDCs are positive for both beta-galactosidase (blue) and TFF2 (red). (G) Dysplastic glands in the infected ROSA26 mouse express abundant beta-galactosidase activity. (H) Mitotic activity in BMD

epithelial cells demonstrated by coexpression of cytoplasmic beta-galactosidase activity (short arrows; blue) and chromosomal BrdU incorporation (long arrows; brown). 10- μ m frozen sections. Magnification: [(A) to (G)], 600X; (H), 1,000X.

fundic glands (Fig. 1E). In mice transplanted with ROSA26 marrow and infected with *H. felis*, TFF2 expression is seen within blue beta-galactosidase-positive BMDCs (Fig. 1F). Histological alterations were similar in infected wild-type and ROSA26-transplanted mice, with both showing equivalent metaplasia and dysplasia. Of the few parietal cells or chief cells that persisted in the infected stomach, none were beta-galactosidase positive, which indicates that under these experimental conditions of *H. felis* infection, marrow cells do not differentiate toward the parietal or chief cell phenotype.

Epithelial dysplasia increased in severity over time, and by one year after inoculation resulted in carcinoma or high-grade gastrointestinal intraepithelial neoplasia (GIN) (12). In the mouse model of *Helicobacter*-mediated gastric cancer, dysplasia is considered a direct precursor of gastric adenocarcinoma and is found both at the squamocolumnar junction and at the antral-pyloric junction (13, 14). In the *H. felis* model, the majority of dysplastic glands stained blue with X-gal (Fig. 1G), and many BMDC within the epithelium, were bromodeoxyuridine (BrdU) positive (Fig. 1H), which demonstrates active proliferation. To further confirm the presence of beta-galactosidase, we used immunohistochemistry (IHC) for bacterial beta-galactosidase (9). Gastric tissue from wild-type mice did not stain for beta-galactosidase (Fig. 2, A and C), whereas all observed intraepithelial neoplasia in the 52-week infected mice were beta-galactosidase positive (Fig. 2, B and D; brown intracellular staining), which proves that these cells arose

from donor marrow and strongly suggests an inherent vulnerability of this population to malignant progression. Bone marrow-derived GIN displayed features consistent with this histological diagnosis (12), including elongation and branching, crowding and distortion of gland structures, presence of hyperchromatic nuclei, pronounced cellular and nuclear atypia, and loss of polarity. Double-label immunofluorescence staining revealed that the beta-galactosidase-positive cells (red) within deep gastric glands were also pan-cytokeratin positive (green; merged seen as yellow) (Fig. 2F and fig. S1), with CD45 expression specifically restricted to infiltrating leukocytes (fig. S1). These studies confirmed that the marrow-derived cells had differentiated to a gastric epithelial phenotype, ruling out the unlikely possibility that the observed staining pattern was due to lymphocytes intercalating into the gland structure. Although these analyses directly showed beta-galactosidase enzyme activity (X-gal staining) and protein abundance (IHC), we further evaluated BMDCs within the epithelium for the lacZ/Neo fusion gene specific to donor cells. Laser-capture microdissection was used to capture and isolate entire X-gal-positive glands from chronically *H. felis*-infected ROSA26 and wild-type transplanted mice (9) (fig. S2, A and B). Polymerase chain reaction (PCR) with specific lacZ/Neo fusion gene primers followed by sequence analysis verified the cells to be of donor origin (9) (fig. S2C).

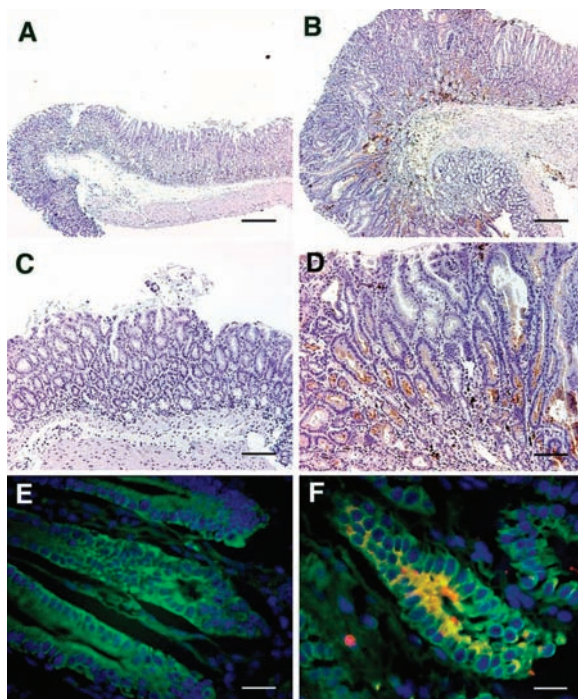
As a further additional test for bone marrow origin, we used a completely independent model of labeled bone marrow reconstitution. Female C57BL/6 mice were

lethally irradiated, transplanted with bone marrow from male transgenic mice expressing chicken beta-actin-EGFP (enhanced green fluorescent protein), and infected with *H. felis* for 15 to 16 months. Dispersed gastric mucosal cells from these mice were sorted by flow cytometry (Fig. 3A) into GFP⁺/CD45⁺ (P4), GFP⁺/CD45⁻ (P5), and GFP⁻/CD45⁻ (P6) populations, subsequently stained for pan-cytokeratin, and also analyzed by fluorescent in situ hybridization (FISH) for X and Y chromosomes (9). The CD45⁻ populations were consistently positive for pan-cytokeratin (Fig. 3, D and F), which indicates their epithelial nature, whereas CD45⁺ cells were negative for this marker (Fig. 3B). GFP⁻/CD45⁻ cells contained two X chromosomes (Fig. 3G), which confirms them to be of host origin, whereas all GFP⁺ cells were consistently positive for both X and Y chromosomes by FISH (Fig. 3, C and E), which demonstrates that they are of donor bone marrow origin. Analysis of tissue sections (Fig. 4) from these mice demonstrated that tumor cells were GFP positive (brown stain) and Y chromosome positive (green signal) and expressed cytokeratin (red signal) (9). These studies, using two independent markers (GFP and Y chromosome), confirmed that in *Helicobacter*-infected mice, bone marrow-derived cells can give rise to gastric epithelial cancer.

We examined whether lesser degrees of injury would result in BMDC engraftment in the stomach. Engraftment of BMDCs in the gastrointestinal tract has been reported to occur infrequently (6, 15). In our system, lethal irradiation and bone marrow reconstitution without *H. felis* infection did not induce appreciable BMDC engraftment; only 2 glands containing BMDCs were found in 1780 glands examined at 30 weeks after transplantation (fig. S3, A, B, and C). Next, we induced acute gastric ulceration by serosal cryoinjury or submucosal acetic acid application (9) and examined mice 4 (fig. S3, D and E), 10, or 20 (fig. S3, F and G) days later. We found few beta-galactosidase-positive leukocytes and fibroblast-like cells (blue) at the ulcer base and edge but no engraftment of BMDCs as epithelial cells.

Previous studies have shown that targeted ablation of parietal cells with transgenic or chemical approaches results in increased cellular proliferation, altered patterns of differentiation, and mucous cell metaplasia (11, 16). To determine whether parietal cell loss plays a role in recruitment and retention of BMDCs, parietal cells were depleted with DMP777 (9, 11), followed by parietal cell repopulation after drug withdrawal. Tissue was examined for BMDC engraftment by X-gal staining at 9 days or 30 weeks after drug withdrawal. At 30 weeks, scattered leu-

Fig. 2. Beta-galactosidase IHC of stomachs from C57BL/6 mice transplanted with ROSA26 marrow. (A and C) Mock-infected mice do not demonstrate any BMDC engraftment, as evidenced by lack of beta-galactosidase staining. (B and D) *H. felis*-infected mice have substantial architectural distortion and beta-galactosidase-positive (brown) GIN. Fluorescence IHC for cytokeratin (green) and beta-galactosidase (red). (E) Glands within GIN from an infected mouse transplanted with wild-type marrow do not express beta-galactosidase. (F) Glands within GIN from an infected mouse transplanted with ROSA26 marrow demonstrate beta-galactosidase expression (red), colocalized with cytokeratin (green) to form yellow, confirming epithelial differentiation of integrated BMDC. Occasional mononuclear leukocytes are beta-galactosidase positive (red) and cytokeratin negative. Scale bars, 400 μ m [(A) and (B)], 160 μ m [(C) and (D)], 40 μ m [(E) and (F)].



kocytes and fibroblast-like cells were bone marrow derived (blue staining), but we did not demonstrate any gastric epithelial cells of bone marrow origin (fig. S3, H and I).

Using three methods, we next addressed whether fusion occurred between BMDCs and the gastric epithelium. First, we examined histological sections containing bone marrow-derived epithelial cells and found that cells contained only a single nuclei; no binucleate cells were seen. Second, we used fluorescence-activated cell sorting (FACS) of propidium iodide-stained cells to determine DNA content in wild-type tissues, early infection prior to engraftment, and BMDC carcinoma, and did not demonstrate any difference between these groups (fig. S4). Third, in female mice

transplanted with male GFP transgenic marrow, we evaluated 10,000 GFP⁺/CD45⁻ pancytokeratin⁺ FACS-sorted gastric cells, using FISH, and showed a single X and a single Y chromosome in all cells examined (9) (Fig. 3E). These studies strongly suggest that stable fusion did not occur.

In our initial reconstitution studies, whole bone marrow was used to minimize cell manipulation, which can alter growth potential and behavior of stem cells (4, 6). To identify the population of cells within the bone marrow responsible for gastric mucosal engraftment, we cultured hematopoietic stem cells (HSC) (lineage depleted, Rho^{dull}/Ho^{dull}) or adherent mesenchymal stem cell (MSC) populations in transwell culture plates in con-

tact with the soluble components of control medium or culture medium from primary gastric epithelial cell cultures (9). Neither HSC nor MSC populations expressed epithelial markers (TFF2 or KRT1-19) at the time of isolation or after culture with control medium. MSC cultures, but not HSC cultures, showed a marked up-regulation of both KRT1-19 and TFF2 at 24 and 48 hours when exposed to the soluble components of gastric epithelial tissue, which demonstrates that MSC (but not HSC) acquired a gastric mucosal cell-gene expression pattern without cell-to-cell contact or fusion (fig. S5). Western blot analysis performed on whole gastric mucosa from *H. felis*-infected C57BL/6 mice (12 and 16 months after infection) showed a substantial up-regulation of SDF-1 and SCF-1 (two factors identified in mobilization and migration of marrow progenitor cells) compared with uninfected age-matched controls (fig. S6). These data suggest that *Helicobacter* infection can give rise to an environment conducive to marrow stem cell recruitment, with the MSC the most likely candidate.

The experiments described here show that, in response to chronic *Helicobacter* infection, bone marrow-derived cells can home to and repopulate the gastric mucosa and contribute over time to metaplasia, dysplasia, and cancer. Demonstration of malignant progression of a marrow-derived progenitor cell in the setting of chronic inflammation offers the basis for a new model of epithelial cancer. Many features of cancer cells become much clearer when viewed within the context of our model: their undifferentiated nature, ability for self-renewal, relative resistance to apoptosis, and propensity for metastases and early spread. These are properties that may be inherent to BMDCs rather than characteristics acquired over time. Striking similarities have been noted between cancer cells and stem cells (17, 18), with recent *in vitro* studies suggesting that adult MSCs may be targets for malignant transformation (19). On the basis of the data presented here, we conclude that *H. felis*-induced gastric cancer originates from a cell population within the adherent MSC population. Our data further support that stable fusion between the BMDCs and the gastric mucosa does not occur; however, our experiments were not designed to evaluate fusion with reductive division. The concept that epithelial cancers can arise from BMDCs greatly alters our overall understanding of cancer initiation and progression and has broad implications for the development of anticancer therapies.

References and Notes

1. F. Balkwill, A. Mantovani, *Lancet* **357**, 539 (2001).
2. T. C. Wang *et al.*, *Gastroenterology* **114**, 675 (1998).
3. D. S. Krause *et al.*, *Cell* **105**, 369 (2002).
4. Y. Jiang *et al.*, *Nature* **418**, 41 (2002).
5. D. J. Anderson, F. H. Gage, I. L. Weissman, *Nature Med.* **7**, 393 (2001).

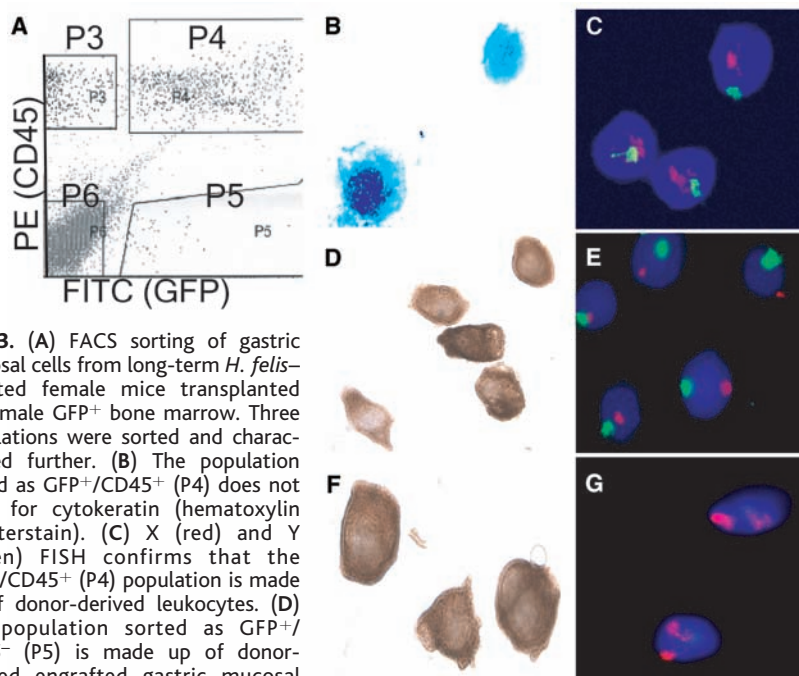


Fig. 3. (A) FACS sorting of gastric mucosal cells from long-term *H. felis*-infected female mice transplanted with male GFP⁺ bone marrow. Three populations were sorted and characterized further. (B) The population sorted as GFP⁺/CD45⁺ (P4) does not stain for cytokeratin (hematoxylin counterstain). (C) X (red) and Y (green) FISH confirms that the GFP⁺/CD45⁺ (P4) population is made up of donor-derived leukocytes. (D) The population sorted as GFP⁺/CD45⁻ (P5) is made up of donor-derived engrafted gastric mucosal cells that stain for cytokeratin (brown) and (E) contain both X and Y chromosomes by FISH. (F) GFP⁻/CD45⁻ cells (P6) are cytokeratin positive and (G) contain two X chromosomes, confirming that they are host-derived gastric epithelial cells.

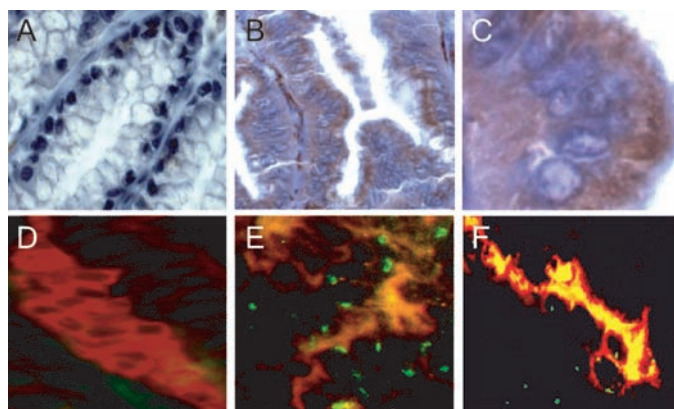


Fig. 4. (A) Female wild-type mouse transplanted with female wild-type marrow does not stain for GFP by IHC. (B and C) Female mouse transplanted with male GFP marrow shows IHC for GFP (brown staining) in tumor cells. (D) FISH for Y chromosome (green) is negative in the female-to-female transplant (cytokeratin; red). (E and F) Tumor from male-to-female transplants show numerous Y chromosomes (green) within the nuclei (black) of cytokeratin-positive (red) cells.

6. A. J. Wagers, I. L. Weissman, *Cell* **116**, 639 (2004).
 7. M. LaBarge, H. M. Blau, *Cell* **111**, 589 (2002).
 8. J. G. Fox *et al.*, *Cancer Res.* **62**, 696 (2002).
 9. Materials and methods are available as supporting material on Science Online.
 10. P. H. Schmidt *et al.*, *Lab. Invest.* **79**, 639 (1999).
 11. J. R. Goldenring *et al.*, *Gastroenterology* **118**, 1080 (2002).
 12. G. P. Boivin *et al.*, *Gastroenterology* **124**, 762 (2003).
 13. A. D. Clouston, *Pathology* **33**, 271 (2001).
 14. J. G. Fox *et al.*, *Cancer Res.* **63**, 942 (2003).
 15. R. Okamoto *et al.*, *Nature Med.* **8**, 1011 (2002).
 16. Q. Li, S. M. Karam, J. I. Gordon, *J. Biol. Chem.* **271**, 3671 (1996).
 17. D. Normille, *Science* **298**, 1869 (2002).
 18. J. Couzin, *Science* **299**, 1002 (2003).
 19. N. Serakinci *et al.*, *Oncogene* **23**, 5095 (2004).
 20. We thank K. Cormier and the Division of Comparative Medicine histology lab for technical support and expertise in IHC, and D. Altieri and E. Kurt-Jones for their helpful comments and suggestions. Supported by NIH grants K22 CA90518 (J.H.), RO1 CA87958 (T.C.W. and J.G.F.), RO1 DK58889 (T.C.W.), and a VA

Merit Review and Vanderbilt GI SPORE 1P50 CA95103 (J.R.G.).

Supporting Online Material
www.sciencemag.org/cgi/content/full/306/5701/1568/DC1
 Materials and Methods
 Figs. S1 to S6
 Table S1

23 April 2004; accepted 7 October 2004

Nucleosome Arrays Reveal the Two-Start Organization of the Chromatin Fiber

Benedetta Dorigo,^{1*} Thomas Schalch,^{1*} Alexandra Kulangara,¹ Sylwia Duda,¹ Rasmus R. Schroeder,² Timothy J. Richmond^{1†}

Chromatin folding determines the accessibility of DNA constituting eukaryotic genomes and consequently is profoundly important in the mechanisms of nuclear processes such as gene regulation. Nucleosome arrays compact to form a 30-nanometer chromatin fiber of hitherto disputed structure. Two competing classes of models have been proposed in which nucleosomes are either arranged linearly in a one-start higher order helix or zigzag back and forth in a two-start helix. We analyzed compacted nucleosome arrays stabilized by introduction of disulfide cross-links and show that the chromatin fiber comprises two stacks of nucleosomes in accord with the two-start model.

DNA in eukaryotic cell nuclei assembles with histone proteins into chromatin (1). The nucleosome constitutes the first level of organization (2, 3). The “30-nm” chromatin fiber consists of nucleosome arrays in their most compact form and is typically posited as the second structural level of DNA organization (4). The hierarchy continues with increasing DNA-packing density until the metaphase chromosome is attained (5). The structure of the 30-nm fiber, or nucleosome higher order structure, has been contentious for two decades. Most models have in common that an open zigzag string of nucleosomes self-assembles into a helical structure ~30 nm in diameter. The models can be grouped into two classes: (i) the one-start helix, with bent linker DNA connecting each pair of nucleosome cores, which follow each other immediately along the same helical path (6) (Fig. 1A), and (ii) the two-start helix, based on straight linker DNA connecting between two adjacent stacks of helically arranged nucleosome cores (7). The most prominent representative of the one-start class is the

solenoid, where the nucleosomes coil around a central cavity with ~six to eight nucleosomes per turn (8–10). The two-start class is divided between two main models named the helical ribbon model (7, 11) (Fig. 1B) and the crossed-linker model (12) (Fig. 1C).

With the aim of elucidating the higher-order structure of compact nucleosome arrays, we developed an *in vitro* system for producing highly regular arrays incorporating all recombinant components (13). With these arrays, we

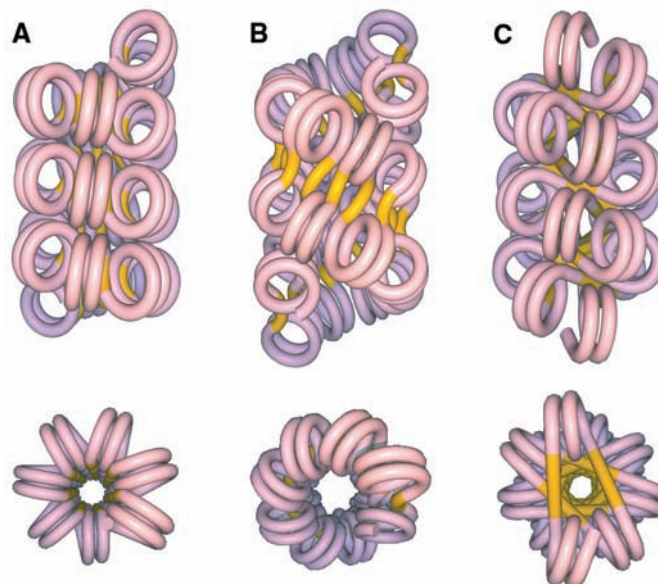
have shown that the base of the histone H4 tail is crucial for compaction. The crystal structure of the nucleosome core particle reveals that this region (amino acids 14 to 19) makes an interparticle contact with H2A/H2B of a neighboring particle (2, 3). We used this information to select a pair of cysteine-replacement mutants that stabilizes the higher order structure by disulfide formation. We constructed mutant versions of histones H2A, H2B, and H4 by replacing one selected amino acid with cysteine in each version [for H2A, Glu⁵⁶, Glu⁶¹, and Glu⁶⁴ (H2A-E56C, H2A-E61C, and H2A-E64C); for H2B, Gln⁴⁴, Val⁴⁵, and Glu¹¹⁰ (H2B-Q44C, H2B-V45C, and H2B-E110C); and for H4, Lys²⁰, Val²¹, Arg²³, and Asp²⁴ (H4-K20C, H4-V21C, H4-R23C, and H4-D24C)], and nucleosome arrays were assembled by using 12 different pairings of a mutant H4 with either a mutant H2A or H2B (table S1). The range of distances between the side-chain γ atoms of the selected pair of amino acids spans 3.8 to 9.7 Å determined from the nucleosome core structure. Cross-links were formed in solutions containing a 1:1 ratio of reduced and oxidized glutathione to promote disulfide formation without driving cross-linking irrespective of array folding. MgCl₂ at ~1 mM or ~100 mM was used to cause compaction, or alternatively the linker histone H1 was used to compact arrays in the absence of divalent cation. Initial trials cov-

¹Eidgenössische Technische Hochschule (ETH) Zürich, Institute for Molecular Biology and Biophysics, ETH-Hönggerberg, CH-8093 Zürich, Switzerland. ²Max Planck Institute for Medical Research, Department of Biomechanical Mechanisms, Jahnstrasse 29, 69120 Heidelberg, Germany.

*These authors contributed equally to this work.

†To whom correspondence should be addressed. E-mail: richmond@mol.biol.ethz.ch

Fig. 1. Models for the DNA path in the chromatin fiber. Higher order structure models: (A) one-start solenoidal (6), (B) two-start supercoiled (7), and (C) two-start twisted (12). Upper views have the fiber axis running vertically; lower views are down the fiber axis. DNA associated with the nucleosome core is red/blue, and linker DNA running between cores is yellow. These models are idealized, with nucleosome cores in each start contacting each other. The open three-dimensional zigzag seen in conditions not fully compacting may be a precursor (21).



ered a range of reaction conditions for all 12 mutant-containing arrays, but only the H4-V21C/H2A-E64C combination yielded a major cross-linked species (Fig. 2). Therefore, the H4-V21C/H2A-E64C combination was used in all subsequent experiments.

Disulfide formation in this system requires array compaction, and compaction requires inclusion of divalent cation or histone H1. Sedimentation velocity analysis shows that dodecanucleosomes containing the H4-V21C/H2A-E64C histones have a similar degree of compaction as compared to arrays containing wild-type histone sequences (13), both in the unfolded state with no divalent cation present and after crosslinking in the fully compacted state (fig. S1A). The crosslinked arrays maintain a fully compacted structure to lower divalent cation concentration as compared with the wild-type arrays (0.5 mM versus 1.0 mM MgCl₂), indicating that the disulfide bonds formed stabilize the folded, compact state (fig. S1B). Once formed, the cross-links prevent arrays from full unfolding in conditions lacking divalent cation. The diminished compaction of the mutant array compared with that of wild type in the presence of dithiothreitol (DTT) above 0.5 mM MgCl₂ indicates that H4-V21 and H2A-E64 contribute to internucleosome interaction in the folded fiber.

Cross-linked arrays can be cleaved under nonreducing conditions in each linker DNA segment by Sca I endonuclease. The maximum length of the cleaved arrays observed by native agarose-polyacrylamide gel electrophoresis (APAGE) after this treatment reveals the number of starts, or columns of nucleosomes, in the chromatin fibers. We show that, for arrays with either 12 or 10 nucleosome repeats, the maximum number of nucleosomes remaining after cross-linking and cleavage is 6 or 5, respectively (Fig. 3). We confirmed that virtually all linker DNA segments are cleaved by observing that essentially only mononucleosomes exist after reduction of cross-links with 100 mM DTT. This result demonstrates that the compacted nucleosome arrays have a two-start geometry. The nucleosomes in each start are connected by disulfide cross-links, so that after linker DNA cleavage the arrays are separated into individual nucleosome stacks that are maximally one-half the length of the starting array. For a one-start arrangement, the linker DNA and nucleosome-nucleosome cross-links would reinforce the same connectivity between nucleosomes, and therefore the longest bands expected would correspond to the uncleaved starting lengths of 12 and 10 nucleosomes, respectively. We have used arrays with different repeat lengths to demonstrate that the one-start versus two-start result is independent of DNA linker length. Furthermore, arrays with one copy of histone H1 bound per nucleosome yield the same result.

The ladders of bands observed by native APAGE for nucleosome arrays after disulfide crosslinking and Sca I cleavage indicate that not all cysteine thiol groups form crosslinks.

The maximum theoretical yield for a two-start structure given end effects and the possibility of two cross-links between adjacent nucleosomes is 83.3% for a dodecanucleosome.

Fig. 2. Internucleosome disulfide cross-linking of histones H4 and H2A with compaction of nucleosome arrays. SDS-PAGE shows that nucleosome arrays (12 repeats of 177 bp) containing histones H4-V21C and H2A-E64C yield a specific disulfide cross-link on compaction with 100 mM MgCl₂ at 37°C (lane 2) and at 22°C (lane 3). Noncompacted arrays (no MgCl₂, 0.5 mM EDTA, 37°C) under the same conditions show nearly undetectable disulfide formation (lane 6) and are comparable to starting material (lane 1). A competing internucleosome disulfide cross-link between two H4 molecules occurs for arrays compacted under conditions of 50 mM KCl and 1 mM MgCl₂ at 22°C (lane 5) but not at 37°C (lane 4). All cross-linking reactions were arrested by addition of 10 mM iodoacetamide. Cross-links within compacted arrays (lane 2) can be completely reversed after arrest by addition of 100 mM DTT (lane 7). A separate gel shows the cross-linking of a nucleosome array (10 repeats of 208 bp) with ~one histone H1 molecule bound per nucleosome (lane 8).

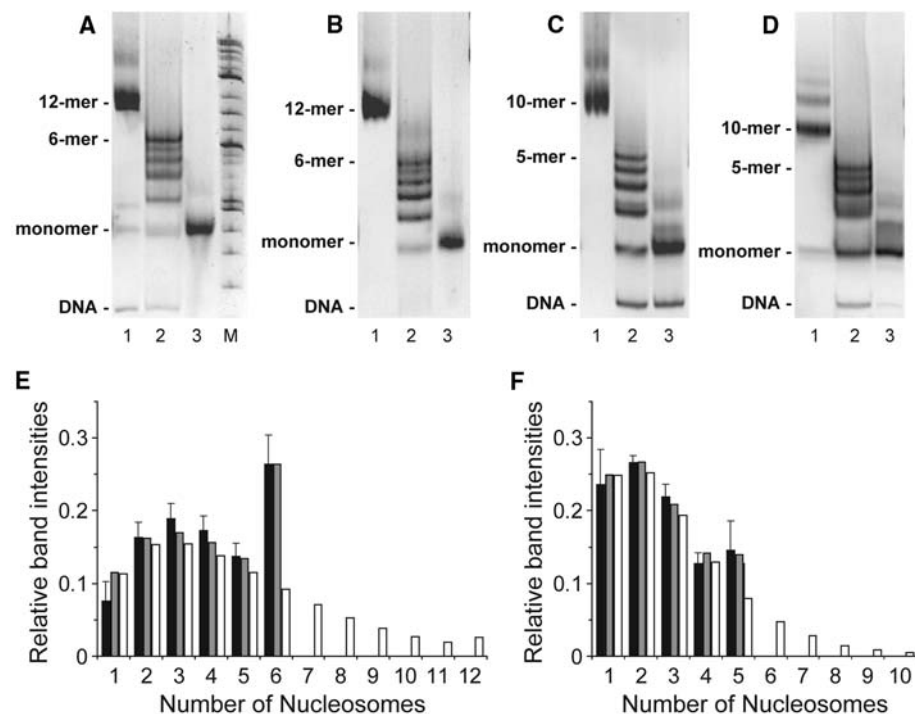


Fig. 3. Fragmentation of nucleosome arrays with Sca I after disulfide cross-linking. Nucleosome arrays containing (A) 12 repeats of 177 bp, (B) 12 repeats of 167 bp, (C) 10 repeats of 208 bp, and (D) 10 repeats of 208 bp with histone H1 bound were cross-linked via H4-V21C/H2A-E64C disulfide formation under conditions causing compaction. The products of the reactions were separated by native APAGE before (lane 1) and after (lane 2) digestion with Sca I restriction endonuclease (markers, lane M). Cross-links were reduced with 100 mM DTT after cleavage to produce mononucleosomes (lane 3). The positions of starting material, cleaved species of maximum size, and mononucleosome are indicated. The higher bands (lane 1), present before cross-linking, represent less than 5% of the material. Arrays with 12 repeats of 172 bp gave compatible results (22). (E) Analytical comparison of Sca I cleavage products for a dodecanucleosome with theoretical values. The band intensities for 15 experiments (A) were quantified from the fluorescence intensity of the ethidium bromide stain (black). Error bars correspond to one standard deviation from the mean for multiple measurements. The band intensities for one-start (white) and two-start (gray) structures were calculated based on the measured yield of cysteine to disulfide conversion of 42.8%. (F) Analytical comparison of Sca I cleavage products for an H1-bound decanucleosome with theoretical values. The band intensities for five experiments (D) were quantified as for (E) (black). The theoretical values were calculated on the basis of the measured yield of 29.9%.

Nonreducing SDS-PAGE followed by Coomassie Blue gel staining was used to estimate the fraction of cysteine sulfhydryl groups in disulfide bridges. Quantification of the band patterns for uncrosslinked and cross-linked samples resulted in a value of $42.8\% \pm 4.7\%$ (for example, Fig. 2, lane 2). With this disulfide yield, bands corresponding to DNA lengths greater than one-half the initial number of repeats would be expected for a one-start nucleosome arrangement. Comparison of the observed with the theoretical fragment distributions for two-start and one-start structures shows that the dodecanucleosome (Fig. 3A) has a two-start geometry (Fig. 3E). Disulfide cross-linking of decanucleosomes with histone H1 incorporated resulted in a cross-linking yield of $29.9\% \pm 5.0\%$, sufficient to reveal a fragmentation pattern also indicative of two-start geometry (Fig. 3, D and F).

Assuming random formation of up to two disulfide bonds per nucleosome-nucleosome interface, the measured yields of disulfide formation suggest cross-linking probabilities ($2p-p^2$) of 76.3% ($p = 42.8\%/83.3\%$) and 55.6% ($p = 29.9\%/83.3\%$) for arrays compacted with divalent cation and H1, respectively. The corresponding fits ($R = 0.949$ and $P = 0.004$ and $R = 0.980$ and $P = 0.003$) of the observed gel distributions with those calculated for two-start organization validates this model. The lack of complete cross-linking suggests that disulfide formation depends on static disorder or dynamic fluctuations of nucleosomes within the higher order structure.

We have directly imaged the cross-linked arrays by electron microscopy (EM) to complement the native APAGE analysis. To see the direction of the fiber axis clearly, we prepared mutant arrays with a mean length

of 48 repeats (48-mer) of 177 base pairs (bp) from ligated dodecamer DNA. After compaction with concurrent disulfide crosslinking, these arrays were applied to grids and negative-stained with uranyl acetate. Fixatives such as formaldehyde or glutaraldehyde were not used. The particles appear most frequently as two equal-length parallel rows with widths of ~ 25 to 30 nm (Fig. 4A). The rows correspond to a width of ~ 12 nm and are interpreted as nucleosomes stacked on their histone octamer faces, consistent with the cross-link experiments. The two rows are indicative of two-start organization. In contrast, when the cross-link is reversed by 100 mM DTT treatment, the particles lose their fiberlike appearance (Fig. 4B).

The APAGE experiments suggest that the nucleosomes in each of the fiber starts should be visible as separate stacks in electron micrographs after treatment with Sca I. Images of the 48-mer samples after Sca I digestion show that the fibers are indeed separable into single columns (Fig. 4C). The length of the columns is reduced compared with the undigested material because of incomplete internucleosome cross-linking. Furthermore, pairs of columns sometimes appear to be coupled at points, because the DNA connections introduced by DNA ligation are not Sca I-cleavable.

H1-bound 48-mer arrays fixed with formaldehyde and negative-stained reveal fibers with regions that are two-start in appearance (fig. S2A). These images have an appearance similar to those from studies using native chromatin (7, 14). Decanucleosomes disulfide-cross-linked with one copy of histone H1 bound per nucleosome clearly display two parallel stacks of nucleosomes (fig. S2, B and C). Evidently, the one-start versus two-start secondary structure organi-

zation of chromatin is not affected by the binding of one copy of the linker histone per nucleosome. In this regard, mass-corrected s values from sedimentation analysis measured for the dodecanucleosomes result in the same degree of compaction whether or not H1 is bound, despite the increased stability it affords (15). In vivo studies have shown that H1 is inessential for viability of one-cell eukaryotes (16–19) and that substoichiometric amounts of H1 are tolerated in mice (20), consistent with our results for the chromatin fiber based on nucleosome arrays. Additional specifics of the form(s) of the two-start structure (for example, Fig. 1, B and C) remain to be elucidated by cryo-EM and x-ray crystallography.

References and Notes

- K. E. van Holde, *Chromatin*, Springer Series in Molecular Biology, A. Rich, Ed. (Springer-Verlag, New York, 1988).
- K. Luger, A. W. Maeder, R. K. Richmond, D. F. Sargent, T. J. Richmond, *Nature* **389**, 251 (1997).
- C. A. Davey, D. F. Sargent, K. Luger, A. W. Mäder, T. J. Richmond, *J. Mol. Biol.* **319**, 1097 (2002).
- T. J. Richmond, J. Widom, in *Chromatin Structure and Gene Expression*, S. C. R. Elgin, J. L. Workman, Eds. (Oxford Univ. Press, Oxford, 2000), pp. 1–23.
- Y. G. Strukov, Y. Wang, A. S. Belmont, *J. Cell Biol.* **162**, 23 (2003).
- J. Widom, A. Klug, *Cell* **43**, 207 (1985).
- C. L. F. Woodcock, L.-L. Y. Frado, J. B. Rattner, *J. Cell Biol.* **99**, 42 (1984).
- J. T. Finch, A. Klug, *Proc. Natl. Acad. Sci. U.S.A.* **73**, 1897 (1976).
- F. Thoma, T. Koller, A. Klug, *J. Cell Biol.* **83**, 403 (1979).
- J. D. McGhee, J. M. Nickol, G. Felsenfeld, D. C. Rau, *Cell* **33**, 831 (1983).
- A. Worcel, S. Strogatz, D. Riley, *Proc. Natl. Acad. Sci. U.S.A.* **78**, 1461 (1981).
- S. P. Williams et al., *Biophys. J.* **49**, 233 (1986).
- B. Dorigo, T. Schalch, K. Bystricky, T. J. Richmond, *J. Mol. Biol.* **327**, 85 (2003).
- J. B. Rattner, B. A. Hamkalo, *Chromosoma* **69**, 363 (1978).
- L. M. Carruthers, J. Bednar, C. L. Woodcock, J. C. Hansen, *Biochemistry* **37**, 14776 (1998).
- X. Shen, L. Yu, J. W. Weir, M. A. Gorovsky, *Cell* **82**, 47 (1995).
- H. G. Patterson, C. C. Landel, D. Landsman, C. L. Peterson, R. T. Simpson, *J. Biol. Chem.* **273**, 7268 (1998).
- J. L. Barra, L. Rhounim, J. L. Rossignol, G. Faugeron, *Mol. Cell. Biol.* **20**, 61 (2000).
- A. Ramon, M. I. Muro-Pastor, C. Sczozocchio, R. Gonzalez, *Mol. Microbiol.* **35**, 223 (2000).
- Y. Fan et al., *Mol. Cell. Biol.* **23**, 4559 (2003).
- J. Bednar, R. A. Horowitz, J. Dubochet, C. L. Woodcock, *J. Cell Biol.* **131**, 1365 (1995).
- B. Dorigo, T. J. Richmond, data not shown.
- We thank M. Müller and H. Gross for assistance with EM and V. Ramakrishnan for providing the H1 expression plasmid. We are grateful for financial support from the Swiss National Science Foundation through the National Center for Competence in Research Structural Biology and a grant to T.J.R.

Supporting Online Material

www.sciencemag.org/cgi/content/full/306/5701/1571/DC1

Materials and Methods

Figs. S1 and S2

Table S1

References

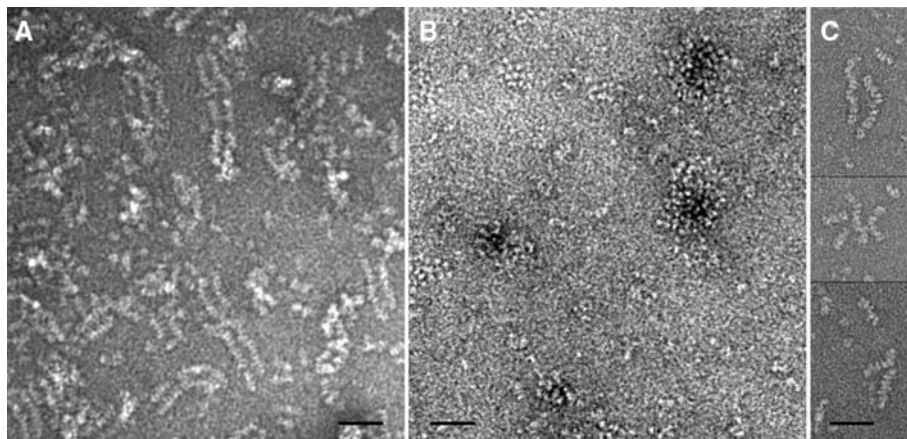


Fig. 4. Electron micrographs showing the two-start organization of nucleosome arrays. (A) 48-mer nucleosome arrays were cross-linked via H4-V21C/H2A-E64C-mediated disulfide formation under compacting conditions and prepared for EM with the use of negative stain. (B) Arrays were treated with 100 mM DTT to relieve the disulfide cross-link and then prepared as for (A). (C) Arrays (three separate examples are shown) prepared as for (A) were cleaved at the Sca I site in the linker DNA. Scale bars indicate 50 nm. EM magnification was 13,000 \times for (A) and (B) and 26,000 \times for (C).

22 July 2004; accepted 6 October 2004

Chromatin Compaction by a Polycomb Group Protein Complex

Nicole J. Francis,^{1,2*} Robert E. Kingston,^{1,2,†}
Christopher L. Woodcock³

Polycomb group proteins preserve body patterning through development by maintaining transcriptional silencing of homeotic genes. A long-standing hypothesis is that silencing involves creating chromatin structure that is repressive to gene transcription. We demonstrate by electron microscopy that core components of Polycomb Repressive Complex 1 induce compaction of defined nucleosomal arrays. Compaction by Polycomb proteins requires nucleosomes but not histone tails. Each Polycomb complex can compact about three nucleosomes. A region of Posterior Sex Combs that is important for gene silencing *in vivo* is also important for chromatin compaction, linking the two activities. This mechanism of chromatin compaction might be central to stable gene silencing by the Polycomb group.

Specific patterns of gene expression underly the diverse array of cell types comprising an organism. Some of these patterns are established early in embryogenesis by transient regulatory events and are then maintained through differentiation and the multitude of cell divisions that occur during development. One maintenance mechanism is encoded by the essential Polycomb group (PcG) genes, which were identified in *Drosophila melanogaster*. PcG genes maintain repression of *HOX* genes (1), thereby preserving body patterning along the anterior-posterior axis. In mammals, they also influence cell cycle control, cancer, and stem cell self-renewal (2, 3). PcG proteins were proposed to alter chromatin structure to maintain gene repression (4–6), but it has proven difficult to test this hypothesis. We previously characterized one PcG complex, Polycomb Repressive Complex 1 (PRC1) (7), and showed that both PRC1 and complexes reconstituted from its core PcG components inhibit chromatin remodeling and transcription *in vitro*, suggesting that they might alter chromatin structure (8, 9). We visualized the effects of complexes reconstituted from core PcG proteins on nucleosomal arrays by electron microscopy (EM) to investigate the hypothesis that PcG proteins alter chromatin conformation.

We compared 12-nucleosomal arrays in the presence and absence of PRC1 core complexes (PCCs) (10). Arrays incubated with PCC were transformed from a classical

“beads-on-a-string” conformation (Fig. 1A) into highly compacted structures in which individual nucleosomes could not be resolved (Fig. 1B). One core PcG component of PRC1, Polyhomeotic (Ph), is not required for inhibition of chromatin remodeling or transcription by PCC (11). At a ratio of one complex to eight nucleosomes, PCCs assembled without Ph also compacts chromatin (Fig. 1C). Because the complex lacking Ph is less prone to aggregation and can be isolated in large quantities, it was used to elucidate molecular mechanisms of compaction.

To quantify the effects of PCCs on chromatin, we measured two parameters of the arrays: (i) diameter (*d*) of the smallest circle completely encompassing the array (Fig. 1, D and E) and (ii) number of discrete particles (*np*) per array (Fig. 1, D and F). On control arrays, most of these particles are single nucleosomes, whereas on PCC-compacted arrays the large particles observed likely represent multiple nucleosomes brought into close proximity and also likely include bound PCC. Both parameters were significantly reduced on arrays incubated with PCC [*d* = 201 ± 44 (SD) nm in control arrays versus 129 ± 35 nm in PCC arrays; *np* = 9 ± 1 in control arrays versus 4 ± 2 in PCC arrays; *P* << 0.001]. Similar results were seen in 13 independent experiments (10). Thus, at ratios of less than one complex per nucleosome, PCC induces compaction of chromatin under conditions that otherwise favor extended conformations.

Chromatin compaction by PCCs could occur by bridging the “linker” DNA between nucleosomes, as suggested for H1-family proteins (12) and the chromatin condensation factor myeloid and erythroid nuclear termination stage-specific protein (MENT) (13). Alternatively, proteins or complexes that bind the unstructured, protruding N-terminal “tails” of the histone proteins on different nucleosomes could promote compaction, as suggested for HP1 (14) and SSN6/Tup1 (15). Finally, nucleosomes themselves could be

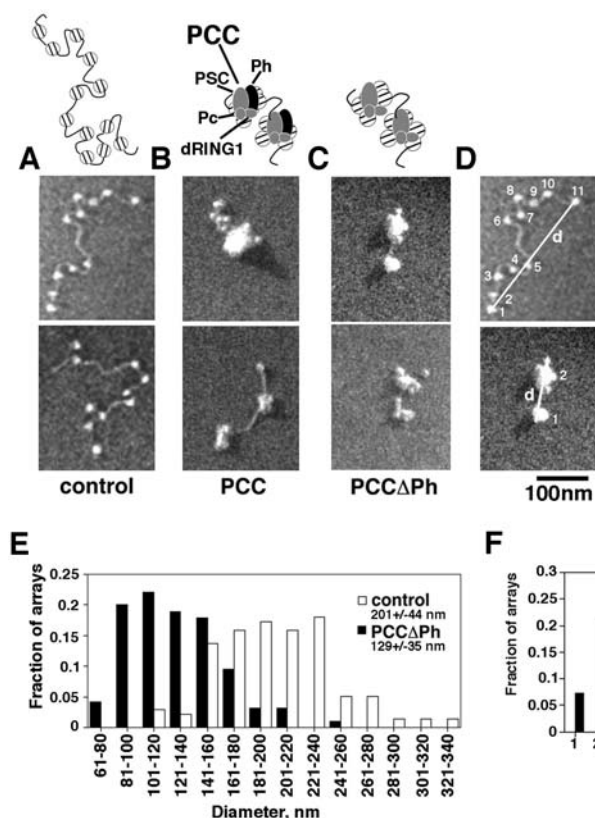


Fig. 1. A PcG complex alters the structure of chromatin. EM of nucleosomal arrays alone (A), with a ratio of 1 PCC to 16 nucleosomes (B), or with a ratio of one PCCΔPh to eight nucleosomes (C). (D) Lines indicate diameter (*d*) and numbers particle counts. Scale bar in (D) is for images (A) to (D). Distributions of diameters (E) or numbers of particles (F). Numbers on all graphs represent mean ± SD.

¹Department of Molecular Biology, Massachusetts General Hospital, Boston, MA 02114, USA. ²Department of Genetics, Harvard Medical School, Boston, MA 02115, USA. ³Department of Biology, University of Massachusetts, Amherst, MA 01003, USA.

*Present address: Department of Molecular and Cellular Biology, Harvard University, Cambridge, MA 02138, USA.

†To whom correspondence should be addressed. E-mail: kingston@molbio.mgh.harvard.edu

bridged by chromatin compacting factors. To distinguish among these possibilities, we first compared PCC effects on nucleosomal arrays and bare DNA. If PCC interacts with linker DNA to compact chromatin, it should alter the structure of bare DNA, as observed for other factors that compact chromatin, such as MENT, McCP2, and Condensin (13, 16, 17). However, although we observed binding of PCC to DNA (Fig. 2, A and B), this did not induce conformational changes, sug-

gesting that DNA alone lacks components required for compaction.

As a second means of separating the roles of DNA and nucleosomes, we tested the effect of PCCs on subsaturated nucleosomal arrays (containing 4 to 8 nucleosomes instead of 9 to 12). If PCC compacts chromatin by bridging linker DNA, the long stretches of free DNA on subsaturated arrays, rather than the nucleosomes, should be brought together. In contrast, if compaction predomi-

nantly reflects interactions between PCC and nucleosomes, PCC should bring nucleosomes together, allowing linker DNA to loop out. The addition of PCC to subsaturated arrays (Fig. 2C), at the same input ratio used to compact saturated arrays, induced conformational changes in which two or more nucleosomes were brought together, often with associated loops of DNA (Fig. 2D and fig. S2A). Together, the results on bare DNA and subsaturated arrays support interactions between PCC and nucleosomes, rather than PCC and linker DNA, mediating chromatin compaction.

The histone N-terminal tails are central to chromatin regulation. They are essential for chromatin folding in vitro (18), and many chromatin regulatory proteins interact with or covalently modify them (19, 20). One of the PcG proteins used in these experiments, Polycomb, binds the N-terminal tail of histone H3 (21, 22), but PRC1 does not require histone tails for inhibition of chromatin remodeling (7). Furthermore, PCC inhibits chromatin remodeling on arrays assembled with either trypsinized histones lacking tails or intact histones (fig. S2, D and E). In the absence of PCC, nucleosomal arrays assembled with histones that lacked tails were extended and nucleosomes well resolved (Fig. 2E). PCC induced compacted structures on these arrays similar to those observed with control arrays (Fig. 2F). Compaction was confirmed by quantification ($d = 197 \pm 51$ nm for control versus 160 ± 44 nm for PCC; $n_p = 11 \pm 1$ in control arrays versus 6 ± 2 for PCC, $P \ll 0.001$) (fig. S2F and table S2). Thus, histone tails are not required for inhibition of chromatin remodeling or compaction by PCC. These results do not, however, exclude the possibility that interactions between PCC and histone tails or histone tail modifications influence PCC-induced chromatin compaction.

Previously, we found that one subunit of PRC1, PSC, inhibits chromatin remodeling and transcription (8, 9). In vivo evidence is also consistent with a key role for PSC in maintaining gene expression patterns (23). When PSC alone was incubated with nucleosomal arrays at a ratio of one PSC to three or four nucleosomes, compacted chromatin structures were observed (Fig. 3B), indicating that inhibitory activities and chromatin compaction are correlated. Regions between the C terminus and amino acid 572 are important for in vitro and in vivo functions of PSC (24). To further examine the correlation among chromatin compaction, in vitro inhibitory activities, and in vivo gene repression, we tested the effect of N- and C-terminal fragments of PSC on chromatin compaction (Fig. 3A). The C-terminal region of PSC (PSC⁴⁵⁶⁻¹⁶⁰³) can compact chromatin; this fragment can also inhibit chromatin remodeling and transcription in vitro (24). An N-terminal fragment lacking almost half of the protein (PSC¹⁻⁸⁷²)

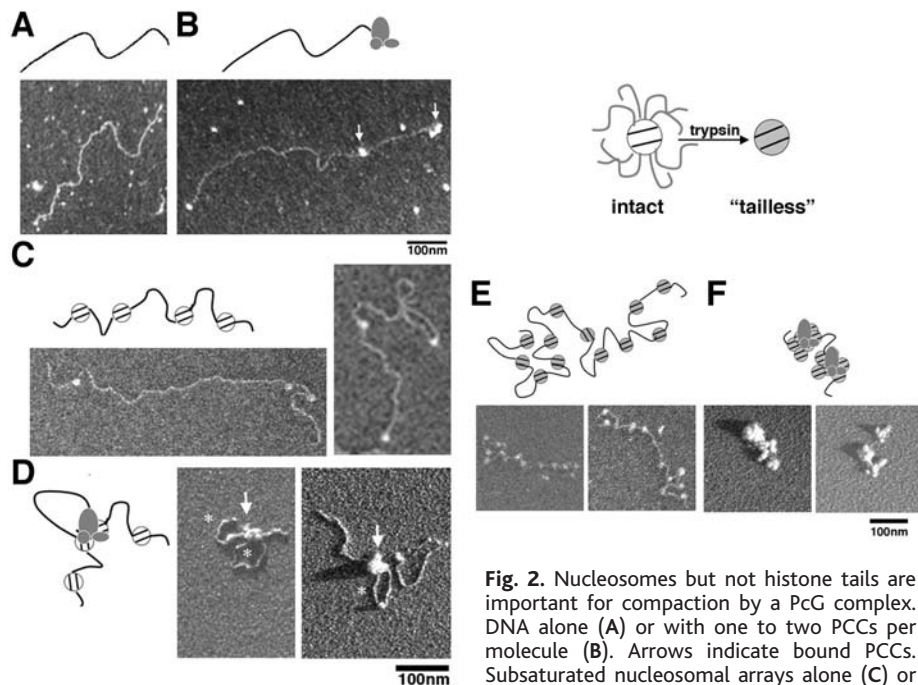
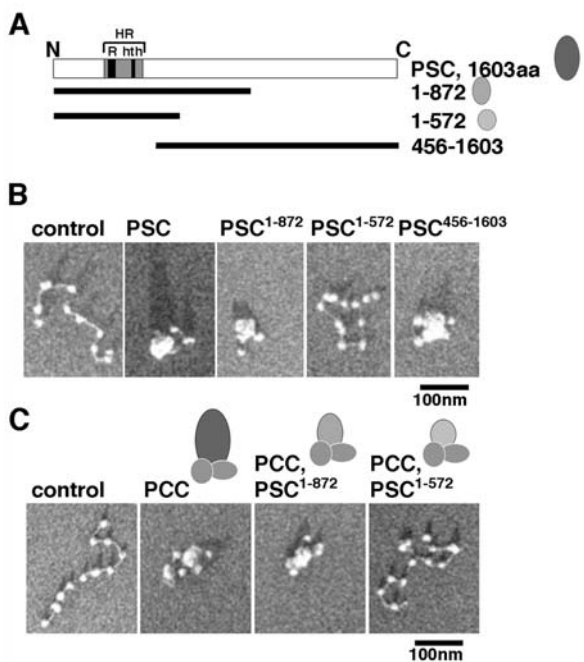


Fig. 2. Nucleosomes but not histone tails are important for compaction by a PcG complex. DNA alone (A) or with one to two PCCs per molecule (B). Arrows indicate bound PCCs. Subsaturated nucleosomal arrays alone (C) or with one to two PCCs per array (D). DNA loops (asterisks) and nucleosome clusters (arrows) occur in the presence of PCC. Arrays assembled with trypsinized histones alone (E) or with a ratio of one PCC to eight nucleosomes (F).

Fig. 3. The C-terminal region of PSC is important for chromatin compaction by a PcG complex. (A) Schematic of PSC and PSC truncations. HR, conserved homology region; R, ring finger; hth, helix turn helix. (B) Nucleosomal arrays alone or with full-length or truncated PSC. (C) Nucleosomal arrays alone or with PCC containing full-length or truncated PSC.



compacts chromatin (Fig. 3B and fig. S3). In contrast, a slightly shorter N-terminal fragment (PSC¹⁻⁵⁷²) does not induce such highly compacted structures, although the nucleosomal arrays are less extended than the controls (fig. S3 and table S3).

To determine whether the C-terminal region of PSC is necessary for chromatin compaction when PSC is combined with other components of PCC, complexes were assembled with PSC¹⁻⁸⁷² and PSC¹⁻⁵⁷². Complexes assembled with PSC¹⁻⁸⁷² compacted chromatin as well as those containing full-length PSC, whereas complexes assembled with PSC¹⁻⁵⁷² had reduced compacting activity (Fig. 3C and fig. S4). Similar to PSC and PCC, PSC¹⁻⁸⁷² and PCC assembled with PSC¹⁻⁸⁷² inhibit chromatin remodeling and transcription in vitro. In contrast, PSC¹⁻⁵⁷² or PCC assembled with PSC¹⁻⁵⁷² are impaired for both activities (24). Thus, gene silencing in vivo, inhibition of chromatin remodeling and transcription, and chromatin compaction are correlated by means of their dependence on a C-terminal region of PSC (24).

A ratio of one PCC to three nucleosomes is sufficient for full inhibition of chromatin remodeling of a 12-nucleosome template (8). Although structural effects are observed on the same template at a ratio of 1:8 (Fig. 1), uniformly compacted structures require a ratio of 1:4 (table S1). These results predict that (i) templates containing fewer than four

nucleosomes will be inhibited less efficiently than longer templates, and (ii) a single PCC can compact a four-nucleosome array. Indeed, PCC inhibits chromatin remodeling more efficiently on templates containing four or more nucleosomes than on shorter templates (Fig. 4A) and many four-nucleosome arrays incubated with about one PCC per array formed highly compacted, round structures, whereas others appeared unaffected (Fig. 4B and fig. S5).

To determine how many PCC were actually bound to four-nucleosome arrays, we used scanning transmission EM (STEM), which can accurately measure particle masses up to 10 MD using the linear relationship between electron scattering and molecular mass. The average measured mass of PCC alone was 270 ± 90 kD (Fig. 4C), consistent with a PSC:dRING:Polycomb stoichiometry of 1:1:1 (predicted mass 262 kD). The mean mass of four-nucleosome arrays was 1.03 ± 0.13 MD, in agreement with the predicted mass (0.91 MD) (Fig. 4D). The mean mass of the compacted structures resembling those in Fig. 4B was 1.41 ± 0.34 MD (Fig. 4E). This is consistent with most particles containing one four-nucleosome array and one PCC. Some masses were less than expected for four nucleosomes plus one PCC; these likely represent arrays containing only three nucleosomes, which were also present in the preparation, complexed with one PCC. EM

and STEM analysis of six-nucleosome arrays complexed with PCC are consistent with these results (fig. S4). Thus, taken together, our data suggest the minimum ratio for full compaction and inhibition is one PCC for three to four nucleosomes.

Our principal conclusion is that core PcG components of PRC1 create compacted chromatin structures through interactions with nucleosomes by a mechanism that does not require histone tails. Experiments with short arrays of nucleosomes suggest one complex can compact about three nucleosomes, distinguishing it from other factors that compact chromatin at ratios of one per nucleosome or higher. Thus, each complex might have binding sites for more than one nucleosome. Alteration of chromatin structure might be central to both the previously identified ability of these PcG proteins to inhibit chromatin remodeling and transcription in vitro, and stable gene silencing in vivo, because the C-terminal region of PSC is important for all of these activities. Our results provide direct support for a model in which PcG proteins in PRC1 create regions of compacted chromatin, and they are consistent with compaction of the PcG repressed homeotic BX-C gene cluster observed in vivo (25) and reduced accessibility of DNA in PcG repressed chromatin (5, 6, 26, 27). We suggest that regulation of chromatin conformation could be central to stable gene silencing by the PcG.

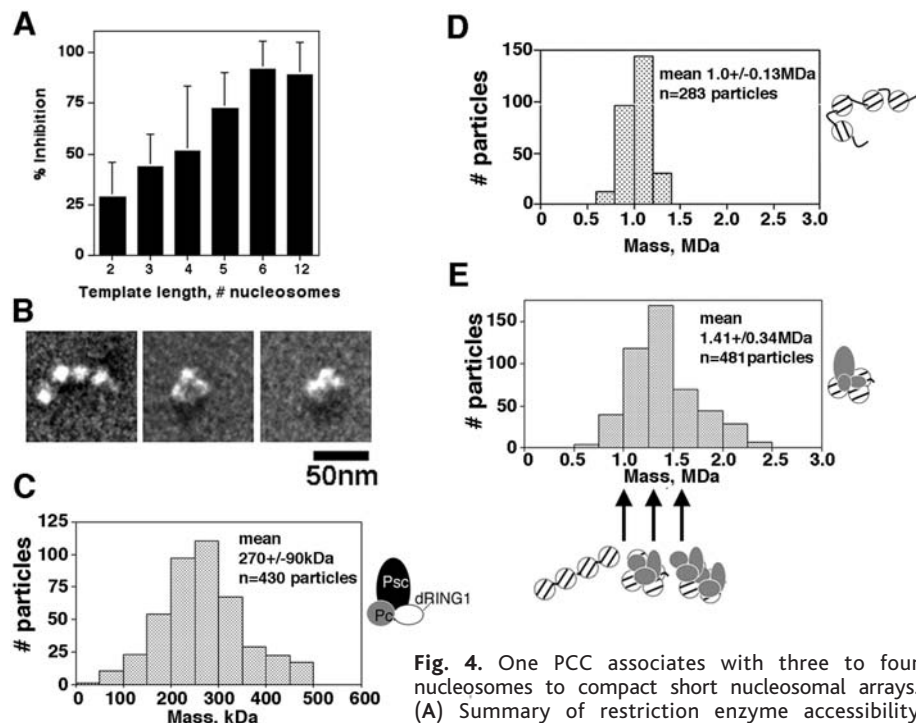


Fig. 4. One PCC associates with three to four nucleosomes to compact short nucleosomal arrays. (A) Summary of restriction enzyme accessibility analysis of inhibition of chromatin remodeling by 1 nM active PCC on 2 to 12 nucleosomal arrays. (B) Four-nucleosomal arrays alone (left) or with a ratio of one PCC to five nucleosomes (center and right). Quantification is presented in fig. S3. Mass distribution of PCCs (C), four-nucleosome arrays alone (D), or four-nucleosome arrays with PCC (E) determined by STEM. Arrows and diagrams under x axis (E) indicate expected masses for arrays alone or with one or two PCCs bound.

References and Notes

1. J. A. Simon, J. W. Tamkun, *Curr. Opin. Genet. Dev.* **12**, 210 (2002).
2. J. Lessard, G. Sauvageau, *Exp. Hematol.* **31**, 567 (2003).
3. M. E. Valk-Lingbeek, S. W. M. Bruggeman, M. van Lohuizen, *Cell* **118**, 409 (2004).
4. R. Paro, *Trends Genet.* **6**, 416 (1990).
5. K. McCall, W. Bender, *EMBO J.* **15**, 569 (1996).
6. D. P. Fitzgerald, W. Bender, *Mol. Cell. Biol.* **21**, 6585 (2001).
7. Z. Shao *et al.*, *Cell* **98**, 37 (1999).
8. N. J. Francis, A. J. Saurin, Z. Shao, R. Kingston, *Mol. Cell* **8**, 545 (2001).
9. I. F. G. King, N. J. Francis, R. Kingston, *Mol. Cell. Biol.* **22**, 7919 (2002).
10. Information on materials and methods available on Science Online.
11. M. Lavigne, N. J. Francis, I. F. King, R. Kingston, *Mol. Cell* **13**, 415 (2004).
12. J. Bednar *et al.*, *Proc. Natl. Acad. Sci. U.S.A.* **95**, 14173 (1998).
13. E. M. Springhetti *et al.*, *J. Biol. Chem.* **278**, 44384 (2003).
14. A. Thiru *et al.*, *EMBO J.* **23**, 489 (2004).
15. C. E. Ducker, R. T. Simpson, *EMBO J.* **19**, 400 (2000).
16. I. M. Porter, G. A. Khoudoli, J. R. Swedlow, *Curr. Biol.* **14**, R554 (2004).
17. P. T. Georgel *et al.*, *J. Biol. Chem.* **278**, 32181 (2003).
18. J. C. Hansen, *Annu. Rev. Biophys. Biomol. Struct.* **31**, 361 (2002).
19. B. M. Turner, *Cell* **111**, 285 (2002).
20. T. Jenuwein, C. D. Allis, *Science* **293**, 1074 (2001).
21. J. Min, Y. Zhang, R. M. Xu, *Genes Dev.* **17**, 1823 (2003).
22. W. Fischle *et al.*, *Genes Dev.* **17**, 1870 (2003).

23. D. Beuchle, G. Struhl, J. Muller, *Development* **128**, 993 (2001).
24. I. King *et al.*, unpublished data.
25. M. Marchetti, L. Fanti, M. Berloco, S. Pimpinelli, *Development* **130**, 3683 (2003).
26. A. Boivin, J.-M. Dura, *Genetics* **150**, 1539 (1998).
27. D. Zink, R. Paro, *EMBO J.* **14**, 5660 (1995).
28. We thank J. Wall and M. Simon of Brookhaven National Laboratory (BNL) for collecting mass data; S. Levine, A. Seto, C. Woo, and J. Dennis for comments on the manuscript; R. Emmons, J. Muller, I. King,

and C.-t. Wu for permission to cite unpublished observations regarding the structure function relationships of PSC in vivo; and R. Emmons and C.-t. Wu for discussions illuminating the genetics of PSC function. N.J.F. thanks the Woodcock lab and Central Microscopy Facility for technical advice. The BNL STEM is a NIH Supported Resource Center, NIH-P41-RR01777, with additional support provided by the Department of Energy Biological and Environmental Research program. This work was supported by a Charles King Trust Fel-

lowship (N.J.F.), and by the NIH (R.E.K and C.L.W., GM43786).

Supporting Online Material

www.sciencemag.org/cgi/content/full/306/5701/1574/DC1

Materials and Methods

Figs. S1 to S5

Tables S1 to S4

References

21 May 2004; accepted 14 October 2004

Turn
a new
page
to...

— Science —
Books et al.
= HOME PAGE =

- ▶ the latest book reviews
- ▶ extensive review archive
- ▶ topical books received lists
- ▶ buy books online

www.sciencemag.org/books

NEW PRODUCTS

<http://science.labvelocity.com>

NucleoSpin Extract II Kit

The NucleoSpin Extract II Kit is suitable for both gel extraction and polymerase chain reaction (PCR) purification. The procedure is quick and simple. The spin column binds DNA to a silica membrane in the presence of chaotropic salt. Once the binding mixture is loaded directly onto the column, only a single wash step with a buffer is required. Downstream applications include sequencing, ligation, labeling, cloning, and restriction enzyme digestion.

BD Biosciences For more information 877-232-8995
www.bdbiosciences.com/clontech

Protein Interaction Analysis

The One-STrEP system is a fast and efficient method for identifying protein complexes. Unlike systems that require tedious optimization because of high background or two successive purification steps, the One-STrEP system requires only one step to isolate protein complexes. In this system, Strep-Tactin columns are used for fast protein purification under physiological conditions with low background, enabling even the isolation of weakly associated binding partners. The system is suitable to identify several binding partners or co-factors at once with minimal background.

IBA For more information +49-551-50672-114 www.iba-go.com

Spectrometer for Raman Microscopy

The UHTS 300 is a spectrometer designed for confocal Raman microscopy. Its high throughput enables nearly twice as much transmission as conventional spectrometers. High transmission is important in Raman spectral imaging, which requires thousands of Raman spectra to be acquired in a few minutes. With the UHTS 300, the acquisition time for a single Raman spectrum per image pixel is less than 100 ms. The new spectrometer delivers exceptional image quality and is supplied as an optional component for the WITec Confocal Raman Microscopy System CRM 200.

WITec For more information +49 (0) 700 94832 366 www.WITec.de

Technical Publishing Software

Publicon is software for composing sophisticated technical documents. Created for the growing number of academic researchers and industry professionals who need to create or publish documents with technical content, it produces platform-independent files that can be exported to HTML, XML, or custom Publicon formats. Built-in palettes, templates, and style sheets simplify the creation of documents that conform to industry-standard formats, but also allow for complete customization to match any style. Its many features that streamline the publication process include a guided, template-driven document creation system, a scrolling, WYSIWYG interface suitable for online presentation, automatic conversion to and from MathML, math and chemistry typesetting for word processor-like equation composition, full searchability within typeset equations for any character, automated reference management for instant bibliographies, notes and cross-reference insertion tools, style sheets that control all

For more information visit **GetInfo**,
Science's new online product index at
<http://science.labvelocity.com>

From the pages of GetInfo, you can:

- Quickly find and request free information on products and services found in the pages of *Science*.
- Ask vendors to contact you with more information.
- Link directly to vendors' Web sites.

aspects of a document's functionality and appearance, spell-checking with a built-in technical dictionary, platform-independent document creation, and more.

Wolfram Research For more information 217-398-0700 www.wolfram.com

Treadmill

The Rota-Rod treadmill can accurately test motor coordination and fatigue in rodents in order to measure the effects of drugs, brain damage, or disease on animal behavior. New features help researchers accurately measure motor coordination and fatigue. Easy-to-operate controls let the user alter the speed at which the treadmill turns, and an advanced timing mechanism allows for precise measurements. The Rota-Rod can be set at either a constant speed or a gradual acceleration, controlled by a microprocessor with an LCD display.

Stoelting For more information 630-860-9700 www.stoeltingco.com/physio



IgG Subclasses Kit

Human IgG comprises four different subclasses that differ in their biological functions, which include antigen recognition, complement activation, and receptor binding. Altered serum levels of IgG subclasses have been shown to be associated with many diseases, such as respiratory tract infection, autoimmune diseases, neurological disorders, and HIV infections. Cell Sciences' human IgG subclasses enzyme-linked immunosorbent assay kit is a sensitive, specific, and reproducible assay for quantitative determination of human IgG subclasses in serum.

Cell Sciences For more information 888-769-1246 www.cellsciences.com

Assay Workstation

The Biomek Assay Workstation is suitable for drug discovery research, and has been optimized for cell-based screening and enzyme-linked immunosorbent assays (ELISAs). The new workstation can be configured with either the Biomek FX or NX liquid handlers, providing multiple pipetting and configuration options for different capacity, throughput, and lab space requirements. The system is integrated with the DTX Series multimode detector, which offers absorbance, fluorescence, and luminescence detection. The system's software incorporates new dynamic scheduling capabilities that allow the user to create methods and run multiple assays for increased throughput and resource utilization. The new graphical interface, with language geared specifically to the scientist, makes assay design easier.

Beckman Coulter For more information 800-742-2345 www.beckmancoulter.com

Newly offered instrumentation, apparatus, and laboratory materials of interest to researchers in all disciplines in academic, industrial, and government organizations are featured in this space. Emphasis is given to purpose, chief characteristics, and availability of products and materials. Endorsement by *Science* or AAAS of any products or materials mentioned is not implied. Additional information may be obtained from the manufacturer or supplier by visiting www.science.labvelocity.com on the Web, where you can request that the information be sent to you by e-mail, fax, mail, or telephone.